Observing shelf sea oxygen dynamics with autonomous observation systems

A thesis submitted to the School of Environmental Sciences at
the University of East Anglia in partial fulfilment of the
requirements for the degree of Doctor of Philosophy

Tom Hull

September 2020

Abstract

This thesis provides new estimates for net community production (NCP) from two North Sea regions, using high temporal resolution oxygen measurements from a long-term monitoring buoy and from a fleet of submarine gliders during a pilot monitoring program. The buoy study reveals a net-heterotrophic system (O_2 NCP $= (-5.0 \pm 2.5)\,\mathrm{mol\,m^{-2}\,a^{-1}}$), despite a highly productive spring phytoplankton bloom (maximum O_2 NCP $>(485 \pm 129)\,\mathrm{mmol\,m^{-2}\,d^{-1}}$). The glider study uses both oxygen and nitrate mass-balances and demonstrates new production rates consistent with Redfield (an O:N ratio of 8.7) during the Spring bloom (O_2 NCP $= (232 \pm 12)\,\mathrm{mol\,m^{-2}\,d^{-1}}$, NO_3^- NCP $= (26.8 \pm 0.7)\,\mathrm{mmol\,m^{-2}\,d^{-1}}$).

In addition, bottom mixed layer oxygen dynamics are explored using an array of seabed landers in the Celtic Sea. The oxygen fluxes, including respiration, are calculated and compared with incubation studies performed during the same observation campaign. The bottom mixed layer oxygen consumption is shown to be broadly similar to that as calculated by the incubation studies (O_2 NCP ranged between $30\,\mathrm{mmol\,m^{-2}\,d^{-1}}$ to $47\,\mathrm{mmol\,m^{-2}\,d^{-1}}$). However, the time series reveals temporal variations which are missed with the incubations, including post-bloom increases in consumption and possible re-suspension-driven events. There is also evidence for large persistent vertical fluxes of oxygen.

For shelf sea oxygen time series based NCP estimation, the largest source of uncertainty is derived from the determination of a representative water mass with which to perform an analysis, and the subsequent integration of oxygen observations. Spatial heterogeneity is often overlooked in both open-ocean and shelf-sea based studies. It is shown that the choice of which fluxes need to be quantified, and the length scales that observations should be integrated over, is highly dependent on the dynamics of the particular study region.

Access Condition and Agreement

Each deposit in UEA Digital Repository is protected by copyright and other intellectual property rights, and duplication or sale of all or part of any of the Data Collections is not permitted, except that material may be duplicated by you for your research use or for educational purposes in electronic or print form. You must obtain permission from the copyright holder, usually the author, for any other use. Exceptions only apply where a deposit may be explicitly provided under a stated licence, such as a Creative Commons licence or Open Government licence.

Electronic or print copies may not be offered, whether for sale or otherwise to anyone, unless explicitly stated under a Creative Commons or Open Government license. Unauthorised reproduction, editing or reformatting for resale purposes is explicitly prohibited (except where approved by the copyright holder themselves) and UEA reserves the right to take immediate 'take down' action on behalf of the copyright and/or rights holder if this Access condition of the UEA Digital Repository is breached. Any material in this database has been supplied on the understanding that it is copyright material and that no quotation from the material may be published without proper acknowledgement.

Contents

List of Figures

List of Tables

Acknowledgements

I would like to blame Martin for not nipping this ridiculous ”get a PhD” idea in the bud when he had the chance. For believing in me, offering his guidance and his great ideas. I thank Naomi as mentor and for basically turning me into a scientist, assuming I count as one now. Jan for his apparent boundless drive to make things correct. His attention to detail and perseverance has made my work infinitely better. I don't know how you get some much done with your day.

Thanks to The Centre for Environment, Fisheries and Aquaculture Science for providing the space, freedom and funding. This work was made possible through Cefas Seedcorn and the Cefas-UEA strategic alliance. The Warp SmartBuoy is funded through DEFRA SLA25. The Celtic Sea lander and buoy deployments were funded though the UK NERC/DEFRA Shelf Sea Biogeochemistry (SSB) program. (https://www.uk-ssb.org/) grant numbers NE/K001914/1 and NE/K001957/1. AlterEco (https://projects.noc.ac.uk/altereco/) was funded by NERC/DEFRA grant numbers NE/P013899/1, NE/P013902/2, NE/P013740/1 and NE/P013864/1. Additional thanks to those who provided supplementary data.

To Bastien Queste for the various (mostly) glider related shenanigans. Charlotte Williams for her contributions to AlterEco, and as fellow comrade united against the forces of bad oxygen data. Tim Jickells, Clare Ostle, Julianne Wihsgott, Rob Hall and Matthew Palmer for the fruitful discussions. Jonathan Fellows for his long friendship, mathematical insights and supportive suggestions, which were frequently humbling as much as they were helpful.

Most importantly I thank Briony for her support, understanding and love. Her humour, positive outlook and moral compass makes this world so much better and brighter.

Chapter 1

Shelf seas in the context of oxygen, gas exchange and productivity

The coastal shelf seas are a vitally important human resource for numerous ecosystem services, including food, carbon storage, biodiversity, energy and livelihoods (Halpern et al., 2015). 90 % of the global fish catches are provided from the shelf and coastal waters (Pauly et al., 2002; Sharples et al., 2013). They have a disproportionately large impact, relative to their surface area, on global carbon cycling (Thomas, 2004) as these regions provide 10-30 % of all marine primary production while comprising less than 10 % of the ocean surface (Harris et al., 2014; Sharples et al., 2019). The shelf seas are commonly defined as comprising the zone starting at the coast and moving down to 200 meters depth (Halpern et al., 2008; Harris et al., 2014). These regions are 3-4 times more productive than the open ocean (Muller-Karger et al., 2005) and host a high diversity of primary producers which are supplied with abundant nutrients from the shelf edge and rivers (Sharples et al., 2017). They are thought to contribute 12 % of the global primary production, 71 % of the carbon flux to sediments (McKinley et al., 2017) and provide more than 55 % of natural marine carbon storage (Diesing et al., 2017; Legge et al., 2020). The coastal seas therefore play a particularly important role by linking the oceanic, atmospheric and terrestrial carbon reservoirs (Thomas, 2004). Given their global role in carbon cycling, understanding the mechanisms driving these processes is vital for predicting how these systems will respond to and influence climate change (Palevsky et al., 2013; Legge et al., 2020).

The shelf seas are also the marine regions which are most vulnerable to direct anthropogenic impacts; through overfishing, resource exploitation, habitat loss and pollution (Jickells, 1998; Halpern et al., 2015). They are the locations of greatest human density with 9 % of the global population live within 20 km of the coast (Kummu et al., 2016). The impact of overfishing has been enormous to shelf sea ecosystems and the associated damage to the trophic structure makes the remaining ecosystem components more vulnerable to other disturbances (Jackson et al., 2001). The potential for the shelf seas to mitigate climate change though carbon storage is being reduced by habitat loss and benthic disturbances (Luisetti et al., 2019). Various pollutants have been introduced including heavy metals, radionuclides and organic contaminants such as PAH and PCBS (Emeis et al., 2015). High nutrient inputs, typically from agricultural run-off and wastewater, can result in enhanced biological oxygen demand with deleterious consequences for coastal ecosystems and fisheries (Jickells, 1998; Diaz and Rosenberg, 2008). In addition to the negative impact on biodiversity and ecosystem function (Plumeridge and Roberts, 2017).

1.1 The biological carbon pump

Multiple ocean processes play key roles in the cycling of carbon. Of particular interest is the so called biological carbon pump (Volk and Hoffert, 1985), through which carbon is removed from the atmosphere, fixed by photoautotrophic organisms and some fraction of it is subsequently exported from the euphotic zone to subsurface waters.

Within the shelf seas the biological pump is strong, with high productivity driven by high nutrient inputs from rivers and atmospheric deposition coupled with efficient use of those nutrients (Thomas, 2004). In some shelf seas much of the fixed carbon is not stored or respired locally, but exported to the deep open ocean, a process known as the continental carbon pump (Bozec et al., 2005). This is a major flux and a vital component of the earth carbon system as these regions are thought to account for 20 % of the worlds ocean uptake of anthropogenic carbon dioxide (Thomas et al., 2005a).

Understanding how these pumps change in response to climate change is important to allow the prediction of potential feedbacks to anthropogenic CO_2 increases. However, there are significant uncertainties in both the mechanisms and magnitude of the fluxes involved (Bauer et al., 2013). Indeed for many ecosystems, including large parts of the open ocean, it is unclear if they are net sources or sinks for carbon (Ducklow and Doney, 2013). While most of the present day coastal ocean is believed to be a net sink for atmospheric CO_2 the large degree of heterogeneity in coastal systems leaves most carbon fluxes with high uncertainties (Laruelle et al., 2018). Typically the estimated fluxes in enclosed seas have uncertainties up to 75 % and even the best constrained coastal carbon fluxes are only within 50 % (Bauer et al., 2013). Over the last two decades the shelf sea uptake of CO_2 has increased (Laruelle et al., 2018), a trend thought to be driven by faster shelf-edge exchange and increased primary production through increased anthropogenic nutrient inputs (Jickells, 1998; Legge et al., 2020). As in the temperate shelf seas, productivity is limited by the availability of light in winter and nitrogen sources in summer (Smyth et al., 2014).

1.2 Shelf sea oxygen dynamics

Shallow fully mixed regions of the shelf seas consist of a water column which is entirely ventilated through persistent vertical mixing and constant exchange with the atmosphere. Other deeper or less turbulent regions see seasonal stratification, where the upper layers of the water column become separated from those below by a seasonal pycnocline. This acts as a semi-permeable barrier to the exchange of heat, salt, nutrients and gases such as oxygen.

The spring phytoplankton bloom is a characteristic feature of productivity in the temperate shelf seas. The exact mechanisms for controlling bloom initiation are still an open question (Powley et al., 2020), but it is generally believed to be through a complex function of nutrient availability, reduced turbulent mixing, light climate and predator-prey interactions (Smyth et al., 2014; Behrenfeld and Boss, 2014). The bloom is typically short in duration, lasting no more than a few weeks, with growth becoming limited by nutrient availability and/or by predation. The magnitude of the carbon fluxes due to the high productivity and subsequent respiration can be large, and contribute a large fraction of the annual carbon budget.

Following the bloom, stratified regions typically develop a subsurface chlorophyll maximum. Here at the base of the seasonal pycnocline, supplied with nutrients from below by diapycnal mixing or entrainment while still experiencing the necessary irradiance, phytoplankton productivity persists throughout the summer (Weston et al., 2005; Wihsgott et al., 2019). In winter the cooling water temperatures and reducing light availability limit phytoplankton production.

While the shelf seas share many common characteristics, they do vary significantly in their physical and biogeochemical properties. They are each, to some extent, unique, and care should be taken not to assume processes or rates observed in one shelf sea will readily translate to another.

1.2.1 Oxygen depletion

There has been a global decline in oceanic dissolved oxygen and an increase in the extent of oxygen minimum zones, which given oxygen's vital role in biological processes has serious implications for ecosystem function (Schmidtko et al., 2017). At it's most simplistic, oxygen depleted waters can not sustain many forms of life and even a slight reduction in oxygen can influence the behaviour of larger, and often commercially important marine species.

Deoxygenation can occur over several different timescales, ranging from daily (diel) cycles, to tidal or otherwise episodic, seasonal and permanent (Kemp et al., 2009). The primary driver of ocean deoxygenation is believed to be increasing global ocean temperature which decreases the solubility of oxygen in water (Schmidtko et al., 2017). These changes to the oxygen inventory are tightly associated with changes in the air-sea oxygen flux, which itself is controlled by a variety of biological and physical processes (Najjar and Keeling, 2000; Doney and Steinberg, 2013). Increasing temperatures are also associated with enhanced metabolic rates and reduced ventilation of deeper waters due to increased stratification (Greenwood et al., 2010). Globally ventilation is expected to continue to decrease with increasing stratification and weakening of oceanic overturning circulation (Breitburg et al., 2018).

Oxygen minimum zones (OMZ) are those areas, through natural or anthropogenic forcing exhibit a permanent oxygen deficiency. These low oxygen regions see their ecosystem constrained to be less energy-intensive, with associated shifts in marine food webs and reduced biodiversity (Breitburg et al., 2018). These regions can arise naturally due to a region's natural tendency for long water residence times with restricted ventilation or through high inputs of organic carbon. The expansion of these regions however is associated with changes in ventilation and biological activity (Große et al., 2016). Stronger or more enduring stratification is thought to reduce ventilation of bottom waters, and increased temperatures increasing metabolic rates and associated oxygen consumption (Greenwood et al., 2010; Große et al., 2016). Changes in community productivity can affect how organic material is exported to and respired within the non-ventilated sub-thermocline waters (Große et al., 2017).

Many forms of biogeochemical cycling are strongly influenced by changing oxygen conditions, forming a complex and at times poorly constrained system. The expansion of the low oxygen zones can increase the production of nitrous oxide, a potent greenhouse gas, and contributing to climate change as a negative feedback loop (Kitidis et al., 2017). Nitrification is an oxic process and is thus confined to areas with sufficient dissolved oxygen present. In the absence of oxygen, nitrate and nitrite are used by microbial denitrifiers (dissimilatory nitrate reduction to ammonium) and together with anammox (anaerobic ammonium oxidation) serve to remove nitrogen from the marine system. Thus the marine nitrogen cycling is closely coupled to oxygen concentration (Neubacher et al., 2013; Kitidis et al., 2017). The cycling of iron, an essential micro-nutrient for marine primary productivity, is also affected, as oxygen concentrations influence iron bioavailability (Klar et al., 2017).

The stratified shelf seas are particularly vulnerable to deoxygenation partly due to their small sub-thermocline volume and large organic carbon inputs (Emeis et al., 2015). The majority of the shelf sea sediment is well below the photic zone such that the distribution and consumption of oxygen is controlled by sediment type and the supply of organic matter from surface waters (Queste et al., 2016; Thompson et al., 2017). Future ocean model predictions suggest that some coastal systems will have the additional pressure of increased nutrient delivery from watersheds which experience increased rainfall due to climate change (Breitburg et al., 2018). Other studies suggest reducing nutrient inputs in some seas, with associated reduced primary production affecting the oxygen dynamics in a counteracting way (Capuzzo et al., 2018). Predicting the magnitude and spatial distribution of future oxygen loss is hampered by insufficient data and the lack of mechanistic understanding of oxygen dynamics at a variety of scales (Doney and Steinberg, 2013; Greenwood, 2016; Breitburg et al., 2018).

1.3 Net community production

The first stage of the aforementioned biological carbon pump is the removal of carbon from the atmosphere by photoautotrophic organisms (primary production, P). Some of the newly fixed carbon is respired (R) locally within the euphotic zone, while some fraction may sink below to subsurface waters as particulate organic carbon. The balance between the primary production and respiration is known as the net community production (NCP) (Williams, 1998), denoted by the symbol J.

$$J = P - R \tag{1.3.1}$$

If production exceeds the community respiration (positive NCP) then there is a net draw down of CO_2 into the ocean and indicates a net autotrophic system. Negative NCP signifies a net release of CO_2 and net heterotrophy. NCP therefore quantifies the flux of carbon between the atmosphere and the ocean, while the sign of the term signifies if the ocean is acting as a source or sink. In environments devoid of primary production NCP is a useful measure of quantify carbon remineralisation (Larsen et al., 2013; Glud et al., 2016; Hicks et al., 2017).

In the open ocean on annual time scales NCP is thought to be in approximate equilibrium with export production; the flux of organic carbon in particulate or dissolved form from the surface ocean to the interior (Laws, 1991; Pelland et al., 2018). This does not appear to hold for many shelf sea systems as a significant fraction of the annual production appears to be stored as organic matter within some shelf sea sediments (Johnson et al., 2013). This long-lived pool of carbon, which has a lifetime of at least several months, contributes to a non-steady state of the carbon integrated over a full seasonal cycle (Humphreys et al., 2018).

Estimating NCP rates in the ocean is notoriously difficult (Williams et al., 2013a; Duarte et al., 2013). This is in part because the net state is finely balanced between large opposing fluxes, the measurements of which have large uncertainties (Ducklow and Doney, 2013). Observational studies are relatively few in number and often fail to resolve the seasonal, inter-annual and spatially heterogeneous shelf sea dynamics. These fluxes are therefore not well represented in global or regional biogeochemical models and improvements are needed to better out understanding of this important component of the global carbon cycle.

Observational approaches have broadly fallen into 3 categories; in-vitro incubation experiments, ocean colour remote sensing products and in-situ geochemical mass-balance methods. It is primarily the latter which is explored within this thesis.

1.3.1 Net community production as an indicator of ecosystem health

NCP, in addition to describing an key process within the carbon cycle is also useful as a purely biological indicator. From a ecosystem function perspective NCP can be considered an indicator of the "vigour" of an ecosystem; the ability for a system to maintain or renew it's structure (Tett et al., 2013). It has already been used in this context as a monitoring tool for tracking the health of coral reefs ecosystems (Silverman et al., 2004; Takeshita et al., 2016), and could be expanded more broadly to other ecosystems.

The continental shelf regions are under significant pressure from various anthropogenic stresses, and many of these directly impact carbon cycling, ecosystem function and the oxygen dynamics (Bauer et al., 2013; Laruelle et al., 2018). Which, given the importance of the shelf seas can have global consequences. Effective management of the shelf seas requires adequate monitoring (Painting and Forster, 2013). This drives the demand for good quality, cost-effective observations of environmental status indicators (Platt and Sathyendranath, 2008). Furthermore monitoring studies provide a vital context for marine science and has driven the development of a critical scientific understanding of the marine system (Bean et al., 2017). There is a demand for a more holistic ecosystem function-based approach to monitoring the oceans, rather than traditional threshold based measures (Painting et al., 2013; Bean et al., 2017). The rates of autotrophic production and oxygen consumption hold the potential for becoming important indicators of ecosystem health (Painting et al., 2013).

There is also the need for compliance with local and international legislation which has substantially increase the demand for monitoring the status and health of marine ecosystems (Bean et al., 2017). The OSPAR Commission define eutrophication as “the enrichment of water by nutrients causing an accelerated growth of algae and higher forms of plant life to produce an undesirable disturbance to the balance of organisms present in the water and to the quality of the water concerned” (Foden et al., 2011). Importantly it is the undesirable ecological consequences from anthropogenic nutrient enrichment, and not the normal conditions seen with a naturally enriched system which are the concern (Tett et al., 2007). Tett et al. (2007) argue that algal biomass and primary production measurements alone do not provide the necessarily information for determining and predicting undesirable consequences. One of the primary undesirable consequences is the aforementioned oxygen depletion (Tett et al., 2013) therefore, quantifying NCP and related marine oxygen fluxes is important for understanding eutrophication.

1.3.2 Monitoring and autonomous systems

As mentioned above, a large fraction of the production in the shelf sea is localised to episodic events with patchy spatiotemporal dynamics (Greenwood et al., 2012; Johnson et al., 2013; Wihsgott et al., 2019). Stanley et al. (2010) determined that even in the open ocean the spatiotemporal variation inherent in the ocean must be taken into account to correctly assess NCP. Using traditional "station" type sampling would mean several high-productivity events would not be observed. For shelf seas the scales of variability are often even shorter such that resolving these events using a typical biweekly or monthly ship-based sampling program, using either underway or incubation based methods, would not have sufficient resolution to capture the productivity of a shelf sea spring bloom (Greenwood et al., 2011).

In both the shelf seas and open ocean NCP has been shown to sometimes disagree with export estimates over both small (< 10 km) (Alkire et al., 2012) and large (Haskell and Fleming, 2018) spatiotemporal scales, it is currently unclear if the disparity is due to biases inherent in the methods or if there are actual differences between NCP and export due to decoupling of the processes. Haskell et al. (2019) argue that higher-resolution measurements of either NCP or export are required to quantify the spatiotemporal variability in these processes and to understand the causes of the disparity. Monitoring of our oceans at appropriate temporal and spatial resolution and sustaining the observations to disentangle seasonal and inter-annual variability is essential to understand and predict future change.

There is a desire to reduce the costs associated with marine monitoring (Bean et al., 2017). The cost of vessel based monitoring can be prohibitive, and increasing the frequency of a ship based sampling programs is not usually feasible (Bean et al., 2017). Efforts have been made to incorporate ships of opportunity, such as ferries into monitoring programs (Hydes et al., 2009) and Ostle et al. (2014) used such a platform for determination of large scale NCP. Autonomous monitoring systems, such as buoys, landers and vehicles such as buoyancy gliders offer the ability to observe oxygen dynamics at high temporal resolutions over long periods of time (Greenwood et al., 2011).

It has been suggested that there is potential to improve monitoring and better inform decision-making by adopting a “total ecosystem approach” (Bean et al., 2017). Such an approach consists in establishing a dynamic model of the ecosystem, which presents a coherent view of the current state of the system, and useful predictions of future change. Initial monitoring is essential to parameterise the relationships within this model, and can be targeted at the areas where the model shows greatest uncertainty (Bean et al., 2017). NCP represents a key structural element within this monitoring model and as such observations of NCP can be used to validate the coherence of said monitoring model.

1.3.3 History of NCP determination

Over 60 years ago Odum (1956) proposed a framework for the estimation of gross primary production (GPP) and community respiration (CR) from open-water diel oxygen curves. This approach, often referred to as the Odum method (Cox et al., 2015), has a focus on lakes, wetlands, streams and estuaries at the local scale (Hoellein et al., 2013). Independently and with a more global perspective, Emerson (1987) proposed a broader scale method for determining NCP from longer term observations of oceanic oxygen concentrations. There appears to be little overlap in citations between the followers of Emerson or Odum (Ducklow and Doney, 2013; Hoellein et al., 2013; Bushinsky and Emerson, 2015; Holtgrieve et al., 2016). The core idea is the same however; to predict the non-biological evolution of oxygen over time and compare it with subsequent observations, any deviation from the prediction is assumed to be due to biological processes. The limnology studies typically consider air-water gas exchange a relatively minor term, and some approaches resolve to infer the air-water gas exchange from the diel curve (Holtgrieve et al., 2010). Net community production is referred to by various other names across the marine and freshwater literature; in limnology circles it is often referred to as aquatic ecosystem metabolism (Hoellein et al., 2013).

1.3.4 Why use oxygen to derive NCP?

O_2 can be measured accurately and at high temporal resolution over long periods with relative ease (Wikner et al., 2013) and is the most widely measured property of seawater after temperature and salinity (McNeil and D’Asaro, 2014). The dominant process which determine atmospheric O_2 on short timescales ($<$ 1000 years) are chemical reactions with organic matter, photosynthesis, respiration and combustion (Keeling and Shertz, 1992). Biological oxygen production, at least over periods of a year or longer, is stoichiometrically related to net biological carbon production and export (Anderson and Sarmiento, 1994). This ratio is typically $\Delta O_2/\Delta C = 1.40$, although it can vary between 1.1 and 1.6 depending on the proportion of ammonium to nitrate used as the phytoplankton's nitrogen source (Laws, 1991; Anderson, 1995). While typically assumed to be static, Moreno et al. (2020) have recently demonstrated a positive temperature dependence of the O:C ratio in exported organic matter.

Oxygen is also the fundamental component for aerobic life on Earth, and more than half of it is produced by marine plants (Canfield, 2014). One species of marine phytoplankton (*Prochlorococcus*) is thought to contribute 5 % of global photosynthesis and be responsible for 20 % of global oxygen production (Canfield, 2014). Globally observations have shown that the open oceans have lost approximately 2 % of their oxygen content over the past 50 years (Helm et al., 2011; Schmidtko et al., 2017). Open ocean oxygen minimum zones (regions with $<70\,\mu\mathrm{mol\,kg^{-1}}$ at 200 m depth) expanded by 4.5 million $\mathrm{km^{-2}}$ between 1960-1974 to 1990-2008 (Stramma et al., 2010). In both the open ocean and hundreds of coastal zones oxygen concentrations are low enough to limit animal populations and impact nutrient cycling (Breitburg et al., 2018). The rapid expansion of these oxygen-minimum zones have crucial implications for marine productivity, biodiversity, and ecosystem services and threaten the survival of marine biota (Doney and Steinberg, 2013). Specifically, there is evidence that expanding hypoxia within the shelf seas could induce state changes to the structure and function of marine ecosystems (Stramma et al., 2010), with associated changes to biogeochemical processes such as organic matter and metal recycling, nutrient cycling (Neubacher et al., 2013), and changes to the efficiency of the biological pump.

Given that dissolved oxygen has been measured accurately for a relatively long time, parametrisation-based approaches to calculating NCP, detailed later, can be applied to historic data sets. Oxygen-based methods offer many opportunities to reveal new insights into historic data collected for other purposes.

1.3.5 Why not just measure CO_2 directly?

Typically oxygen fluxes are easier to observe and quantify than those of CO_2. Dissolved O_2 is chemically neutral while CO_2 reacts with water to form carbonic acid which further reacts with other compounds such as carbonates (Keeling and Shertz, 1992). Fluxes in dissolved CO_2 are typically 15 times smaller than fluxes of O_2, which requires more precise instrumentation to resolve fully. The equilibration time in the open ocean for dissolved CO_2 is 15 times longer ($\approx$ 1 year) compared to O_2 (a few weeks) (Keeling and Shertz, 1992; Kitidis et al., 2019). Measuring O_2 can constrain aspects of the global carbon cycle that cannot be constrained by CO_2 alone (Keeling and Shertz, 1992), and for many global CO_2 models, oxygen uptake rates are required for estimating the respired CO_2 inventory (Duteil et al., 2013).

Direct observation of CO_2 is particularly challenging for autonomous platforms where power, size and instrument stability is a significant concern. In-situ pCO_2 instruments exist although these are still in development and are not currently used within monitoring programs (Clarke et al., 2017; Possenti et al., 2020). Oxygen optodes by contrast are being frequently used across all autonomous platforms and most biogeochemical monitoring programs (Bittig et al., 2018b).

1.3.6 Bottle incubations

There has generally been poor agreement between NCP calculated using biogeochemical mass-balance and classical incubation techniques, both in-vitro or in-situ (Mouriño-Carballido and Anderson, 2009; Williams et al., 2013b). There is an implicit assumption with in-vitro approaches that the organisms of interest are both correctly captured within the sample and that they behave the same in-vitro as they do in-situ. Karl et al. (2003) argued that as ocean productivity is typified by short intensive bursts of photosynthesis followed by slow and steady respiration, random discrete sampling will tend to incorrectly bias NCP estimates, typically towards net heterotrophy. They argue that mass-balance techniques, which integrate over both the autotrophic and heterotrophic phases are required to estimate the true metabolic state of the oceans. Long incubations may also lead to overestimates of community respiration as a result of a non-representative increase in the abundance of heterotrophic bacteria and a reduction of picophytoplankton (Mouriño-Carballido and Anderson, 2009). Therefore, failing to sample at a suitably high temporal resolution has the potential to severely bias production and respiration estimates (Karl et al., 2003). When the incubations are performed in-situ there are still issues regarding the so called "bottle effects" as even if the light and temperature conditions are representative of the local conditions, processes which exchange material with the rest of the water column are absent. These process can be important, as without this exchange biological processes may be controlled by the buildup of waste-products, accumulation of pathogens, changes in heterotrophic feeding behaviour or the depletion of nutrients to an extent which is not representative of the larger water column (Robinson et al., 2009). The highly seasonal nature of phytoplankton blooms, as well as the patchy nature of their distribution makes them particularly difficult to study without high resolution sampling (Alkire et al., 2012, 2014). Kaiser et al. (2005) similarly concluded that bottle incubations are not suitable to correctly represent the net metabolic balance over larger temporal and/or spatial scales.

1.3.7 Photochemistry

Respiration is not the only process which consumes oxygen in euphotic pelagic waters. Kitidis et al. (2014) demonstrated that non-biological photochemical oxygen demand can occasionally exceed respiration. Their study in the tropical Mauritanian upwelling showed rates of photochemical oxygen demand of up to 16 mmol m^{-3} d^{-1}. Oxygen photolysis rates correlated with absorbance of CDOM, indicating a potential avenue for a correction to NCP. Kitidis et al. (2014) therefore argue that all O_2 based methods underestimate NCP, as photochemical oxygen consumption will be incorrectly interpreted as respiration by a typical oxygen mass balance analysis. The implications for temperate waters will depend on CDOM load and local irradiance. This is particularly true for bottle incubations where the reactive oxygen species and hydrogen peroxide given off during photo-oxidation can inhibit photosynthesis.

1.3.8 Chlorophyll based methods

Ocean colour satellite products can be used to estimate gross primary production (Tilstone et al., 2015). However, the relationships between chlorophyll and productivity vary in different ocean regions, and ocean colour products must be calibrated and validated against in-situ data (Campbell et al., 2002; Palevsky et al., 2016). Satellites offer reasonable temporal and excellent spatial coverage but have several limitations. They can only observe the upper ocean, and are thus unable to observe the deep chlorophyll maximum, which can contribute a significant fraction (> 40 %) of annual shelf sea primary production (Fernand et al., 2013; Wihsgott et al., 2019). The spatial resolution of satellites often limits their use in coastal areas where land intersects the observation grid cell. Ocean colour products rely on reflectance from within the visible wavelengths of light and are thus further limited by cloud cover obscuring the view of the ocean surface. Interference from CDOM and suspended particulate matter can reduce the accuracy of ocean colour products in shelf sea waters (Jafar-Sidik et al., 2017). This is an issue particularly for high-latitude shelf seas, where cloudless days are infrequent and months can pass without acceptable imagery. Typically ocean colour products have a daily temporal resolution, with a single image being generated coincident with local noon. Remote sensing of NCP via ocean colour is in its infancy and similarly still requires calibration against reliable in-situ measurements (Tilstone et al., 2015).

Direct observation of chlorophyll in-situ can be combined with estimated or observed light fields to calculate gross primary production (Capuzzo et al., 2018). However, the relationship between chlorophyll fluorescence as measured with an in-situ fluorometer and chlorophyll, is not static and is dependent on several factors; which species of phytoplankton are present, their pigment composition, the species growth and life-stage; and the current degree of chlorophyll quenching due to incident light (Hemsley et al., 2015).

Active fluorescence methods, such as fast repetition rate fluorometry, are in-situ techniques for determining marine primary production at very high resolution (Robinson et al., 2009). This approach requires estimates of the electron transfer rates from which CO_2 uptake can be derived (Lawrenz et al., 2013), and these transfer rates vary related to environmental factors such as nutrient availability, salinity, temperature and light. While showing promise, these techniques are not currently used on long-term monitoring programs. As mentioned with regard to Odum (1956), it is possible to estimate both gross and net production using oxygen, but respiration can not be quantified with chlorophyll based techniques.

1.3.9 Look-behind vs look-ahead

Oxygen mass balance studies differ primarily based on what information is used to separate the physical and biological signals, which fluxes are observed, modelled or ignored and this is discussed further in later chapters. Calculating NCP from an oxygen mass balance can be split into two main approaches:

(1) A look-ahead approach where repeat observations are made in a discrete water mass. The evolution of oxygen in time is compared to that predicted through purely physical forcing, and the residual between the predicted and observed changes is inferred to be due to biological activity. This is suitable for a continuous oxygen time series of the same water mass (Emerson et al., 2008; Bushinsky and Emerson, 2015; Barone et al., 2019).

(2) A look-behind approach more suited to creating a synoptic view, typically from a research ship or with discrete samples (Kaiser et al., 2005; Seguro et al., 2019). Here historic physical forcing (i.e. wind) is used to estimate the amount of NCP that would result in an observed disequilibrium. A further approach is to use a secondary biologically inert tracer gas such as argon (Kaiser et al., 2005) or nitrogen (Emerson et al., 2008), which helps to separate the biological signal from the physical signal. Argon is a particularly good candidate due to its similar solubility to oxygen. The dual measurement of oxygen and an inert analog tracer allows determination of solubility changes with fewer uncertainties than using gas solubility parametrisations. However, while oxygen is a relatively routine parameter determined within monitoring programs and autonomous observing systems systems, observations using these secondary tracers have been restricted to a few dedicated research projects (Seguro et al., 2019).

1.4 Sources of uncertainty

Accurately quantifying NCP from oxygen time series can be challenging, with multiple sources of uncertainty. In part this is because NCP is the sum of two large opposing fluxes. Furthermore, the relevant sources of uncertainty can change depending on the platform from which the oxygen measurements are taken, the availability of ancillary data, and the structure of the environment in question. For instance with a strongly fully mixed water column the uncertainty regarding the volume of water which is being ventilated can be very small. It is simply reduced to the total water column depth, which even with a non-profiling observation platform can be well constrained with bathymetry products such as GEBCO. However with a stratified water column the number and magnitude of the sources of error increases. The primary source of uncertainty relates to the volume of water being ventilated which is both more difficult to determine and variable, potentially on

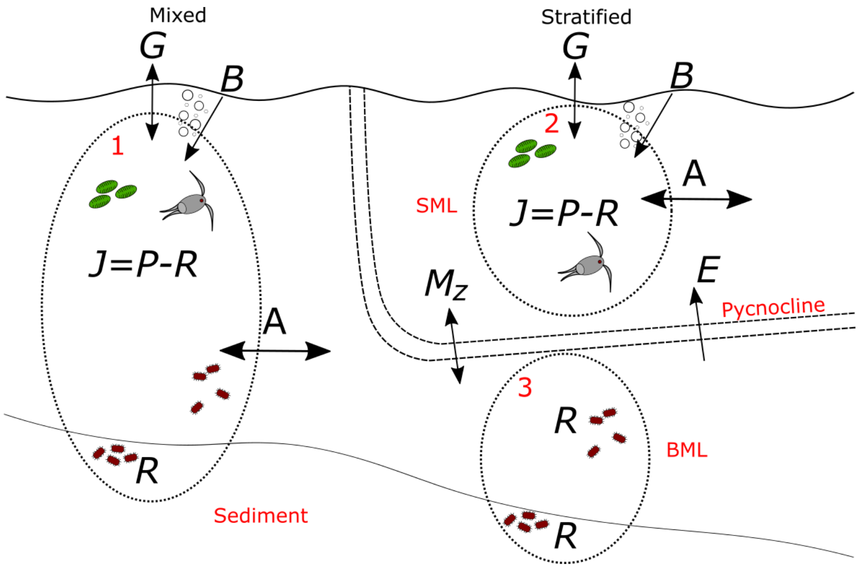

Figure 1.4.1: Summary of the various fluxes which need to be quantified for a shelf sea oxygen mass-balance. $G=$ air-sea gas exchange, $B=$ bubble induced supersaturation, $J=$ net community production (NCP), $P=$ primary production, $R=$ community respiration, $M_z=$ diapycnal mixing, $E=$ entrainment, $A=$ horizontal advection and mixing.

hourly timescales.

Figure 1.4.1 summarises the various fluxes which need to be quantified for a shelf sea oxygen mass balance. The dotted zone 1 represents a well mixed system, as at the Warp SmartBuoy in Chapter 3 and also, due to the way we determine the mass balance for the AlterEco dataset in Chapter 5. Zone 3 describes a stratified bottom mixed layer as seen by the landers in Chapter 4, while zone 2 represents a surface mixed layer only mass-balance, an example of which is discussed in section 6.1.2.

Woolf et al. (2019) argue that for air-sea CO_2 fluxes the largest source of uncertainty is the air-sea gas transfer velocity. However, for oxygen-based net community production estimates which also require accurately tracking changes in oxygen inventory this is not likely to be true. In systems close to equilibrium with the atmosphere it is important to note that air-sea gas transfer velocity uncertainty only changes the magnitude of the flux, not the sign, i.e. whether the gas flux is into or out of the sea. We explore the uncertainties associated with air-sea gas transfer in Chapter 2.

1.4.1 Shelf sea complexity

Shelf sea regions are typically more dynamic than the open ocean and have extensive natural variability on a variety of scales (Emeis et al., 2015). For example, on short time scales, tidal forcing on cross-thermocline fluxes has been shown to be a major control of primary production, as the spring-neap tide can drive nutrient fluxes from the bottom mixed layer into the productive euphotic waters above (Sharples et al., 2007; Wihsgott et al., 2019). While on longer timescales, multidecadal variations in the atmospheric circulation in the North Atlantic have been shown to influence the circulation within the semi-enclosed North Sea (Emeis et al., 2015; Stanev et al., 2019).

These dynamics remain a challenge for numerical models (Polton et al., 2013). The complexity, resolution and integration time of shelf sea biogeochemical models are often insufficient to unravel natural variability from anthropogenic perturbation (Emeis et al., 2015), and implementing models that constrain the exchanges and fates of different forms of carbon in coastal settings remains difficult (Bauer et al., 2013).

Many of the assumptions made for global or open ocean NCP studies, such as horizontal homogeneity, do not hold for shelf seas. In addition, within the shallow shelf-seas benthic processes can be important controls on the water column properties (Kitidis et al., 2012), which would be negligible in the open ocean.

1.4.2 Mixed layer depth as a proxy for ventilation depth

The height of the ventilated water volume (z_{mix}) is equivalent to the active turbulent mixing depth, the depth to which wind stress forcing is overcoming buoyancy (Moum and Smyth, 2001). Within this region temperature, salinity, oxygen and most other seawater properties are almost homogeneous in the vertical (Woolf et al. (2016), 1.4.2). Direct observations of the depth to which turbulent mixing is occurring are rare (Kara et al., 2000; Palmer et al., 2008). Typically the surface mixed layer depth (SMLD) is estimated from density or temperature profiles, and this is used as a proxy for the actively mixed depth. There are a range of definitions for SMLD (Kara et al., 2000; Thomson, 2003; de Boyer Montégut, 2004), using a variety of methods. However the most common approach consists of selecting a reference depth and defining the SMLD as the depth where a water property differs from the reference by some threshold value. From an oxygen mass balance point of view it would seem sensible to define z_{mix} based on the vertical structure of oxygen (Castro-Morales and Kaiser, 2012). Many studies use 10 m as the reference depth, which may not be appropriate for shelf-sea studies with high temporal resolution data or where there are significant vertical gradients in the top 10 m of the water column.

Heating of the sea surface, which is primarily by solar (short-wave) radiation, stabilizes the water column and reduces upper ocean mixing (Moum and Smyth, 2001). Solar radiation during the day penetrates the air–sea interface but is limited by absorption and scattering to a few tens of meters, such that only the surface waters are warmed. Heat is also lost at the surface by long-wave radiation, evaporative cooling and conduction throughout both day and night.

When daytime heat inputs are high, and are combined with light winds, the actively mixed layer can become separate from the persistent thermocline during the day (Woolf et al., 2016). This diurnal layer is generally remixed into the bulk surface mixed layer by convention in the evening. However, during the day, it is the properties within this layer which control the air-sea gas exchange. This layer will usually be slightly more saline due to evaporation, but this may be counteracted by precipitation. We see that the ventilated volume could easily double with a rapid mixing event on timescale of hours, which has important implications for determining the oxygen mass-balance when using sub-daily observations.

A relaxation of wind stress also causes a reduction in the depth of turbulent mixing. This reduction occurs much faster than the erosion of the stratification at the base of the mixed layer, such that when mixing is reduced the actively mixed depth will be shallower than the apparent mixed layer depth (Kara et al., 2000). Put another way, observing a vertically homogeneous surface volume of water is not necessarily evidence for complete ventilation of that volume.

1.5 Oxygen observations

The "gold standard" method of determining the concentration of oxygen in seawater remains the Winkler method. Developed more than a hundred years ago the classical Winkler method if executed with care by a skilled operator offers very low uncertainty. It is however a demanding task that is affected by numerous uncertainty sources, such as contamination of the sample and reagents by atmospheric oxygen and iodine volatilization. Ultimately the accuracy of the

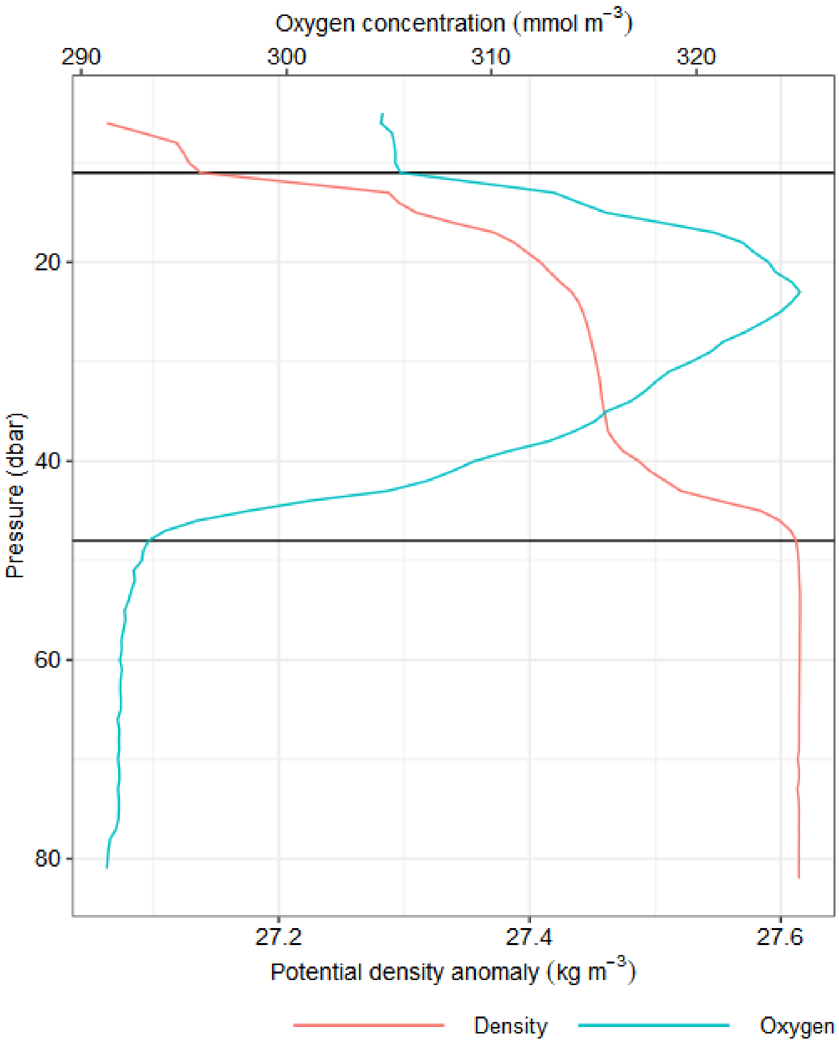

Figure 1.4.2: A vertical CTD profile taken during May 2018 in the central North Sea demonstrating the typical two-layer system encounter in much of the stratifying temperate shelf sea. A surface mixed layer shown above 11 dbar depth and demarcated by a horizontal line, and the bottom mixed layer between 47 dbar and the seabed. The pycnocline lies between and here we see evidence of oxygen production within this layer.

method is dependent on the quality of the KIO_3 standard. Various refinements have been made to the original Winkler method to increase accuracy and precision such that a routine shipboard precision of $\pm 0.15\,\mu\mathrm{mol\,kg^{-1}}$ can be achieved (Langdon, 2010). Gravimetric methods can achieve greater accuracy than the more typical volumetric technique, but these are not practical for use on board research vessels (Helm et al., 2012)

Plastic (typically PVC) Niskin bottles are the most popular form of sampling equipment for use with Winkler titration. These have also been shown to dissolve considerable amounts of oxygen and can take hours to ventilate out (Stevens, 1992). This can introduce artefacts in regions with sharp vertical oxygen gradients and can have implications for observations in oxygen minimum zones (Anders Tengberg. pers. comm.).

1.5.1 Optodes

Compared to membrane or galvanic marine oxygen sensors, optodes, such as as those manufactured by Aanderaa offer several advantages; they consume less power enabling use on platforms such as submarine gliders, are less vulnerable to fouling, and they do not consume oxygen, which is useful for closed system experiments. They are comparably stable, requiring less frequent recalibration and less maintenance (Tengberg et al., 2006; Tengberg and Hovdenes, 2014). While they are sensitive to pressure, there is no evidence for hysteresis (Uchida et al., 2008).

Optodes work by illuminating a fluorescing sensing foil known as a luminophore. The phase delay and amplitude of the light emitted is proportional to the partial pressure of oxygen in contact with the foil. The optode electronics measure this phase delay, which combined with the ambient temperature and calibration coefficients can be used to calculate the oxygen partial pressure (Tengberg et al., 2006). This partial pressure is then converted to a concentration using the oxygen saturation concentration using the temperature-solubility relationship of Garcia and Gordon (1992). The foil is not permeable to salts so a salinity and pressure correction is required to the measured concentration (Uchida et al., 2008). The most widely used foil is the PSt3 foil manufactured by PreSens, and used in the optode instruments made by Aanderaa, Seabird and RBR.

The "F" type foils previously mentioned omit the black opaque protective layer to the sensing foil, to reduce diffusion time of oxygen across the foil and thereby improve the response time of the instrument. The standard and fast foils have a response time (τ) of 25 s and 8 s respectively (Bittig et al., 2014). For mooring applications the response time of the standard foil is adequate, and offers improved long-term stability from the opaque layer. For profiling applications, such as on a shipborne CTD or submarine glider, the slow response of the optode will introduce "lag" artefacts (Bittig et al., 2018a). A comparison of two approaches used for correcting these artefacts is provided in appendix section D.2

The optode illuminates the sensing foil with both a red and blue LED. Since the red light does not produce fluorescence in the foil the phase measurements are obtained from the difference between the blue (P_1) and the red (P_2) excitation.

$$P_T = A(T) + (P_1 - P_2) \cdot B(T)$$

Where P_T is the temperature compensated phase (known as 'TCphase'). A and B are temperature dependent coefficients which allow for temperature compensation of the phase measurement. However for most 4330, 4831 and 4835 optodes these are not used such that $A(T) = 0$ and $B(T) = 1$. This can be confirmed by communicating with an optode and inspecting the 'PTC0Coef' and 'PTC1Coef' properties. For older optodes (serial numbers < 1000) temperature compensated phase is then used to calculate 'calphase' (P_c). For newer optodes $P_T = P_c$. Similarly older optodes have their calibration (and recalibration) applied though the modification of the 'PhaseCoef'coefficients. On later optodes the calibration is not applied in phase space, but on the oxygen concentration though the use of the 'ConcCoef0' and 'ConcCoef1' coefficents ('PhaseCoef0' and 'PhaseCoef1' are set to zero and 1 respectively). Unfortunately there is no visual indicator on the optode to represent which method is being used. Understanding these differences in how the calculations are performed is important when recalculating oxygen from the phase readings, such as when compensating for lag.

Over time the sensing foil becomes less sensitive to oxygen. For unknown reasons this drift in sensitivity occurs more rapidly when the sensor is in storage rather than when it is in use (Bittig and Körtzinger, 2015; Bittig et al., 2018b). Perhaps counter-intuitively, an old continuously used optode has much better long term stability than a new one freshly calibrated from the factory. Several studies have reported no detectable drift; Nicholson et al. (2008) reported no drift over a 9 month glider study and Hydes et al. (2009) determined no drift over a year of continuous use in a ferrybox system. Aanderaa describe the in-situ drift characteristics of the 4330 and 4831 series optodes as being < 0.5 % per year and they make no distinction between the standard or fast ("F"-type) foils (Tengberg and Hovdenes, 2014). The drift is believed to be due to bleaching of the luminophore foil via ambient light, it is particularly sensitive to fluorescent lights. The bleaching effect is partly counteracted by a destabilising effect on the luminophore. Together this manifests as a positive factor on the oxygen concentration (slope > 1) and a positive offset at zero oxygen. Optode foils appear to have a burning-in period; older optodes drift less, while new optodes can show drift of 6 % in two months (Tengberg and Hovdenes, 2014). Since 2016 Aanderaa optodes undergo a burning-in period before initial calibration. The drift is thus considered to be well described by a linear change in sensitivity with regard to time with the newer foils. Anecdotally is it clear to the UEA glider group that the drift observed in the fast response optodes is larger than that seen with the standard foils. A drift of 0.0004 % d^{-1} has been calculated based on UEA seagliders against Baltic deep water oxygen climatology (Possenti et al., 2020). Queste (2013) calculated a drift equivalent to 0.003 % d^{-1} for a 4330F type optode fitted to a Seagliders. Bittig and Körtzinger (2015) report a 10 % drift over 3 years, but this is a combination of in-situ and ex-situ drift. Bittig et al. (2018b) determined the drift to be typically 0.1-0.2 % per year in-situ. The drift correction should be applied to the oxygen concentration not measured phase (Bittig et al., 2018b). Optodes need to be kept moist before deployment, as they will typically read up to 2 % higher when dry (fig. 1.5.1). Hydration of the foil can take up to 24 hours. Recommendations are to keep optodes dark and moist prior to deployment and when in storage (Bittig et al., 2018b).

Optodes measure the partial pressure of oxygen in air as well as they measure in water. The mole fraction of oxygen in air is well known (0.20946) such that, given knowledge of the local atmospheric pressure and the relative humidity, in-air concentration can be easily determined. Thus for long term autonomous moorings, such as gliders or floats, in-air calibrations offer an opportunity to calculate and correct for optode drift (Bushinsky and Emerson, 2013; Bittig and Körtzinger, 2015; Bushinsky et al., 2016). Long term stability is only part of the picture however in terms of NCP estimation. While relative changes in concentration can provide estimates for the rates of change to the inventory, air-sea gas exchange is controlled by the actual disequilibrium, thus accuracy is still important. For ocean systems which are close to equilibrium with the atmosphere even the sign of the gas exchange may be difficult to determine. Thus it is essential that there is in-situ validation of optode observations with discrete Winkler samples.

In-situ calibration is essential for good oxygen data; the instruments cannot be

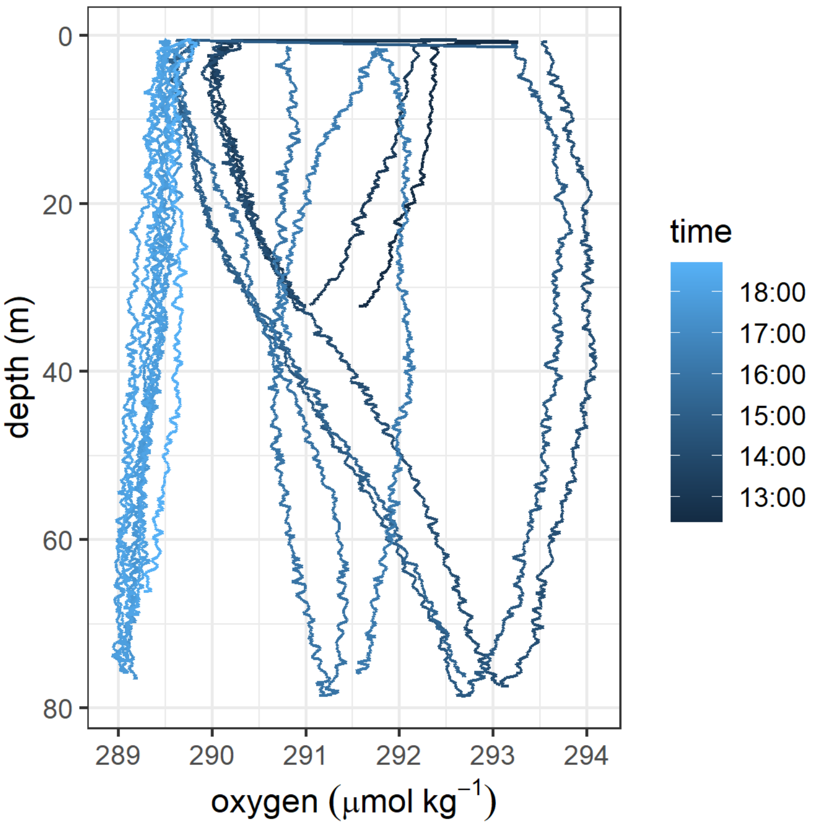

Figure 1.5.1: Oxygen profiles from Slocum glider "Stella" during AlterEco, Febuary 2018 in the central North Sea. Oxygen concentrations are anomalously raised by 2 % during the first few dives due to a dry optode foil.

expected to maintain their calibration parameters between lab or factory calibration and deployment (Bittig et al., 2018a). Aanderaa suggest the accuracy of a newly calibrated optode is within 3 % for a standard optode, and 1 % for a multi-point calibrated instrument using the Stern-Volmer equation, rather than the “mk2” equation (Uchida, 2010).

1.6 Statistical modelling of NCP

Determining NCP and other fluxes from an oxygen time series is a form of time series signal analysis. Classical time series analysis typically makes various assumptions regarding the nature of the data (Durbin and Koopman, 2012) such as stationarity or equal variance. Oxygen time series however can be characterised by several factors which confound the classical methods, including non-normal distributions, non-stationarity, serial correlations, fluctuating means and variance, data gaps, outliers, and regime shifts within the time series (Wikle et al., 2013).

Classical statistical methods usually model the data generating process as being highly idealised and simplistic, such as autoregressive and moving average models. However, when there is good understanding of the processes by which data is generated, a more robust approach is to use a mechanistic model that describes the temporal dynamics of the target phenomenon, such as the mass balance equation described above, and then optimise the model parameters so that the theory and observation are consistent. State-space models, also known as hidden Markov models, provide a methodology for this, and are applicable to a wide range of problems relating to time series analysis (Durbin and Koopman, 2012). The core principle is that the time evolution of the modelled system is determined by an unobserved (latent) series of variables corresponding to the system’s current state which are associated with a series of observations. Inferring the underlying system parameters from an observed processes is often also referred to as inverse-modelling. The relationship between the unobserved state and the observations is thus specified by the probabilistic state space model (Durbin and Koopman, 2012). The Kalman filter is a special case of state-space model which provide an analytical solution if the state space model is both linear and Gaussian. Such methods are used widely in data-assimilation; the blending of deterministic numerical models with observations (Wikle et al., 2013).

1.6.1 A Bayesian approach

While there are both frequentist and Bayesian interpretations for the state-space framework, there are several advantages to using a Baysian model. Primarily it forces the consideration and clear communication of what prior information we have used to best inform our mass balance flux estimates.

Uncertainty in inverse modelling of biogeochemical systems can arise from three types of source: observation uncertainty, process uncertainty, and model uncertainty. Observation uncertainty comprises the sensitivity, precision and measurement bias of the observations. This is usually relatively easily determined through experiment and calibration. All measurements contain some level of error, which when quantified can and should be included in a biogeochemical model. Process uncertainty comprises the inherent stochasticity or natural variability of the system components which comprise the model. Lastly the model uncertainty is the inability of the model to fully describe the processes of the real system, it is the mismatch between reality and the model (Holtgrieve et al., 2010).

When implemented in a Bayesian context, we can not only readily include all of the various sources of error, we can also include domain knowledge which would not normally be considered data. For example, when estimating autotrophic production we know that, by definition, this process does not consume oxygen and does not occur in the absence of light. We also know that past a certain point rates of autotrophic production are impossible. Thus despite having no data on the rates of production we can add a prior to production such that it is never negative. It is equal to zero when light is unavailable, and has a reasonable upper bound. Selecting good priors such as these reduces uncertainty in our parameter estimates (Gelman et al., 2017). Bayesian hierarchical models, also known as multi-level models, random or mixed effects models and a myriad of other names is a type of model specification where parameters sit at various levels and pool observations and other parameters together (Wikle et al., 2013).

This pooling has several advantages; estimates are improved for repeat sampling, such as when more than one observation exists for a location or time, as a single-level model will always maximally under fit or over fit these data; estimates are improved when there is an imbalance in sampling, such that if one group has many more observations, a hierarchical model prevents over-sampled groups dominating. They model variation between groups explicitly, such that we can avoid averaging, and thus arbitrary data transformations while retaining variation.

Although the hierarchical modelling paradigm is extremely powerful, it can often come at a substantial computational cost. When extending the state space modelling to non-linear or non-Gaussian models the model probability densities are no longer analytically tractable and must be approximated via simulation methods (Monte-Carlo). Markov chain Monte-Carlo (MCMC) are a class of algorithms which allow the sampling of the joint posterior distribution of a Bayesian model. The unobserved (hidden or latent) state variables in a time series analysis with N time steps will consist of N different highly correlated parameters. Such high correlation between variables tends to substantially slow down the mixing of MCMC and therefore increases computation time (Durbin and Koopman, 2012).

In chapters 4 and 5 we present the results of the probability models using credible intervals. These are analogous to the confidence limits used by frequentist methods, and indeed many researchers incorrectly interpret confidence limits as credible intervals (Wikle et al., 2013).

1.7 Summary and aims

As we have shown within this chapter, quantifying oxygen fluxes in the shelf seas is an important area of research. We therefore pose a series of questions. Can we improve the state of knowledge regarding shelf sea net community production using data collected from autonomous platforms? Specifically, can we reduce the uncertainties in NCP estimation to determine the overall metabolic balance within a region, and if so, do the regions appear to be in a steady state? Can we determine at what scale (temporal and spatial) future monitoring efforts would need to be performed to provide a useful metric of carbon cycling and ecosystem health? Can this all be done without radical change to existing autonomous marine monitoring infrastructure, and if not, what needs to be modified?

This thesis thus explores the general principle of isolating a biological signal from the physically driven elements within an oxygen time series at a series of shelf-sea locations. We see how depending on the choice of observation platform, availability of ancillary data and the local oxygen dynamics changes, which processes need to be included. The first chapter outlines the presumed most important flux in the oxygen mass-balance, air-sea gas exchange, as this is a complex topic and is known to be a significant source of uncertainty (Bushinsky and Emerson, 2015). This also lays the groundwork for the flux calculations used in the subsequent chapters where

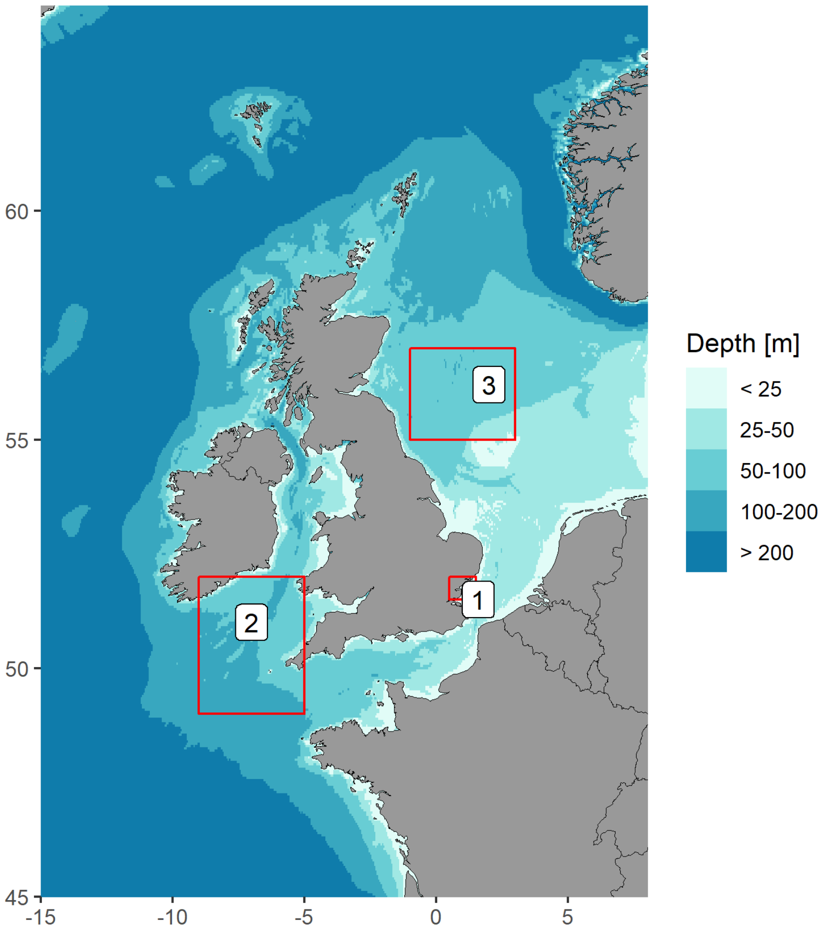

Figure 1.7.1: An overview of the study locations used in this thesis. (1) The Warp SmartBuoy, (2) The central Celtic Sea (3) The central North Sea, north of the Dogger Bank.

the largely open ocean based approaches to NCP are applied to the significantly more dynamic shelf seas. Chapter 3 explores the sensitivity and uncertainty of NCP using a half-hourly oxygen time series from a monitoring buoy in a fully mixed shelf sea location (fig 1.7.1 (1)). Here the system is assumed to have one degree of complexity removed as the uncertainty associated with a stratified water column is not present. The aim is to determine the largest sources of uncertainty and to determine the net metabolic state of the system over an annual cycle. Chapter 4 uses seabed landers fitted with current profilers to quantify the advection oxygen flux in a stratified shelf sea system (fig 1.7.1 (2)), a poorly constrained problem highlighted in Chapter 3. Accurate determination of oxygen consumption rates in the bottom mixed layer is required to better understand and predict oxygen depletion in stratified regions. In addition, the multiple landers and the long time series allow the exploration of the time dynamics and spatial heterogeneity in the oxygen inventory, a key knowledge gap in our understanding of how carbon is cycled on the North West European shelf (Thompson et al., 2017). Chapter 5 quantifies NCP from a prototype shelf sea glider monitoring program (AlterEco) (fig 1.7.1 (3)). Building on the prior work using gliders in a shallow and dynamic shelf sea setting (Queste et al., 2013) the implications and limitations of the monitoring strategy are explored. The large transect area allows the partial determination of biogeochemical patchiness, a potentially large and unconstrained uncertainty in understanding shelf sea productivity. The combined nitrate and oxygen data provides opportunities to compare spring bloom productivity between the methods. Recommendations for optimising future glider based monitoring programs are provided. The thesis concludes with a brief exploration of a particularly challenging buoy-based monitoring location, a discussion of the challenges of estimating NCP from underway platforms and recommendations for future work. An aim throughout is to provide insight into how oxygen mass balance NCP based monitoring can be operationalised for use in the shelf seas. In addition, efforts are taken to formalise our knowledge and uncertainty though modern statistical models, and explore the ”unknown unknowns” though simulation using our prior understanding of the systems of interest.

The data presented in the following chapters were all collected as part of wider observational programs. For quality assurance we developed a suite of software tools in the form of two `R` packages. The `airsea` package is publicly available (Hull and Johnson, 2015) and is discussed in more detail in 2, while the more general purpose `cefasMOS` package documentation is restricted for use by Cefas MOS staff.

Throughout this thesis the author is referred to with "we" (nosism). This is primarily for consistency with the published parts of the thesis. However, Tom has been responsible for all model design, data analysis and writing for all of the chapters and associated papers. Naomi, Jan and Martin have provided guidance, comments and review. Tom also contributed extensively to the maintenance, calibration and deployment for many of the SmartBuoy and lander deployments since 2010, and was responsible for deploying and calibrating the Seagliders during AlterEco. The quality assurance of these data was also his responsibility. He was also chiefly responsible for the CTD rosette on the Cefas Endeavour and the RV Princess Royal used in Chapter 5.

Chapter 2

Air sea gas exchange of oxygen

Woolf et al. (2016) describe the upper ocean from the perspective of air-sea gas exchange as consisting of several layers. There is an absolute interface in contact with the atmosphere, below which is a mass (or molecular) boundary layer. It is the disequilibrium across the mass boundary layer (ΔC, mol m^{-3}) which drives the air-sea gas exchange and turbulence near this interface controls the speed of gas transfer. The flux (G, mol m^{-2} s^{-1}) can be defined as the product of ΔC and the gas transfer coefficient k (m s^{-1}). k is also known as the gas transfer velocity or piston velocity under some models (Beale et al., 2014). Below the mass boundary layer is an actively mixed layer.

$$G = k\Delta C \tag{2.0.1}$$

Typically G is defined as negative for a flux from the atmosphere into the ocean (Wanninkhof et al., 2009).

It is not possible to directly measure the mass boundary layer concentration and we thus infer it from the atmospheric partial pressure under the assumption of Henry's Law (See section 2.1). This together with the "bulk" mixed layer concentration (C) is used as the concentration gradient across the air-sea interface (Woolf et al., 2016). The mixed layer concentrations can be observed by various means, whilst the atmospheric concentration for oxygen is formulated based on the equilibrium saturation concentration, calculated from the Henry's law solubility-corrected atmospheric mole fraction (C_{sat}, (Garcia and Gordon, 1992; Johnson, 2010)). Thus $G = k(C - C_{\text{sat}})$

Different gases are transported across the air-sea interface at significantly different rates (Wanninkhof et al., 2009). The bulk of the air-sea gas exchange literature concerns CO_2 and Dimethyl sulfide (DMS) (Wanninkhof et al., 2009). Compared to these gasses O_2 has a much lower solubility and is much more abundant (20.946 % of atmosphere). Bubble mediated transfer and supersaturation effects are proportionally more important to O_2 gas exchange than for CO_2 or DMS (see section 2.4), (Garbe et al., 2014). Due to it's low solubility in water oxygen transport is controlled primarily by the water side gas transfer coefficient ($k = k_{\mathrm{w}}$, see section 2.2) At low wind speeds (< 7 m s^{-1}) gas exchange is governed by diffusive and turbulent processes within the layer close to surface. While at higher wind speeds gas bubbles entrained in to the ocean by breaking waves significantly affect the total air-sea flux and this phenomenon is much less well studied, with the direction and magnitude of the effect depending on the gas in question (Bell et al., 2017; Liang et al., 2017). Bubbles act as small reservoirs of atmospheric gas which exchange said gases with the surrounding water as they are entrained and subsequently dissolve or return to the surface. Because bubbles are forced below the water surface they are subjected to increased hydrostatic pressure, this means that bubble mediated transfer is asymmetric and biased towards a gas flux into the ocean (Woolf and Thorpe, 1991). The size and distribution of the bubbles changes their behaviour and contribution to the air-sea gas flux. Small bubbles tend to rise slowly or dissolve completely, while larger bubbles rise faster and increase turbulence at the sea surface (Woolf et al., 2007). Bubbles that do not penetrate deep or dissolve can scavenge oxygen when the waters are supersaturated and therefore contribute a negative gas flux (Woolf and Thorpe, 1991). These bubble processes modify the apparent transfer velocity and complicate the general applicability of gas transfer parametrisations between gasses (Garbe et al., 2014).

To aid in calculating oxygen air-sea gas exchange the `airsea` R package (Hull and Johnson, 2015) has been designed to provide various parametrisations for the interactions of gases at the air-sea interface. These are based on the framework outlined by Johnson (2010), which provides a means to generalise gas transfer coefficients for any gas and is used throughout this thesis. Johnson et al. (2011) note that while it is unrealistic for all future studies to investigate all the possible sources of uncertainty for a gas of interest, there is unfortunately no rule of thumb which can be applied. Here we explore the differences between the parametrisations and discuss the uncertainties associated with calculating the air-sea flux specifically for oxygen in a shelf sea setting.

2.1 The equilibrium saturation concentration (C_{sat})

C_{sat} represents the concentration of O_2 in water which is in equilibrium with the atmosphere at 1 atmosphere (1013.25 hPa). Garcia and Gordon (1992), who refer to this variable as C^*, provide a parametrisation based on the O_2 solubility in seawater results of Benson and Krause (1984) (BK). This is the parametrisation recommended by SCOR working group 142 for oceanographic applications (Bittig et al., 2015, 2018a,b). However, various biogeochemical models and many other applications use the values derived from Weiss (1970) (Bozec et al., 2005; Aldridge et al., 2017; Wakelin et al., 2020). Figure 2.1.1 shows the disparity between the two for a range of temperatures and salinities. Garcia and Gordon (1992) also provide a combined fit based on the BK data along with two earlier studies, and while this is not recommended for general use it is the parameterisation used internally by Aanderaa optodes to calculate oxygen saturation and concentration. The root mean square error between the Benson and Krause data and the combined fit is 0.26 mmol $\mathrm{m^{-3}}$. RMSE is 0.53 mmol $\mathrm{m^{-3}}$ between Garcia and Gordon (1992) (BK) and Weiss (1970). Gruber et al. (2010) suggested air-sea gas exchange studies should target and an overall oxygen concentration accuracy of 1 mmol $\mathrm{m^{-3}}$ for accurate NCP estimation. We can see the differences between the C_{sat} formulations are thus not an insignificant source of uncertainty. Cumulatively these errors can be substantial. If we assume a marine system which is 0.5 % supersaturated relative to atmospheric equilibrium, as determined with GG92, with moderate winds and temperatures ($9\,\mathrm{m\,s^{-1}}$, $15\,^{\circ}\mathrm{C}$, $k_{\mathrm{w}} = 5.3 \times 10^{-5}\,\mathrm{m\,s^{-1}}$) then using W70 would result in an annual air-sea flux 36 % larger than that predicted with the GG92 (2.12 vs 2.89 $\mathrm{mol\,m^{-2}\,a^{-1}}$).

2.2 The air-sea gas transfer coefficient (k)

As discussed above for low-solubility low-reactivity gases (i.e. oxygen) air-sea gas transfer is mostly controlled by the water-side transfer coefficient (k_{w}) (Beale et al. (2014)). `airsea` provides an array of various k_{w} parametrisations including the four most widely used. For a more thorough review see Garbe et al. (2014) or Beale et al. (2014).

- The bomb C_{14} derived parametrisation of Wanninkhof (1992) (WA92, Eq. 2.2.1), and the updated version from Wanninkhof (2014) (WA14, Eq. 2.2.3).

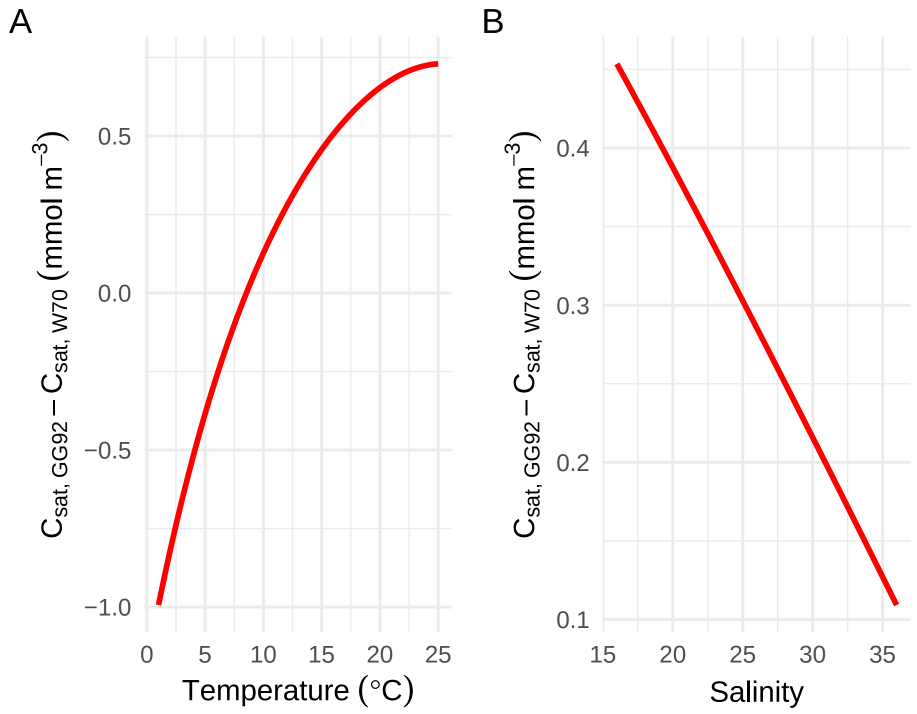

Figure 2.1.1: Difference in oxygen saturation concentration (C_{sat}) between Garcia & Gordan, 1992 (GG92) and Weiss 1970 (W70), subplot A showing temperature dependence (S = 35), and B showing salinity dependence (T = 10)

- Nightingale et al. (2000) 's North Sea dual tracer experiment (NG00, Eq. 2.2.2)
- The FA11 parametrisation used in NOAA-COAREG from Fairall et al. (2011) (as implemented by Liang et al. (2013)).

These are compared in figure 2.2.1. All of these are empirically derived based on the assumption that the kinetic energy input into the water from wind forcing is the primary driver of air-water exchange. The energy input from wind is known to increase non-linearly with wind speed, due to wave generation and the breaking of said waves. Wind speed (U) based parametrizations of k assume that k will increase proportional to U^x where $x > 1$. k is often expressed normalised to a Schmidt number of 660 for comparing transfer velocities derived from different tracer gases (Beale et al., 2014).

$$k_\mathrm{w} = 0.31 \cdot U^2 \cdot (S_c/660)^{-0.5} \tag{2.2.1}$$

$$k_\mathrm{w} = 0.222 \cdot U^2 + 0.333 \cdot U(S_c/600)^{-0.5} \tag{2.2.2}$$

$$k_\mathrm{w} = 0.251 \cdot U^2 \cdot (S_c/660)^{-0.5} \tag{2.2.3}$$

Where U is the wind speed at 10 meters height and S_c is dimensionless the Schmidt number. 660 corresponds to the Schmidt number of CO_2 in seawater at 20°C. These parametrisations by convention provide units of k_w in cm h^{-1} while U is in m s^{-1}. The `kw` function in `airsea` however always provides k_w in m s^{-1}.

2.3 Schmidt number

All of the k_w parametrisations are sensitive to the calculation of the Schmidt number (S_c). It is generally accepted that $k_\mathrm{w} \propto S_c^{0.5}$ (Johnson, 2010). S_c is defined as $Sc = \nu/D$ (Wanninkhof et al., 2009), where ν is the kinematic viscosity (momentum diffusivity, m^2 s^{-1}) and D is the mass diffusivity (m^2 s^{-1}) and is therefore dimensionless. $\nu = \mu/\rho$ where μ is the dynamic viscosity of seawater (kg/m s) (Laliberté (2007)) and ρ is seawater density (kg m^{-3}) (Millero and Poisson (1981)). For seawater (S = 35) the S_c of O_2 is 589 ± 5 % at 20°C (Wanninkhof

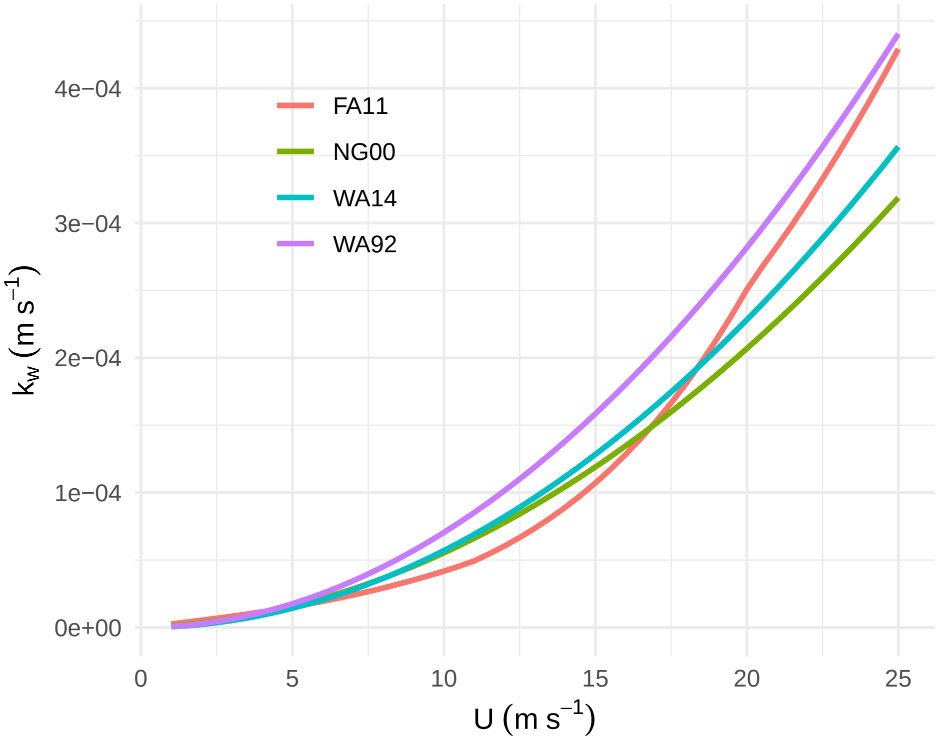

Figure 2.2.1: Comparisons of four widely used k_w parametrisations for oxygen, assuming 10 °C and S = 35. FA11 = Fairall et al. (2011), NG00 = Nightingale et al. (2000), WA14 = Wanninkhof (2014), WA92 = Wanninkhof (1992).

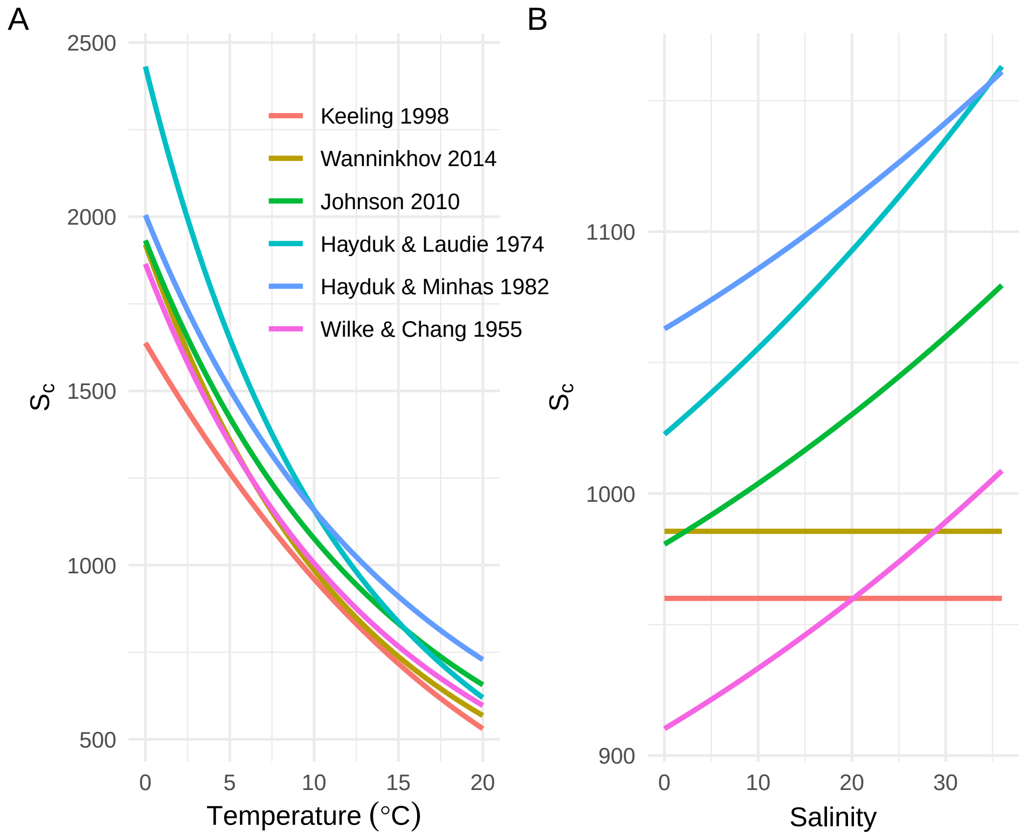

Figure 2.3.1: A. Temperature dependence and B. salinity dependence of the Schmidt number for oxygen for a selection of parametrisations. In A, salinity is fixed at 35, in B, temperature is fixed at 10°C

et al. (2009)) `airsea` provides a range of formulations for Sc:

- Wilke and Chang (1955)
- Hayduk and Laudie (1974)
- Hayduk and Minhas (1982)
- Keeling et al. (1998)
- Wanninkhof (2014)

By default the `airsea` package uses the method from Johnson (2010) by calculating the Schmidt number using the mean of the diffusion coefficient calculated per Wilke and Chang (1955) and Hayduk and Minhas (1982). The temperature dependence of the various Schmidt numbers for oxygen are shown in figure 2.3.1 A.

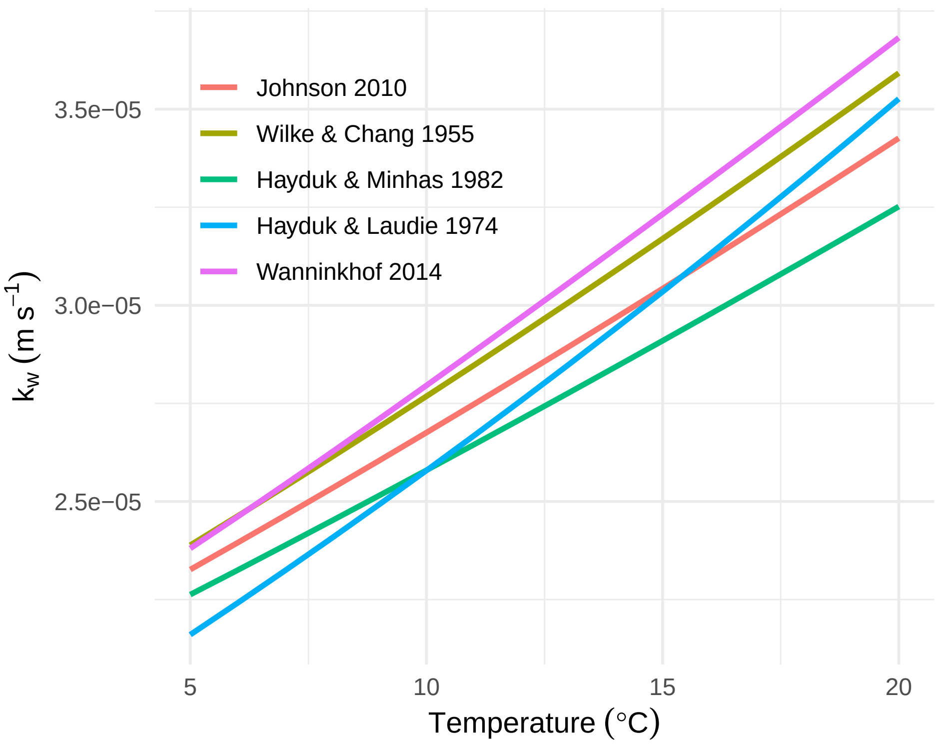

Figure 2.3.2: Effects of the different Schmidt number methods on the WA14 k_w with U_{10} = 7 m s^{-1}

At at fixed salinity of 35 the parametrisations differ by up to 13 % at the extremes of temperature, while at a fixed temperature varying salinity accounts for up to ±8 of the difference between each method. The Keeling et al. (1998) parametrisation uses freshwater measurements and applies a 1.13 “salting out” factor assuming a salinity of 35. Wanninkhof (2014) also assumes a salinity of 35. Variation in the calculation Schmidt number accounts for 5-8 % for the final k_w (figure 2.3.2).

2.4 The bubble equilibrium fractional supersaturation coefficient (B)

Bubbles have two effects, they increase the raw transfer rate and modify the apparent solubility. Care must be taken when combining the various k_w parametrisations with bubble processes, as for k_w derived from gas-tracer studies the bubble mediated transfer rate effects will already be included in the empirical formulation (Beale et al., 2014), while others such as Fairall et al. (2011) model it explicitly. Bubble injection can result in supersaturation of the surface waters by up to a few percent (Keeling (1993), Woolf et al. (2007)). The supersaturation is caused by the asymmetry between evasion and invasion associated with the bubbles rising to the surface after injection (Keeling (1993), Woolf and Thorpe (1991), Liang et al. (2017)). As such gas transfer via bubbles is not simply proportional to the air-sea concentration gradient. This is typically formulated as in equation 2.4.1 (assuming the k_w formulation includes bubble mediated gas-transfer).

$$G = k_w(C - C_{\text{sat}}(1 + B)) \tag{2.4.1}$$

Where B is a dimensionless term accounting for the supersaturation effect of bubbles.

`airsea` provides the parametrisations of Woolf and Thorpe (1991) (WT91, eq.2.4.2) and Liang et al. (2013) (LI13, eq.2.4.3) for B. Both parametrisations are derived from calculated bubble fields. The WT91 method is simple to implement but assumes no solubility dependence. Their work assumed seawater at 10°C. The LI13 parametrisation accounts for changes in solubility through salinity and temperature changes. Note that, Liang et al. (2013), (equation 9) describes the atmospheric friction velocity following the conventions of NOAA-COAREG, while the water-side friction velocity is used elsewhere in the paper using the same symbol (Junhong Liang, pers. comms.).

$$B = 0.01 \cdot \left(\frac{u}{u_i}\right)^2 \tag{2.4.2}$$

where u is the wind speed at 10 m and u_i is the wind speed at which equilibrium supersaturation is 1 %, which for oxygen is $9\,\mathrm{m\,s^{-1}}$.

$$B = \frac{k_b C_{\text{sat}} \Delta_{\text{b}} \frac{P}{P_0} + F_i}{k_T C_{\text{sat}} \frac{P}{P_0}} \tag{2.4.3}$$

Where k_b is the bubble mediated gas transfer rate, Δ_{b} is the supersaturation due to partially dissolved bubbles, k_T is the total gas transfer rate (bubble mediated and across the sea surface) and F_i is the gas flux caused by small bubbles which completely dissolve. P is local atmospheric pressure and P_0 is the standard sea level pressure of 1013.25 hPa. These are reproduced in the appendix as equation A.0.1. For oxygen $k_T = k_w$ and therefore could be substituted with any of the aforementioned k_w parametrisations. For comparison with Woolf and Thorpe (1991) we use the k_T of Fairall et al. (2011) within this chapter.

Woolf and Thorpe (1991) do not provide any uncertainty estimates for their parametrisation. Liang et al. (2013) demonstrates similar but slightly lower values for argon between their bubble supersaturation parametrisation and that of Woolf and Thorpe (1991), they do not provide example values for O_2. For oxygen, Woolf and Thorpe (1991) estimates a larger bubble supersaturation effect at any temperature (figure 2.4.1).

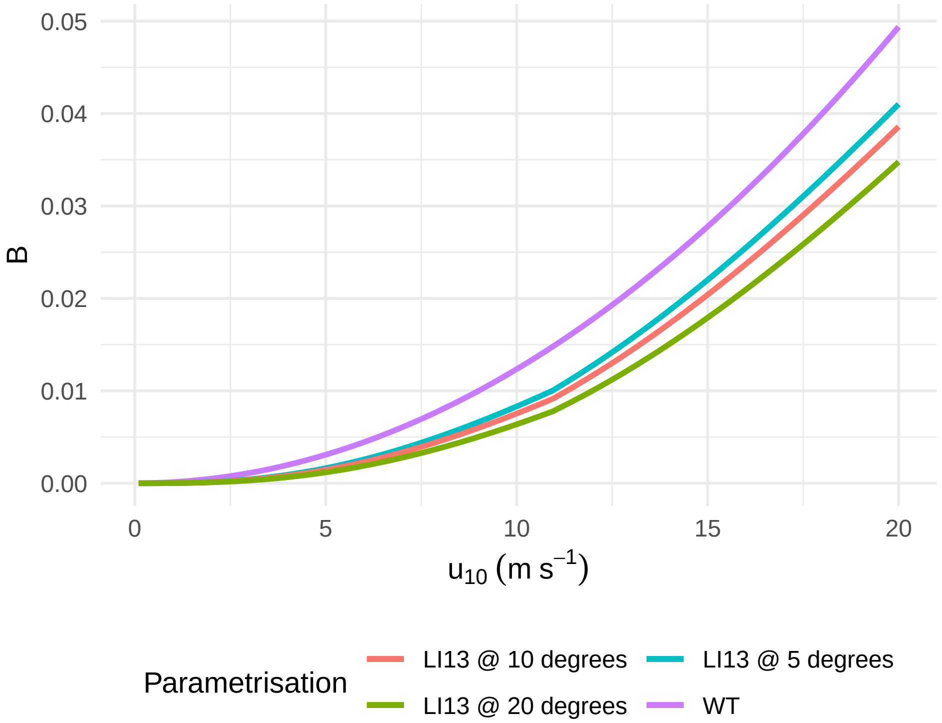

Figure 2.4.1: Comparison of the WT91 and LI13 bubble supersaturation terms.

It is unclear which parametrisation is best or most applicable for shelf sea studies. The LI13 temperature dependence would indicate better performance when temperatures are significantly different from the WT91 test case (10 °C). Either way, the differences between the two methods across a range of wind speeds suggests that uncertainties for this term are within 50 %.

2.5 Pressure

Local atmospheric pressure also changes the solubility of oxygen, as C_{sat} assumes sea level pressure at 1013.25 hPa (eq. 2.5.1).

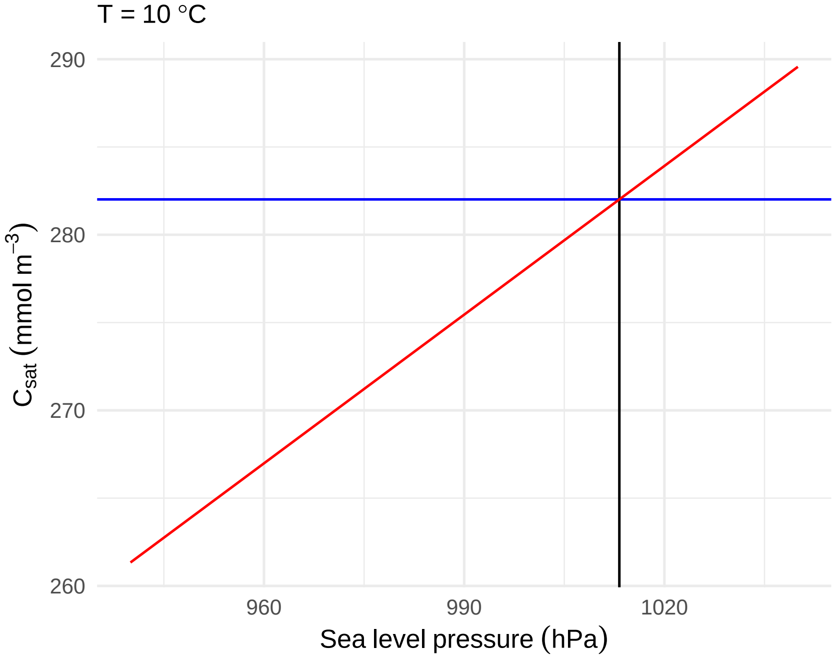

Figure 2.5.1: The effects of atmospheric pressure on the equilibrium saturation concentration (C_{sat}) in red, standard atmospheric pressure shown by vertical black line, saturation concentration at standard atmosphere shown in blue

$$C_{\mathrm{sat_p}} = C_{\mathrm{sat}} \frac{P - p_v}{P_0 - p_v} \tag{2.5.1}$$

where p_v is the saturation vapour pressure (hPa) (Weiss and Price, 1980). A 1 hPa change in sea level pressure translates to a 0.23 mmol m^{-3} change in C_{sat} at 10 °C. In many formulations for the air-sea gas exchange flux, the vapour pressure correction is neglected (e.g. Liang et al. (2013)). The effect on C_{sat} is small ($0.2\,\mathrm{mmol\,m^{-3}}$ to $0.2\,\mathrm{mmol\,m^{-3}}$ given typical temperate atmospheric pressures and sea water temperatures) it is stilllshould nonetheless be included.

2.6 Sampling frequency

Gas flux estimates are generally based on the assumption that the concentration gradient is constant throughout the integration period (Johnson et al., 2011). This represents a challenge for oxygen based studies, as the potentially rapid biogenic oxygen dynamics are the process we wish to observe. The fact that wind driven bubble supersaturation is such an important component of the air-sea oxygen concentration gradient adds further complexity, given the potentially high variability of local winds.

Aanderaa quote a resolution of 0.1 mmol m^{-3} or 0.05 % for the 4330 series oxygen optodes and 1 mmol m^{-3} for the 3835 series (the oxygen optodes used in later chapters, see section 1.5.1). Given typical winds (9 m s^{-1}) and a 20 m mixed layer depth, what sampling frequency would be required to detect a pulse of episodic NCP? The predicted concentration given just air-sea gas exchange can be determined by equation 2.6.1.

$$C_t = (C_0 - C_{\mathrm{sat}}) \exp(\frac{-k_w t}{h}) + C_{\mathrm{sat}} \tag{2.6.1}$$

Solving for time provides equation 2.6.2.

$$t = \log(\frac{C_t - C_{\mathrm{sat}}}{C_0 - C_{\mathrm{sat}}}) h \frac{1}{-k_w} \tag{2.6.2}$$

where C_t is the concentration we observe in the future, assuming the only driver is a constant k_{w}. If we take 0.5 mmol m^{-3} as our limit of detection, we can see from figure 2.6.1 that under these typical North Sea conditions a pulse of NCP which produces a disequilibrium of 5 mmol m^{-3} would be undetectable after 16 days.

Infrequent sampling leads to the integration of air-sea gas exchange over larger ranges of wind speed (Wanninkhof et al., 2009). Wind speeds can be highly variable and much information can be lost as the time-step between observations increases. To demonstrate we take 10 minute sampled wind speed data from an anemometer on board a UK research vessel (Cefas Endeavour). We assume an air-sea ΔC of 10 mmol m^{3} and calculate instantaneous gas fluxes. Figure 2.6.2 demonstrates how variability in wind speed can lead to wildly different estimates for the air-sea gas exchange. These uncertainties are often hard to determine as the reason for a long integration

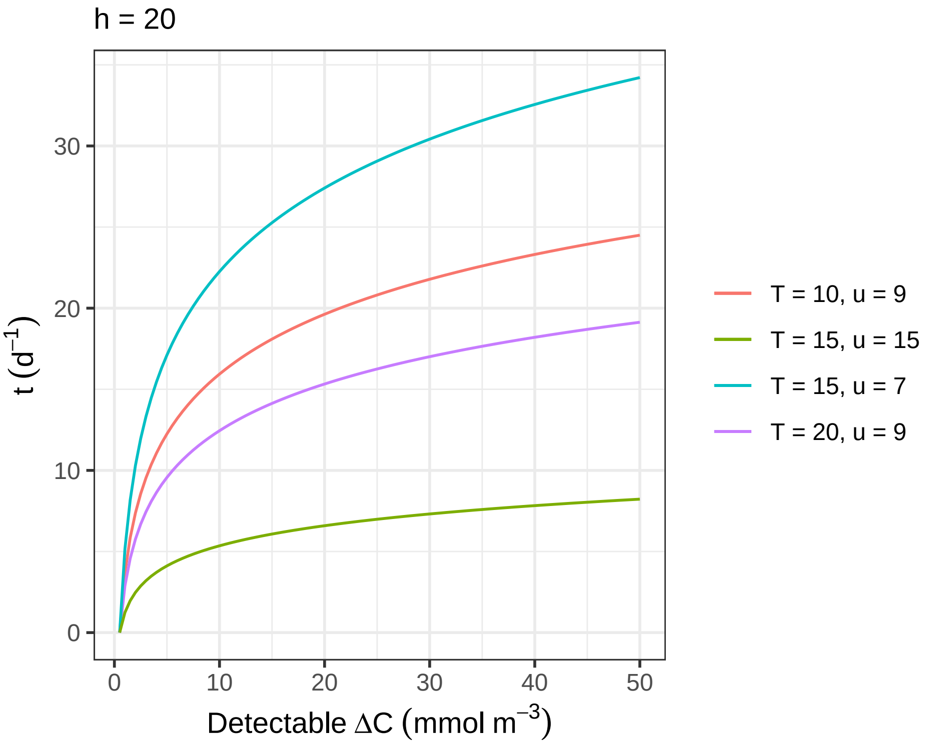

Figure 2.6.1: The effect of wind speed (u) and temperature (T) on the sampling interval (t) needed to detect a given pulse of NCP (ΔC)

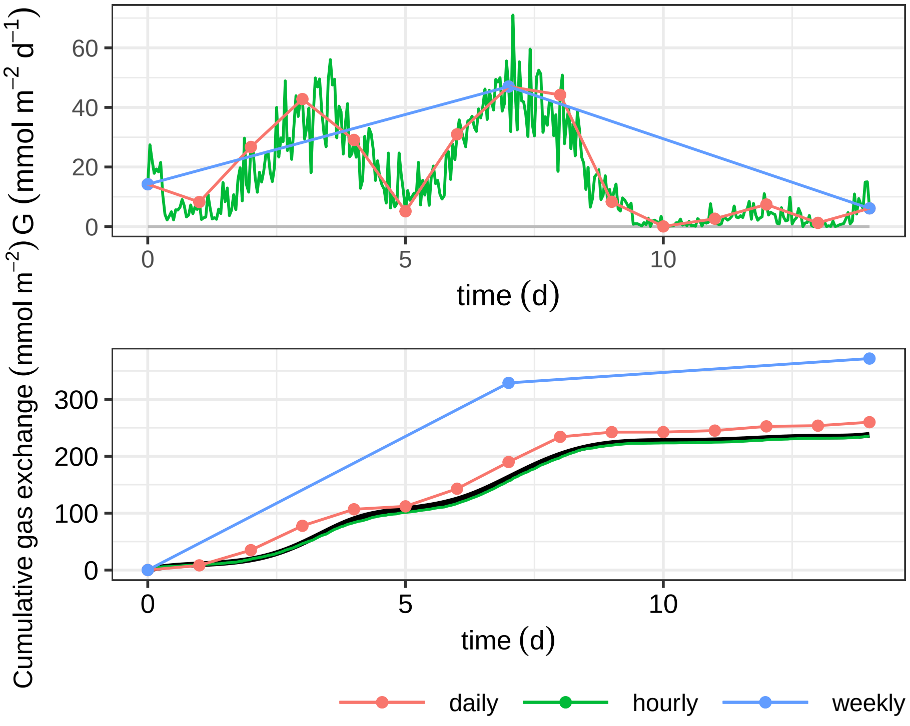

Figure 2.6.2: Effects of sampling frequency on cumulative gas exchange estimates, 'true' value shown in black

period is typically due to the lack of high frequency observations. Simulation of the potential fluxes such as the example given here provides one way of assessing the likely uncertainties of a given sampling strategy.

2.7 Discussion

Woolf et al. (2019) state that, depending on expert opinion, the transfer velocity for CO_2 has an uncertainty of either 5 % or 10 %. Wanninkhof (2014) suggest a combined (additive relative) uncertainty for global CO_2 as 20 %, comprising a 5 % error from Schmidt number formulation, a 10 % chemical enhancement term and the rest from winds partitioned into different errors for low, moderate and high winds. Typically the assumption taken by Wanninkhof (2014) of non-correlated errors would suggest a quadratic addition of the relative uncertainty terms, resulting in a 7 % total error. These uncertainties are all for global estimates of CO_2 and the uncertainties associated with oxygen air-sea gas exchange are different. Specifically oxygen is is unaffected by the chemical enhancement seen with CO_2, and is more strongly influenced by bubble induced supersaturation.

While these parametrisations discussed here are simple to implement and apply to climatological calculations or earth-system models they do ignore mechanistic processes (Johnson et al., 2011; Woolf et al., 2019). Approximating air-sea gas transfer to a wind-driven temperature dependent process ignores the full complexity of various processes including wave breaking, rainfall (Ashton et al., 2016), sea spray, surfactants (Frew et al., 2004) and wind-wave-current interactions (Beale et al., 2014; Woolf et al., 2019). All of these complications likely introduce regional and seasonal biases that probably have little effect on the global gross flux but may have significant effects on smaller scale fluxes.

Woolf (2005) and Liang et al. (2017) both demonstrate that the bubble-mediated gas fluxes are controlled by the wave conditions, and wind speed is only a proxy for this process. In both studies a time dependence was noted with bubble mediated gas fluxes being dependent on wave age. However, Liang et al. (2017) conclude that these fluxes are larger during rising winds with smaller wave age. Woolf (2005) conversely argued that the fluxes are larger with older waves as whitecap coverage and bubble generation is thought to increase with wave age. Wave age dependence is not included in any existing bubble-mediated gas flux parametrisations, but this represents another source of unknown uncertainty.

Given the haline and thermal dependence on the transfer velocity, biases can be introduced by neglecting to include the “cool skin” effect. This is the phenomenon that the top few millimetres of the upper ocean is generally slightly cooler than the bulk mixed layer temperature (Woolf et al., 2016). The “cool skin” can however partly be balanced by the haline effect associated with the increased salinity within the ocean skin. These biases can have a significant impact on calculated net air-sea flux, for CO_2 it has been reported to increase the net flux by up to one third. A correction from the bulk mixed layer temperature of -0.17 K and +0.1 salinity is widely accepted (Woolf et al., 2019), and this is the correction we apply for subsequent air-sea gas exchange calculations. For O_2 a -0.17 C bias in temperature at 10^{o}C corresponds to a bias in oxygen solubility of 1 mmol m^{-3}, reduced to 0.86 mmol m^{-3} with the associated change in salinity (Garcia and Gordon, 1992).

2.7.1 Wind products

Another potential major source of error is the wind products used to drive the gas transfer parametrisations mentioned above. Nightingale et al. (2000) determined that 80 % of the variability in gas exchange was explained by uncertainty in the wind products, in particular at high wind speeds. Low resolution wind products tend to negatively bias the magnitude of wind stress, and thus underestimate gas exchange (Powley et al., 2020) Wanninkhof et al. (2009) demonstrated that global average wind speed varied significantly, with the QuikSCAT product provided 7.9 m sˆ-1, but the NCEP estimating 6.6 m s ˆ-1. There is more uncertainty associated with very low (< 4 m s^{-1}) and very high (> 15 m s^{-1}) wind speeds (Wanninkhof et al., 2009; Wanninkhof, 2014).

2.7.2 Precipitation

While relatively poorly studied rainfall can further modify air-sea gas exchange. Falling precipitation can disrupt the viscous boundary layer and may inject bubbles into the water. Rain causes a reduction in breaking wave intensity and reduced white capping, which may also reduce the rates of gas exchange. Heavy rains can reduce the depth of wind based turbulence due to the addition of low density fresh water which suppresses turbulent mixing (Moum and Smyth, 2001).

2.7.3 Surfactants

Surfactants present at the sea surface are also thought to contribute a substantial fraction to air-sea gas exchange uncertainty (Liss and Duce, 1997). Data described in Liss and Duce (1997) suggest transfer velocities for coastal waters can be as much as five times lower than for oligotrophic areas. Pereira et al. (2018) demonstrated a 32 % reduction in gas transfer due to surfactants. McNeil and D'Asaro (2007) argued that surfactants are only important during calm conditions, and Nightingale et al. (2000) found no measurable change in k_w during an North Sea algal bloom with a 300 % increase in Chlorophyll. Given that surfactants effect transfer even at highest wind speeds studies, practically surfactants are always in effect and could be considered part of the parametrisation uncertainty (Wanninkhof et al., 2009). There is currently no parametrisation for use with autonomous observations to correct for surfactant effects.

2.8 Conclusions

Global synthesis estimates for k_w may not scale well to regional biases. However, the parametrisation of Nightingale et al. (2000) is conveniently based on observations within the north-western European shelf so is particular appropriate for the studies within this thesis. We see the overall uncertainty in k_w as a combination of several sources of error, and we note that, as discussed by Wanninkhof (2014) and Johnson et al. (2011), “the uncertainties of the uncertainties” are not well determined. Taking the same approach as Wanninkhof (2014) we combine the various known uncertainties, but neglect those of chemical enhancement which are specific to CO_2. Thus for small scale studies of oxygen air-sea gas exchange an overall uncertainty of 15 % for k_w and 50 % for B is appropriate. If uncertainty in wind speed (u) can be directly quantified and is thought to be either highly variable or significantly different from the assessment above, u can be treated as a separate source of uncertainty k_w. The implications of the gas-exchange uncertainty on NCP estimates are explored in later chapters.

Chapter 3

Estimating net community production at the Warp SmartBuoy

The peer reviewed paper Hull et al. (2016) forms the basis of this chapter, within which we explore the uncertainties associated with calculating NCP using observations from an autonomous monitoring buoy located at the Warp Anchorage; a permanently well mixed shallow area within the Thames river plume. The introduction has been edited and reduced to avoid repetition of Chapter 1.

3.1 Introduction

To date the majority of oxygen-based NCP estimates have focused on open ocean waters (Alkire et al., 2012). Emerson (2014) noted that coastal NCP values can be three times greater than open ocean values, however, there are too few measurements to be confident in geographical variability. Palevsky et al. (2013) also found during their Gulf of Alaska O_2/Ar survey that the transitional coastal zone contributed 58 % of the total NCP whilst representing only 20 % of the total area surveyed. The nature of the metabolic balance is particularly important in river-dominated margins, where high carbon and nutrient inputs stimulate primary production and microbial respiration with large seasonal variations (Guo et al., 2012).

The Cefas (Centre for Environment, Fisheries and Aquaculture Science) SmartBuoy network consists of autonomous data collection moorings placed at key locations in the UK shelf seas (Greenwood et al., 2010). The long term high temporal resolution multi-parameter datasets produced by the program provide unique opportunities for observing biogeochemical processes in temperate coastal and shelf seas (Foden et al., 2008). Here we present new estimates of NCP from a long term SmartBuoy mooring situated in the southern North Sea. We explore the uncertainty in these estimates, and their sensitivity to uncertain input parameters.

3.1.1 Study Site

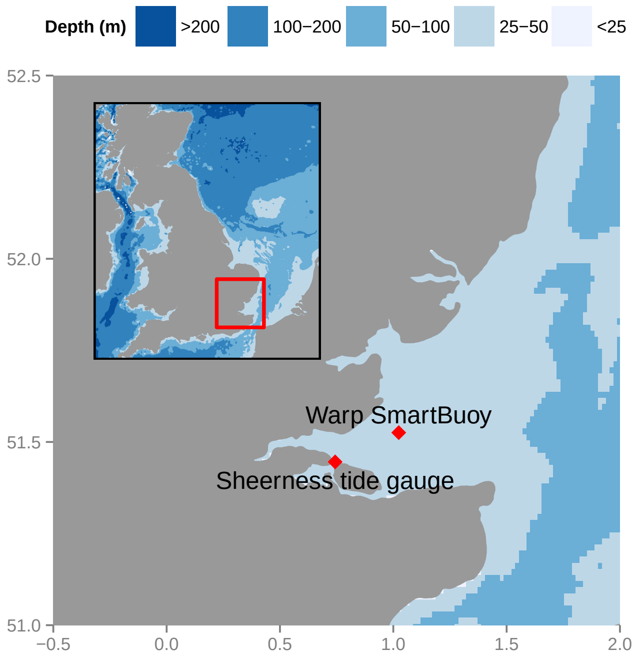

Figure 3.1.1: Map of the Warp Anchorage study site.

The SmartBuoy sensor package consists of a Cefas ESM2 datalogger coupled with Falmouth Scientific OEM conductivity and temperature sensors (Falmouth Scientific, USA), an Aanderaa 3835 series Optode (Aanderaa Data Instruments, Norway), a chlorophyll fluorometer (Seapoint Inc. USA), and a quantum photosynthetically active radiation meter (PAR; LiCor Inc. USA). The ESM2 includes a 3 axis roll and pitch sensor with a internal pressure sensor (PDR1828 – Druck Inc). The data-logger was configured to sample for a 10 min burst every half hour. Salinity, temperature, chlorophyll and PAR are sampled at 1 Hz during the measurement period, oxygen at 0.2 Hz.

The Warp Anchorage SmartBuoy site, shown in Fig. 3.1.1 is located on a shallow

Table 3.1: Study site characteristics for ^{w}Winter (November–February) and ^{s}Summer (June–September), based on multi-year seasonal means.

Warp Anchorage	
Position (WGS84)	51.31° N, 1.02° E
Monitoring Period	2001–present
Mean water depth (m)	15
Tidal range (m)	4.3
Tidal period	semidiurnal
Salinity (PSS-78)	33.8^{w}–34.3^{s}
Temperature (°C)	7.6^{w}–17.5^{s}

bank in the mouth of the River Thames. The site is highly turbid with significant riverine inputs and experiences a 15 day Spring-neap cycle with 12 h 25 min semidiurnal tides. CTD profiles taken over the last 15 years [Cefas Data] have always shown the Warp to be vertically well mixed. This mixing, together with the shallow water depth has important implications to the application of oxygen based NCP methods which will be discussed later. The main characteristics of the study site are summarised in Table 3.1.

3.2 Methods

3.2.1 Data processing

SmartBuoy data undergo rigorous automated and manual quality assurance processes. Automated processes apply a quality flag to data which fall outside realistic value bounds. Manual processes assess the instrument performance and apply flags where the data quality is compromised, e.g. due to biofouling or sensor damage. The CT sensor salinity data are corrected using in-situ bottle samples analysed using a Guildline Portsal 8410A (Guildline, Canada) standardised with IAPSO standard seawater.

Water depth was calculated using a global tidal model forced with European shelf area constituents (TPX08-atlas). Tidal waves have been shown to arrive almost simultaneously at both Sheerness and the Warp SmartBuoy (Blauw et al., 2012) thus model output was validated against the nearby Sheerness tide gauge (UK National Tide Gauge Network) and demonstrated good agreement visually. Windspeed and sea level air pressure were taken from ECMWF MACC reanalysis with a 0.125° grid. ECMWF data were found to compare well with in-situ ship borne anemometers used during mooring servicing (see Fig. B.1.1). Details of the ECMWF and tidal model validations and their bearing on the sensitivity analysis are discussed later.

Continuity of the 10 year Warp oxygen data set is hampered primarily by biofouling of the instrumentation. To avoid extrapolation or interpolation of the data, only periods of complete data were used in the analysis. Two contrasting periods were selected, a spring–summer period of 150 days from January to June 2008 and a autumn–winter period of 95 days from September to December of the same year. The 10 min half hourly burst data from the buoy and the tidal model output was combined with the 6 hourly ECMWF data. These burst means were further smoothed to 25 h averages to remove any structural biases in the data caused by the tidal cycle (Blauw et al., 2012).

3.2.2 Optodes

Aanderaa instruments model 3830 and 3835 optodes (Aanderaa, Norway) have been fitted to the Cefas SmartBuoys since 2005. Optodes drift due to foil photobleaching in a predictable way (Tengberg et al., 2006), that is well described by a decaying exponential with a decay constant of approximately 2 years (McNeil and D'Asaro, 2014). All optodes used were fitted with the opaque black silicon protective coating. Thus drift is significantly reduced after a burning-in period and the temperature correction is unaffected (D'Asaro and McNeil, 2013). Sensor drift was corrected with an offset calculated from frequent discrete samples measured with volumetric Winkler titrations (Langdon, 2010). Titrations were performed using a automatic photometric end-point detection system (Metrohm Dosimat 665 Autotitrator), the thiosulfate was intermittently standardised with a standard potassium iodate solution (Carpenter, 1965). The classical Winkler method if executed with care by a skilled operator offers very low uncertainty. It is however a demanding task that is affected by numerous uncertainty sources, such as contamination of the sample and reagents by atmospheric oxygen and iodine volatilization. Photometric endpoint detection is further affected in highly turbid waters which can limit the number of successful samples.

3.2.3 Model Implementation

NCP is calculated here using a modified version of the 0-dimensional oxygen mass balance (box) model of Emerson (1987) and Emerson et al. (2008). This describes the oxygen mass balance in the mixed layer assuming no vertical or horizontal advection and no turbulent diffusion across any mixed layer boundary.

Given that The Warp is permanently mixed there is in effect direct connection between the atmosphere and the benthos. It is thus an important distinction from prior studies that our community productivity estimate considers both the pelagic and benthic processes as one system. This method assumes that other oxygen consuming processes in the water column such as nitrification, methanotrophy and photoxidation are negligible relative to respiration (Reuer et al., 2007). In our discussion we explore the implications for a site, such as the Warp, where all of these assumptions may not hold.

The model (Eq. 3.2.1) is used to predict the concentration of oxygen at a subsequent point in time given measured physical parameters. Any deviation from the predicted value is assumed to be from biological activity, with a positive value corresponding to net production. This method of NCP estimation makes no distinction between matter which is imported then locally respired, and that which is fixed locally. All of these terms introduced below and their estimated uncertainties are summarised in Table 3.2

$$h\frac{\mathrm{d}C}{\mathrm{d}t} = E + G + J \tag{3.2.1}$$

where h is the mixed layer depth, C is the oxygen concentration in the mixed layer, E is entrainment of oxygen though changes in the mixed layer depth Eq. (3.2.2), G is the gas exchange though diffusive and bubble processes Eq. (3.2.3), and J is the net community production.

$$E = \frac{\mathrm{d}h}{\mathrm{d}t}(C_\mathrm{b} - C) \tag{3.2.2}$$

where C_b is the oxygen concentration below the mixed layer.

$$G = k_\mathrm{w}\left((1+B)\frac{P}{P_0}\,C_\mathrm{sat} - C\right) \tag{3.2.3}$$

where k_w is the parametrisation of Wanninkhof (2014) Eq. (3.2.4). C_sat is the

Table 3.2: Parameters and their uncertainty distributions used for LHS/PRCC and eFAST at the Warp. SE = the standard error of the mean.

Parameter	Description	PDF	Range	Unit
C_0	Oxygen concentration at t = 0	normal	0.54 + SE	$\mathrm{mmol\,m^{-3}}$
ΔC	Change in oxygen concentration	normal	SE	$\mathrm{mmol\,m^{-3}}$
S	Salinity	normal	0.1 + SE	dimensionless
T	Temperature	normal	0.1 + SE	°C
h	Mixed layer depth	normal	0.4 % + SE	m
U	wind speed	normal	1.2 + SE	$\mathrm{m\,s^{-1}}$
P	Sea level air pressure	normal	0.1 % + SE	hPa
C_{sat}	Oxygen solubility	uniform	0.3 %	$\mathrm{mmol\,m^{-3}}$
k_{w}	Gas transfer velocity	uniform	15 %	$\mathrm{m\,s^{-1}}$
B	Equilibrium bubble saturation	uniform	50 %	dimensionless

concentration of oxygen in equilibrium with the one atmosphere as per Garcia and Gordon (1992) using the Benson and Krause (1984) data, B is supersaturation caused by bubble processes Eq. (3.2.5), P is sea level pressure, P_0 is standard atmospheric pressure (101 325 Pa).

$$k_{\mathrm{w}} = 0.251\ U^2 \left(\frac{Sc_{\mathrm{O_2}}}{660}\right)^{-0.5} \tag{3.2.4}$$

where U is the wind speed at 10 m, $Sc_{\mathrm{O_2}}$ is the dimensionless Schmidt number for oxygen. 660 is the typically quoted Schmidt number for CO_2 at 20 °C in salt water ($S=35$). Note the result of Eq. (3.2.4) is converted from $\mathrm{cm\,h^{-1}}$ to $\mathrm{m\,s^{-1}}$ for use in Eq. (3.2.3).

The square root of the squared mean was used for wind speed to fit with the quadratic k_{w} parametrisation used. Wanninkhof et al. (2009) argues that comprehensive surface forcing models provide little to no improvement over simple wind speed algorithms, and although simple parametrisations cannot capture all the processes that control gas transfer, they appear to capture most.

The injection of bubbles into the mixed layer through wave action can supersaturate the surface waters even if net gas exchange is zero (Liang et al., 2013). Here we utilise a modern k_{w} parametrisation with an explicit bubble equilibrium fractional supersaturation parametrisation B, which enables the influence of the two elements on the NCP estimate to be quantified independently. For B the bubble supersaturation parametrisation of Woolf and Thorpe (1991) is used:

$$B = 0.01 \cdot \left(\frac{U}{U_i}\right)^2 \tag{3.2.5}$$

where U_i is the wind speed at which the equilibrium supersaturation is 1 %. For oxygen Woolf and Thorpe (1991) report this value to be $9\,\mathrm{m\,s^{-1}}$.

Liang et al. (2013) argues that bubble supersaturation effects at a given temperature differ significantly among parametrizations, and their comparison between Stanley et al. (2009), Woolf and Thorpe (1991) and their own parametrization demonstrates differences in the order of 50 % for argon. The Woolf and Thorpe (1991) parametrisation does not account for any temperature or solubility dependence and is derived from calculated bubbled fields; implementation is however straightforward and the large relative uncertainties in the bubble term will be accounted for in the sensitivity analysis outlined below.

We solve Eq. (3.2.1) for NCP (J) using the analytical solution shown in Eq. (3.2.6), providing mean values for each variable except oxygen concentration and assuming a constant rate of NCP over the time step, which for this study corresponds to 25 hours. The numerical scheme used in this paper was implemented using R, the open-source language and environment for statistical computing (R Foundation for Statistical Computing, `www.r-project.org`). The analytical solution, along with k_w and B parametrisations are included in the “airsea” package (Hull and Johnson, 2015). The scheme was validated in silico using numerical estimation; air-sea fluxes were simulated every half second forced with a known value of NCP, the resultant change in oxygen concentration was provided to our model and the calculated value of NCP compared to the known forced value. This was repeated over a range of input scenarios.

$$J = rh\left(\frac{C_1 - C_0}{1 - e^{-rt}} + C_0\right) - Fh \tag{3.2.6}$$

Where C_0 is the oxygen concentration at the initial time-step ($t = 0$), and C_1 is the concentration at t.

$$r = \frac{k_{\mathrm{w}}}{h} + \frac{1}{h}\frac{\mathrm{d}h}{\mathrm{d}t} \tag{3.2.7}$$

$$F = \frac{k_{\mathrm{w}}}{h} C_{\mathrm{sat}}(1+B)\frac{P}{P_0} + \frac{1}{h}\frac{\mathrm{d}h}{\mathrm{d}t} C_{\mathrm{b}} \tag{3.2.8}$$

It should be noted that for this study the entrainment ($\frac{\mathrm{d}h}{\mathrm{d}t}$) term is neglected as the Warp is a perpetually fully-mixed site, as such the entrainment term of Eqs. (3.2.7) and (3.2.8) are set to 0.

3.2.4 Sensitivity analysis methods

Accurately assessing the sensitivity of a model output to uncertain input variables has many uses. Primarily it is to determine the precision of the model output, and the sources of output uncertainty, knowledge of which informs future research in targeting the main sources of uncertainty if robustness is to be increased (Saltelli, 2008).

Local sensitivity analysis methods, such as the so called one-at-a-time techniques, are limited to providing information only in a very specific location of the parameter space. These methods rely on the selection of an applicable baseline, and varying a single input parameter, which ignores the effects of covariant parameter uncertainty (Saltelli, 2008).

Global methods such as Latin Hypercube sampling with partial rank correlation coefficients (LHS/PRCC) and the extended Fourier Amplitude Sensitivity Test (eFAST) are capable of assessing multiple locations across the entire parameter space, thus covariant parameter uncertainty is captured.

LHS/PRCC and eFAST have proven to be two of the most efficient and reliable methods in each of their classes, sampling-based and variance decomposition-based respectively (Marino et al., 2008). These two popular methods have differing strengths and weaknesses and measure different properties of the model which together can provide a complete uncertainty analysis. LHS/PRCC is a robust technique for non-linear but monotonic relationships assuming little to no correlation exists between inputs (Saltelli, 2008). LHS is an improved method of Monte-Carlo which generates more efficient estimates of the desired parameters with far fewer simulation runs. PRCCs are a ranked measure of monotonicity after removing the linear effects of all but one of the variables, A simple one-at-a-time analysis reveals that the variables do indeed demonstrate the monotonic relationships required for effective PRCC. eFAST provides first and total order Sobol' indices which indicate the variance of the conditional expectation of the output for a given variable (Saltelli, 2008).

LHS is performed by assigning a error probability density function (PDF) to each of the parameters. Each PDF is split into n equiprobable divisions and each area randomly sampled once without replacement. This table of input variables is then used to calculate NCP, with a new hypercube being generated for each time step. A column-wise pair-wise algorithm is then used to generate an optimally designed hypercube, where the mean distance between each point and all other points in the hypercube is maximised. We utilise the "improved" LHS implementation within the "lhs" R package (Carnell, 2012) together with the PRCC routine from "epiR" (Nunes et al., 2014) The eFAST scheme is provided by the "sensitivity" package (Pujol et al., 2014).

While there is no a priori exact rule for determining sensible sample size for these methods, minimum values are known to be $n = k + 1$ for LHS/PRCC and $n = 65$ for eFAST (Saltelli, 2008), where k is the number of parameters. Here we took the usual approach of systematically increasing sample size and checking if the sensitivity index is consistent at least for the main effects, thus demonstrating there is no advantage to increasing sample size as the conclusions remain the same.

LHS/PRCC and eFAST analyses were run 500 times for each 25 h step of the time series and the results aggregated. For cumulative calculations k_{w}, B and C_{sat} and the bias element of each measurement parameter was applied globally for the entire time series, that is to say, a single hypercube ($n = 500$) is used to set the bias and scaling factors for multiple runs over the entire time series, while the stochastic uncertainties are applied at each time step independently.

3.2.5 Uncertainty distributions

Critical to the value of any sensitivity or uncertainty analysis is the selection of adequate probability distribution functions for each input parameter (Marino et al., 2008). Table 3.2 summarises the probability distribution functions used for each of the NCP model input parameters.

The two oxygen terms (C_0, ΔC) were determined though replicate anchor station

Winkler samples taken close to the mooring during maintenance surveys, combined with an estimate of Winkler method error and water bath tests of optode precision. C_0 represents the precision and accuracy of the initial (t = 0) oxygen concentration. We estimate this residual standard error in oxygen determination from the corrected optode, combined with the accuracy of the Winkler samples, to be within $\pm 0.52\,\mathrm{mmol\,m^{-3}}$. The error bounds for ΔC, unlike the other measured parameters are derived solely from the standard error of the difference between the oxygen concentration at each time time step. This standard error represents both the variability within each 25 h mean and the precision of the optode.

The calculation of k_{w} is conservatively assumed to be accurate to ±15 % (Wanninkhof, 2014), The root-mean-square error from regressions between ECMWF and ship anemometer, shown in Fig. B.1.1, is used to give an estimated wind speed error. For salinity we use the RMS error between the corrected CT, as detailed above, and the bottle samples (0.1). Water bath calibrations have confirmed the SmartBuoy temperature sensors to be accurate to within ±0.1 °C. Garcia and Gordon (1992) provides an uncertainty estimate for the measurement of their oxygen solubility parametrisation of 0.3 %. We have selected a 50 % uniform uncertainty distribution for B, the equilibrium bubble supersaturation term, based on the assessment of parametrisations by Liang et al. (2013).

At the Warp, given the assertion it is always fully mixed, the uncertainty in h is reduced to an estimate for the inaccuracies in the tidal model.

Regressions between the predicted height from the model and the Sheerness tide gauge results in a RMS error of approximately 0.4 %. These estimates of parameter measurement uncertainty were combined, using the square root of the sum of squares, with the standard error of each mean observed value. The uniform bias was found to be relatively small compared to the observed standard errors and thus the overall parameter error is considered to be normally distributed.

Uncertainty distributions for k_{w}, B and C_{sat} were applied by multiplying the parametrised output by a scaling factor sampled from a uncertainty probability distribution. This renders the uncertainty in the parametrisation independent of the input parameters, i.e. k_{w} uncertainty is independent of U uncertainty.

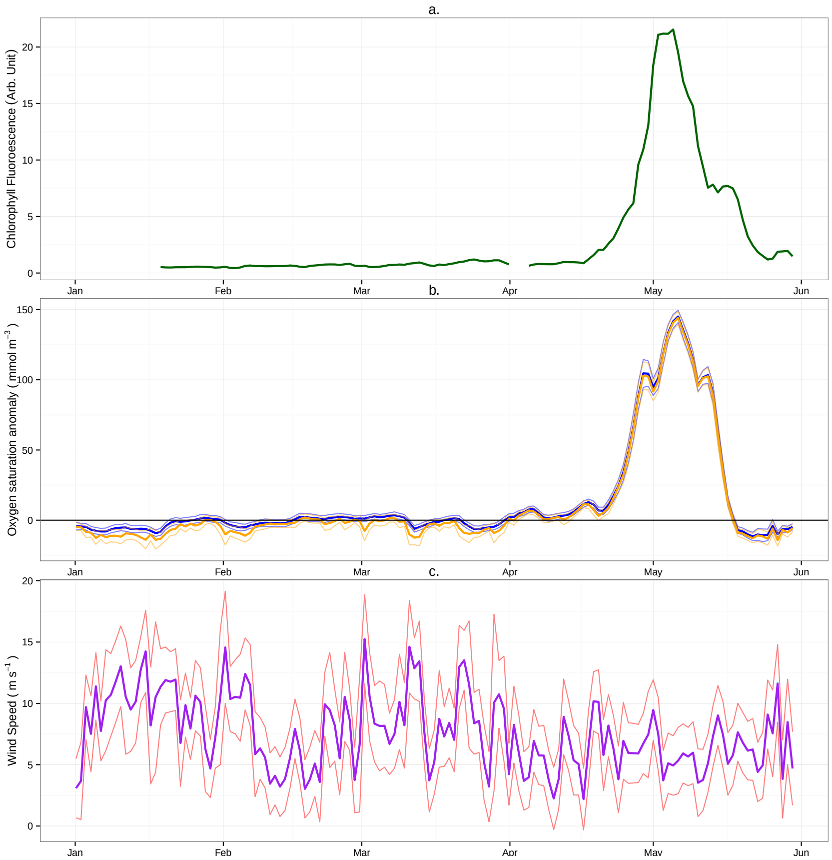

Figure 3.3.1: Spring 2008 Warp Anchorage time series. **(a)** Chlorophyll fluorometry. **(b)** Oxygen saturation anomaly (oxygen concentration minus the solubility). Orange and blue lines represent oxygen saturation anomaly with and without bubble supersaturation effects respectively. **(c)** ECMWF MACC reanalysis 10 m wind speed. For **(b)** and **(c)** thin lines represent 2σ confidence bounds.

3.3 Results

3.3.1 NCP

The 25 h mean chlorophyll time series for Warp is shown in Fig. 3.3.1a showing the low levels of chlorophyll in Winter, before a marked phytoplankton bloom in late spring. This bloom is known from prior studies to be triggered by improved light climate though increased solar radiation and reduced turbidity (Weston et al., 2008). The oxygen saturation anomaly (Fig. 3.3.1b), the oxygen concentration minus the equilibrium saturation concentration (C_{sat}), demonstrates mostly under-saturated near equilibrium conditions before the bloom, with a large degree of supersaturation during the bloom. Figure 3.3.1b illustrates how the effects the B term on increasing

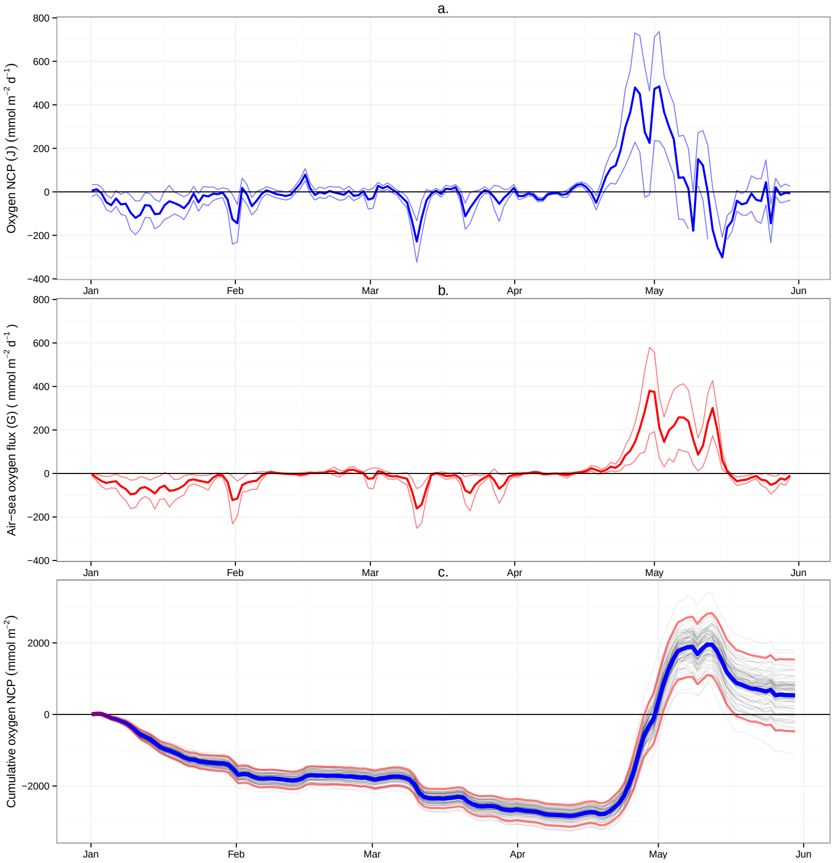

Figure 3.3.2: Spring 2008 Warp Anchorage time series. **(a)** Net community production (J), negative values correspond to net respiration. **(b)** Oxygen air-sea gas exchange (G), negative values correspond to movement into the sea. For **(a)** and **(b)** thin lines represent 2σ confidence bounds. **(c)** Cumulative net community production, mean value shown in blue, each run shown in grey, 2σ confidence bounds in red.

the equilibrium saturation concentration, and thus reducing the apparent saturation anomaly. Figure 3.3.1c shows the ECMWF wind speed data for our study period demonstrating a high degree of variability between days and within our 25 h mean. Figure 3.3.2a shows the calculated NCP for the Spring 2008 study period at the Warp.

All NCP values are given as oxygen equivalents unless otherwise stated. It is characterised by small mostly negative fluxes for the first 3 months. This is followed by a marked phytoplankton bloom (Fig. 3.3.1a) and resulting positive net community production lasting approximately 3 weeks. Large negative NCP is seen following the bloom indicating enhanced community respiration. The observed NCP signal is in good agreement with chlorophyll fluorescence (Fig. 3.3.1a).

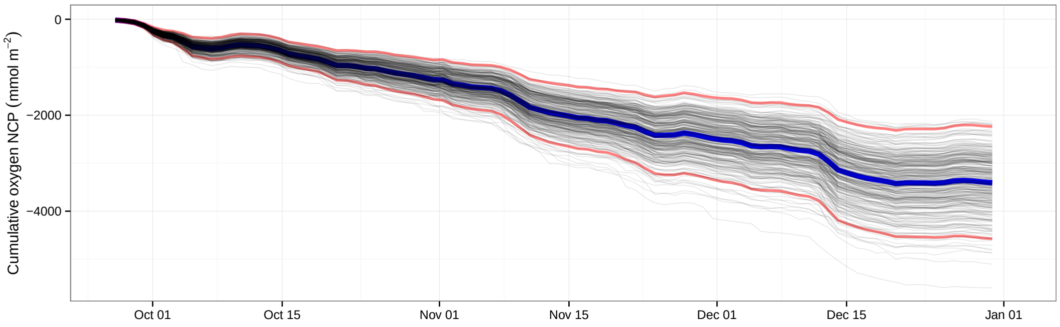

Figure 3.3.3: Warp 2008 Winter cumulative NCP. Mean value shown in blue. Red lines indicate 95 % confidence limits. Black lines correspond to each simulation run.

The maximum rate of net community oxygen production was calculated as $(485 \pm 129)\,\mathrm{mmol\,m^{-2}\,d^{-1}}$ with 2σ confidence and precedes maximum observed chlorophyll by three days. The mean rate during non-productive period (January to April) is estimated as $(-30.0 \pm 9.5)\,\mathrm{mmol\,m^{-2}\,d^{-1}}$. The maximum rate of O_2 influx from the atmosphere was $(161 \pm 47)\,\mathrm{mmol\,m^{-2}\,d^{-1}}$ measured on 1 February 2008, which was concomitant with $14\,\mathrm{m\,s^{-1}}$ winds (Fig. 3.3.1c) and a $-2.5\,\mathrm{mmol\,m^{-3}}$ oxygen anomaly. The maximal rate of oxygen out-gassing was observed 1 May 2008 of $(380 \pm 102)\,\mathrm{mmol\,m^{-2}\,d^{-1}}$ after the initial peak of the phytoplankton bloom. Mean gas residence time for oxygen was calculated to be 5 days. Calculating the seasonal net balance (Fig. 3.3.2c) at the end of the spring study period (January to June), the cumulative NCP is estimated as $(0.5 \pm 1.0)\,\mathrm{mol\,m^{-2}}$ at $2(\sigma)$ confidence. The net balance for the winter period (Fig. 3.3.3) between 26 September to 30 December is calculated as $(-3.4 \pm 1.1)\,\mathrm{mol\,m^{-2}}$.

We estimate the cumulative NCP for the missing four month period of 2010 (July to October) using the mean rate for this period across other years of the 10 year Warp dataset, a subset of which is shown in appendix figure B.2.2. We calculate the mean value $(-18.2 \pm 2.3)\,\mathrm{mmol\,m^{-2}\,d^{-1}}$ giving a cumulative estimate for this period of $(-2.2 \pm 0.4)\,\mathrm{mol\,m^{-2}}$. There are no significant net autotrophic periods observed between June and September in any other year. We thus determine that the Warp site is net hetrotrophic with an annual oxygen NCP of $(-5.0 \pm 2.5)\,\mathrm{mol\,m^{-2}a^{-1}}$. However the validity of this assertion is discussed further later.

3.3.2 Sensitivity

Figure 3.3.4a shows total order Sobol' indices for the same period computed with eFAST. Here “total” is given to mean the factors main effects on the NCP estimate,

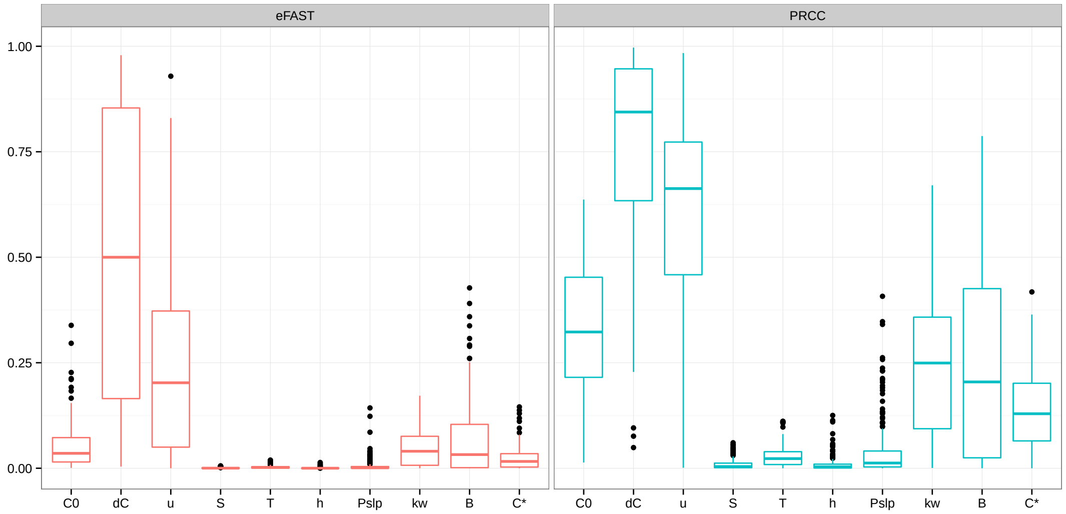

Figure 3.3.4: Warp sensitivity analysis indices. **(a)** eFAST total order Sobol' indices (fractional uncertainty contributions). **(b)** PRCC squared indices (ranked uncertainty contributions). Box plot upper and lower hinges correspond to first and third quartiles, whiskers extend to 1.5x of the inter-quartile range, outliers marked with dots. See Table 3.2 for variable definitions.

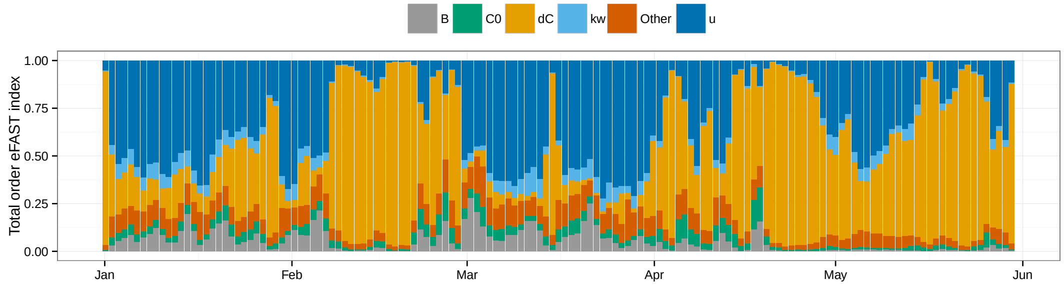

Figure 3.3.5: Warp eFAST total-order Sobol' indices over time, indicating changing fractional contributions to uncertainty from each of the main parameters.

combined with all the interacting terms involving that factor as per Saltelli (2008). The Sobol' indices are normalised to the total variance giving an indication of the fractional contribution to the variance for each factor. Note that unlike first order indices, the sum of the total indices can exceed one, In Fig. 3.3.4a and 3.3.5 we have normalised the total order indices to one to aid visualisation.

The squared PRCC values from spring 2008 are shown in Fig. 3.3.4b. These values are ranked measures, normalised to one, of the degree of monotonicity of each variable on NCP. In plainer terms, these are a measure of the independent effect of each input parameter on NCP regardless of whether any input parameter variables correlate. Using squared values makes for easier comparison with the eFAST indices as the ranked coefficients can be both negative and positive. The relationship between each of the variables and NCP is monotonic for the parameter ranges generated for each time step and thus each PRCC calculation. However, in aggregate over the dataset some of the variables can demonstrate a positive and negative (non-monotonic) relationship with NCP.

Both techniques indicate the determination of the change in oxygen concentration (ΔC) has the largest influence on overall uncertainty, with both the highest PRCC ranking and Sobol' total order indices. The eFAST analysis indicates that ΔC typically accounts for 53 % of the overall uncertainty. Wind speed U is the second largest contributor, typically comprising 26 % of the uncertainty budget. The bubble supersaturation parametrisation B accounts for 9 %. The gas transfer velocity parametrisation (k_w) and the initial oxygen concentration accuracy (C_0) are shown to have similar contributions of 6 %. The Garcia and Gordon (1992) oxygen saturation parametrisation contributes 4 %. Similar results from both sensitivity analyses indicates the model is well characterised by these methods.

The large confidence limits shown for U, k_w and B in Fig. 3.3.4 illustrates the large variability in PRCC ranking and Sobol' indices over the period studied. This indicates how the relative importance of these factors varies greatly over the data set. The timings for this variability is illustrated in Fig. 3.3.5. Here we observe periods (early January and most of March) where ΔC uncertainty is of minimal importance and wind speed uncertainty dominates. The uncertainty in NCP during the onset of the bloom (Mid April to mid May) is almost completely dictated by uncertainty in ΔC.

LHS/PRCC is not suitable for assessing the effects of measurement and parametrisation bias on the cumulative NCP estimate. Uncertainty in some of the parameters, principally U k_w, do not demonstrate monotonic relationships with the output measure. That is to say, uncertainty in U can lead to both increased or decreased cumulative NCP. Thus we present only eFAST indices for cumulative uncertainty in Fig. 3.3.6. B is shown to have the largest contribution, accounting for 40 % of the uncertainty in NCP alone, with a further 7 % from interactions with primarily with U.

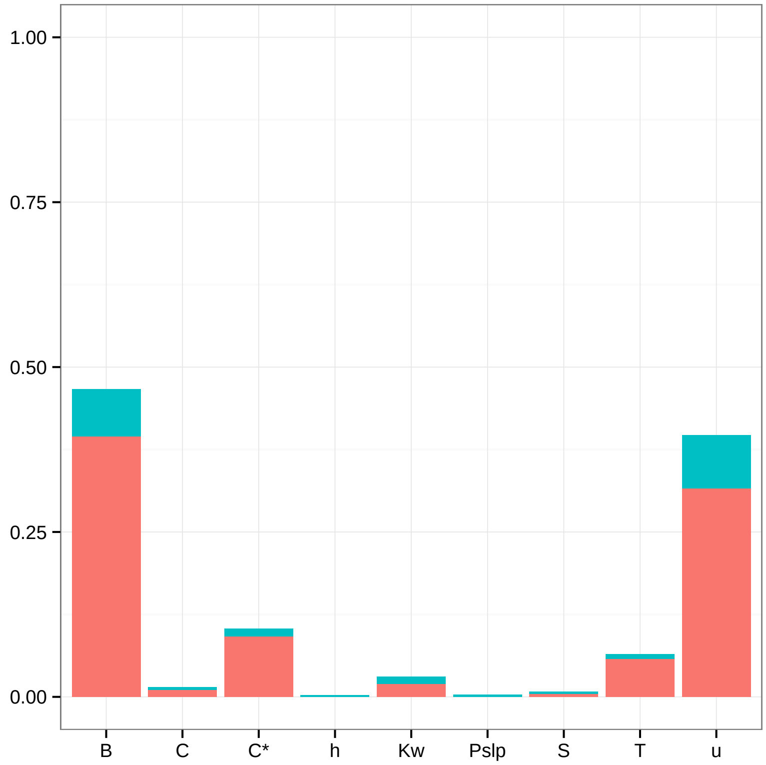

Figure 3.3.6: Warp eFAST first-order (red) and total-order (Cyan) Sobol' indices for cumulative NCP, indicating relative contributions from parameter bias uncertainty to cumulative NCP uncertainty.

3.4 Discussion

3.4.1 NCP

As the water column at the Warp is fully mixed, processes occurring at or in the sea bed are incorporated into the mixed layer mass balance and thus the NCP estimate. This includes non respiration oxygen-consuming processes such as nitrification and the oxidation of reduced compounds other than ammonia and nitrite. A previous study at the Warp using incubated sediment cores provides estimated rates of sedimentary oxygen uptake of 55 in July, and 26 mmol m^{-2} d^{-1} in April (Trimmer et al., 2000). Braeckman et al. (2014) observed maximal mean rates of nitrification reaching 6 mmol m^{-2} d^{-1} and similar for mineralization in muddy coastal North Sea sediment. This combined with sediment respiration equated to a sediment community oxygen consumption of 15 for Febuary and 20 mmol m^{-2} d^{-1} for April. This indicates that a large fraction (perhaps 50 %) of the observed negative NCP at Warp could be due to sedimentary processes.

It is important to consider that chemoautrophic processes, such as nitrification, contribute positively to the metabolic balance but negatively to the oxygen inventory. This is true, not just for benthic coupled sites like the Warp, but for any system where these processes occur. These processes, while assumed small relative to respiration and photoautorophy by (Reuer et al., 2007) in the Southern Ocean, are likely more important for shelf sea systems.

There are two events, one at the start of February, another in the second week of March where high winds appear to coincide with increased negative NCP (Fig. 3.3.2a). This could be considered non-intuitive as one may expect increased ventilation to drive the system closer to equilibrium but this is not the case as shown in figure 3.3.1b. There are several possible explanations. The optode may be underestimating, or the estimation of saturation concentration incorrect while in truth the system is supersaturated and is being driven closer to equilibrium during the windy events. We think this unlikely given our error bounds, calibration procedures and the results from our sensitivity analysis which indicate the bulk of the contribution to uncertainty is from the U term (Fig. 3.3.5). The windy periods could be driving resuspension events which could induce the apparent negative NCP. Lastly, this could be an artefact of the bubble supersaturation term overestimating at high wind speed. The orange line of figure. 3.3.1b shows the effects of the bubble term, and uncertainty, relative to the uncorrected blue line.

While its use in improving our knowledge of carbon cycling is well known, NCP also represents a potential next-generation indicator of ecosystem health. The short duration of the bloom and the large impact a two week period has on the annual budget could indicate that annual estimates, while vital for carbon cycling studies, are a less useful indicator for ecosystem health. A carefully resolved bloom period NCP may be more informative.

3.4.2 NCP as carbon equivalents

The commonly used “Redfield” stoichiometric ratio for O : C of 1.45 (Anderson and Sarmiento, 1994; Hedges et al., 2002) was applied to our positive oxygen NCP estimates for easier comparisons with other studies. Tijssen and Eijgenraam (1982) calculated net community oxygen production in the southern bight of the North Sea using shipboard 4 hourly winkler samples. They performed two surveys of 2 to 3 days in March and April 1980 with 24 h net community oxygen production estimates of 26 and 304 $\mathrm{mmol\,m^{-2}\,d^{-1}}$ respectively. The rates of net production seen at Warp, when expressed in units of carbon are of comparable magnitude to other estimates, With a maximal carbon NCP rate of $(346 \pm 92)\,\mathrm{mmol\,m^{-2}\,d^{-1}}$. Guo et al. (2012) report similar magnitudes of peak NCP from other studies in large river plume regions. Bozec et al. (2006) reported an annual carbon NCP estimate for the entire Thames plume region of $3\,\mathrm{mol\,m^{-2}\,a^{-1}}$. Their study integrated their four seasonal survey tracks into ICES regions, of which the Thames plume is one. Our annual carbon NCP estimate of $(-3.6 \pm 1.8)\,\mathrm{mol\,m^{-2}\,a^{-1}}$, represents a much smaller area, measured at considerably higher temporal resolution, for a much longer duration.

3.4.3 Measurement and model uncertainty

Prior oxygen NCP studies have neglected to include the production of oxygen within the time step, that is to say they assume an instantaneous production of NCP at the end of their time step when the measured oxygen concentration and abiotically predicted concentration are compared. This results in the underestimation of the magnitude of NCP. For example, oxygen produced at the start of the time step will out-gas quicker due to the increased air-sea concentration gradient, when the degree of supersaturation is later measured at the end of the time step the true magnitude of the supersaturation will be masked. The effect of neglecting the within-time-step NCP is negligible when conditions are near equilibrium saturation. However, during the bloom, neglecting the within-time-step NCP would result in a $45\,\mathrm{mmol\,m^{-2}\,d^{-1}}$ (9 %) underestimation of peak oxygen NCP.

The results from both LHS/PRCC and eFAST techniques support the conclusion that the bulk of the uncertainty in the NCP calculation is dependent on the determination of changing oxygen in the mixed layer. This is in keeping with the observations of Emerson et al. (2008) uncertainty analysis of their O_2/N_2 method where 54 % of the uncertainty was due to oxygen determination.

The mean and median value for ΔC standard error were 1.1 and $0.6\,\mathrm{mmol\,m^{-3}}$. Greater variability is seen during the bloom with values up to $7.0\,\mathrm{mmol\,m^{-3}}$. During calibration in a thermostatic bath the optodes used typically demonstrated a precision of $\pm 0.3\,\mathrm{mmol\,m^{-3}}$. This is within the specification from the manufacturer of $\pm 0.4\,\mathrm{mmol\,m^{-3}}$ and in agreement with the findings of Wikner et al. (2013). Thus it would appear that the largest source of uncertainty constrained here is the large degree of variability captured within the 25 h mean rather than the instrument. The range of values observed within any 25 h period differed by up to 91.2 mmol m^{-3} during the bloom. During the non-productive period the observations within each 25 h period varied by on average 9.2 mmol m^{-3}. This variability is shown with the small subsection of the raw oxygen time series presented in Fig. B.2.3. The variability seen here represents both tidal movement of water past the buoy, together with diel cycling of production. Thus we believe improvements in identifying homogeneous water masses over the tidal cycle, rather than integrating it entirely, is the best approach to reducing uncertainty with this scheme.

Shipboard transect studies (typically utilising O_2/Ar methods in open ocean environments) observe any disequilibrium oxygen in relation to the gas residence time, that is, they assume constant NCP in the period leading up to the measurement (Kaiser et al., 2005). It would thus appear that single shipboard transects will struggle to fully capture the tidal induced variability found in areas such as the Warp.

For the investigation of cumulative uncertainty we consider only the bias in each parameter. The bubbles supersaturation term (B), while small in regards to PRCC and eFAST values for an individual estimate (Fig. 3.3.4), has a large effect on the cumulative mass balance (Fig. 3.3.6). We calculate a pseudo-cumulative spring period NCP of (2.3 ± 0.9) mol O_2 m^{-2} resulting from neglecting B, four times our true estimate. This relatively large effect is due to the biased nature of the supersaturation term, which serves to only increase the oxygen concentration in the mixed layer.

Optodes tend to drift towards underestimating oxygen concentrations (Wikner et al., 2013) which will typically result in underestimates of NCP. We re-ran our analysis simulating a 1 mmol m^{-3} per month negative linear drift, which provides a pseudo-cumulative oxygen NCP estimate for the Spring period of (-0.5 ± 0.8) mmol m^{-2}, which contrasts with our corrected value of (0.5 ± 1.0) mmol m^{-2}. This reinforces the requirement for well calibrated, drift corrected measurements.

Future studies are likely to benefit from newer Optode designs than those used here. Together with the improved multi-point calibration equation (Stern-Volmer) of McNeil and D'Asaro (2014), these can offer greater accuracy and precision. The in-air calibration procedures outlined by Bushinsky and Emerson (2013) can reportedly offer frequent in-situ calibrations of ±0.1 %. The in-air measurements could also be used to calculate the concentration gradient between the mixed layer waters and the air, which eliminates the requirement for a C_{sat} parametrisation

Emerson et al. (2008) noted that at Hawaii Ocean time series site small daily fluctuations in the measured oxygen concentration caused large fluxes, but these were both positive and negative and had little impact on the cumulative NCP. Fluctuations around zero are seen in the Warp. These do not tend to cancel out and combine to form a significant negative NCP flux. Emerson (2014) observed the standard deviation of the individual mean annual values is up to ±50 % which reflects both real inter annual variability and measurement/model error. This study has produced NCP estimates for the spring period of up to almost 100 % due primarily to the large uncertainty centred around the bloom. Our winter period estimate demonstrates a degree of uncertainty similar to that of the open ocean study of Emerson (2014), albeit with a net heterotrophic system.

3.4.4 Advection and sampling uncertainty

Previous studies in open ocean environments have ignored horizontal advection (Emerson et al., 2008; Nicholson et al., 2008). Air-sea gas exchange is typically considered to be sufficiently rapid that horizontal gradients are too small to drive a significant flux (Alkire et al., 2014). Semi-diurnal tidal systems such as at the Warp demonstrate horizontal displacement of water masses with a periodicity of 12 h 25 min, with maxima in current speeds every 6 h 12 min which drive significant horizontal variability (Blauw et al., 2012).

The box model presented here relies on the assumption that the instruments are measuring the same body of water twice, i.e. the comparison of two consecutive 25 h averages represent the same mass of water evolved over time. If we assume that conditions along the path length are homogeneous on 25 h time scales, in effect the NCP estimates presented here can be thought of as integrating over a length scale proportional to the residual flow. Historic acoustic Doppler current profiler data gathered over 3 months at the Warp (See Appendix A) shows a residual mean current flow estimated at 1.9–2.2 $\mathrm{cm\,s^{-1}}$, bearing 120°. This combined with the average tidal excursion of 1.7 $\mathrm{km\,d^{-1}}$ equates to a observational window of approximately 3.5. km for $t = 25\,\mathrm{h}$.

While our 25 h averages and dC error bounds most likely capture the tidal and diel dependent variability, further uncertainty is introduced by submesocale variability such as phytoplankton patches and eddies. Given Tijssen and Eijgenraam (1982) observed horizontal oxygen gradients of up to 3 $\mathrm{mmol\,m^{-3}}$ over a few hundred meters, Determining to what extent our assumption of homogeneity holds over 25 h, and to what extent patchiness within this timescale can influence our estimates is a further step to ensuring a robust NCP estimate.

Residual currents will also affect the NCP estimates by the addition and loss of water from outside of our observational window. (Alkire et al., 2014) calculated the advective flux during their glider study and observed daily mean flow of up to $2\,\mathrm{cm\,s^{-2}}$. This when combined with their measured horizontal gradient produced the mean removal of $(18 \pm 10)\,\mathrm{mmol\,m^{-2}\,d^{-1}}$ oxygen though horizontal advection.

We have attempted to estimate the oxygen concentration gradient from the tidally driven oxygen variability; that is the difference between the oxygen concentration at low and high tide. We calculate this for our January period to be approximately $2\,\mathrm{mmol\,m^{-3}}$, with low tide concentration greater than high tide. From which we can estimate a advective flux of $51\,\mathrm{mmol\,m^{-2}\,d^{-1}}$ using Eq. 3.4.1 (Emerson and Stump, 2010).

$$A_F = u(\frac{dC}{dx})h \tag{3.4.1}$$

Where u is the Ekman advection velocity.

This is not an insignificant flux relative to our calculated winter heterophy and would indicate that our site could actually be autotrophic with the heterotrophic processes occurring upstream. It is clear that consideration of advection is required to accurately estimate the annual metabolic state at this site.

3.4.5 Other sources of uncertainty

There are several other known contributors to NCP uncertainty which are outside the scope of this study. Kitidis et al. (2014) argues that all O_2 based methods underestimate NCP due to photochemical processes, and they report that their modelled photochemical oxygen demand was shown to occasionally exceed respiration, with demand ranging between $3\,\mathrm{mmol\,m^{-3}\,d^{-1}}$ to $16\,\mathrm{mmol\,m^{-3}\,d^{-1}}$. Oxygen photolysis was found to correlate with CDOM absorbance at 300 nm. While significant concentrations of CDOM can be found at the Warp (Foden et al., 2008), the effects are likely mitigated by the typically high turbidity, and the associated rapid light attenuation, and shallow (frequently $< 6\,\mathrm{m}$) photic depth.

Takagaki and Komori (2007) found the maximum enhancement to CO_2 gas transfer by rainfall is similar in magnitude to that of high wind speeds. This enhancement is thought mainly to be though increased turbulence and surface area at the air-water interface and as such it is likely to be most significant where heavy rain is coincident with light winds (Beale et al., 2014).

Frew et al. (2004) found that surfactants may be responsible for coastal waters having significantly lower transfer velocities than oligotrophic areas. However Nightingale et al. (2000) found no measurable change in k_w during a 30 fold increase in Chlorophyll during an algal bloom. We, like Wanninkhof et al. (2009) consider that practically surfactants are always in effect and are thus incorporated into empirically derived k_w parametrisations.

Similarly while sea spray may also enhance gas transfer, we believe this to also already be accounted for in the parametrisation. Further uncertainties relating to the parametrisation of k_w are likely of little concern without first reducing other, more significant sources.

3.5 Conclusions

Our work identifies the Warp SmartBuoy site as an annually net heterotrophic location with strong seasonal variability and autotrophy during the growth phase of the bloom. However, this assertion is bought into question due to significant unconstrained uncertainties from horizontal advection, the determination of which is outside the scope of this study and these data. We have demonstrated that the largest constrained source of uncertainty in our NCP estimates comes not from the selection of gas exchange parametrisation, or the quality of remote sensed and modelled parameters, but from the measurement of the changing oxygen concentration. For cumulative annual estimates, the strongly biased uncertainty from bubble induced supersaturation is the dominant source of uncertainty. Constraining the degree of horizontal advection is vital to improving long term NCP estimates, and to accurately determine the overall metabolic balance.

Chapter 4

Bottom mixed layer oxygen dynamics in the Celtic Sea

The peer reviewed paper (Hull et al., 2020) forms the basis of this chapter. The introduction has been shortened to avoid repetition. Here we use oxygen observations taken from seabed landers to determine the oxygen dynamics in the bottom mixed layer of a stratified temperate shelf sea. We exploit the local tidal dynamics to allow the determination to the horizontal oxygen fluxes using a Baysian state-space approach.

4.1 Introduction

The continental shelf seas play a disproportionately important part in the global cycling of carbon, and in particular organic carbon storage (Legge et al., 2020). Shelf seas also vary over short temporal and spatial scales, therefore long term and spatially broad averages do not well represent their dynamics. In particular there is a lack of understanding regarding how the rates of shelf sea biogeochemical processes vary across sediment types, or how they change over the annual cycle (Hicks et al. (2017)). For large parts of the shelves it is unclear if the sediments are a source or sink for carbon (Thompson et al. (2017)).

Retrieving intact seabed sediment samples for incubation to determine biogeochemical rates has some disadvantages. Sample recovery is often accompanied by physical changes, notably a reduction in pressure, differing temperature and the introduction of light, which can make it difficult to obtain representative data (Tengberg et al. (2006)). Furthermore, for permeable sediments it is extremely difficult to maintain sediment advection under any realistic regime, which can result in anaerobic mineralization to be overestimated due to the reduction in sediment ventilation (Larsen et al. (2013)). It is similarly challenging to integrate over wide spatial and temporal scales as the short term changes or local processes seen in shelf seas may be missed with discrete sampling (Thompson et al. (2017)). Mesoscale studies can capture these shorter scale dynamics which both discrete sampling and more coarse modeling approaches can miss. Improved management and conservation of coastal systems requires predictions of the effects of deoxygenation at the spatial and temporal scales most relevant to the ecosystem services provided (Breitburg et al. (2018)).

In the seasonally stratified seas the bottom mixed layer (BML) is partially isolated from the atmosphere and is thus controlled by interplay between oxygen consumption processes, vertical and horizontal advection. Oxygen consumption rates can be both spatially and temporally dynamic, but these dynamics are often missed with incubation based techniques. Quantifying total oxygen uptake rates provides us with critical information for understanding both deoxygenation and carbon cycling.

Here we adopt a Bayesian state-space approach to determining total BML oxygen consumption rates from a high resolution oxygen time series. This incorporates both our knowledge and our uncertainty of the various processes which control the oxygen inventory. Total BML rates integrate both processes in the water column and at the sediment interface. These observations span the stratified period of the Celtic Sea and across both sandy and muddy sediment types. We show how horizontal advection, tidal forcing and vertical mixing together control the bottom mixed layer oxygen concentrations at various times over the stratified period. Our muddy-sand site shows cyclic spring-neap mediated changes in oxygen consumption driven by the frequent resuspension or ventilation of the seabed. We see evidence for prolonged periods of increased vertical mixing which provide the ventilation necessary to support the high rates of consumption observed.

4.1.1 The Celtic Sea

The Celtic Sea is a semi-enclosed seasonally stratified shelf sea on the north-western European shelf (fig. 4.1.1), with open exchange with the North Atlantic at its south-west boundary. The southern Celtic Sea is thought to be a net sink for atmospheric CO_2 over an annual cycle (Marrec et al. (2015)), with the fate of this carbon being exported back to the open ocean (Humphreys et al. (2018)) or sequestered in shelf sea sediments (Diesing et al. (2017)).

Tides in this region are semidiurnal with the M2 constituent representing 75 % and S2 a further 15 % of the total tidal kinetic energy of the currents (Brown et al. (2003)). There is considerable variability in tidal stream amplitude over the region with typical spring currents varying between 0.3 and in excess of 1 m s^{-1} depending on location (Carrillo et al. (2005)). These tides are the primary driver of current variability, but play little role in long-term residual flow which is predominately controlled by wind forcing and density changes (Carrillo et al. (2005)).

The water column is fully mixed during winter, transitioning into a two-layer stratified system with a transitional thermocline during early spring. We refer to these layers as the surface mixed layer (SML) and bottom mixed layer (BML). The onset of stratification is driven by increasing heat inputs overcoming tidal and wind mixing (Pingree et al. (1976), Wihsgott et al. (2016)). Thus the thermocline is first established in areas of weak tides (Pingree et al. (1976)). Coincident with the formation of the thermocline is the initiation of a spring phytoplankton bloom, typically dominated by diatoms (Joint et al. (1986)). This is followed by a persistent subsurface chlorophyll maximum (Hickman et al. (2009)) and subsequent autumn bloom (Wihsgott et al. (2019)). Production at the thermocline is thought to contribute half of the summer shelf production (Williams et al. (2013a)). In winter the loss of heat to the atmosphere triggers the breakdown of stratification (Thompson et al. (2017), Wihsgott et al. (2019)). Stratification is thus temperature driven with little influence from salinity (Wihsgott et al. (2019)).

In the Celtic Sea a bottom mixed layer (BML) forms where tidal mixing is strong enough to homogenise near bed density gradients (Wihsgott et al. (2019)). Disconnected from direct gas exchange with the atmospheric and below the photic zone (>50 m, Platt et al. (1993)), the BML oxygen concentrations are controlled by oxygen consumption processes within the water column, at the sediment-water interface and indirect ventilation across the thermocline (Greenwood et al. (2010), Große et al. (2016), Queste et al. (2016)). These sediment and water column processes comprising primarily of respiration and nitrification will consume oxygen and are fueled by the available organic matter. While mixing across the thermocline is a positive flux into the BML, the majority of the oxygen available for respiration during the stratified period is set at the onset of stratification. The magnitude of this flux can vary substantially. Short term changes in SML oxygen concentration, such as during the spring or autumn blooms, can rapidly change the vertical oxygen gradients. Vertical mixing rates have been shown to be highly dynamic, with wind-tide interactions increasing rates over two orders of magnitude (Palmer et al. (2008), Williams et al. (2013a), Wihsgott et al. (2019)). This initial oxygen concentration is thus controlled primarily though the water column temperature just prior to the formation of the thermocline (Queste et al. (2016)). With a near-fixed oxygen inventory and enhanced rates of respiration driven by sinking organic material, the bottom mixed layer experiences oxygen depletion during the summer months (Greenwood et al. (2010), Breitburg et al. (2018)).

Different sediment types have been shown to exhibit variable consumption rates and responses to changes in the overlying water (Klar et al. (2017)). This variation is thought to be due to the composition of the sediment, cohesive properties and permeability, together with the presence and activity of the benthic fauna (Silburn et al. (2017)). The Celtic Sea has a diverse range of sediment types, spanning mud to gravel, with variable rates of oxygen consumption (Hicks et al. (2017)).

4.1.2 This study

In this study we explore the temporal variability in bottom mixed layer oxygen consumption at two contrasting sites in the Celtic Sea during 2014 as part of the NERC-DEFRA Shelf Sea Biogeochemistry (SSB) project (Thompson et al. (2017)). Although vertical mixing is typically described as the primary source of ventilation for the stratified shelf sea bottom mixed layer, in the Baltic sea horizontal (water-column) advection has been shown to be an additional important control on local oxygen concentrations (Bendtsen et al. (2009), Holtermann et al. (2019)).

Recent modeling studies have highlighted the importance of these processes for predicting deoxygenation (Bahl et al. (2019)). We implement two novel oxygen mass-balance methods to separate out local consumption processes from the horizontal advection. This integrated measure incorporates processes occurring within the bottom mixed layer and also at the sediment-water interface.

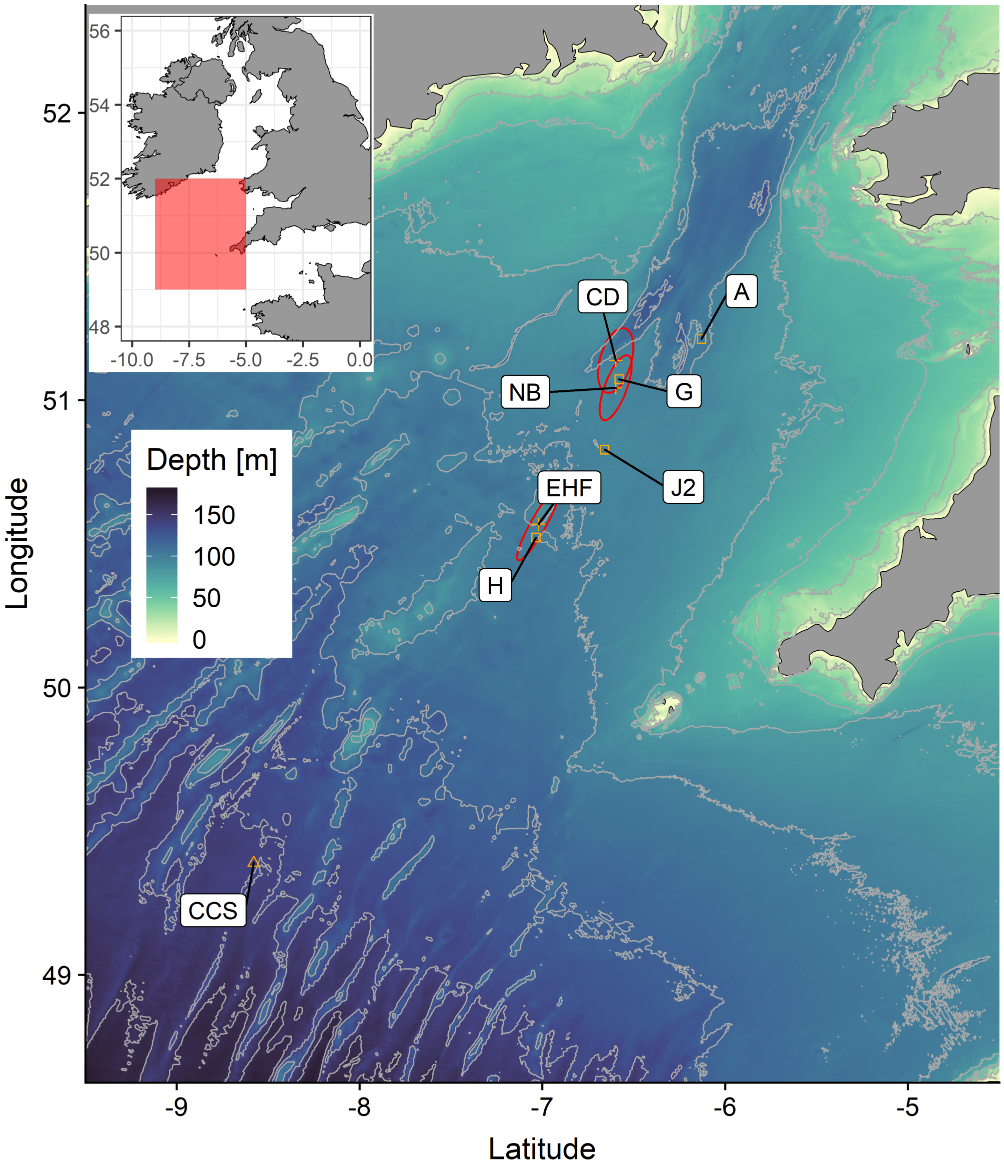

Figure 4.1.1: The Celtic Sea study sites. Red circle indicate tidal elipses at each lander site (NB, EHF and CD). G, H are sample sites for benthic incubations, J2, A and CCS are sample sites for pelagic incubations. CCS and CD are also the locations for two Cefas SmartBuoy moorings. Bathymetry from GEBCO 2019, 15 arc-second grid.

4.2 Method

4.2.1 Landers and sensors

Table 4.1: Study site sediment characteristics for for Nymph Bank (NB), East of Haig Fras (EHF) and Celtic Deep Lander (CD), sediment composition predicted using the parametrisation of Diesing et al. (2017)

Site	Lat (°N)	Lon (°W)	Depth (m)	Mud (%)	Sand (%)	Gravel (%)	Folk class
NB	51.04	-6.60	110	5	93	2.4	gravelly sand
EHF	50.57	-7.02	117	23	77	<0.1	muddy sand
CD	51.14	-6.60	109	7	92	0.9	sand

Cefas benthic landers were placed at four sites during the SSB program (Thompson et al. (2017), table 4.1, table 4.2, fig. 4.1.1), two of which are included in this study: EHF, a benthic lander situated east of Haig Fras (Hull et al. (2017b)), a 45 km long submarine rocky outcrop and NB, a lander on the Nymph Bank, West of Celtic Deep (Hull et al. (2017c)). The East of Celtic Deep (ECD) site, was damaged by fishing activities during the first 10 days of deployment and is not used in this study. In addition, figure 4.1.1 shows the central Celtic Sea (CCS) study site (García-Martín et al. (2017b)) and CD, the long term Celtic Deep site which included a surface mooring (Hull et al. (2017a)) and a thermistor chain (Wihsgott et al. (2016)). A lander was also deployed at CD in October 2014 (table 4.2). Two nearby study sites, G and H, were used for sediment core incubation studies during SSB and are also shown in figure 4.1.1.

The landers were fitted with Aanderaa 3835 oxygen optodes (Aanderaa data instruments, Norway), Seapoint SCF chlorophyll-α fluorometers and Seapoint STM optical backscatter turbidity meters (Seapoint Sensors Inc, USA). The optode and Seapoint sensors were fitted with an anti-fouling wiper (Zebra-Tech inc. NZ). RDI Workhorse 600 acoustic Doppler current profilers (ADCP) were configured to observe the bottom 40 m of the water column, with the ADCP first bin at 1.9 m. The biogeochemical observations were recorded via Cefas ESM2 dataloggers (Hull et al. (2016)) set for 5 minute burst sampling every 30 minutes synchronised with the hourly ADCP samples. The sensors were all mounted at 0.5 m above the seabed.

The optodes were two-point calibrated prior to deployment (Bittig et al. (2018b)). A linear offset correction was applied, determined from post-deployment and pre-recovery in-situ Winkler samples. No detectable drift was observed; the difference between the post-deployed and pre-recovery offsets is smaller than the standard deviation for each (< 5 mmol m^{-3}). This lack of drift is likely due to the relatively short duration of the deployment and the care taken in keeping the optodes wet and in the dark prior to use. These optodes have also had extensive use prior to this study, and thus the luminophore foils were thoroughly “burnt in” (Bittig et al. (2018b), Tengberg et al. (2006)).

Table 4.2: Study site current characteristics for Nymph Bank (NB) deployment 1, East of Haig Fras (EHF) deployents 1 to 3 and Celtic Deep Lander (CD) deployment 1. Current speeds shown in $\mathrm{m\,s^{-1}}$

Deployment	Start date	End date	Duration	Mean BML current speed, (max)
NB 1	2014-04-01	2014-06-17	77 d	0.18 ± 0.09 (0.42)
EHF 1	2014-04-09	2014-05-31	52 d	0.21 ± 0.11 (0.50)
EHF 2	2014-06-17	2014-08-19	63 d	0.20 ± 0.11 (0.56)
EHF 3	2014-08-21	2014-10-02	42 d	0.21 ± 0.12 (0.60)
CD1	2014-10-24	2014-12-24	61 d	0.18 ± 0.08 (0.47)

4.2.2 Oxygen mass balance

We describe the bottom layer oxygen mass balance as follows.

$$h_\mathrm{b}\frac{dC_\mathrm{b}}{dt} = M_z - A_u - A_v - R \tag{4.2.1}$$

Where C_b is the bottom mixed layer oxygen concentration, M_z is diapycnal eddy diffusion and $A_u + A_v$ is horizontal advection. R is oxygen uptake, though bottom mixed layer processes, primarily respiration. h_b is the bottom mixed layer thickness.

$$M_z = K_z \frac{dC}{dz} \tag{4.2.2}$$

Where dC is the difference between the SML (C_s) and BML oxygen concentration (C_b). dz corresponds to the thickness of the thermocline (h_TC). K_z is the vertical (diapycnal) eddy diffusion coefficient estimated to be in the region of 4.5 x 10^{-5} m^2 s^{-1} (Palmer et al. (2008)). M_z is constrained as a purely positive flux as SML oxygen concentrations at these sites are always greater than those in the BML ($C_s > C_b$). as indicated by long term mooring data (Hull et al. (2017a)) and CTD casts (fig. 4.2.1).

$$A_u = u\beta_u h_\mathrm{b} \tag{4.2.3}$$

Where A_u is the advection in the east-west direction, u is the horizontal velocity in the east-west direction. β_u is the east-west gradient defined as.

$$\beta_u = \frac{C_u - C_\mathrm{b}}{dx} \tag{4.2.4}$$

Where dx is the gradient length scale and C_u is the upstream oxygen concentration. The same formulation applies for the v north-south velocity. Here, given the tidally driven flow, "upstream" will refer to different directions depending on the current flow.

Similar oxygen modeling studies such as Emerson et al. (2008) and Bushinsky and Emerson (2015) include a vertical entrainment term. However, in this study we have very little evidence for such processes, our estimate of the bottom mixed layer thickness does not feature any large scale changes with any associated increase in oxygen or temperature. We determine it is thus not appropriate to include an entrainment term, and all vertical mixed processes are encapsulated in our M_z term.

Constraining the depth of the bottom mixed layer (h_b) and the thickness of the thermocline (h_TC) is vital to enable good estimates of R. As equation 4.2.1 indicates, uncertainty in h_b has a multiplicative effect on R. The depth of the seasonal thermocline is typically shallower than the range of the bottom mounted ADCP, making direct observation impossible. Water column temperatures were thus taken from the UK Met Office FOAM Atlantic Margin Model 7 km reanalysis

(AMM7) (O'Dea et al. (2017)). Further details of the AMM7 processing and validation with our thermistor string observations is found in the appendices C.2.

4.2.3 Probabilistic mass balance model

Oxygen based metabolic balance estimates can have multiple large uncertainties (Hull et al. (2016)). By adopting a Bayesian approach we leverage the explicit use of probability for quantifying uncertainty in inferences (Grace et al. (2015), Holtgrieve et al. (2010)). To this end, we define a probabilistic relationship between our observations, our prior knowledge of unobserved processes, such as the acceptable range of possible values for the diapycnal eddy diffusion coefficient and unknown parameters such as the respiration rate. In short, this Monte-Carlo method allows us to simultaneously estimate R, h_{TC}, K_w, β_u, β_v and h_b as parameters, and provide probable intervals for each. Full details of the model equations, prior distributions, implementation and validation are found in the appendices C.1.

4.2.4 Regressive matched-water method

In this dynamic environment with known horizontal gradients, some approach must be taken to separate out spatial and temporal variability. The observation sites, and in particular Nymph Bank (fig. 4.3.2 A), have periods of highly circular flow. Given the assumption that currents measured by the lander ADCP are reasonably representative of the surrounding area, we can observe multiple points where the cumulative vector intersects with itself. That is to say the previously observed patch of water has been observed again. We define a pair of observations as being within the same water mass when the cumulative vector intersection is within 150 m spatially and more than one full tidal cycle away temporally. That is to say we only compare points where the water mass horizontal position is within 150 m of where it was previously, and more than 6 hours have passed since the last observation. Fitting a linear model to the change in oxygen observed between each spatially-temporally matched pair over time provides an estimate for the oxygen consumption rate in the BML without the influence of horizontal advection. This method can only be used where the tidal flow is reasonably circular and residual currents are either small or periodic. We use this method as a further validation of the probability model.

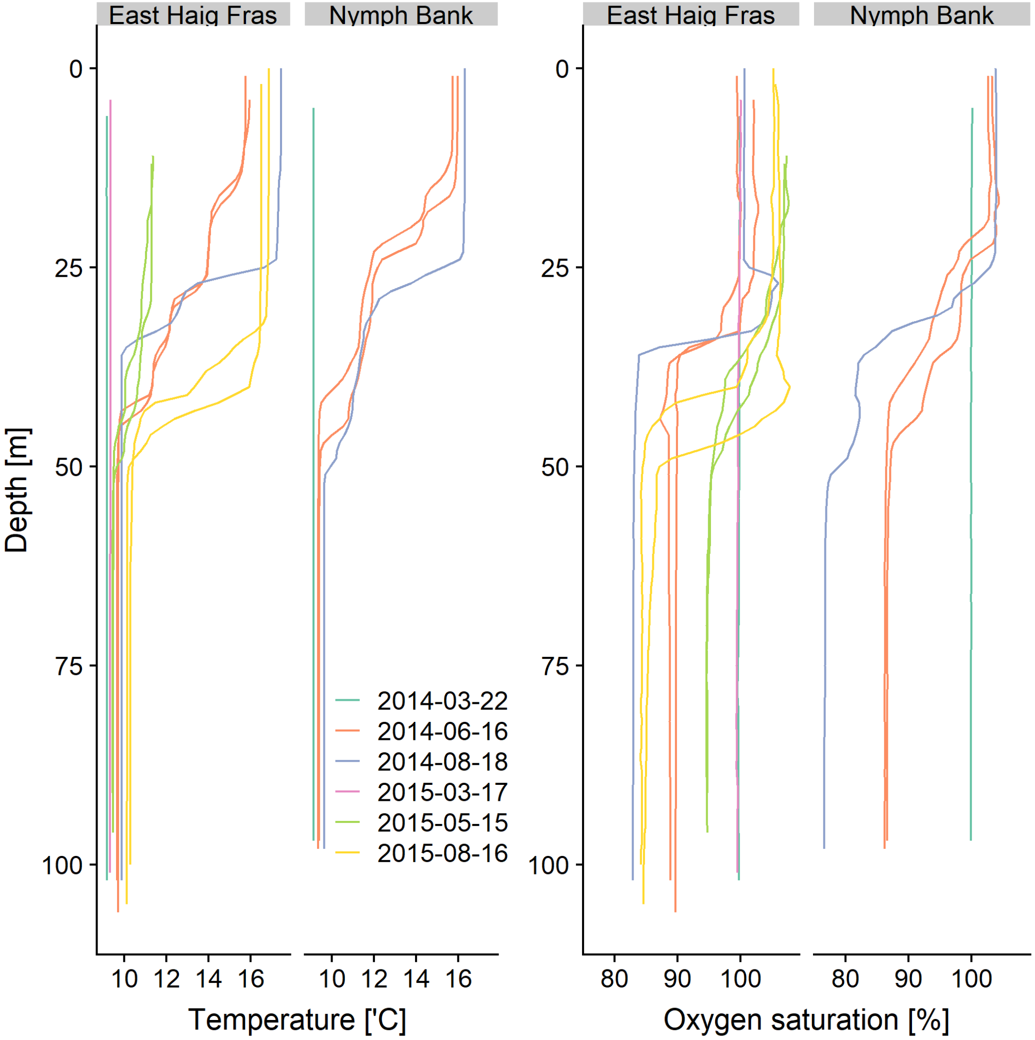

Figure 4.2.1: Temperature and oxygen saturation profiles from CTD rosette casts at the East of Haig Fras and Nymph Bank sites. Colours indicate date of cast.

4.3 Results

In 2014 the central Celtic Sea began to stratify in late March, as confirmed by a thermistor array at the CD site. The analysis is thus restricted to the stratified period from the 5th of April (fig. 4.3.1 A). All sites show a decline in oxygen concentration after the onset of stratification. Throughout this section ± will be used to express 2 σ uncertainties where values are normally distributed and 95 % quantile range [2.5 %, 97.5 %] if they are not.

4.3.1 Nymph Bank

The tidally averaged (25 h) observations from Nymph Bank indicate a reduction in oxygen from 290 to 245 mmol m^{-3} over this 73 day period, equating to 0.62 mmol m^{-3} d^{-1} (fig. 4.3.1 B). Tidal current flow is in a NE-SW direction (fig. 4.1.1). Residual flow is variable, with water moving first to the west, before returning east (fig. 4.3.2 A, and fig. 4.3.1 C). The semi-diurnal cycle shown in figure 4.3.1 B suggests that the bottom oxygen concentration is influenced by tidal advection. This indicates a horizontal oxygen gradient within the BML. The u (east-west, zonal) vector inversely correlates with oxygen; positive u (current moving water to the east) is reducing the apparent local oxygen concentration and implies a negative β_u ($\beta_u = \frac{dC}{dx}$). Thus lower oxygen water is being advected from the west. AMM7 predicts the bottom mixed layer to be (59 ± 2) m and the thermocline is estimated to be between 5 and 15 m thick (fig. 4.3.1 A).

Linear regression using the matched water approach indicates a slope 0.65 mmol m^{-3} d^{-1} (Standard error = 0.005, Adjusted R^2 = 0.981, n = 451) (fig. 4.3.2 B). This slope represents the average bottom mixed layer oxygen consumption without the influence of horizontal advection. The linear model has a reasonable fit; we have the impression of variable slopes for some clusters indicating a variable relationship with oxygen consumption and time, i.e. variable respiration rates. However, the residuals appear normally distributed and there is fairly equal variance. This volumetric oxygen consumption rate can then be integrated over the BML (h_b = (59 ± 10) m), giving (38 ± 6) mmol m^{-2} d^{-1}. Diapycnal mixing of oxygen using the thermocline thickness and Gaussian kernel smoothed (bandwidth = 1 week) surface oxygen concentrations observed from the Celtic Deep buoy, provides a mean flux of oxygen across the thermocline of 3.8 mmol [0.2, 11.1] m^{-2} d^{-1}. Adding this to the integrated rate gives a total local bottom mixed layer oxygen consumption of (42 ± 8) mmol m^{-2} d^{-1},

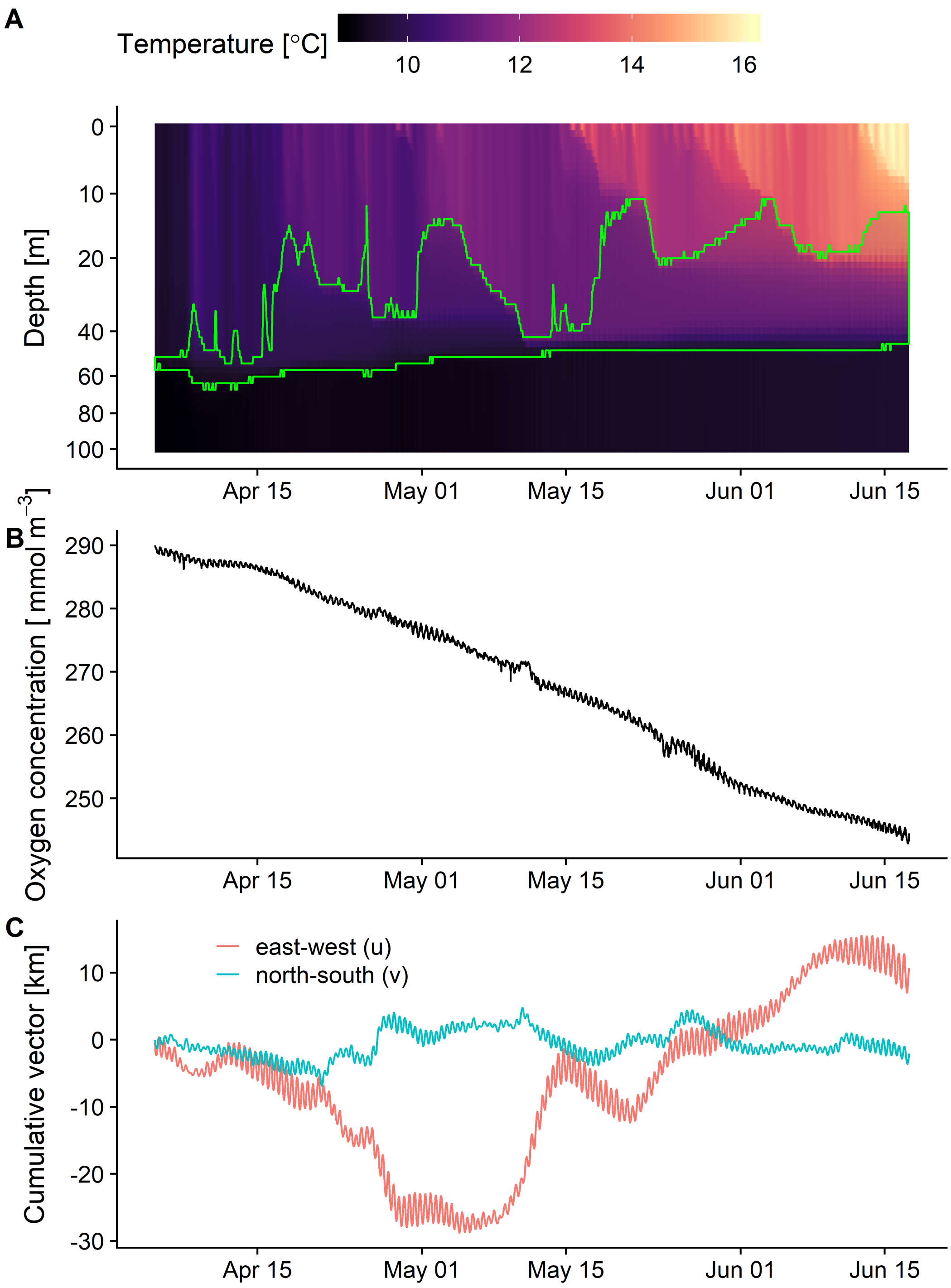

Figure 4.3.1: Nymph Bank time series (NB), **(A)** AMM7 water column temperature with the upper and lower bound of the thermocline highlighted in green. **(B)** Bottom mixed layer oxygen concentration measured by the benthic lander. **(C)** Cumulative horizontal advection as measured from lander ADCP in the east (red) and north (blue) directions

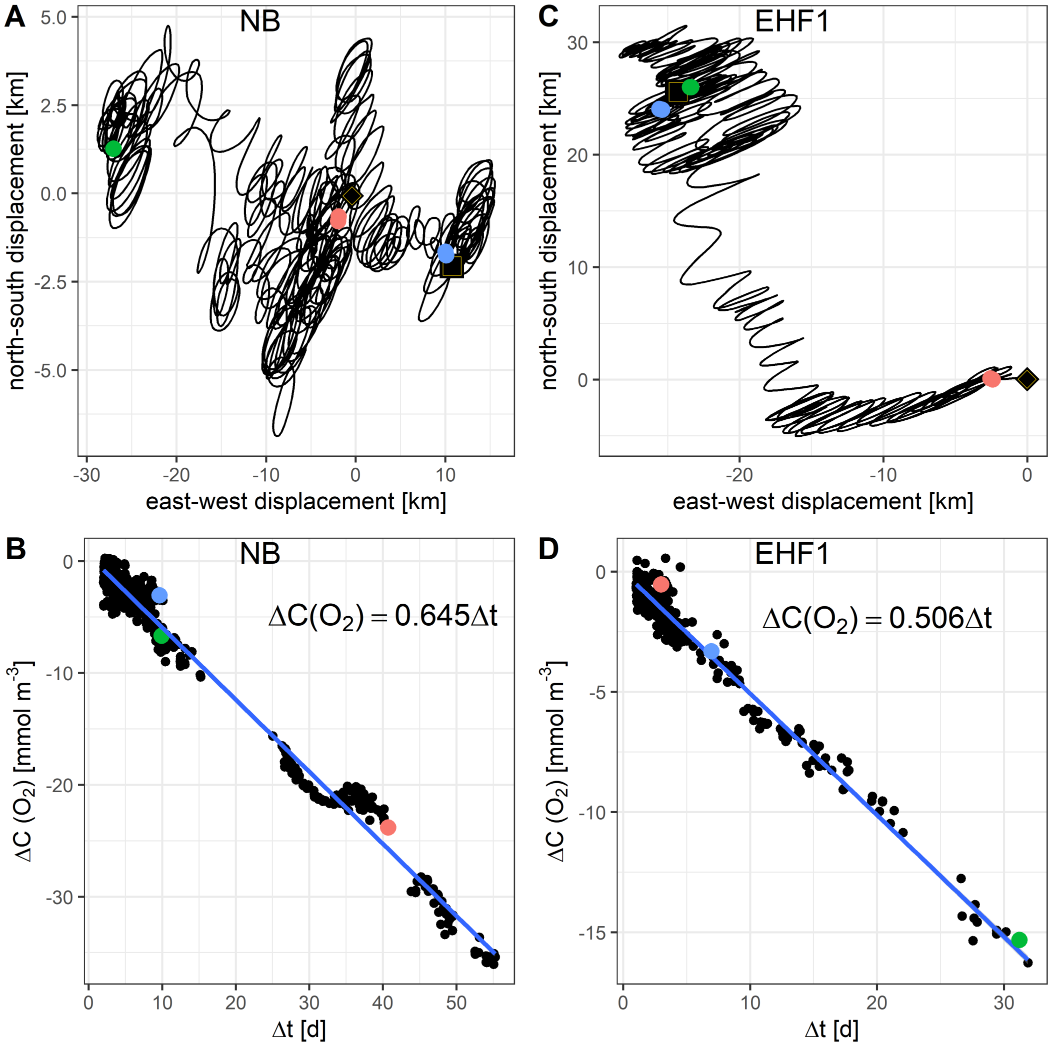

Figure 4.3.2: **(A & C)** Cumulative vector diagrams for Nymph Bank **(A)** and East Haig Fras deployment 1 **(C)**, black diamond indicates start of the time series, while black square represents the end. **(B & D)** linear model fits of matched water observations for Nymph Bank **(B)** and East Haig Fras deployment 1 **(D)**. Each point represents a spatial paired observation, slope indicates average bottom mixed layer oxygen consumption without the influence of horizontal advection. Coloured markers indicate selected spatially paired points and their location in the linear model.

equating to (0.72 ± 0.09) mmol m^{-3} d^{-1}.

We fit these same data using the probabilistic mass balance model. The residual random noise term σ is small and normally distributed (fig. C.1.3), (0.30 ± 0.004) mmol m^{-3}, indicating the model fits well to the observations. Mean oxygen consumption (R) over this 73 day period is estimate as (0.63 [0.01, 1.62]) mmol m^{-3} d^{-1}, but demonstrates short term variability as shown in figure 4.3.3 B and D. Peak consumption occurs around 2014-05-22 with an estimated rate of (100 ± 25) mmol m^{-2} d^{-1} (fig. 4.3.3 B). Lowest R is seen prior to the increase in BML chlorophyll associated with the spring bloom in around the 2014-04-08, here R is indistinguishable from zero. Similarly low BML oxygen consumption is seen between 2014-05-10 and 2014-05-15.

Peak chlorophyll is seen at the Celtic Deep Buoy on 2014-04-14 as shown in figure 4.3.3 B. We surmise this BML chlorophyll signal is associated with falling phytoplankton material produced in the SML. Increases in turbidity are seen following the increase in chlorophyll. The chlorophyll signal returns to pre-bloom levels around the 2014-05-02. A second increase in turbidity is observed in mid May with a much reduced associated chlorophyll signal. This is associated first with a very low oxygen consumption rate, indistinguishable from zero by the model. There is then a sharp spike in turbidity followed by another increase in consumption (fig. 4.3.3 D).

Horizontal gradients are are also estimated (fig. 4.3.3 A). We observe a persistent eastward gradient of (-0.19 ± 0.12) μmol m^{-4} and a northward gradient of (0.53 ± 0.26) μmol m^{-4}. This indicates lower oxygen water to the west and higher concentration to the south. Given the observed residual flow (fig. 4.3.1 C) this equates to a cumulative horizontal flux of (11.9 ± 0.8) mmol m^{-2} for this period.

Inspection of the K_z and h_{TC} parameters comprising the modeled M_z (fig. 4.3.3 C) indicates this model and these data are most compatible with slightly increased diapycnal mixing rates compared to our prior (5.4 x 10^{-5} m s^{-1}). Wihsgott et al. (2019) demonstrated that K_z rates show short term variability and can vary over several orders of magnitude in shelf seas. Our model however is configured to estimate an average K_z over the entire deployment. Therefore, short term pulses in mixing rates will increase the uncertainty and move the average estimate (the posterior distribution for K_z) towards higher values.

Figure 4.3.3 B shows a period between 2014-05-08 and 2014-05-15 where respiration

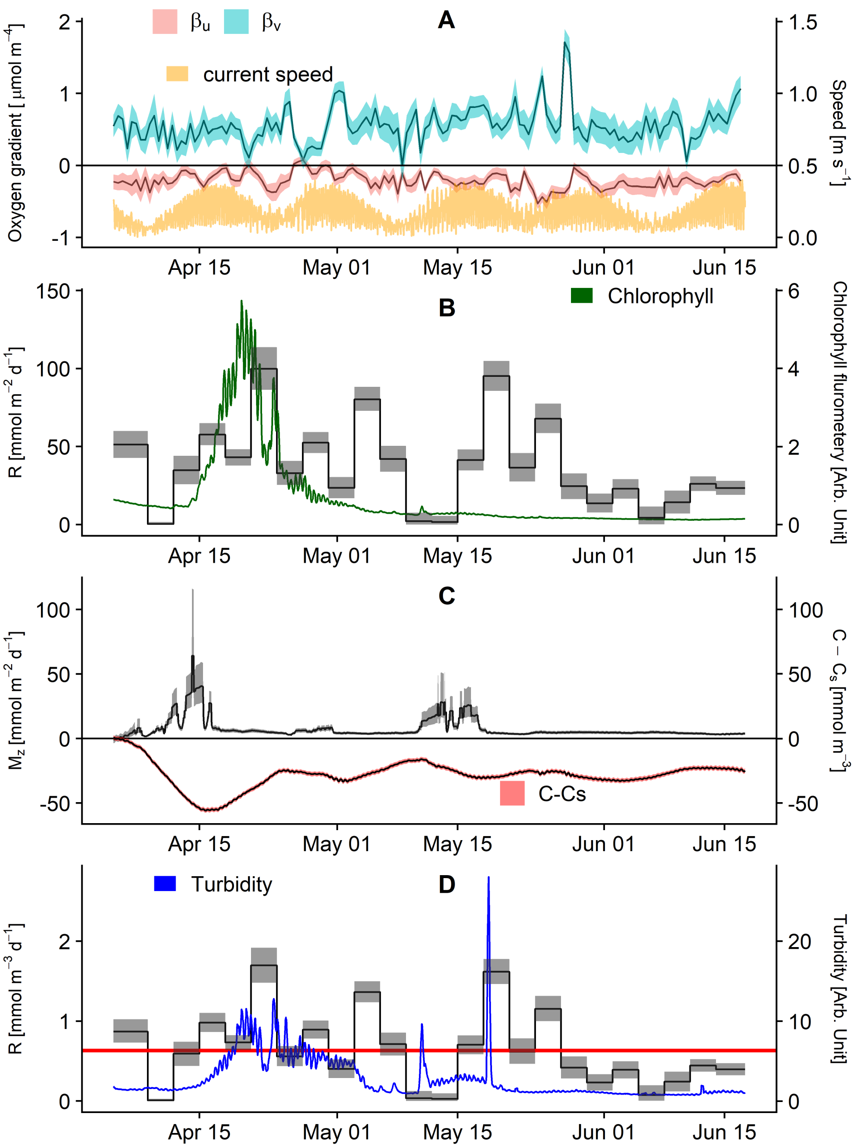

Figure 4.3.3: Statistical model parameter estimates for Nymph Bank (NB). Solid lines represent mean posterior estimate, with 95 % quantiles of the posteior shown with shaded region. Red line shows mean value over deployment. **(A)** Horizontal oxygen gradients, u = east-west, v = north-south. **(B)** Bottom mixed layer respiration, in depth integrated units, with bottom mixed layer chlorophyll fluorometery in green. **(C)** Estimated Diapycnal mixing rates, with horizontal current speed in orange. **(D)** Bottom mixed layer respiration, in volumetic units, with bottom mixed layer turbidity in blue.

is determined to be very low. This coincides with a deepening of the surface mixed layer and a thinning of the thermocline (20 m to 5 m) (fig. 4.3.1 A). Assuming the surface observations from the nearby buoy are reasonably representative of the oxygen concentration above the thermocline, the resulting cross-thermocline oxygen gradient is in the order of 3 μmol m^{-4} (fig. 4.3.3 C), with a temperature gradient of 0.63 °C m^{-1}. We would thus expect to see a increase in temperature in BML in the region of 0.26 °C d^{-1}. However, the observed temperature does not show this degree of warming. We conclude that the cross-thermocline flux is overestimated due to an overestimate of the vertical gradient, as such the respiration for this short period is likely underestimated.

4.3.2 East of Haig Fras 1

The AMM7 data indicates that the East Haig Fras region stratified later than Nymph Bank, on 2014-04-08 (fig. 4.3.4 A). Our analysis is thus restricted to a period of 52 days from 2014-04-09 onwards. The BML is between 43 and 73 m (mean = 64 m), with a thermocline thickness between 5 and 30 m (mean = 17 m). Tidally averaged total oxygen change in the BML is from 285.6 to 262.9 mmol m^{-3} (0.4 mmol m^{-3} d^{-1}). The oxygen observations appear generally more noisy than the NB time series (fig. 4.3.4 B). However, the oxygen optode performed normally during testing after recovery, so we have no reason to suspect bad data. A much weaker semi-diurnal signal is seen, indicating a much smaller horizontal oxygen gradient than that at NB. The tidal currents at EHF are much less circular (fig. 4.1.1) and residual flow is also less variable than NB with flow first to the west and then to the north (fig. 4.3.2 C). This pattern in residual flow matches that seen by Pingree et al. (1976) (Site 014) in October 1975.

For the April EHF deployment the matched water approach provides an integrated consumption rate of 0.51 m^{-3} d^{-1} (Standard error = 0.003, Adjusted R^2 = 0.972, n = 618) (fig. 4.3.2 D). Mean diapycnal mixing rate is calculated to be (8.3 [1.8, 25.7]) mmol m^{-2} d^{-1}. This equates to BML respiration rates of (41 ± 12) mmol m^{-2} d^{-1} ((0.64 ± 0.09) mmol m^{-3} d^{-1}), following the same procedure as for Nymph Bank.

The statistical model oxygen consumption rates demonstrate a near 14 day cyclic pattern which closely matches the spring-neap tidal cycle (fig. 4.3.5 A and B). Rates vary between 13 and 58 mmol m^{-2} d^{-1} (0.20 and 0.91 mmol m^{-3} d^{-1}). Increased rates are observed during, or shortly after, the periods of strongest tidal current flow (fig. 4.3.5 C). The mean rate is (36 ± 7) mmol m^{-2} d^{-1} ((0.57 ± 0.10) mmol m^{-3} d^{-1}).

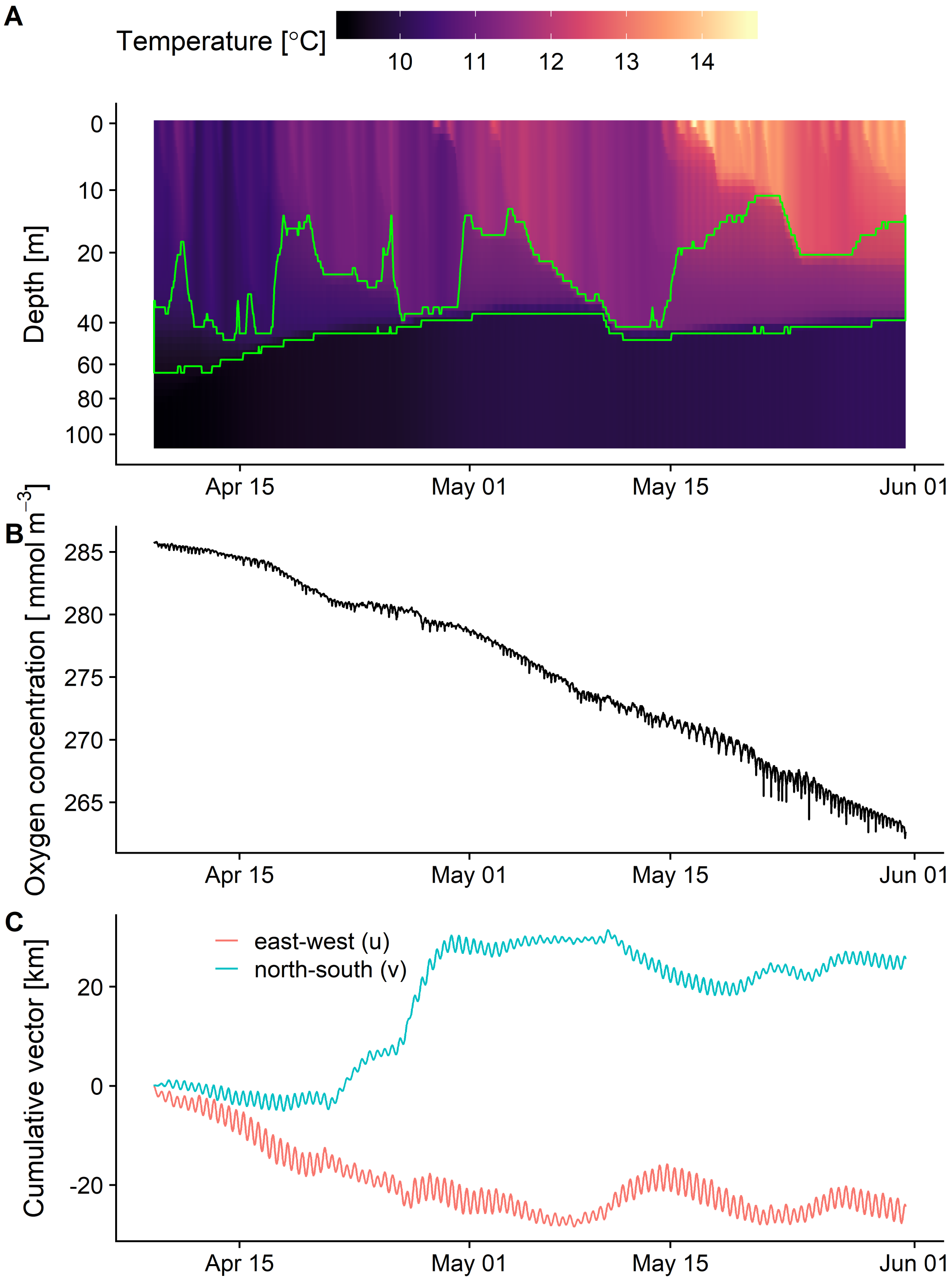

Figure 4.3.4: East Of Haig Fras #1 (EHF1) time series, **(A)** AMM7 water column temperature with the upper and lower bound of the thermocline highlighted in green. **(B)** Bottom mixed layer oxygen concentration measured by the benthic lander. **(C)** Cumulative horizontal advection as measured from lander ADCP in the east (red) and north (blue) directions

There are three periods of enhanced vertical flux (M_z, fig. 4.3.5 C) which are driven by a reduction in thermocline thickness. A horizontal oxygen gradient (fig. 4.3.5 A) is only detectable during a brief period towards the end of May. Here a negative east-west gradient of -0.09 to -0.02 μmol m $^{-4}$ is seen for approximately one week, indicating a lower oxygen concentration to the east.

4.3.3 East of Haig Fras 2 - Summer

Observations continued at the East of Haig Fras site with a replacement lander and second time series between the 16th June and the 19th August 2014. The oxygen concentration in the BML decreased from 257.2 to 234.1 mmol m^{-3} over the 64 days (0. 32 mmol m^{-3} d^{-1}). The water matching method provided a less than ideal fit and resulted in a low number of observations (R^2 = 0. 71, n = 422). This highlights a limitation of this method; that the number of matched points is dependent on the residual flow pattern.

As with the previous deployments the output from the statistical model is shown in figure 4.3.7. The average and peak rates from the statistical the vertical and horizontal fluxes together with oxygen consumption are summarised in table 4.4. There are three periods (25th to 27th June, 9th to 19th July and 8th to 12th August) which show a persistent increase in oxygen concentration (fig. 4.3.6 B). These periods are not associated with a horizontal advective flux or increased mixing through thinning of the thermocline or movement (entrainment) of the BML boundary (fig. 4.3.6 A). We discuss these periods in more detail in section 4.4.3.

Towards the end of the deployment the east-west horizontal oxygen gradient is particularly strong, approaching -1 mmol m^{-4} (fig. 4.3.7 A). This coincides with a change in the residual flow moving from west to east (fig. 4.3.6 C) resulting in a large negative horizontal advective flux of (20 ± 2) mmol m^{-2} d^{-1}) We can also see a thinning of the thermocline (panel A), and an associated increase in the estimated (positive) vertical flux (fig. 4.3.7 C). The horizontal flux while large does not fully explain the observed reduction in oxygen concentration and thus the model determines very high rates of consumption (fig. 4.3.7 B).

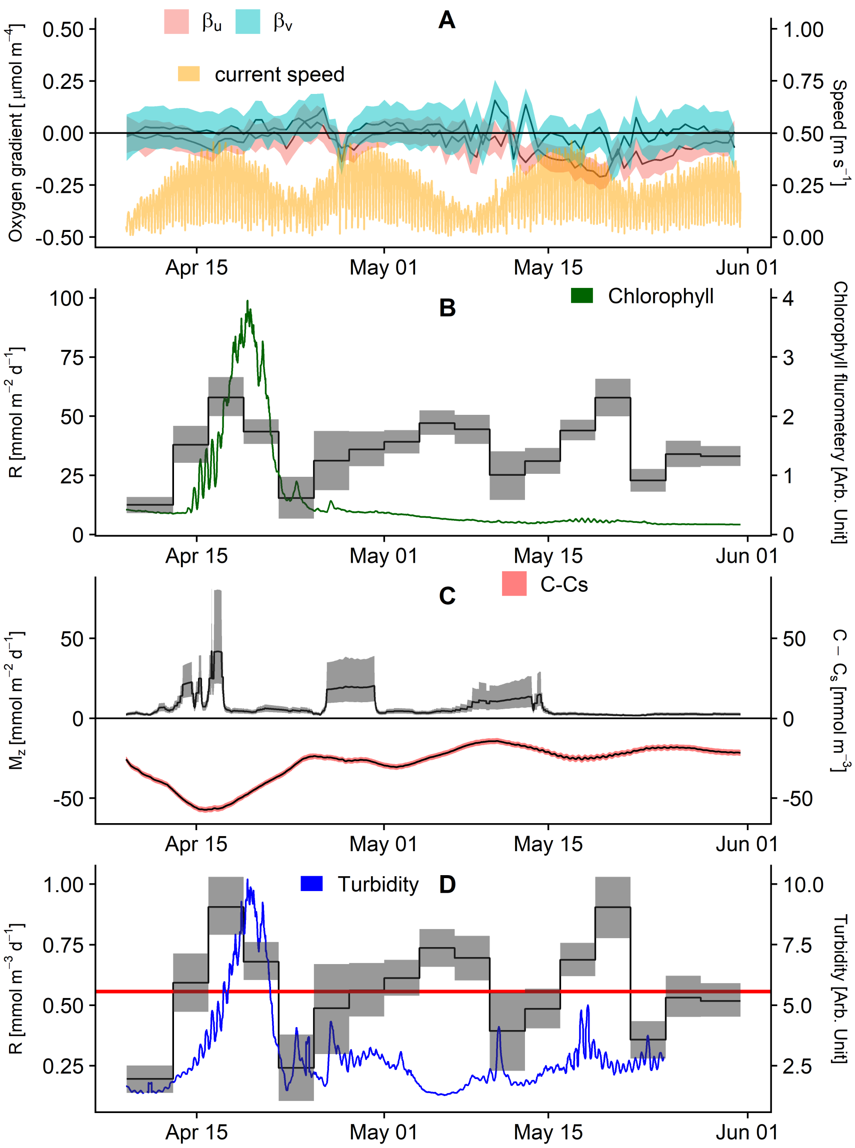

Figure 4.3.5: Statistical model parameter estimates for East of Haig Fras #1 (EHF1). Solid lines represent mean posterior estimate, with 95 % quantiles of the posteior shown with shaded region. Red line shows mean value over deployment. **(A)** Horizontal oxygen gradients, u = east-west, v = north-south. **(B)** Bottom mixed layer respiration, in depth integrated units, with bottom mixed layer chlorophyll fluorometery in green. **(C)** Estimated Diapycnal mixing rates, with horizontal current speed in orange. **(D)** Bottom mixed layer respiration, in volumetic units, with bottom mixed layer turbidity in blue.

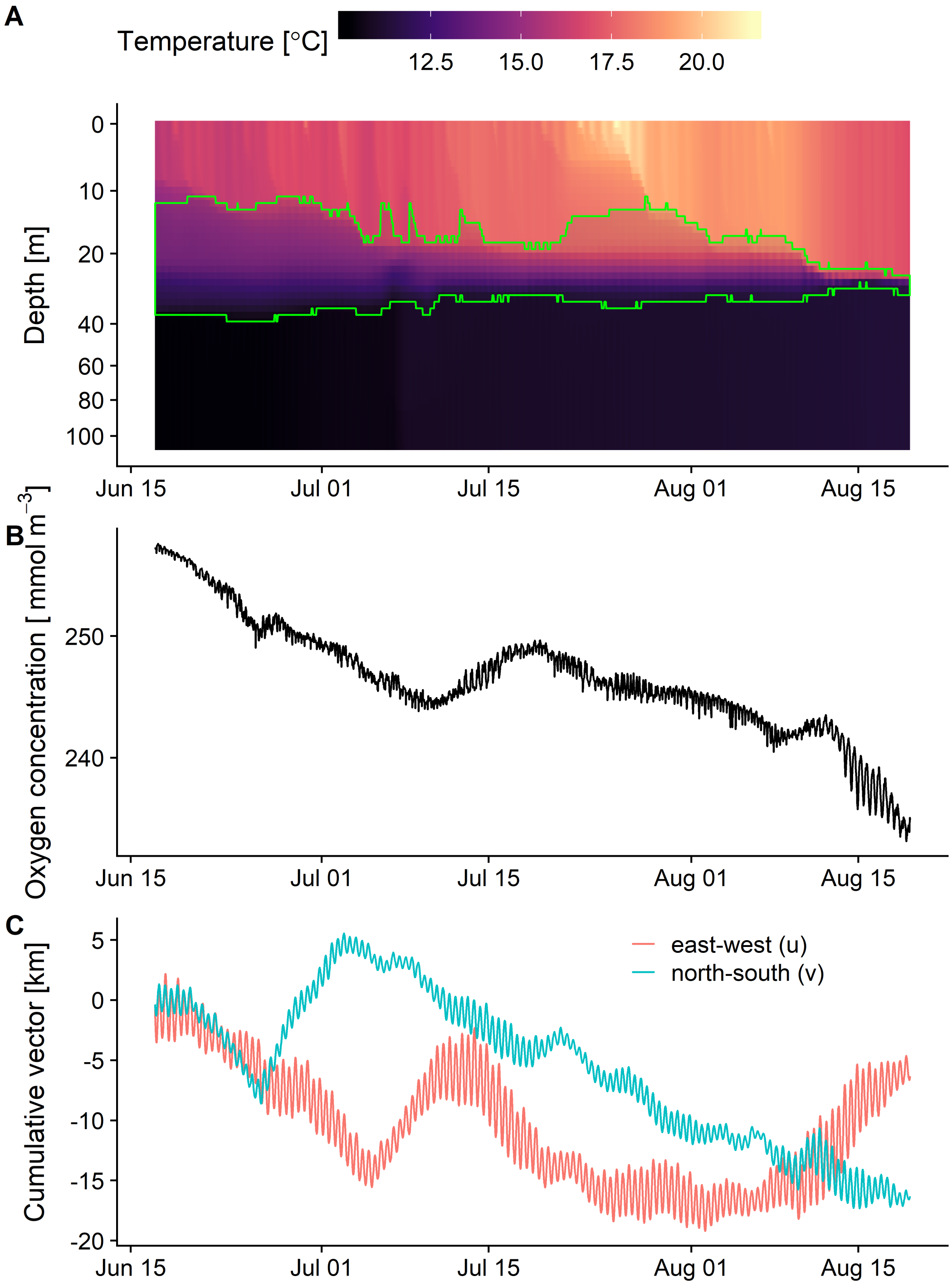

Figure 4.3.6: East Of Haig Fras #2 (EHF2) time series, **(A)** AMM7 water column temperature with the upper and lower bound of the thermocline highlighted in green. **(B)** Bottom mixed layer oxygen concentration measured by the benthic lander. **(C)** Cumulative advection as measured from lander ADCP in the east (red) and north (blue) directions.

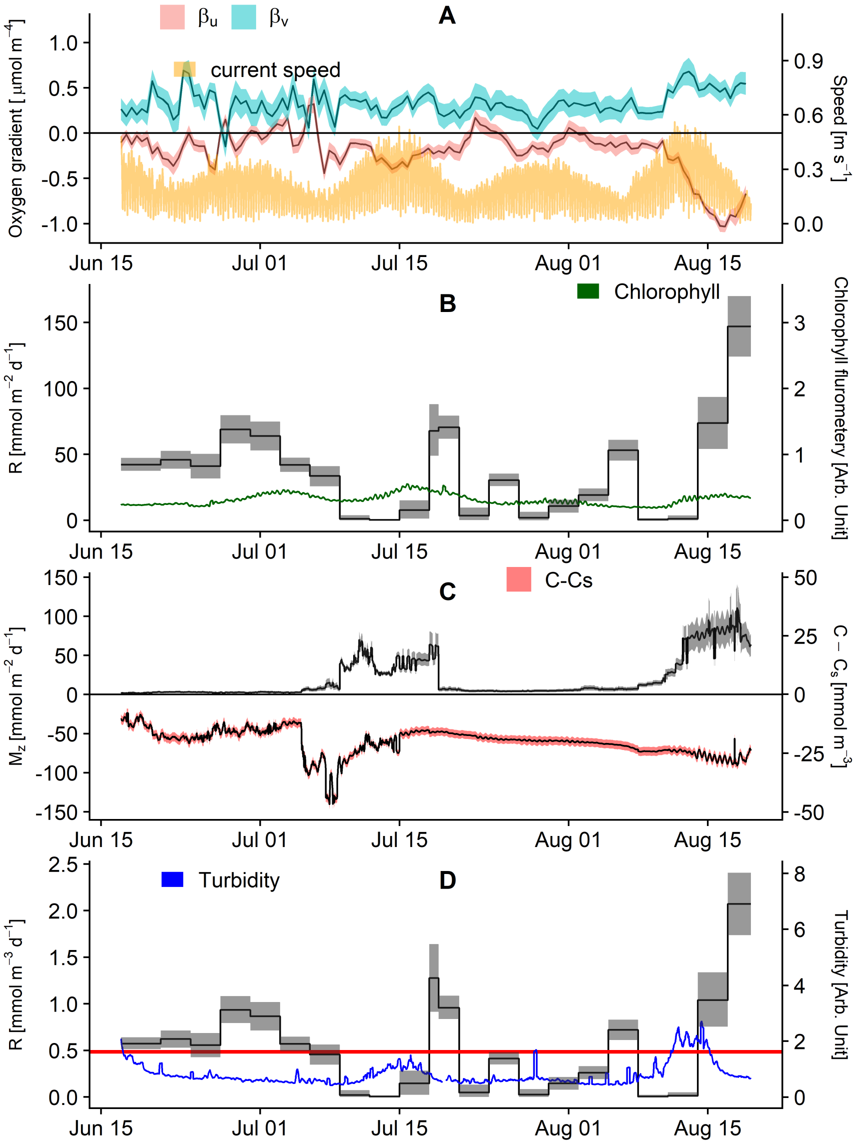

Figure 4.3.7: Statistical model parameter estimates for East of Haig Fras #2 (EHF2). Solid lines represent mean posterior estimate, with 95 % quantiles of the posteior shown with shaded region. Red line shows mean value over deployment. **(A)** Horizontal oxygen gradients, u = east-west, v = north-south. **(B)** Bottom mixed layer respiration, in depth integrated units, with bottom mixed layer chlorophyll fluorometery in green. **(C)** Estimated Diapycnal mixing rates, with horizontal current speed in orange. **(D)** Bottom mixed layer respiration, in volumetic units, with bottom mixed layer turbidity in blue.

4.3.4 East of Haig Fras 3 - Autumn

A third lander was deployed at the East of Haig Fras site between 20th of August and the 2nday of October 2014. During this period the thermocline is thin ((7 ± 3) m) and stable, with a BML thickness of (77 ± 1.7 m) (fig. 4.3.8 A). BML oxygen concentration decreased from 234.0 to 227.9 mmol m^{-3} over the 43 days (0.14 mmol m^{-3} d^{-1}) (fig. 4.3.8 B). The matched water method is not viable with this deployment, with too few matched points to provide an adequate fit. Horizontal advection is predominantly to the south-west (fig. 4.3.8 C)

The statistical model reveals the strong horizontal gradients seen at the end of the previous deployment persist until the first week of September (fig. 4.3.9 A). However the residual flow is reduced (fig. 4.3.8 C), resulting in a reduced horizontal advective flux. The spring-neap cycle of oxygen consumption seen in the spring is now absent despite measurable increases in turbidity and thus presumably sediment resuspension (fig. 4.3.9 D). Mean consumption is estimated as 46 ± 13 mmol m^{-2} d^{-1} (0.59 ± 0.18 mmol m^{-3} d^{-1}).

4.4 Discussion

4.4.1 Temporal variability

The EHF data demonstrates a convincing, approximately 14-day cycle in oxygen consumption, consistent with a spring-neap tidal cycle (fig. 4.3.5). Increased respiration rates are correlated with the stronger spring currents. This is indicative of the tidal resuspension of bed material (e.g. sediment or benthic fluff, and the organic carbon contained within) which is then aerobically respired. Tidal resuspension is understood to be frequent in the Celtic Sea, with year round reworking of the sediments (Thompson et al. (2017)). This is particularly true for EHF which has a higher fine sediment concentration (table 4.1). This follows that the sandier NB site would experience less tidal resuspension than EHF. Flow dependent benthic oxygen consumption has also been ascribed to increased ventilation of the sediment with increasing currents (Glud et al. (2016)). Hicks et al. (2017) supplied fully saturated overlying water to their incubations. This could partially mitigate the reduction ventilation from vertical water movement by increasing the diffusive concentration gradient between the overlying water and the sediment. This however does not represent the in-situ conditions.

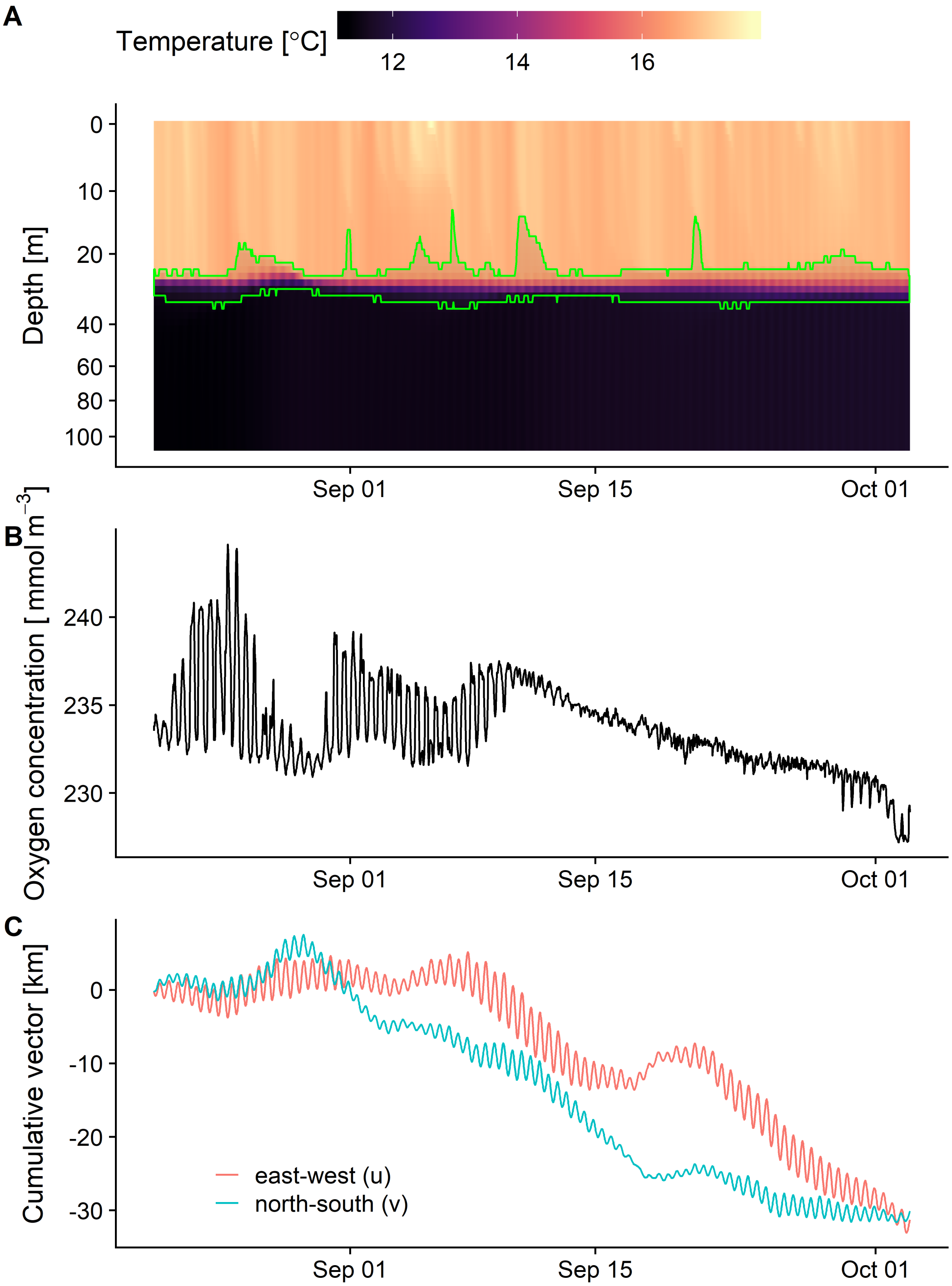

Figure 4.3.8: East Of Haig Fras #3 (EHF3) time series, **(A)** AMM7 water column temperature with the upper and lower bound of the thermocline highlighted in green. **(B)** Bottom mixed layer oxygen concentration measured by the benthic lander. **(C)** Cumulative advection as measured from lander ADCP in the east (red) and north (blue) directions.

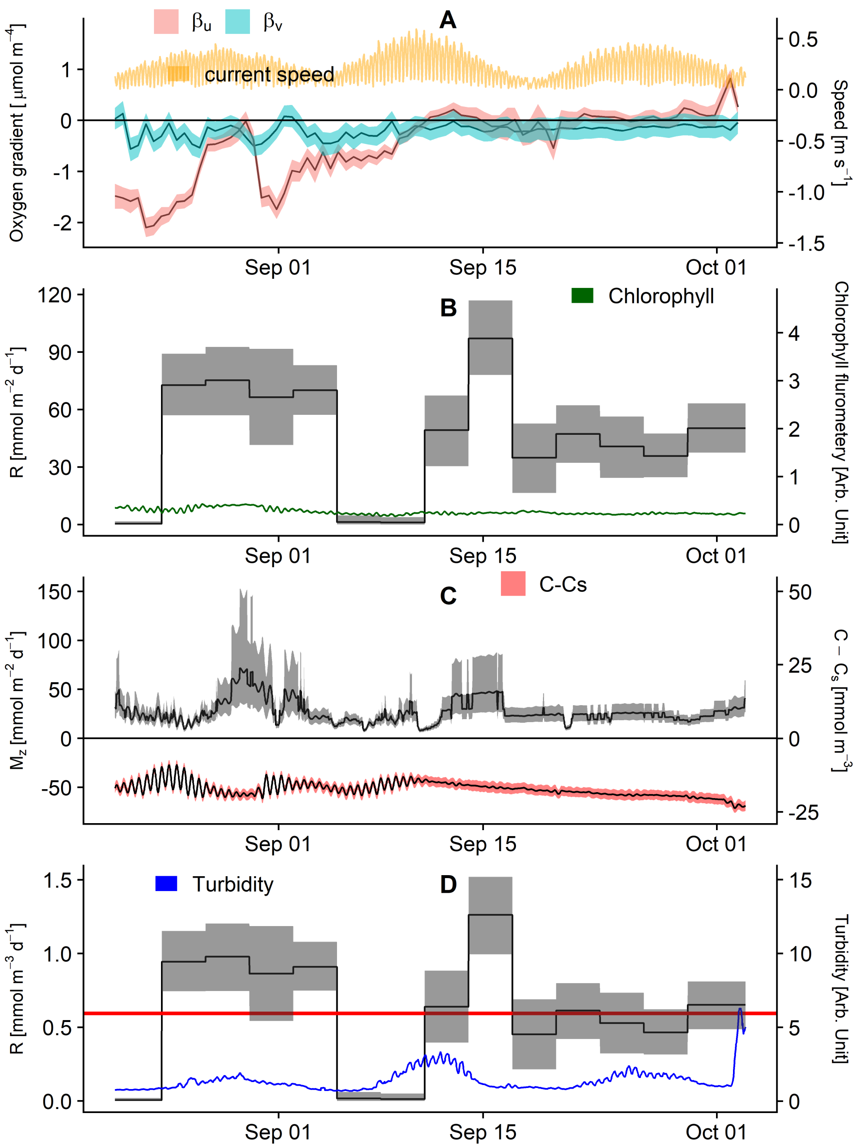

Figure 4.3.9: Statistical model parameter estimates for East of Haig Fras #3 (EHF3). Solid lines represent mean posterior estimate, with 95 % quantiles of the posteior shown with shaded region. Red line shows mean value over deployment. **(A)** Horizontal oxygen gradients, u = east-west, v = north-south. **(B)** Bottom mixed layer respiration, in depth integrated units, with bottom mixed layer chlorophyll fluorometery in green. **(C)** Estimated Diapycnal mixing rates, with horizontal current speed in orange. **(D)** Bottom mixed layer respiration, in volumetic units, with bottom mixed layer turbidity in blue.

NB by contrast does not demonstrate such a clear cycle. Highest rates are seen after the peak in BML chlorophyll. Higher rates are also observed immediately after brief large increase in turbidity toward the end of May (fig. 4.3.3 D). These very short term increases in turbidity increases could be due to resuspension from fishing activities, as these periods do not correlate with tidal currents or with chlorophyll, indicating it's not caused by frictional resuspension or falling phytoplankton material. The Celtic deep experiences the greatest fishing pressure within the Celtic Sea (Sharples et al. (2013), Thompson et al. (2017)), additionally the loss of the second NB deployment is attributed to trawling activity.

Queste et al. (2016) calculated BML oxygen consumption rates from the central North Sea in summer 2011 of (2.8 ± 0.3) mmol m^{-3} d^{-1} using a short-term Seaglider deployment. They noted the apparent high consumption rates and questioned how representative these rates could be over longer timescales. We observe similarly high rates for short periods at NB.

In the Celtic Sea we see the BML oxygen concentration reducing from an atmospheric equilibrium concentration of approximately 285 mmol m^{-3} to 180 just prior to remixing in winter, as observed by NB in March and Celtic Deep lander in December. This equates to a average consumption rate over the stratified period of 0.42 mmol m^{-3} d^{-1}. We see declining BML oxygen consumption rates post-bloom at EHF over the year, which is in agreement with Kitidis et al. (2017), Hicks et al. (2017) and García-Martín et al. (2017a) for 2015.

4.4.2 Advective Dynamics

At NB the statistical model output shows a persistent positive north-west gradient. This indicates that more oxygenated waters lie to the south-east. Stratification in the Celtic Sea is generally reduced as you move towards the south-east from NB due to increased tidal forcing in shallower water (Brown et al. (2003)).

For EHF the pattern is of typically negligible horizontal gradients for much of the year, with a very strong positive north-west gradient observed first in August which persists until mid September (fig. 4.3.5, 4.3.7 and 4.3.9 A). The absence of horizontal gradients suggest similar rates of processes occurring within the local area, with 'local' being the extent of tidal excursion. The brief occurrence of the strong gradient suggests a localised area of oxygenated water to the south east, perhaps from a summer phytoplankton bloom (e.g. as shown by Williams et al. (2013a)). However subsurface blooms are not typically observable from remote sensing, and no direct observations are available from this region at this time to confirm this hypothesis.

4.4.3 Evidence for enhanced persistent vertical mixing

At EHF between 9th and 19th of July we observe 0.4 °C of warming in the BML. This can be explained by the observed cross-thermocline temperature gradient of 7 °C, the estimated 15 m thick thermocline and a moderately enhanced K_z of 7.5 x 10^{-5} m^{-2} s^{-1} which would provide a temperature change of 0.04 °C d^{-1}. We also measured a 9 mmol m^{-3} increase in oxygen over the same period. Large oxygen gradients of up to 45 mmol m^{-3} over 5 m (9 mmol m^{-4}) were observed in CTD casts from August 2014 (fig. 4.2.1). Assuming oxygen consumption remains a constant 0.4 mmol m^{-3} d^{-1}, this increase could be explained by a diapycnal oxygen flux of 111 mmol m^{-2} d^{-1}. Using the same mixing parameters as inferred from the temperature changes this would indicate a cross-thermocline oxygen concentration gradient of at least 15 mmol m^{-4}. However, the bulk of the oxygen is being produced at the subsurface chlorophyll maximum at the base of the thermocline resulting in a much stronger gradient. The preceding period with declining oxygen concentrations also showed similar warming. However, this can be shown to be controlled by northward advection, that is warmer water moving from the south. The shorter periods of increasing BML oxygen do not correlate with increasing BML temperatures. The main limitation of this dataset is thus highlighted; we lack observations to quantify the cross-thermocline concentration gradient. However, our approach does allow us to incorporate our available knowledge regarding the reasonable bounds for the surface oxygen concentration to improve the estimates.

Rovelli et al. (2016) used a combination of turbulence measurements and fast galvanic oxygen sensors to calculate vertical oxygen fluxes and a BML mass budget over a 3 day period in the North Sea. They calculated a M_z flux ranging between 9 - 134 mmol m^{-2} d^{-1} (average 54 mmol m^{-2} d^{-1}) . We summarise our calculated fluxes and compare those to Rovelli et al. (2016) in table 4.4 Our results show similarly substantial vertical fluxes of oxygen.

Queste et al. (2016) demonstrated occasional short term mixing (<6 hour) events, which supply oxygenated water to the BML in the North Sea at rates of 2 mmol m^{-3} d^{-1}. Williams et al. (2013a) similarly describe frequent wind-driven inertial oscillations which increased vertical mixing rates by up to a factor of 17. These events are estimated to occur every 2 weeks during the summer. However, both of these studies describe events with large fluxes but much shorter durations than the persistent ventilation over several days we observe.

4.4.4 Oxygen uptake rates compared

Benthic processes studies were conducted in parallel with the seabed lander deployments which can further contextualise the observed rates of oxygen consumption. The estimates are integrated over the BML and thus combined processes occurring in the water column and at the seabed interface. For comparison with the SSB processes studies, in terms of both sediment type and location, Nymph Bank (NB) and the Celtic Deep (CD) (table 4.1) are best represented by the "sand" process site G (Thompson et al. (2017)). East of Haig fras (EHF) is most similar to and nearest the "muddy sand" site H. These processes study sites are within 10 km of the lander positions.

Hicks et al. (2017) calculated total benthic oxygen uptake rates from sediment core incubations in March 2014, March 2015, May 2015 and August 2015. The March observations occurred prior to the onset of stratification and are thus not directly comparable with this study.

Site G showed low total benthic oxygen uptake rates (1.5-2.5 mmol m^{-2} d^{-1}) in March, with increased rates in May and Aug (5-6 mmol m^{-2} d^{-1}). Site H rates had little seasonal variability with values 7-8 mmol m^{-2} d^{-1} for all observations. Hicks et al. (2017) derived further rates from a set of incubations designed to simulate resuspension. These produced larger rates of approximately 8-9 mmol m^{-2} d^{-1} for site G and 13 mmol m^{-2} d^{-1} for site H.

Kitidis et al. (2017) provide additional total oxygen consumption rates from an alternative core incubation experiment in 2015. Site H showed more variability between pre and post bloom compared to those of Hicks et al. (2017). Pre bloom (March) rates were estimated at 2.4 mmol m^{-2} d^{-1} with post bloom (May and August) rates of 6.1 and 6.6 mmol m^{-2} d^{-1}. Site G had pre-bloom rates of 4.5, increasing to 6.3 mmol m^{-2} d^{-1} in May. August rates were much lower than those seen by Hicks et al. (2017) (1.7 mmol m^{-2} d^{-1}).

Klar et al. (2017) calculated a late spring seasonal average oxygen consumption 15.4 mmol m^{-2} d^{-1} at site A. Site A consists of sandy mud and thus has a larger organic carbon content and higher rates of oxygen consumption. Their study suggests a very small contribution to oxygen consumption from Fe(II) oxidation; in the order of 30 μmol m^{-2} d^{-1} for spring and 5 μmol m^{-2} d^{-1} for summer. The contribution to oxygen consumption from Fe(II) oxidation at sits H or G is likely to be smaller.

The above studies show large differences in observed rates despite the similar sampling methods and with near identical spatio-temporal parameters. This is possibly due to very small scale spatial differences, or the presence or absence of fauna. Hicks et al. (2017) estimated the fauna mediated benthic oxygen uptake to be between 5 and 6 mmol m^{-2} d^{-1} for site H. Estimates are not available for site G.

García-Martín et al. (2017a) performed incubations of the BML plankton community respiration in November 2014, April, 2015 and July 2015. These observations were made at the CCS site, which is 163 km to the south west (fig. 4.1.1). The incubation derived rates were calculated as between 0.1 and 1.1 mmol m^{-3} d^{-1} in April, and between undetectable and 0.5 mmol m^{-3} d^{-1} in July. Further BML incubations were also performed using water from site A and J2 (fig. 4.1.1) in late April 2015 although these measurements were not included in their paper (Garcia-Martin, per. comms.). Site A is to the north-east of NB, while J2 sits between NB and EHF. These provide rates of (0.96 ± 0.3) mmol m^{-3} d^{-1} for site A and (0.42 ± 0.18) mmol m^{-3} d^{-1} for J2. Bacterial respiration contributed 21-38 % of the plankton community respiration (García-Martín et al. (2017a)). The incubation derived rates are summarised, scaled to the observed BML depth and compared with the matched water and statistical model rates from this study in table 4.3.

Both the statistical model and co-located regression provide estimates within the error bounds of the combined benthic and pelagic incubation derived oxygen consumption rates. It should be noted that these incubation were from the following year. We observe very similar mean rates from the statistical model for both NB and EHF sites between March and May.

The winter of 2013-2014 had atypically extreme wave conditions (Thompson et al. (2017)) which may affect the validity of using the 2015 water column rates as a comparison. However, given the similar April benthic uptake rates seen by Hicks et al. (2017) we do not believe this to be the case. Larsen et al. (2013) determined sediment total oxygen consumption rates of (5.8 - 9.0) mmol m^{-2} d^{-1} for July 2008 at several muddy-sand sites near CCS (Jones bank) from sediment core oxygen microprofiles. These are very similar to those observed by Hicks et al. (2017) suggesting little interannual variability in sediment rates within this region.

Table 4.3: BML integrated and combined mean incubation rates compared to the statistical model for spring and co-located regression from this study. All rates are given as mmol m^{-2} d^{-1}. Water column incubations are the mean of those from sites A and J2. NB BML thickness = (59 ± 2) m. EHF BML thickness = (64 ± 2) m.

Method	NB (Site G, Sand)	EHF (Site H, Muddy Sand)
Sediment incubation		
Hicks et al. (2017), (May) water column incubation García-Martín et al. (2017a) (April)	30 ± 10	34 ± 12
Resuspended sediment incubation		
Hicks et al. (2017), (May) water column incubation García-Martín et al. (2017a) (April)	47 ± 19	39 ± 12
this study,		
co-located linear regression (April + May)	38 ± 1	32 ± 1
this study,		
statistical time series model (April + May)	37 ± 6	35 ± 7

Table 4.4: Mean (and peak) mass-balance fluxes for each of the study sites compared to the 52 h North Sea study of Rovelli et al. (2016). Horizontal advection is given as an absolute mean, as this can change between a positive and negative flux during a deployment. All rates are given as mmol m^{-2} d^{-1}.

Site	Vertical (M_z)	Horizontal ($A_u + A_v$)	Consumption (R)
NB	7 ± 3 (64 ± 41)	0.1 ± 3 ± 1 (14 ± 2)	37 ± 6 (100 ± 14)
EHF1	7 ± 3 (37 ± 14)	1 ± 0.9 (6 ± 2)	36 ± 7 (58 ± 8)
EHF2	28 ± 12 (133 ± 98)	3 ± 1 (20 ± 2)	41 ± 8 (172 ± 19)
EHF3	27 ± 12 (72 ± 58)	9 ± 2 (55 ± 4)	46 ± 13 (97 ± 20)
North Sea	54 (74)	Assumed 0	≈70

These benthic rates suggest that the largest proportion (60-80 %) of the BML oxygen consumption takes place in the water column not the sediment. Rovelli et al. (2016) similarly determined for the North Sea that 86 % of the respiration was in the water column. This contrasts with the model study of Große et al. (2016) who determined that for the central North Sea benthic remineralisation processes are responsible for more than 50 % of oxygen consumption, which corresponded to 3.9-6.5 mmol m^{-2} d^{-1}. This disparity could be due to differences in remineralisation rates between the two shelf seas, or the choice of parametrisations and forcing data for the model.

4.4.5 Carbon

Ultimately it is the balance between carbon fixation by autotrophic production and remineralisation rate of the benthic organic carbon which determines if organic carbon is sequestered into the sediment (Diesing et al. (2017)). All sites showed an increase in organic carbon deposition after the bloom in 2015 (Silburn et al. (2017)). The typical benthic respiratory quotient, inferred from dissolved inorganic carbon and O_2 exchange rates, can be considered close to unity (1.03 ± 0.11) (Glud et al. (2016)). Kitidis et al. (2017) determined that ammonium-oxidation accounted for 10–16 % of total oxygen consumption at H and 35-56 % at G, that is to say, 10-50 % of the oxygen consumption in the sediment is not due to carbon mineralization. Larsen et al. (2013) estimated that sulfate reduction, which does not consume oxygen, contributed (12-28 %) of total benthic carbon mineralization. Microbial denitrification has a very small influence of <2 % (Larsen et al. (2013)). Thus each mole of oxygen consumed can be thought of as approximately equivalent to one mole of carbon mineralisation, with the opposing effects of ammonium-oxidation and sulfate reduction potentially balancing out.

4.5 Conclusions

In this study we provide two alternative approaches to quantifying BML oxygen consumption using single point oxygen time series. Our regression method accounts for horizontal advection, but is dependent on favourable patterns in BML residual flow at the study site. By contrast, our statistical method can resolve the short-scale dynamics observed in BML oxygen and horizontal advection, and is more suitable for use in situations with less circular BML residual flow patterns. While we were able to incorporate our limited knowledge of the cross thermocline oxygen gradient into our estimates, one of our sites benefited from co-located surface oxygen observations which helped constrain our vertical flux estimation. The vertical flux could be more directly observed using sheer probes coupled with a fast response optode (e.g. Holtermann et al. (2019)). Concurrent in-situ vertical flux observations would likely reduce the uncertainty associated with our incomplete knowledge of both the diapycnal eddy diffusion coefficient and the cross-thermocline oxygen gradient. This would also provide an opportunity to further validate the limited observation approach described in this paper. We show that, in general, our methods agree with the upper range of estimates from the incubation studies. However, we observe significant short term variability in oxygen consumption rates, which is missed with the cruise-based observations.

Numerical models are known to only predict half the observed global oxygen decline (Breitburg et al. (2018)). Modeled rates, informed from incubations, are typically too low or do not capture the temporal dynamics. In general our understanding of the contributions of offshore benthic communities to carbon sequestration and storage is lacking (Solan et al. (2020)). The estimates we have provided, together with the methodology we have outlined, can capture the temporal variability and may help to close this knowledge gap.

Chapter 5

Estimating NCP from glider based observations in the North Sea

5.1 Introduction

Within this chapter we focus on the glider-based oxygen and nitrate concentration measurements and derive estimates of net community production using observations from the "Alternative framework to assess marine ecosystem functioning in shelf seas" (AlterEco) project. AlterEco represents a pilot study of a novel monitoring framework to deliver improved spatiotemporal understanding of key shelf sea ecosystem drivers though the use of autonomous systems, primarily underwater gliders. It was funded by the UK National Environment Research Council (NERC), the UK government's Department for Environment, Food and Rural Affairs (Defra), the World Wide Fund for Nature (WWF).

5.1.1 Carbon cycling in the Central North Sea

The North Sea is a semi-enclosed region of the Northwest European continental shelf between the island of Great Britain in the west and Norway, Denmark, Germany and the Netherlands in the east and south. The northern boundary is facing the North Atlantic. It can be divided into two hydrologically distinct parts, a seasonally stratified northern part, and a fully mixed southern part (Queste et al., 2013; Emeis et al., 2015). The shallower fully mixed region is believed to act as a net sink for CO_2 during the spring bloom periods, and a source of CO_2 during the rest of the year. Thomas et al. (2005b) suggests the seasonally stratified regions are a sink for carbon throughout the year. A more recent synthesis of Kitidis et al. (2019) indicates that the seasonally stratified regions are a source during December and January in 2015. Dissolved inorganic carbon from organic matter remineralisation (respiration) accumulates in the waters below the seasonal thermocline throughout the spring and summer. In winter the deepening of the thermocline due to increased wind stress and reduction of surface heat fluxes partly remixes waters high in dissolved inorganic carbon back into the surface layer. However, the bulk of water entering the North Sea does so near the surface and leaves the shelf at depth. This downwelling circulation results in a substantial transport below the pycnocline from the North Sea into the Norwegian Trench (13 %) and the subsurface North Atlantic (6 %) prior to remixing (Holt et al., 2009). The majority of the annual primary production is pumped to the North Atlantic, with a very small fraction, less than 1 %, actually being buried in the North Sea sediments (Thomas, 2004) and 90 % exported to the North Atlantic (Thomas et al., 2005a). Overall the majority of pelagic North Sea dissolved inorganic carbon both originated from and is exported back to the Atlantic via cross-shelf exchange and plays a limited role in the net shelf carbon cycle (Legge et al., 2020). These processes may not purely happen on an annual timescale and may be controlled by periodic flushing over longer periods (Humphreys et al., 2018; Chaichana et al., 2019). The combination between tidal, wind and buoyancy forcing tends to develop a general anti-clockwise circulation within the North Sea (Mathis et al., 2015), with vertical mixing being mostly driven by the tidal currents (Stanev et al., 2019). Variability in the circulation is determined mainly by variation in local winds, which are predominantly from the west.

5.1.2 Low oxygen concentrations and eutrophication

The stratified regions of the North Sea have been undergoing a trend of reducing dissolved oxygen concentrations over the last decades (Emeis et al., 2015; Mahaffey et al., 2020). Oxygen depletion in the unventilated bottom mixed layer is a function of supply of organic matter, the rates of respiration and denitrification together with fluxes of oxygen, either though horizontal advection or though vertical turbulent mixing (Rovelli et al., 2016). While some regions of the North Sea still see increased nutrient inputs (Dulière et al., 2019) the North Sea departs from the general global shelf sea trend and overall has seen a reduction in nitrate concentrations over the last decade (Emeis et al., 2015). Observations of gross primary production in the North Sea overall show a significant decline in primary production over the last few decades, attributed to the reduction of nutrient inputs and rising sea temperatures (Capuzzo et al., 2018). Eutrophication mitigation measures have been more effective at reducing phosphorus inputs than nitrogen, and the last few decades have seen a change in the N:P ratios within the North Sea (Burson et al., 2016). These changes can favour differing phytoplankton species and can also change which nutrient becomes limiting to primary production. Nutrient inputs, are an important control on bottom water oxygen concentrations in the North Sea (Große et al., 2017). Increased nutrient inputs, in a non-light limited environment, promote autotrophic production and thus increased oxygen concentrations in the euphotic zone. However, the subsequent increased amount of sinking organic matter increases respiration in the bottom mixed layer, causing a decrease in oxygen concentrations (Mahaffey et al., 2020). Similarly, transient periods of increased vertical mixing during the stratified period simultaneously supply nutrients and promote production within the thermocline while ventilating the bottom waters (Wihsgott et al., 2019). The net result on bottom oxygen concentrations from these counteracting processes can be difficult to determine.

The predominant source of nutrients to the North Sea as a whole is inflow from the North Atlantic, with a quarter being from riverine inputs (Emeis et al., 2015; Große et al., 2017). Riverine nitrogen inputs are thought to be responsible for controlling half of the bottom mixed layer oxygen consumption in the North Sea (Große et al., 2017) Modelling studies have suggested that the nutrient inputs to the central North Sea should continue to decline due to a reduction in supply from the Atlantic, and consequently the region may see up to 20 % reduction in primary production in the future (Holt et al., 2012).

Variability in the North Atlantic Oscillation (NAO) has been shown to affect carbon cycling within the North Sea through several processes. In the central North Sea stratification strength and depth are partly controlled by the NAO-driven changes in circulation patterns and local weather. Positive NAO phases are shown to result in stronger inflows from the Atlantic and thus change inputs of carbon and nutrients to the shelf (Salt et al., 2013). On top of this variability is a general trend of increased stratification though rising sea temperatures which causes the seasonal thermocline, where present, to become more stable or deeper (Große et al., 2016; Wakelin et al., 2020).

Another key factor in determining the susceptibility of a region to oxygen depletion is the size of the sub-thermocline volume. Große et al. (2016) demonstrated that the lowest oxygen concentrations in the North Sea do not occur in the regions with the strongest stratification. The northern North Sea is relatively deep, with a large sub-thermocline volume and is less susceptible to deoxygenation. It is the central North Sea, with both seasonal stratification and a small sub-thermocline volume, that is most at risk. Thus despite reductions in nutrient inputs, deleterious effects of low oxygen concentrations, which are most often associated with eutrophication, are still a concern.

5.1.3 Hydrography and oxygen concentrations at Dogger Bank

One North Sea region which has been identified to undergo seasonal oxygen depletion is located north of the Dogger Bank. The Dogger Bank is a large sandbank within the central North Sea (fig. 5.1.1). Comprising predominantly fine sand and mud this bank rises 20 m above the surrounding sea floor and is 15 m below sea level in its most shallow parts. Tidal forcings are dominated by the M2 constituent, with mean tidal excursion in the region of 1.5 km (fig. 5.1.1). The Dogger Bank sits south of the tidal front, which is located in an arc across the central North Sea from Yorkshire in the United Kingdom to the Frisian coast in the Netherlands. This hydrological divide separates the well-mixed waters to the south from the seasonally stratified waters of the central North Sea to the north (Emeis et al., 2015). Prevailing currents move from the west along this front towards the Dutch coast (fig. 5.1.1). This is supplied with water from the Scottish coastal current, itself fed from the North Atlantic inflow through the Orkney-Shetland gap (Hill et al., 2008). The area on and around Dogger Bank is a highly productive habitat, which is thought to exhibit year-round phytoplankton production (Nielsen et al., 1993). The shallow waters above Dogger Bank are not seasonally stratified, as wind-stress and tidal currents maintain sufficient vertical mixing which replenishes nutrients into the photic zone throughout the year (Riegman et al., 1990). Due to the shallow depth of Dogger Bank, the spring phytoplankton bloom is initiated there months before stratification triggers the bloom within the stratified regions (Nielsen et al., 1993). The Bank North of Dogger Bank, these mixed waters converge with the seasonally thermally stratified waters. The exchange of nutrients and phytoplankton at this transition promotes enhanced primary production along the northern edge of the bank, which acts as a hotspot for marine life and supports several important fisheries (Plumeridge and Roberts, 2017). Since 2017 the bank has been designated as a Special Area of

Conservation (SAC) by the UK government.

The region north of Dogger Bank typically sees a spring phytoplankton bloom commencing at the start of April. Throughout most of the year, production is known to be concentrated at depth, with a deep chlorophyll maximum (DCM) seen typically between 15 and 40 meters (Nielsen et al., 1993). The subsurface production has been estimated to account for over a third of annual new production (Weston et al., 2005; Fernand et al., 2013) in this region. Seasonal low oxygen concentrations have been observed in the stratified waters north of the Dogger Bank since 1916, and various monitoring studies have shown a general decline since at least 1990 (Greenwood et al., 2010; Queste et al., 2013; Rovelli et al., 2016). While these concentrations are still $> 2\,\mathrm{mg\,L^{-1}}$ ($63\,\mathrm{mmol\,m^{-3}}$), which is often considered to be the threshold of hypoxia (Diaz and Rosenberg, 2008), they maybe below or approaching the low-oxygen threshold of $6\,\mathrm{mg\,L^{-1}}$ ($188\,\mathrm{mmol\,m^{-3}}$) used by the OSPAR Commission, and as such are a growing concern for the future of the region. The Dogger bank, being far away from the coasts, has minimal riverine influence, such that maximal nutrient concentrations typically reflect those of the in-flowing Atlantic waters (Greenwood et al., 2010). The changes in N:P ratio observed in more coastal regions of the North Sea are not seen at Dogger Bank and as such nitrate remains the primary limiting nutrient (Burson et al., 2016). Given the high productivity, seasonally varying conditions, and risk of seasonal oxygen depletion this region it was chosen as the location for the AlterEco monitoring pilot study.

5.1.4 Late winter 2018 as an usual period for North Sea meteorology and hydrography

Early 2018 saw an usually strong winter storm pass over the north-west European shelf. Referred to by the UK media as “the Beast from the East”, the period between 2018-02-22 and 2018-03-05 saw persistent easterly winds. Using a fleet of drifters Stanev et al. (2019) observed a persistent reversal of the North Sea circulation during this time lasting for 1.5 months. Surface currents north of Dogger Bank reversed completely such that mean flow during this period was to the west. Such a reversal of the surface circulation of this magnitude has likely occurred only four times in the last 40 years. This highlights 2018 as a particularly unusual year in terms of weather and circulation patterns. As intermittent flushing of the North Sea is thought to be a key driver of the inter-annual variability in the carbon inventory on the North-west

European shelf (Humphreys et al., 2018; Chaichana et al., 2019), changes to the typical circulation are likely to substantially influence carbon cycling in 2018, and possibly into 2019.

5.1.5 The need for improved monitoring

The North Sea represents one of the most well studied marine environments. However, despite the availability of large volumes of data, inferring robust statements on long-term changes, natural variability or predicted process responses to external forcing continue to be challenging (Emeis et al., 2015). As with other shelf regions, the North Sea has high temporal and spatial variability, which makes the analysis of trends more challenging compared with the open ocean (Bozec et al., 2006; Bauer et al., 2013). From a carbon system point of view, it remains currently uncertain whether the shelf sea carbon sink will strengthen or weaken in the near future as this complex system is being influenced by multiple, interacting factors (Legge et al., 2020). The North Sea is changing and as the processes controlling carbon export and oxygen depletion are highly complex and interconnected, improved understanding and monitoring is essential to enable prediction and the mitigation of deleterious effects. Discrete samples from shipborne hydrographic surveys can present a highly detailed synoptic view of various parameters, but these approaches will typically miss much of the temporal variability while also being expensive to operate. Similarly, short-term observations will fail to resolve inter-annual variation. Rovelli et al. (2016) argued that in the absence of targeted long-term studies focusing on oxygen and carbon dynamics across the whole water column, it is not possible to determine the long-term fate of bottom mixed layer oxygen concentrations. Sustained observations are required to detect, understand and predict the conditions controlling the depletion of oxygen in UK marine waters (Mahaffey et al., 2020).

5.1.6 Deriving NCP from glider observations

There are several challenges faced when calculating NCP from observations made with gliders, especially in a dynamic and horizontally heterogeneous environment. Unlike moorings or drifters, gliders are semi-Lagrangian observation platforms (Queste et al., 2013), such that observations are not static relative to either a water mass or a geographical point. Typical approaches to mass-balance analysis requires multiple observations of the same water mass or a good understanding of the advective fluxes (Chapter 3, Hull et al. (2016)). There have been various open ocean studies of NCP from autonomous platforms, but very few for dynamic shelf seas. Many of the assumptions used by such studies are not valid for a shelf-sea environment.

Binetti et al. (2020)'s open ocean Seaglider study assumed a 1D system with gliders on a 15 km wide bow-tie transect. Haskell et al. (2019) similarly adopt at 1D model that neglects any lateral mixing or advection of oxygen into or out of their study region. They argue that the observed horizontal oxygen concentration gradient of 1.5 x 10^{-4} mmol m^{-4} and a horizontal velocity of 2 km d^{-1} result in much smaller fluxes than those due local changes over time or vertical processes. This contrasts with the study of Alkire et al. (2012) who argued that at their North Atlantic study site advection is non-negligible. Alkire et al. (2014) used a Lagrangian drifting buoy as a reference frame, with Seagliders providing supporting information. They argue that the buoy offers an optimal coordinate system for a mass balance analysis with the drifting buoy ballasted to follow a water mass. Budgets were still only constructed over restricted periods of stable stratification so that the effects of lateral and vertical mixing processes were minimised. Barone et al. (2019) use salinity as a tracer for ensuring their observations remain within a water mass, but even then they constrain their analysis to exclude data where advection is observable. Pelland et al. (2018) similarly demonstrate the importance of including horizontal advection in their oxygen balance in the North Pacific. They used Seagliders to augment the monitoring done by a surface mooring within a 50 km bow-tie transect and demonstrated that annual NCP is overestimated by up to 50 % if surface horizontal advection is ignored. Rovelli et al. (2016)'s 2009 three-day study of central North Sea vertical oxygen fluxes was carried out at the Tommeliten site (56.4917 N, 2.9833 E). This lies 68 km north-east of the centre of the AlterEco study area, and 43 km from the eastern end of the E-W transect. Horizontal O_2 gradients and associated horizontal advective O_2 fluxes were not quantified in this study. It was argued that such fluxes would not significantly contribute to the O_2 balance at the Tommeliten site, as their BML O_2 concentration time series did not show any variability at the tidal or inertial frequencies, implying that horizontal O_2 gradients were small. Specifically for the central North Sea, Queste et al. (2016) noted that the horizontal gradients in this region have significant interannual variability, and may or may not be negligible. Over short timescales (< 1 week) local and vertical processes were thought to be dominant over horizontal ones (Queste et al., 2016). However, as the duration of an observation campaign increases, and longer temporal scales are observed, horizontal transport is likely to become more important. Assuming that the horizontal transport is persistent, it is also not possible to implement the approach outlined in Chapter 4 (Hull et al., 2020) to determine the magnitude of the oxygen gradients, as the glider is partially displaced along with the water by tidal advection, such that the glider will not observe the full magnitude of any gradient. Thus it becomes clear that in dynamic environments the estimation of advection and turbulent mixing remains an issue, as even with well sampled time series it is rare to be able to resolve all gradients fully (Pelland et al., 2018).

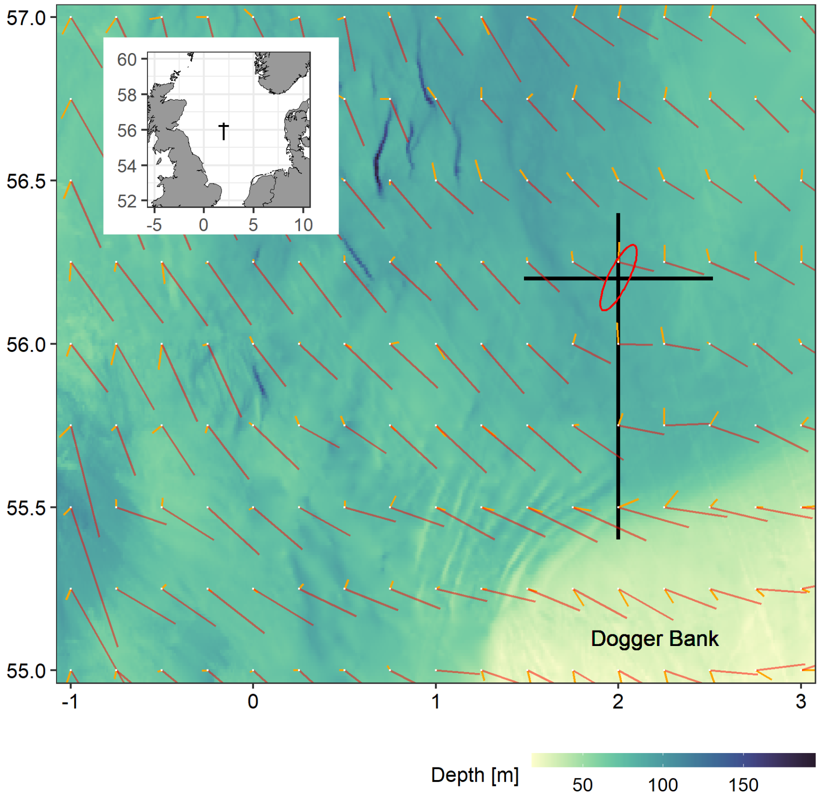

Figure 5.1.1: Glider transects, surface and bottom currents in the AlterEco study area, North-south and east-west glider transects are marked in black. Bathymetry data from GEBCO 2019. Ball-and-sticks point toward the prevailing surface (red) and bottom (orange) current direction. Sticks are scaled based on the magnitude of the current, with the longest stick corresponding to 5 km d^{-1}. Red ellipsis illustrates direction and relative magnitude of tidal ellipsis (not to scale). Current data from UK Met Office aggregated for 2017, Atlantic Margin Model FOAM 7 km.

5.2 Method

5.2.1 Gliders

Observations were collected between November 2017 and April 2019 by a fleet of submersible gliders (table 5.1). The fleet comprised 6 deployments of 5 Seagliders at different times (sg537 “Fin”, sg510 “Orca”, sg620 “Melonhead”, sg579 “Humpback”, sg602 “Scapa”) and 10 deployments of 8 Slocum gliders (units 436 “Stella”, 194 “Cook”, 352 “OMG”, 345 “Cabot”, 305 “Dolomite”, 444 “Kelvin”, 331 “Coprolite”, 304 “Ammonite”) (table 5.1). Seaglider and Slocum glider deployments overlapped in time, but due to platforms developing faults and having to be recovered prematurely, mission end dates often do not coincide. In addition, a Liquid Robotics Waveglider (SV3-028 “Lyra”) surface vehicle was deployed in May and August 2018. The Seagliders were all fitted with the non-pumped Seabird CT sail, while the slocum used the pumped GPCTD. The Slocum gliders and sg602 were fitted with an Aanderaa 4831 type optode with a standard foil, while the other Seagliders were all fitted with the fast foil Aanderaa 4330F optodes. Fast (“F”) type foils lack the black optical isolation coating, this reduces their response times to less than 8 seconds but at the cost of increased noise and vulnerability to sunlight bleaching (Bittig et al., 2018b; Tengberg and Hovdenes, 2014). For this reason optode lag correction (Bittig et al., 2014) provides limited benefit for the majority of the Seaglider deployments as the fast response times resolved the oxygen gradients adequately. The lag correction is however vitally important for the ”Scapa” Seaglider; examples of the lag correction are shown in appendix D.2

The gliders were placed onto one of two transects (fig. 5.1.1, table 5.1), a north-south transect between 55.4 and 56.4 °N, at 2 °E and an east-west transect between 1.48 and 2.52 °E at 56.2 °N. The predominantly deeper east-west transect was favoured for the deployment of the Seagliders, which are more energy-efficient in deeper waters. These transects were designed to cover a range of depths and physical regimes and to allow observation of both mesoscale (100 - 150 km) and sub-mesoscale (¡ 100 km) features.

We focus our analysis on the NSEG deployments for AE1, AE2, AE4 and AE7, as these occupy the same transect and span multiple seasons. The AE3 data is not discussed here. The data is of poor quality due to a combination of sensor biofouling and poor quality reference samples for calibration. The glider speed over ground is variable due to the varying payloads, weather and ballasting. Typically,

Table 5.1: Glider deployment timings and transect occupation. Gliders marked with * are discussed in this chapter. Stella did not arrive at the transect.

Glider	Type	Group	Start	End	Transect
sg537 (Fin)*	Seaglider (NSEG)	AE1	06/11/2017	24/01/2018	E-W
436 (Stella)	Slocum	AE1	06/11/2017	08/11/2017	N/A
194 (Cook)	Slocum	AE1	15/11/2017	07/02/2018	N-S
sg620 (Melonhead)	Seaglider	AE2	07/02/2018	08/05/2018	E-W
436 (Stella)	Slocum	AE2	07/02/2018	08/05/2018	N-S
sg510 (Orca)*	Seaglider (NSEG)	AE2	07/03/2018	27/03/2018	E-W
sg510 (Orca)	Seaglider (NSEG)	AE3	08/05/2018	27/07/2018	E-W
345 (Cabot)	Slocum	AE3	08/05/2018	15/08/2018	N-S
SV3-28 (Lyra)	waveglider	AE3	08/05/2018	05/06/2018	E-W
sg579 (Humpback)	Seaglider	AE3	09/05/2018	25/06/2018	N-S
sg602 (Scapa)*	Seaglider (NSEG)	AE4	13/08/2018	28/09/2018	E-W
305 (Dolomite)	Slocum	AE4	13/08/2018	10/10/2018	N-S
SV3-28 (Lyra)*	waveglider	AE4	15/08/2018	06/09/2018	E-W
444 (Kelvin)	Slocum (OMG)	AE5	26/09/2018	02/12/2018	E-W
305 (Dolomite)	Slocum	AE6	02/12/2018	12/03/2019	N-S
331 (Coprolite)	Slocum	AE6	02/12/2018	12/03/2019	E-W
304 (Ammonite)	Slocum	AE7	12/03/2019	28/05/2019	N-S
345 (Cabot)	Slocum	AE7	12/03/2019	28/05/2019	N-S
sg602 (Scapa)*	Seaglider (NSEG)	AE7	12/03/2019	25/04/2019	E-W

the Seagliders on the east-west transect took 5 days to move from one end of the transect to the other. The Seaglider data were processed and quality assured using the UEA Seaglider toolbox as described by Queste (2013), `http://www.byqueste.com/toolbox.html`. This comprised optimising the Seaglider flight parameters to determine through water speed, which is used for cell thermal mass correction for the CT sensor. This is an iterative process as determining glider flight requires determining the water density, which is calculated from the measured salinity (Garau et al., 2011). Some salinity spikes still persist after performing the cell thermal mass correction, owing to the exceptionally strong temperature gradients, these were manually removed on a per-dive basis. Data were also flagged where the glider speed was too slow ($<0.1\,\mathrm{m\,s^{-1}}$). In addition as discussed in section 1.5.1 poor quality near-surface optode measurements were present for the "F" type optodes. The effect of the incident light manifests as random noise and is present down to 9 m. This was only an issue for up-casts, during daylight hours and shallower than 9 m, as such we removed these data from the analysis.

5.2.2 Calibration

Although they are generally considered to be more stable compared with bare platinum or Clark-type membrane electrodes, oxygen optodes are known to drift over time (Bittig et al., 2018b). There two components to this drift. The first component is a reduction in sensitivity to oxygen by the luminophore foil, which is characterised as a variation in gain factor to derive the O_2 concentration. The second component is a destabilisation of the luminophore, which partly counteracts the first by causing a positive intercept at zero oxygen levels (Bittig et al., 2018b).

For the May and August 2018 glider deployment and recoveries calibration data were collected by a SBE 911plus CTD system from research vessel RV Cefas Endeavour. For all other deployments smaller boats were used and calibration data were collected using a combination of a Seabird SBE55 water sampler and an SBE16 CTD. Discrete samples were taken after deployment and prior to recovery. Samples taken during August 2018 were analysed within 12 hours on board RV Cefas Endeavour using automated Winkler titration with a Metrohm 765 burette to a photometric end point [Carpenter (1965); Langdon (2010); SiS Sensoren Instrumente Systeme GmbH, Germany].

Other samples were analysed between 1 week and 4 months after collection. Storage of oxygen samples is not optimal; however they were inverted and stored in the dark submerged in water, which Zhang et al. (2002) suggest should result in recovery within 0.3 %.

Due to equipment failure, and the nature of a project designed as a low-cost monitoring trial, the number of Winkler samples was lower than desirable. Several of the gliders were recovered at unplanned times by vessels of opportunity, and as a such these data do not have an end of mission sample. This is not ideal: While oxygen optodes provide relatively stable oxygen measurements, they are known to drift by an appreciable amount. 0.1-0.2 % per year has been reported by Bittig et al. (2018b) for 4831 and 4330 type optodes. However, fast response (F-type) optodes appear to be much more sensitive to UV induced drift as seen by Queste (2013), with drift rates in the region of 1 % a^{-1}. Gruber et al. (2010) argued that for NCP and gas-exchange studies an accuracy of 0.5 % (or 1 mmol m^{-3}) should be targeted.

Where only one sample was available for calibration, we adopted the recommendation of Bittig et al. (2018b) that in the absence of reference data spanning a wide range of oxygen values, a gain factor correction is applied to the oxygen concentration. This is in contrast to an offset, or a combination of offset and gain factor, or a correction applied to the raw phase reading of the optode (Uchida et al., 2008). Reference to the discrete samples remained challenging, as the deployment location was within a region of significant horizontal variability. This location was chosen to be as close as possible to the start of the transect, but was restricted based on the distance from port permissible for the small vessel used. We find that our calibrated oxygen accuracy is typically within 2.5 %, with some deployments worse than others due to availability of calibration data, the quality of those data, and coincident equipment failure. Haskell et al. (2019) argued that a 2 % error from spatiotemporal separation is acceptable because there are more significant contributions to the mass-balance error.

The gliders were also inter-calibrated by spatiotemporal proximity, i.e. vertical profiles were compared when the platforms were co-located in space and time. An example of the data processing steps performed for the gliders is provided in the appendices D.1.

5.2.3 Oxygen mass balance

The evolution of oxygen over time can be described as the sum of various fluxes:

$$z_i \frac{dC_i}{dt} = G + M + E - A + J \tag{5.2.1}$$

where C_i is the average oxygen concentration within z_i, an integration depth, G is the air-sea gas exchange with a flux into the ocean being defined as positive, M is mixing comprising horizontal (M_A) and vertical (M_z), E is entrainment, A is horizontal advection and J is net community production.

Air-sea gas exchange term is calculated as

$$G = k_w \left(C_{\mathrm{sat}}(1 + B) \frac{P}{P_0} - C_{\mathrm{s}} \right) \tag{5.2.2}$$

Where k_w is the air-sea transfer velocity parametrisation of Nightingale et al. (2000) derived using the `airsea` R library (Hull and Johnson, 2015), using the Schmidt number parametrisation of Johnson (2010). C_s is the near surface oxygen concentration. C_{sat} is the concentration of oxygen if it were in equilibrium with the atmosphere at a pressure of 1013.25 hPa (Garcia and Gordon (1992), using the fit to the Benson and Krause data). P is local air pressure and P_0 standard atmospheric pressure (1013.25 hPa). B is the wind speed and temperature-dependent bubble supersaturation term from Liang et al. (2013). This bubble term has been shown to have a large effect on net community production estimates (Emerson and Bushinsky (2016), Hull et al. (2016), Liang et al. (2017)). Gas exchange is only relevant to C within the ventilated partition of the water column, which is equivalent to the actively mixed surface layer (known as mixing layer (Brainerd and Gregg, 1995)) (z_{mix}). If $z_i < z_{\mathrm{mix}}$ then G needs to be scaled by the factor z_i/z_{mix}.

$$A = \left(u \frac{dC}{dx} + v \frac{dC}{dv} \right) z_i \tag{5.2.3}$$

Horizontal advection is described by equation 5.2.3. where $\frac{dC}{dx}$ is the zonal oxygen gradient and u is the zonal velocity, with equivalent terms for the meridional (v) advection.

$$E = \frac{dC}{dz} \frac{dz_i}{dt} \tag{5.2.4}$$

$$M_z = K_z \frac{dC}{dz} \tag{5.2.5}$$

$\frac{dC}{dz}$ is typically assumed to be equivalent to $\frac{\Delta C_z}{z_{\mathrm{TC}}}$, where ΔC_z is the difference between the SML (C_s) and BML oxygen concentration (C_b) and h_{TC} corresponds to the thickness of the thermocline. K_z is the vertical (diapycnal) eddy diffusion coefficient (eddy diffusivity) estimated to be $1 \times 10^{-5}\,\mathrm{m^2\,s^{-1}}$ to $1 \times 10^{-4}\,\mathrm{m^2\,s^{-1}}$ (Palmer et al., 2008; Sharples et al., 2009).

Depending on the choice of integration depth i.e. the volume of water we calculate NCP over, the fluxes to consider change. For example Barone et al. (2019) eliminated the influence of entrainment by defining their integration depth corresponding to an isopycnal, which is always deeper than the base of the surface mixed layer. Often the integration is restricted to the productive part of the water column (euphotic depth) e.g. Bushinsky and Emerson (2015) or Binetti et al. (2020). However, the shallow nature of the study area presents an opportunity to reduce the overall uncertainty by calculating the change in oxygen inventory over the whole water column, the depth of which is known with a high level of certainty. There is little variation in depth across the E-W transect and as such we calculate our mass balance in terms of the average total water column depth ($z_i = (83 \pm 1)$ m). Calculating inventory changes this way means we do not need to estimate z_{mix}. We simply need to estimate the oxygen concentration within the mixing layer for use in determining the gas exchange flux. This also means entrainment and diapycnal mixing fluxes can be ignored as these do not influence the full water column inventory. Rovelli et al. (2016) observed that within the central North Sea these vertical fluxes can be substantial, while being both difficult to quantify and temporally variable. Formulating the mass balance to avoid the need for these terms is thus highly advantageous.

In summer a persistent (non-diurnal) shallow thermocline is observed often below 10 m depth. Thus the typical mixed layer depths used for open ocean mass balance studies (de Boyer Montégut (2004), Kara et al. (2000)), which use 10 meters as a reference depth for determining the surface mixed layer depth is not applicable here (Binetti et al., 2020).

z_{mix} is not necessarily equivalent to the thermocline depth, as diurnal warming can reduce the ventilated water column to a region of water above the persistent seasonal thermocline, and it is this volume which is influenced by air-sea gas exchange directly. Typically the dynamic nature of this layer, and the difficulty determining its extent from density profiles can introduce significant uncertainties to the magnitude of the air-sea gas flux. We adopt a conservative temperature based threshold for z_{mix} of 0.2 °C which visually agrees with oxygen profiles; but this is only used for determining the value of C_s. A reference depth between 3 and 6 m is chosen based on a visual inspection of the time series, as a deeper reference depth is required for gliders with less than ideal flight characteristics. In particular the flight of sg537 during the first mission was severely impacted by loss pitch control near the surface. This is attributed to the presence of an air bubble trapped inside the nitrate analyser reagent bag Luer connector. On later missions the procedure for attaching the reagent bags was adjusted to ensure no air was trapped. This lead to the glider losing pitch control within the top 20 m of the water column, with resulting poor temperature and salinity data. Fortunately the sg537 mission was in November where the surface mixed layer extended past 40 m and thus for this mission we used a reference depth of 23 m.

In order to best include our systematic and measurement uncertainties we adopt a Bayesian Marcov-Chain Monte-Carlo approach to infer our parameter estimates (Wikle et al., 2013). By integrating the entire water column, our mass balance differential equation is reduced to equation 5.2.6.

$$\frac{dI}{dt} = G + J \tag{5.2.6}$$

which we implement as the probabilistic state-space model described in equation 5.2.7.

$$
\begin{aligned}
I_{t+1} &= I_t + G_t \Delta t + J_t \Delta t \\
G &= k_w \left(C_{\mathrm{sat}}(1+B)\frac{P}{P_{\mathrm{a}}} - C_{\mathrm{s}} \right) \\
I_0 &\sim \mathcal{N}(\hat{I}_0, \varepsilon_I) \\
\hat{I} &\sim \mathcal{N}(I, \varepsilon_I) \\
\hat{k_w} &\sim \mathcal{N}(k_w, \hat{k_w} 0.15) \\
\hat{C_s} &\sim \mathcal{N}(C_s, \varepsilon_C s) \\
\hat{B} &\sim \mathcal{N}(B, \hat{B} 0.5) \\
\hat{C_{\mathrm{sat}}} &\sim \mathcal{N}(C_{\mathrm{sat}}, 1) \\
J &\sim \mathcal{N}(0, \sigma) \\
\sigma &\sim \mathcal{N}(0, z_I)
\end{aligned}
\tag{5.2.7}
$$

where the ˆ operator signifies our observations of the unknown (latent) state parameter. C_s is the concentration of oxygen in the surface actively mixed layer ($z < z_{\mathrm{mix}}$). I is the oxygen concentration integrated over our integration depth (z_I). $\varepsilon_C s$ is the uncertainty bias in the oxygen measurements, for this study thought to be ± 2.5 mmol m^{-3}. I_0 are our initial conditions, for the inventory at $t = 0$. This model equates to a 15 % error on k_w, a 50 % error on B as discussed in Chapter 2.8. ε_I is calculated as the standard error of I, which ranges between 20 mmol m^{-2} to 200 mmol m^{-2}. Implementation of this model is using the probabilistic programming language Stan (Carpenter et al., 2017).

5.2.4 Nitrate

Several of the Seagliders, (designated NSEG, see table 5.1), were fitted with a micro fluidic wet-chemical nitrate analyser (Vincent et al., 2018). These were fully integrated with the gliders and provided periodic profiles of nitrate concentrations. This sensor takes approximately 20 seconds to draw in a sample, and a further 7.5 minutes to perform an analysis. This is slow compared to the sampling resolution of standard glider sensors and given a dive to 80 meters typically only lasts 40 minutes. So called “loiter” dives were performed to increase the number of nitrate samples. These loiter dives consist of a standard down-cast, during which the sensor would perform on-board standard measurements, followed by a slow ascent (<0.1 m s^{-1}), which allows the glider to carry out several analyses, typically between 6 and 14, despite the shallow water column. Post-recovery of the sensor, the data was corrected based on the calibrated concentration of the on-board reference standard. The on board reference standard was determined by laboratory continuous flow analysis as per Vincent et al. (2018). The data was quality controlled as per Vincent et al. (2018), and throughout this manuscript we present values which are below the limit of detection ($<0.2\,\text{mmol}\,\text{m}^{-3}$ are treated as $0\,\text{mmol}\,\text{m}^{-3}$). Accuracy is determined to be within 2 % for all gliders other than AE2 sg510 as explained later.

Nitrate uptake can be taken as a approximation of new production, but will likely overestimate the true production as some fraction of the consumed NO_3^- will have originated from remineralisation products that have then been oxidised (Laws, 1991). Typically to compare nitrate with oxygen derived NCP, both the nitrate uptake rate and oxygen NCP are converted to carbon equivalents using a standard Redfield ratio. However, C:N uptake rates have been shown to have significant variability. We adopt the approach of Alkire et al. (2012) and compare the O_2 and NO_3^- ratio directly, with a “traditional” ratio of 8.6 (Li and Peng, 2002) or the revised ratio of 10 of Andrieu et al. (2010).

5.2.5 Other data sources

We calculate the mean annual currents using data from the UK Met Office Operational Suite, Atlantic Margin Model FOAM 7 km, run 2018-06-20 (O’Dea et al., 2017) (fig. 5.1.1). For calculating horizontal transport at the AlterEco site we use the 1.5 km (tidal) configuration (run 2020-05-18) (Graham et al., 2018). Hourly meteorological data (10 m-wind speed, sea level pressure) were sourced from the ECMWF ERA5 reanalysis (Copernicus, 2018) and matched to hourly interpolated SML oxygen concentrations from the glider for the calculation of G. Bathymetry was provided from the GEBCO 2019 15 arc-second grid (GEBCO, 2019). Climatological data were from the North Sea Biogeochemical Climatology version 1.1 (Hinrichs et al., 2017).

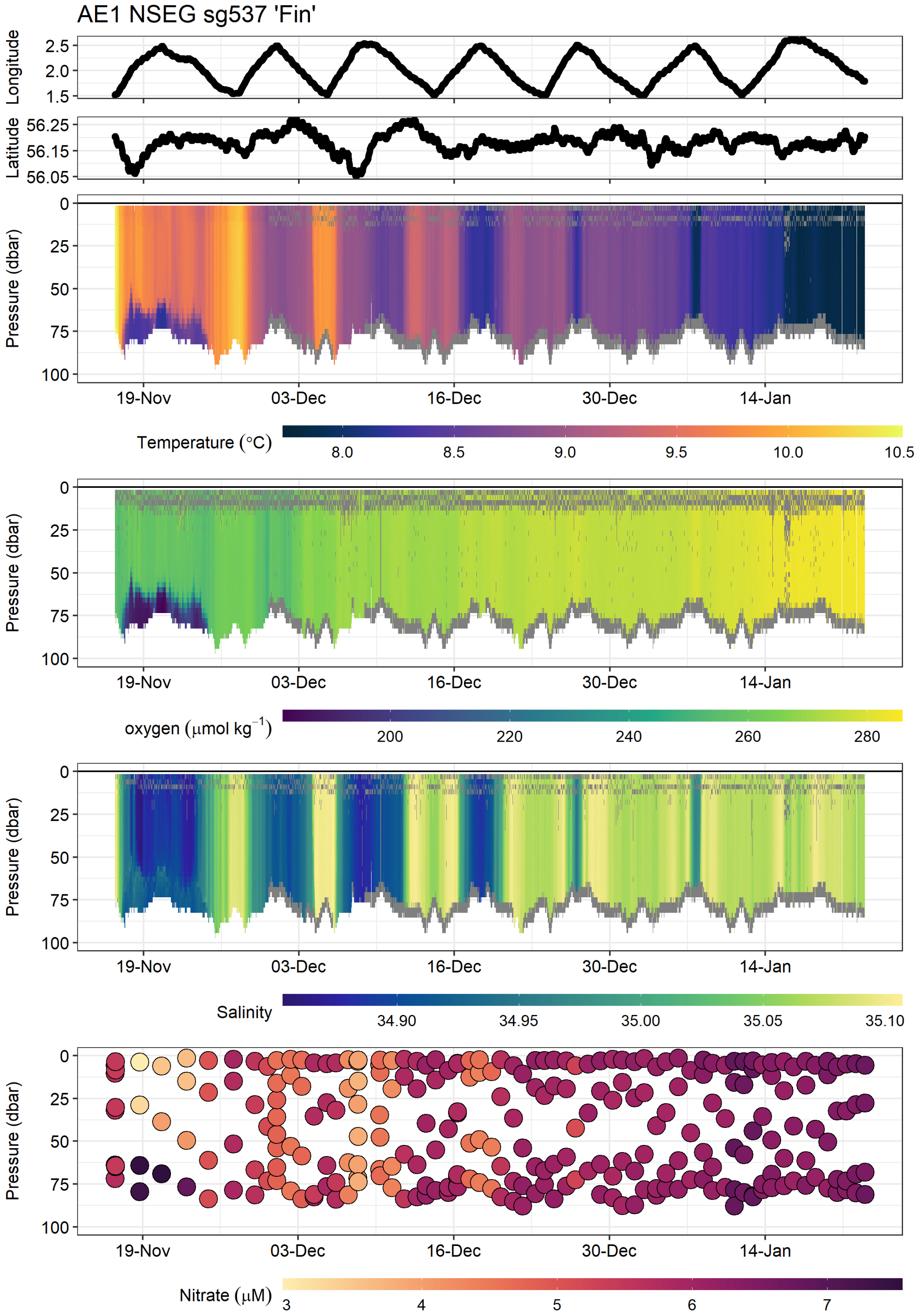

Figure 5.3.1: AE1 sg537 3 m binned glider data, showing geographical position, and vertical structure over time for temperature, oxygen, salinity, and nitrate

5.3 Results

5.3.1 AE1 sg537 ”Fin” (2017-11-06 to 2018-02-07)

AE1 sg537 glider data are shown in figure 5.3.1. Stratification is briefly observed in late November with a deep (60 m) thermocline spanning the entire transect. The bottom water is shown to be replete with nitrate ($7.5\,\mathrm{mmol\,m^{-3}}$), cold (8.2 °C), low in oxygen ($<190\,\mathrm{mmol\,m^{-3}}$) and with salinity 34.25 (0.5 higher than the overlying water). This stratification is seen to break down and the water column is fully mixed throughout the transect by 2017-12-01. Such cold pools have been shown to persist below wind driven mixing until convective overturning rapidly (within 12 h) remixes the water column (Brown et al., 2003; Greenwood et al., 2010). Water column integrated nitrate is $5.5\,\mathrm{mmol\,m^{-3}}$ at the start of the transect, which increases steadily over the time series to a maximum of $6.7\,\mathrm{mmol\,m^{-3}}$ on 2018-01-22 (fig. 5.3.1).

Horizontal temperature, salinity, oxygen and nitrate gradients are observed which reduce in magnitude over the winter. The eastern side of the transect is cooler, less salty with higher nitrate concentrations. A front is seen moving along the transect from east to west, with horizontal gradient of 0.5 °C over 0.5 km at 1.73° E on 2017-12-04, which is observed again by the glider on its return transect 2 days later, by which time the front was 6 km further to the east. This agrees with the predicted surface advection from AMM15 which predicts 5.3 km movement to the east during that period. By January there appears to be little horizontal variability. Modelled surface currents during the AE1 period are to the east (mean = 0.17 m $\mathrm{s^{-1}}$), while near bed currents are to the north (mean = 0.15 m $\mathrm{s^{-1}}$) (fig 5.1.1). Mean tidal excursion is calculated as 0.7 km to the east and 1.4 km to the north. Average wind speeds were $(9.5 \pm 3.7)\,\mathrm{m\,s^{-1}}$, with a maximum of $18.9\,\mathrm{m\,s^{-1}}$ seen on 2017-11-22.

Figure 5.3.2, a, demonstrates no evidence for tidal (0.5175 d), inertial (0.6 d) or diel (1 d) signals in near surface oxygen concentrations. There is a short duration signal of a roughly 12 hr period for one day at the start of the After 2017-12-15, horizontal variability is small. The boundary between the deep cold pool and the rest of the mixed water column is easily defined with either a temperature or oxygen threshold (fig. 5.3.1), we adopt a 0.05 °C temperature threshold relative to 20 m for z_{mix}. We calculate C_s using the average oxygen concentration between 8 and 15 m, as due to the poor flight characteristics of this particular glider near surface data is poor. However, given the mostly mixed water column this has negligible impact on our estimate of the air-sea oxygen concentration gradient. The surface waters are

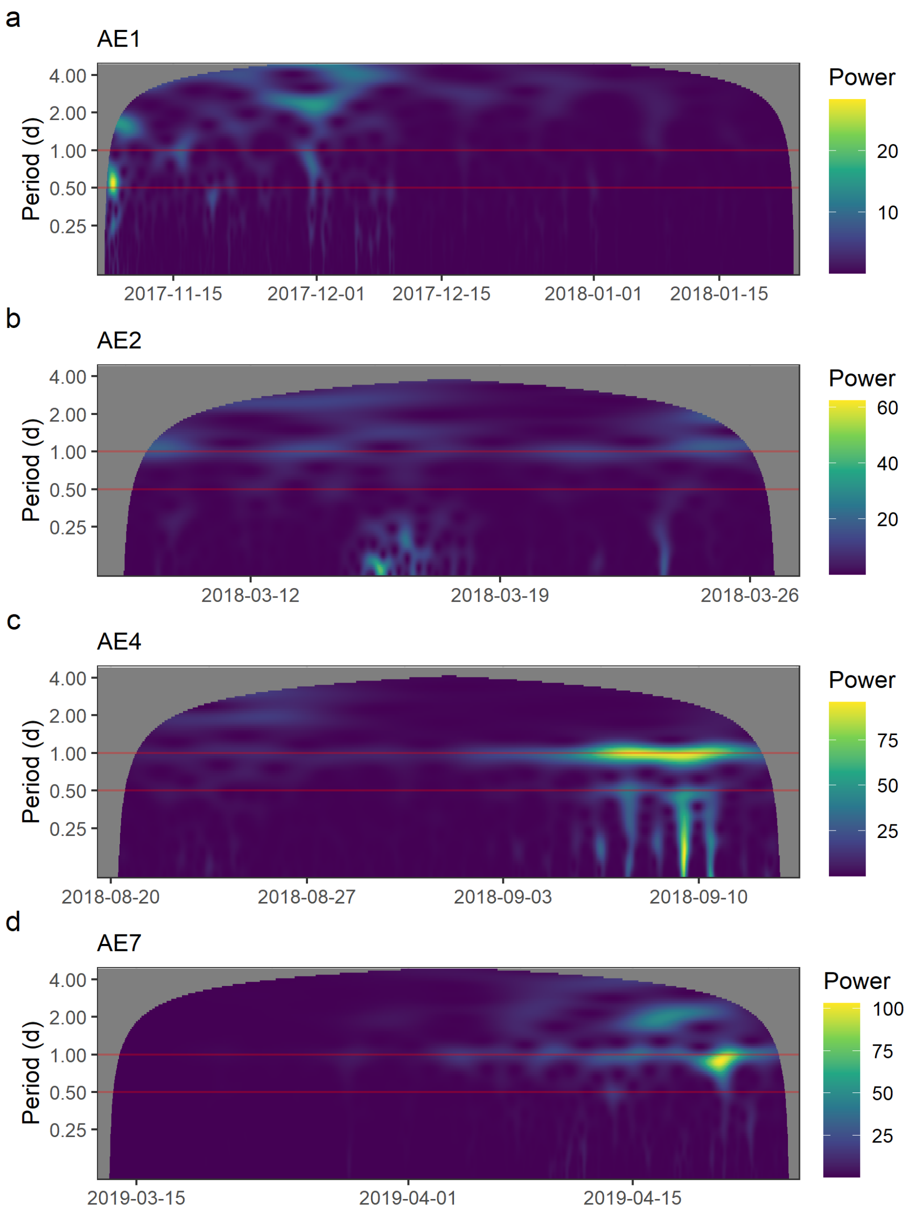

Figure 5.3.2: Continuous wavelet transform of the near surface (C_s) oxygen concentrations for each of the glider missions, 12 hr and 24 hr periods are highlighted with a red horizontal line

under-saturated throughout the deployment and figure 5.3.3 shows the net uptake of oxygen by the ocean as the system moves towards equilibrium between water and atmosphere.

If we treat this period as a 1D time series and calculate gas exchange and NCP using mean hourly observations, then cumulatively (3.6 ± 0.8) mol m^{-2} of oxygen is drawn down into the sea during this 67 day period (5.3.3, d). The increase in oxygen inventory appears to be completely driven by the uptake of oxygen from the atmosphere; NCP is indistinguishable from zero ((0.1 ± 0.8) mol m^{-2}) (5.3.3, d).

To explore horizontal gradients, the time series is split into three discrete regions based on the glider being within 7 km of the east, west and centre points of the transect. We aggregate these data based on each "visit" to the region, which is approximately 30 hours of continuous sampling. While uncertainty is high, there do appear to be differences in cumulative NCP between the regions. The eastern edge appears to be net productive, while the west is a net sink for oxygen.

5.3.2 AE2 sg510 "Orca" (2018-03-07 to 2018-03-27)

Seaglider sg510 suffered a battery failure and was recovered prematurely after 20 days total mission time. The glider was in the study area for 7 days during which time it completed two transects (fig. 5.3.5). The water column was fully mixed at the start and stratifies over the week. Following transient stratification seen on 2018-03-22, a persistent thermocline formed from 2018-03-24. Chlorophyll fluorescence (not shown) doubles between 2018-03-25 and 2018-03-26, and is concentrated in the newly created SML. A slight horizontal nitrate concentration gradient is seen coincident with with horizontal changes in salinity. The western side of the transect had higher salinity and higher nitrate, with a 0.06 increase in salinity correlated with a 0.75 mmol m^{-3} increase in nitrate. Determination of changes to the nitrate inventory is difficult; an issue with the nitrate sensor sampling routine introduced some additional uncertainty due to a carry-over effect between samples. This was confounded by the failure of the sensor on-board memory which meant the data could not be reprocessed from the raw instrument readings. This carry-over issues manifests as anomalously low nitrate for the first sample of each dive, seen in figure 5.3.5 bottom panel, and presumably some mixing between subsequent samples. The first sample is thought to be most strongly impacted by the carry-over from sampling the on-board standard. We have removed the nitrate values for the first (deepest) sample from each dive from the inventory analysis and the remaining values are all

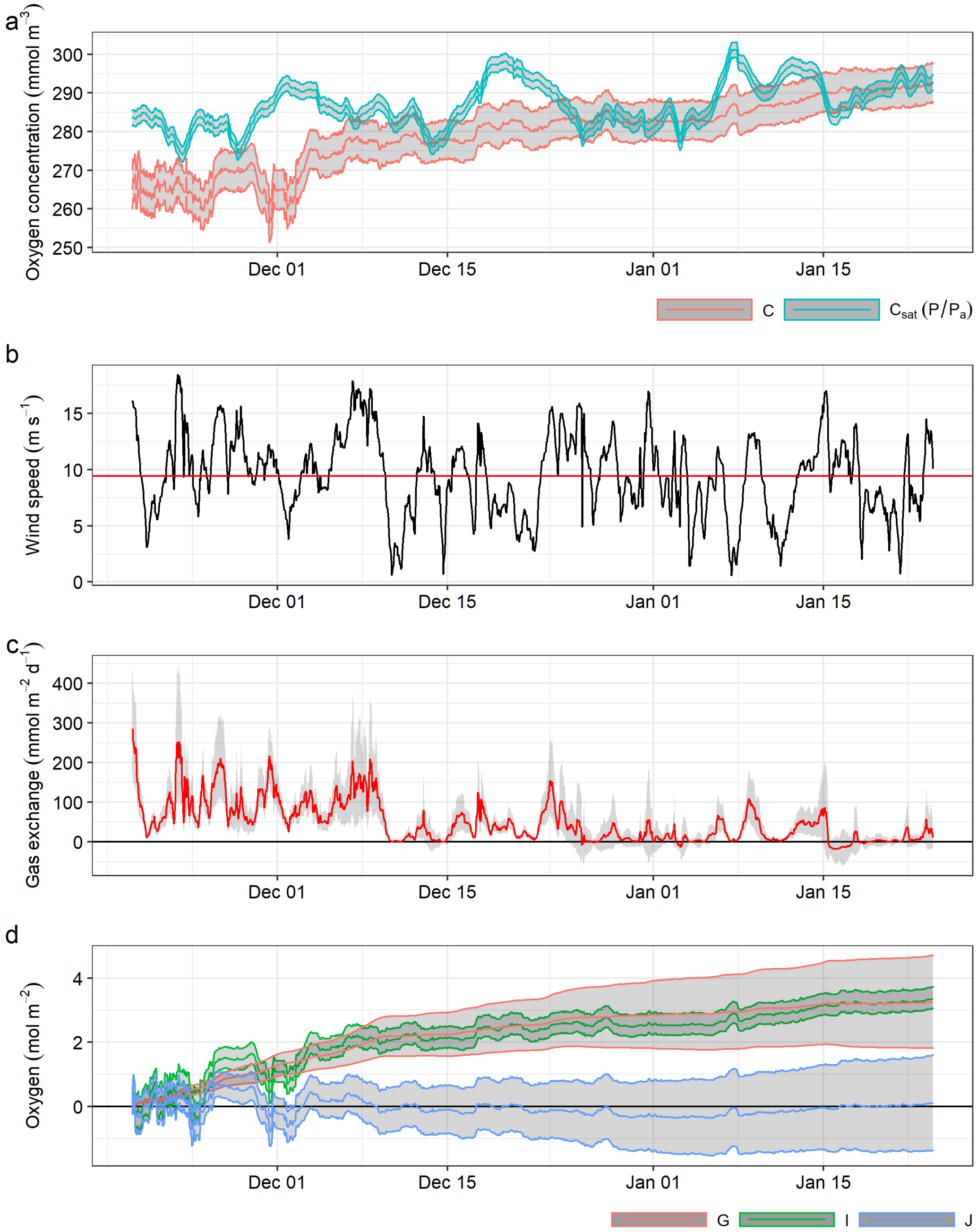

Figure 5.3.3: AE1 sg537 1D total transect oxygen mass-balance, shaded areas represent 95 % credible interval. **(a)** near surface oxygen (C_s, red) with pressure compensated oxygen saturation concentration (C_{sat}, blue). **(b)** ECMWF ERA5 hourly wind speed at 10 m for 56.2° N 2° E (centre of the AlterEco transect). mean wind speed shown in red. **(c)** Instantaneous air-sea gas exchange, (>0: into the ocean). **(d)** Cumulative gas exchange (G, red), Oxygen inventory (I, green) and Cumulative NCP (J, blue).

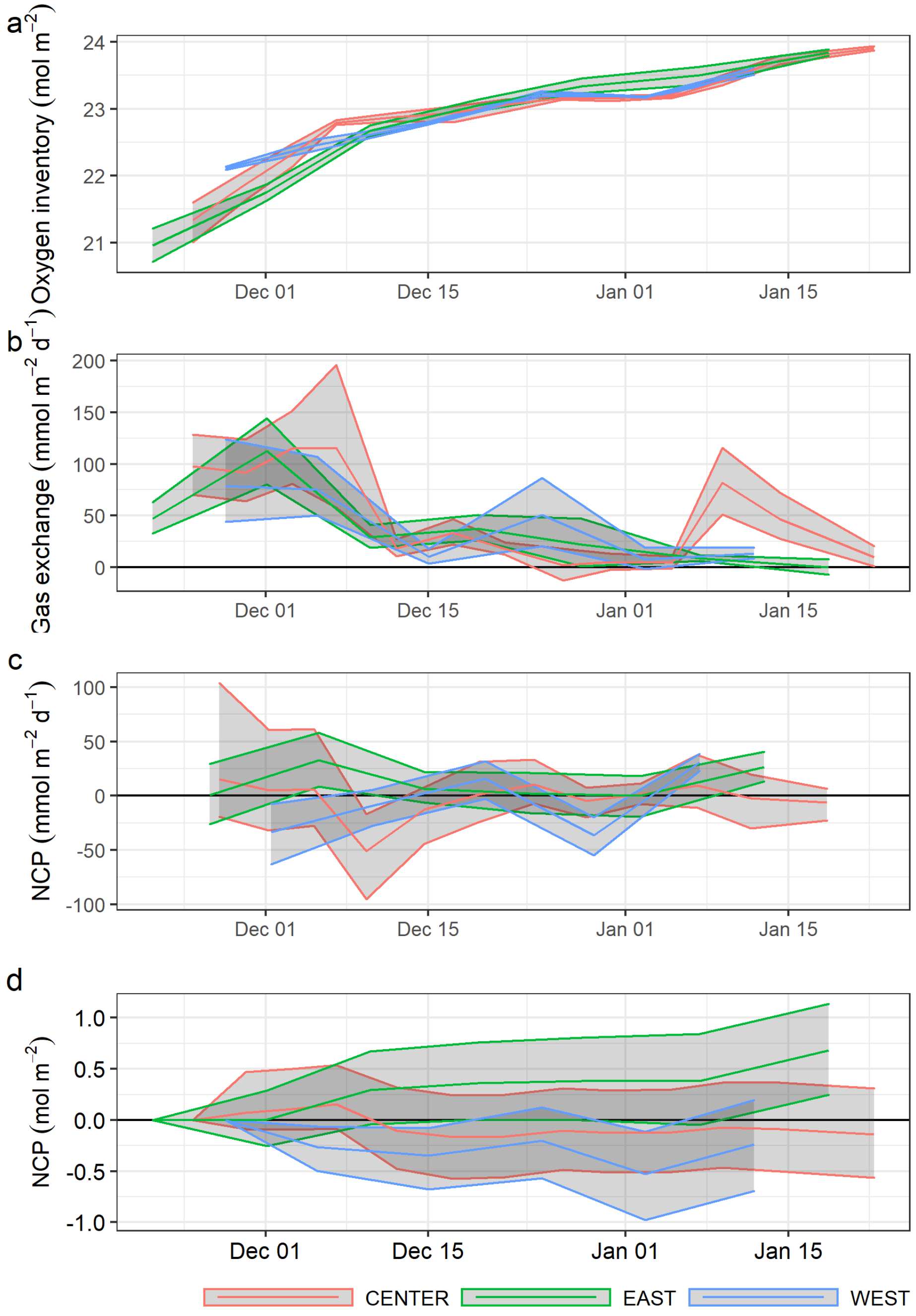

Figure 5.3.4: AE1 sg537 oxygen mass-balance, with transect split into 3 regions, shaded areas represent 95 % confidence limits. **(a)** oxygen inventory for each of the three regions, **(b)** instantaneous gas exchange (>>: into the ocean), **(c)** water column integrated NCP, the values are plotted based on t_0, given NCP is calculated between t_0 and t_1, **(d)** cumulative water column integrated NCP.

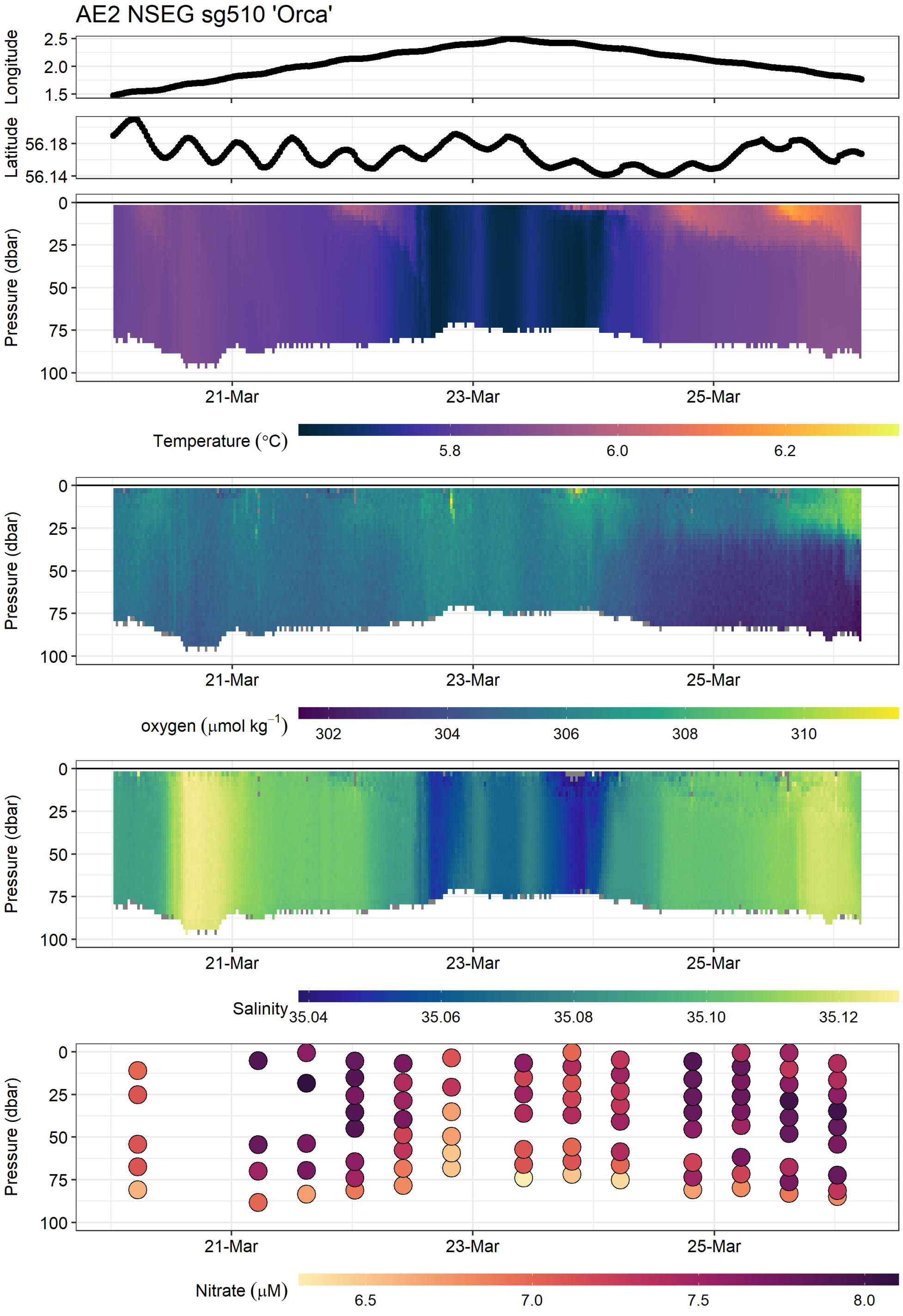

Figure 5.3.5: AE2 sg510 3 m binned glider data, showing geographical position, and vertical structure over time for temperature, salinity, oxygen and nitrate concentrations

treated with an uncertainty of $\pm 0.3\,\mathrm{mmol\,m^{-3}}$ Some horizontal variability is seen, with lower concentrations ($<7\,\mathrm{mmol\,m^{-3}}$) seen at the eastern end of the transect. Peak water column integrated nitrate $(7.6 \pm 0.2)\,\mathrm{mmol\,m^{-3}}$ is associated with salinity 35.11 ± 0.005.

Figure 5.3.5 also demonstrates a relatively rapid change in the BML oxygen concentrations. If we compare the BML region within 3 km of 2.3 °E we see a mean $(1.2 \pm 0.3)\,\mathrm{mmol\,m^{-3}}$ reduction in oxygen concentration over 1.8 days. There is some warming (+0.06 °C) but this would contribute a negligible change in oxygen saturation (0.3 %). Thus we see an apparent oxygen consumption of $(0.66 \pm 0.09)\,\mathrm{mmol\,m^{-3}\,d^{-1}}$, ignoring any vertical mixing processes. The vertical fluxes are likely small, as the system is transitioning from a fully mixed (where the vertical gradient is zero) state to a stratified one. Given the maximal vertical oxygen gradient at the base of the thermocline is approximately 5 mmol $\mathrm{m^{-3}}$ over 12 m, the vertical flux is likely no more than 2 mmol $\mathrm{m^{-2}\ d^{-1}}$, which equates to only $0.024\,\mathrm{mmol\,m^{-3}\,d^{-1}}$ change in concentration. It should be noted that the rates we can determine here are a function of which part of the transect we compare and the speed of the glider. If we choose 2^{o} E as our geographic comparison coordinate we would see a consumption rate of $(0.34 \pm 0.08)\,\mathrm{mmol\,m^{-3}\,d^{-1}}$ as it takes 4.3 days for the glider to return to this location. The total water column inventory within the central region during this period experiences a reduction from 25.71 to 25.66 mol $\mathrm{m^{-2}}$ over 4 days, which is equivalent to a 0.15 mmol $\mathrm{m^{-3}\ d^{-1}}$ reduction in concentration. These rates are comparable to the bottom oxygen consumption rates seen in the Celtic Sea after the spring bloom (Chapter 4, (Hull et al., 2020)), but much smaller than those reported by Queste et al. (2016), $(2.8 \pm 0.3)\,\mathrm{mmol\,m^{-3}\,d^{-1}}$ in August 2011, 94 km further to the north. (Rovelli et al., 2016) reported BML oxygen concentration change of $-0.43\,\mathrm{mmol\,m^{-3}\,d^{-1}}$ ($-15\,\mathrm{mmol\,m^{-2}\,d^{-1}}$) during August 2009, vertical fluxes during this period were determined to be much larger than those we infer ($54\,\mathrm{m^{-2}\,d^{-1}}$) due to the larger cross-thermocline gradient. They determined the BML oxygen consumption to be in the order of $60\,\mathrm{mmol\,m^{-2}\,d^{-1}}$ ($1.7\,\mathrm{mmol\,m^{-3}\,d^{-1}}$).

Average wind speed over this period is 6.7 m $\mathrm{s^{-1}}$ (fig. 5.3.6 b.) Residual surface current flow (0.17 m $\mathrm{s^{-1}}$) is to the south-east. A wavelet transform of the near surface (5 - 15 m averaged) oxygen concentrations reveals a weak diurnal signal(fig. 5.3.2 b), which can also be faintly observed within the oxygen inventory time series (fig. 5.3.5). The water column oxygen is close to saturation with the atmosphere and as such air-sea gas exchange is uncertain but small in magnitude during this period (fig. 5.3.6 c). The 1D mass balance for the whole transect is uncertain (fig. 5.3.6 d) due to the small changes in inventory and oxygen concentrations close to atmospheric equilibrium (fig. 5.3.6 a). Gas exchange is net out of the sea $(-62 \pm 42)\,\mathrm{mmol\,m^{-2}}$ and NCP is very small $(0.13 \pm 0.05)\,\mathrm{mol\,m^{-2}}$ over the 7 d. Given the length of the mission it is not feasible to adopt the three region approach. We do however calculate a cumulative NCP just for the central region which is indistinguishable from zero.

5.3.3 AE4 sg602 "Scapa" (2018-08-16 to 2018-09-10)

The August mission included the SV3 waveglider surface vehicle. This was capable of much faster transit times, taking just 2.5 days for a return occupation (1.3 days per transect), which allows for better separation of the temporal and spatial changes in oxygen concentration, but does not provide any vertical profiles. Figure 5.3.7 shows that the E-W transect does not exist as a simple continuum with the extremes of the transect as end-members of a constant horizontal oxygen concentration gradient. The centre of the transect consistently has lower surface oxygen concentrations, but variation over the transect is typically less than 5 mmol m^{-3}. A wavelet transform demonstrates a strong 2.5 day signal associated with the transect repeat period of the vehicle, and periods of diel cycling. E-W gradients as seen by the Waveglider are at most $0.16\,\mathrm{mmol\,km^{-4}}$ (fig. 5.3.7). Taking the surface water displacement from the modelled currents (33 km) and the maximum E-W gradient seen by the Waveglider we could expect to see a E-W horizontal oxygen flux of 184.8 mmol m^{-2} over the 22 day study period (8 mmol m^{-2} d^{-1}), assuming a SML depth of 35 m. Comparisons between the Waveglider and sg602 were made in a similar way to the glider intercomparison (see Validation), with near surface Seaglider data being compared with the Waveglider data where the two platforms are within 2 km and 1 h. A least squares linear model fit demonstrates fitted residuals with a standard deviation of $1.2\,\mathrm{mmol\,m^{-3}}$.

Mean wind speed is 6.6 m s^{-1} with a peak of 13.6 m s^{-1} (fig. 5.3.9 b). Residual currents are variable, first surface currents flow to the south east until 2018-08-16, and then mostly to the east. Mean surface flow is 0.015 m s^{-1} over the entire deployment. Mean bottom currents are small and to the north.

The vertical structure is characterised by a persistent and very strong thermocline, spanning 17.5 to 5.6 °C between 21 and 39 m at its most extreme in late August, with strongest vertical gradients in excess of 3 °C m^{-1}. These gradients are particularly challenging for the Seaglider with its unpumped CT sensor to resolve.

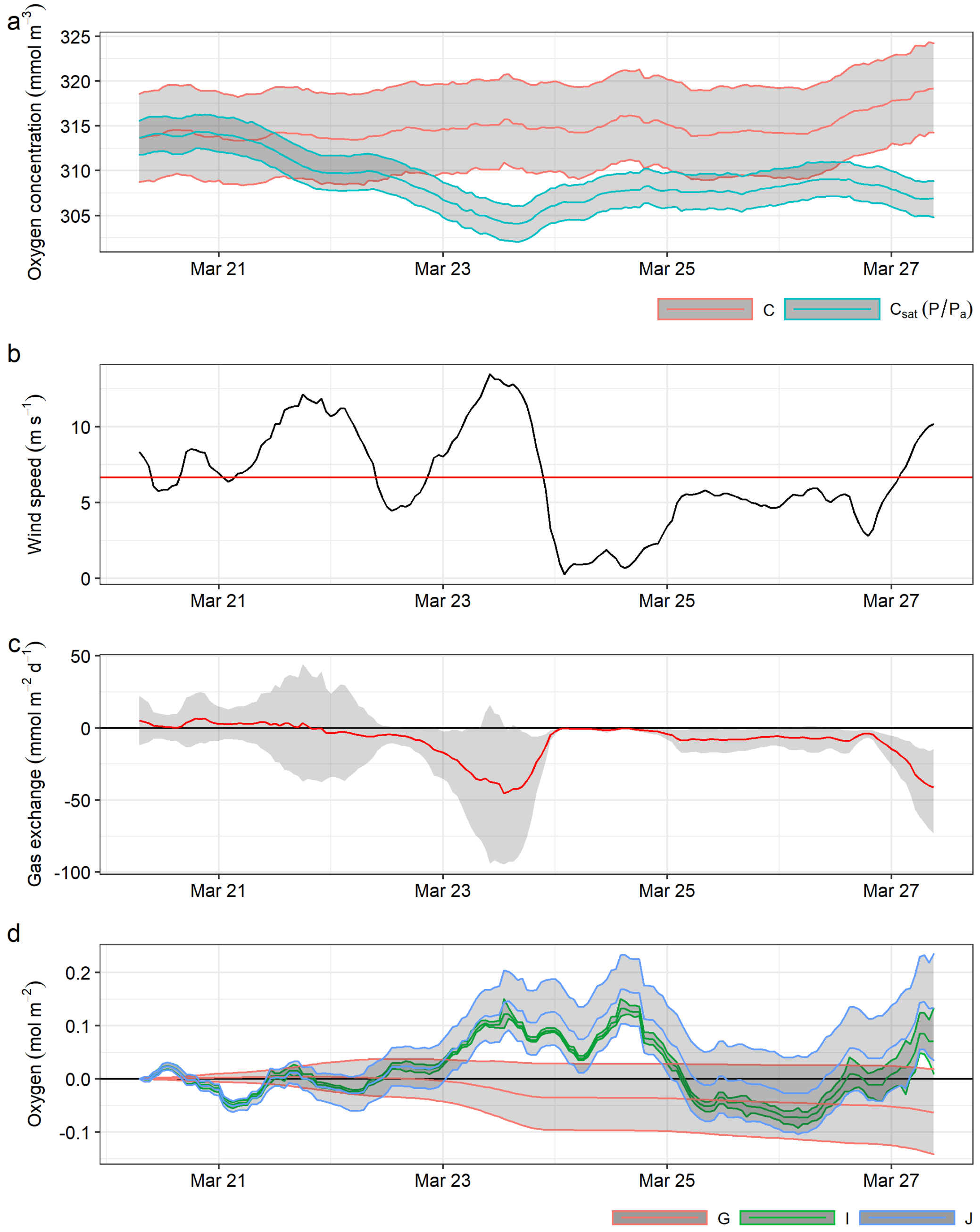

Figure 5.3.6: AE2 sg510 1D total transect oxygen mass-balance, shaded areas represent 95 % credible interval. **(a)** near surface oxygen (C_s, red) with pressure compensated oxygen saturation concentration (C_{sat}, blue). **(b)** ECMWF ERA5 hourly wind speed at 10 m for 56.2° N 2° E (centre of the AlterEco transect). mean wind speed shown in red. **(c)** instantaneous air-sea gas exchange, (>0: into the ocean). **(d)** cumulative gas exchange (G, red), oxygen inventory (I, green) and cumulative NCP (J, blue).

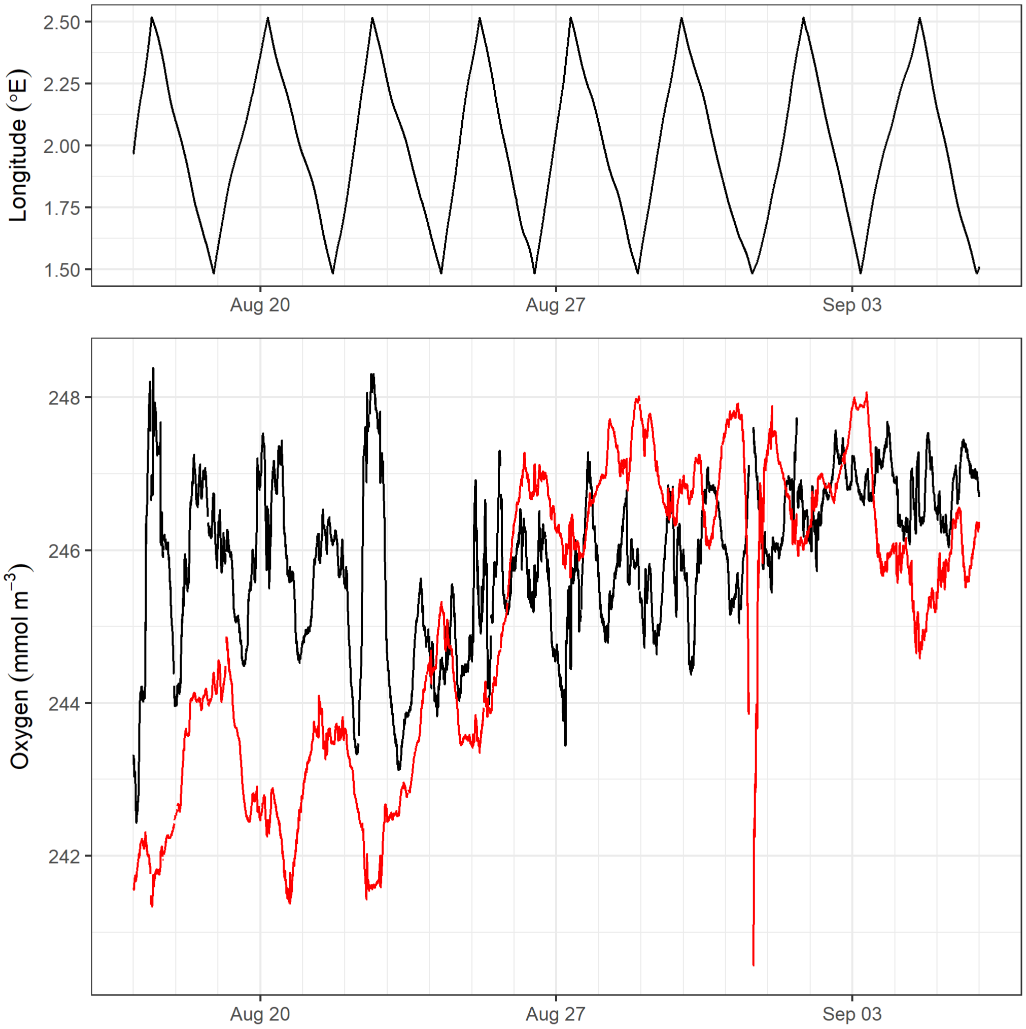

Figure 5.3.7: Horizontal variation in oxygen (black line) and equilibirum oxygen saturation concentration (C_{sat}, red line) from the Waveglider during AE4

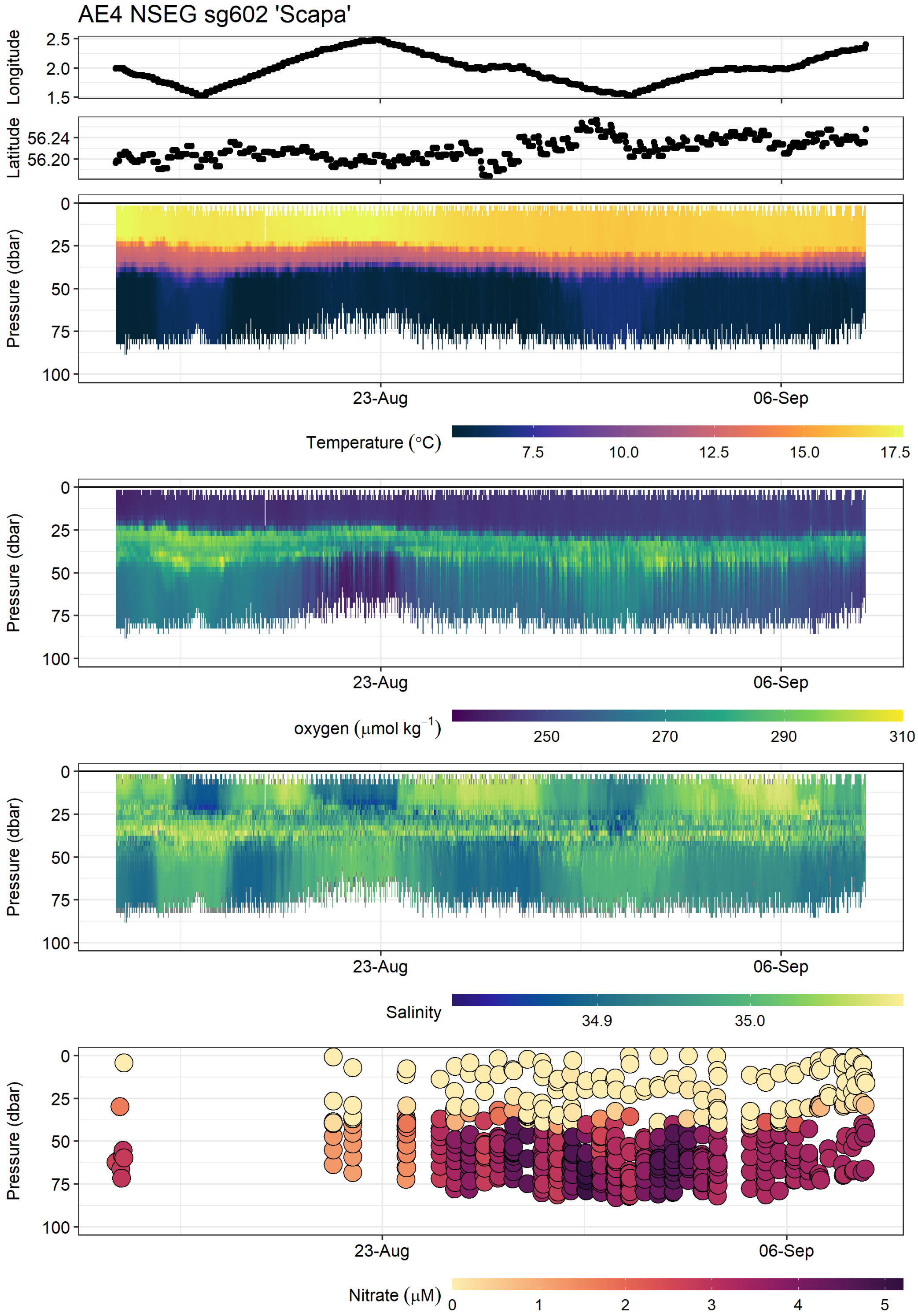

Figure 5.3.8: AE4 sg602 3 m binned glider data, showing geographical position, and vertical structure over time for temperature, oxygen, salinity, and nitrate

Even with a well constrained flight model artefacts in salinity at the thermocline persist (fig. 5.3.8). The salinity structure is characterised by a fresher ($S < 34.8$) SML to the west overlying a saltier BML ($S > 35$), while at the eastern end the SML is saltier than the BML. Surface horizontal temperature gradients were very small unlike salinity which shows an unusual pattern of regions with salty over fresher and vice-versa along the transect. Horizontal variation in the equilibrium oxygen saturation concentration is small and does not exceed 0.06 % km^{-1}.

The BML to the west is 0.5 °C warmer than that in the east. This warmer BML is coincident with elevated BML oxygen. This is perhaps unexpected as higher BML temperatures would be consistent with both reduced oxygen solubility and increased respiration. We would expect this to result in reduced oxygen either because there was a reduction in the amount of oxygen present prior to stratification, or increased consumption rates. This region could be the result of increased vertical mixing or horizontal transport from a more recently ventilated water mass.

Oxygen and nitrate data were not collected during 17 - 19th August, so we restrict our mass-balance analysis to just the period between 2018-08-19 and 2018-09-13. This was primarily due to difficulty trimming the glider during which time loiter dives were not attempted, the optode was switched off at the same time by mistake. The SML is supersaturated (fig. 5.3.9 a) with a net oxygen outgassing (-0.5 ± 0.3) mol m^{-2} over the 25 day mission (fig. 5.3.9 d).

Figure 5.3.10 shows the results from splitting the analysis into the three regions. The eastern end of the transect is net autotrophic, with NCP estimated as (45 ± 8) mmol m^{-2} d^{-1}, while the central region shows variable net heterotrophy (-6 to -12 mmol m^{-2} d^{-1}) and the western region has NCP close to zero, but is most likely also heterotrophic.

5.3.4 AE7 sg602 "Scapa" (2019-03-29 to 2019-04-25)

The water column is already beginning to stratify by the start of the AE7 deployment (fig. 5.3.11). The initiation of the spring bloom is seen with a clear signal of productivity in the surface mixed layer. Salinity is increased throughout the period relative to March 2018. Vertical gradients in nitrate are present from the start of April, with the surface mixed layer becoming depleted over the course of 10 days. The water column-averaged nitrate concentration declines from $7.4\,\mathrm{mmol\,m^{-3}}$ (2019-04-01) to $<2\,\mathrm{mmol\,m^{-3}}$ by 2019-04-22.

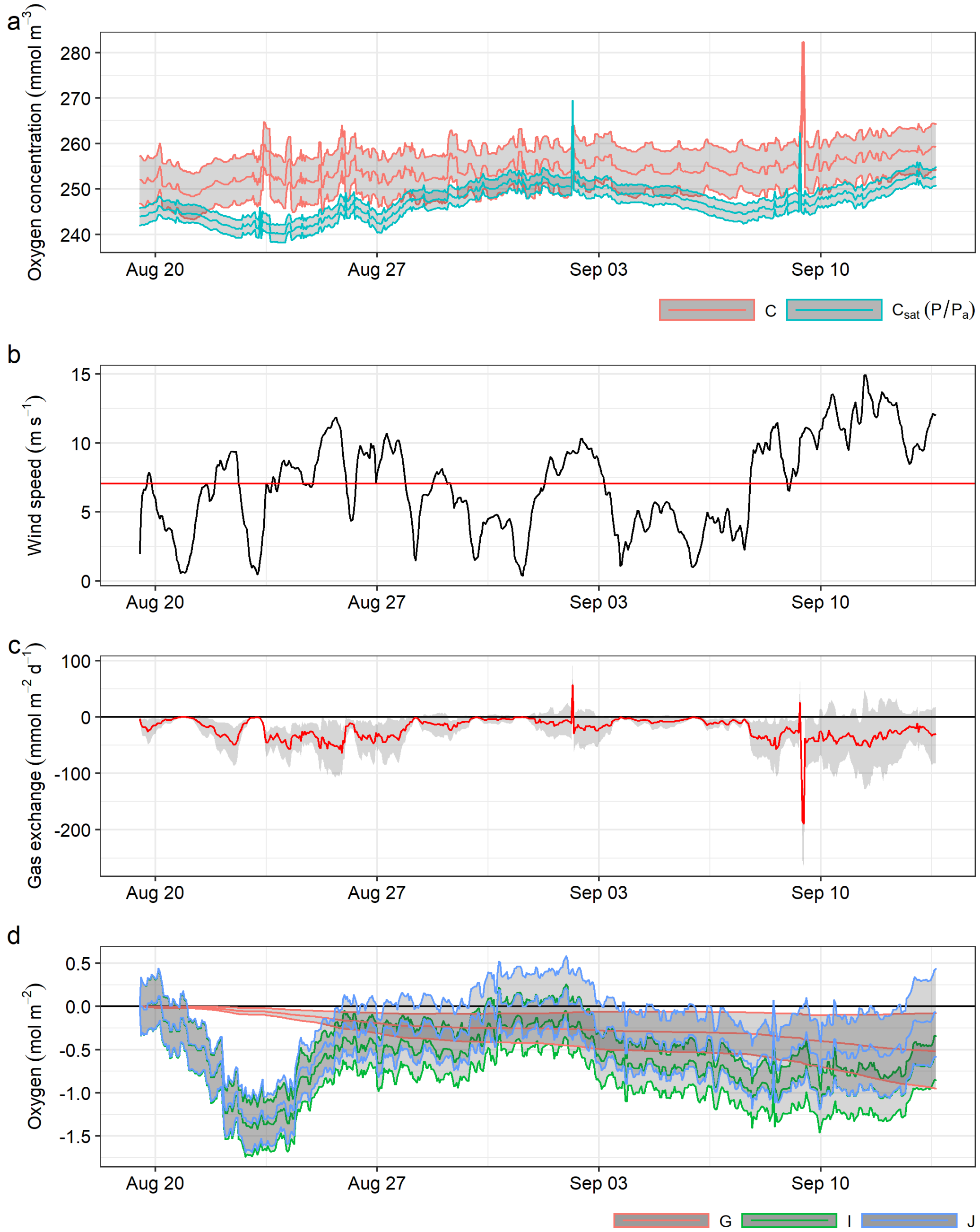

Figure 5.3.9: AE4 sg602 1D total transect oxygen mass-balance, shaded areas represent 95 % confidence limits. **(a)** near surface oxygen (C_s, red) with pressure compensated oxygen saturation concentration (C_{sat}, blue). **(b)** ECMWF ERA5 hourly wind speed at 10 m for 56.2^{o} N 2^{o} E (centre of the AlterEco transect). mean wind speed shown in red. **(c)** Instantaneous air-sea gas exchange, (>0: into the ocean). **(d)** Cumulative gas exchange (G, red), Oxygen inventory (I, green) and Cumulative NCP (J, blue).

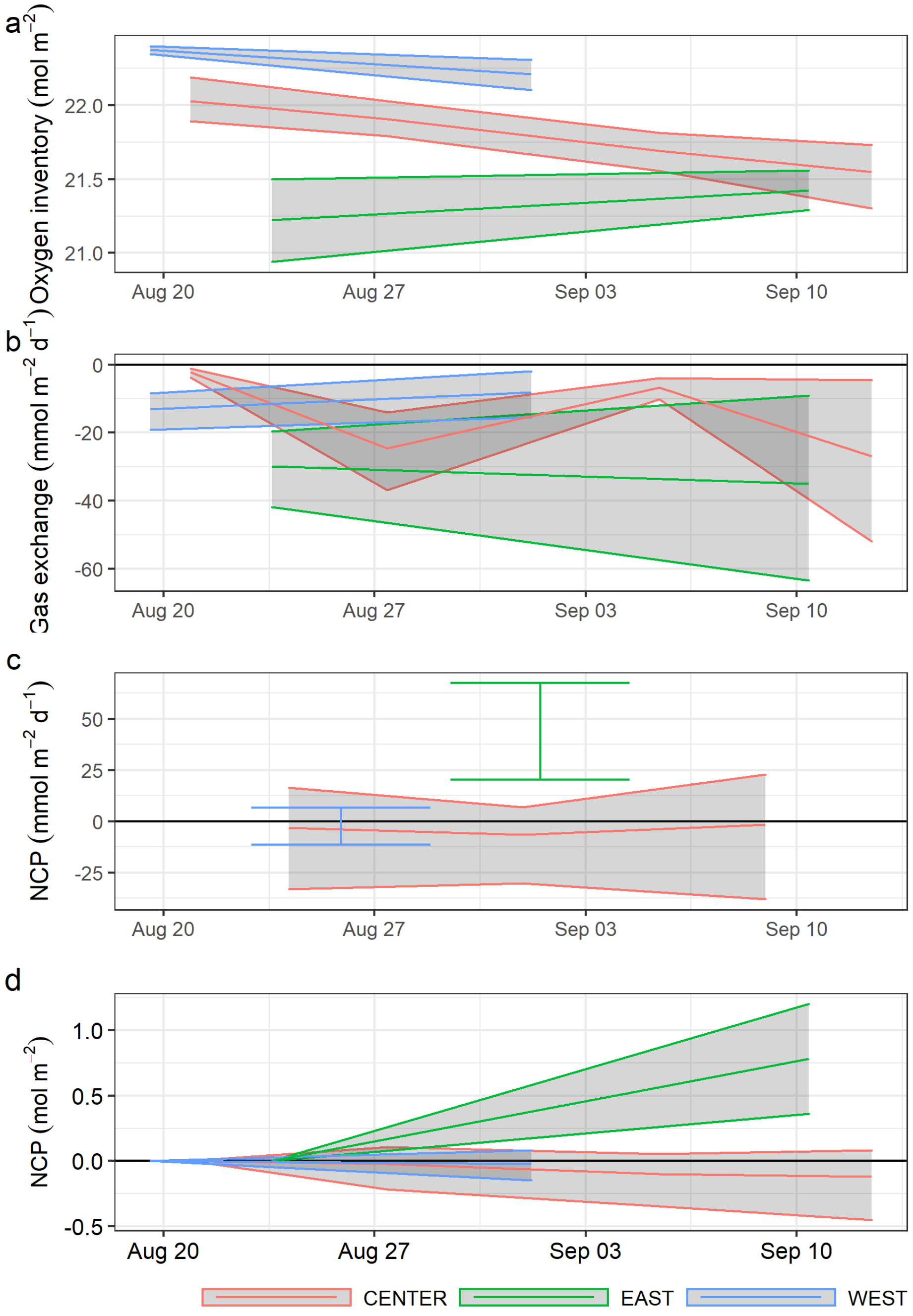

Figure 5.3.10: AE4 sg602 oxygen mass-balance, with transect split into 3 regions, shaded areas represent 95 % credible interval. **(a)** oxygen inventory for each of the three regions, **(b)** instantaneous gas exchange (>0: into the ocean), **(c)** water column integrated NCP, the values are plotted based on t_0, given NCP is calculated between t_0 and t_1, **(d)** cumulative water column integrated NCP.

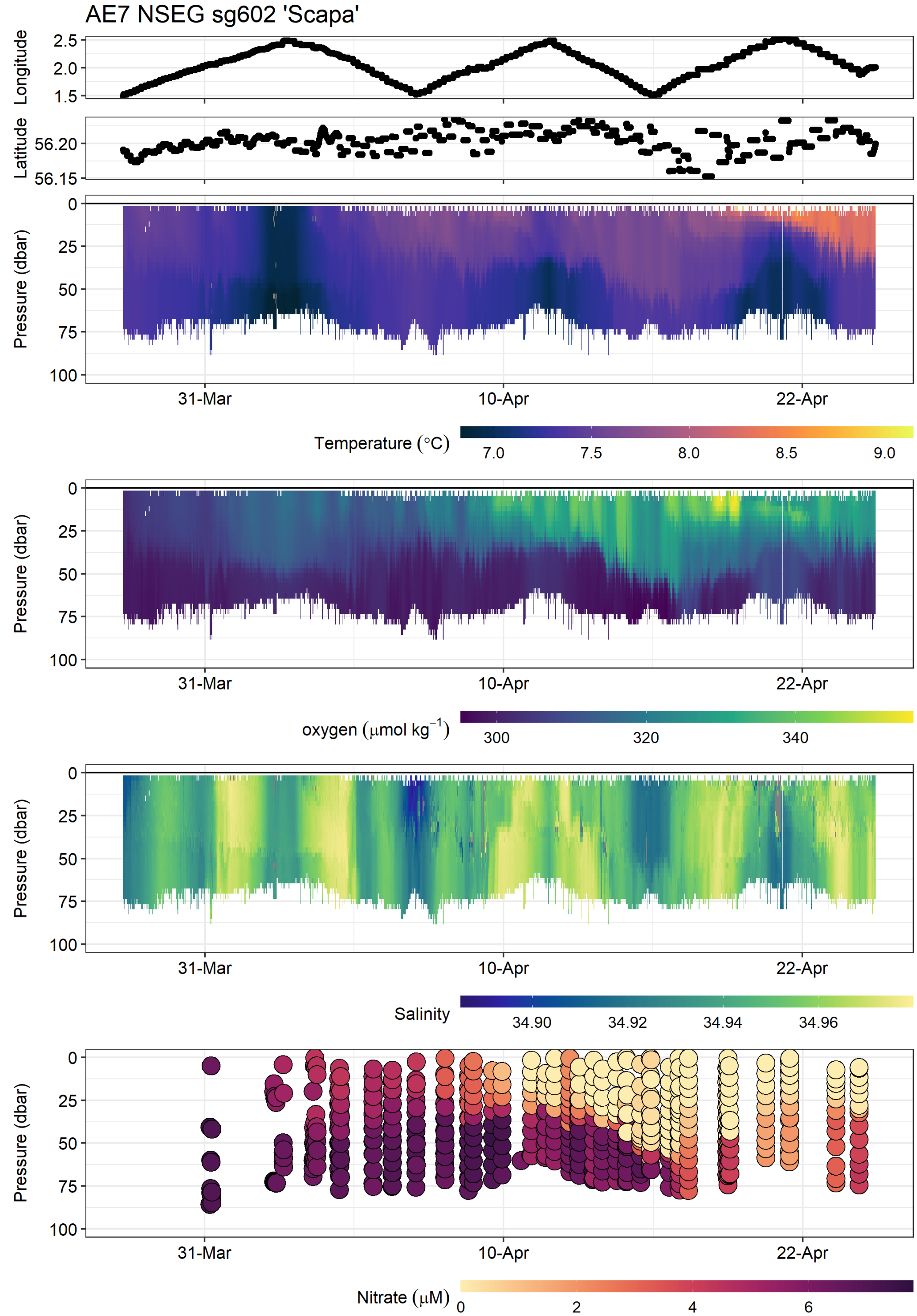

Figure 5.3.11: AE7 sg602 3 m binned glider data, showing geographical position, and vertical structure over time for temperature, oxygen, salinity, and nitrate

Horizontal variability is seen, with the eastern side of the transect persistently cooler (1 °C) than the west. As in 2018 the transect does not follow a clear E-W continuum of water properties. The region at 2° E appears to be distinct with higher salinity compared to the waters both to the east and west (fig. 5.3.11). Salinity is reduced relative to March 2018, ranging between 34.82 and 34.97 compared to 35.04-35.12 for 2018.

Mean wind speed is 6.7 m s^{-1} with a peak of 12.6 m s^{1} (fig. 5.3.12 b.). Residual surface currents during this period are to the north-west (counter to the annual mean flow) with surface waters moving into the transect area from off the bank. Bottom water residual flow is small, with a brief net flow to the north, and then to the south. Given a 10 day transit time for the glider to return to the extreme ends of the transect, and a mean surface current of 0.02 m s^{-1}, surface water is likely to be advected 47 km during that time.

A wavelet analysis of the near surface oxygen concentration shows little evidence for a signal at tidal or inertial periods (fig. 5.3.2), suggesting that the horizontal advection during this period is minimal. However, as mentioned above, gliders are semi-Lagrangian and are displaced by tidal currents, such that a tidal signal may not be observable. This tidal deflection can clearly been seen in figure D.1.1. Figure 5.3.2, bottom panel, does show strong evidence for a diel signal as a high intensity band at $f = 1$, which can also be seen in the total inventory (fig. 5.3.12).

There are several approaches we can take to determine nitrate drawdown. Firstly we restrict the period of analysis to be that between peak nitrate at the start of the deployment (2019-04-08) and when surface nitrate is below the sensor limit of detection (2019-04-16). A linear least-squares fit for this time series, which integrates over 3 complete transects, provides a nitrate consumption rate of (28 ± 5) mmol m^{-2} d^{-1}. Alternatively if we compare just the western side of the transect we see a reduction of 370 mmol m^{-2} over 9.5 days (38 mmol m^{-2} d^{-1}). However, given the transit time of the glider it is possible that nitrate depletion occurred sooner but the glider was not in a position to observe it. As the centre of the transect is sampled more often, a 1D mass balance for the region within 7 km of 2° E reveals a nitrate drawdown of (20 ± 2) mmol m^{-2} d^{-1} using a least squares fit. In each of these analyses the water column is assumed to be 83 m, and horizontal processes are ignored. We can assess that overall the study region demonstrates nitrate consumption rates between 0.25 - 0.5 mmol m^{-3} d^{-1}. There is net outgassing of oxygen throughout this period (fig. 5.3.12 d.), cumulatively (2.2 ± 0.1) mol m^{-2} is released to the atmosphere over 27 days.

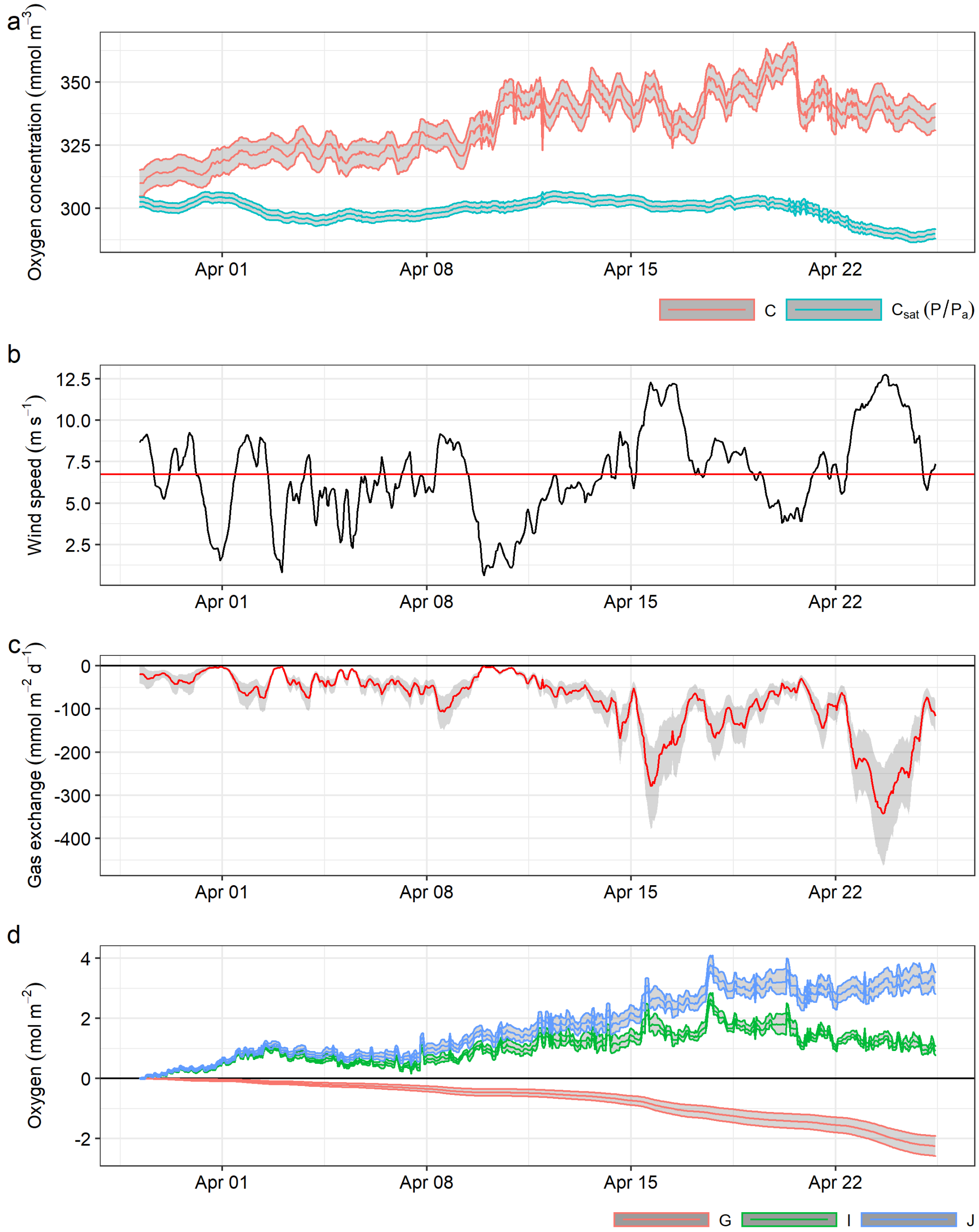

Figure 5.3.12: AE7 sg602 1D total transect oxygen mass-balance, shaded areas represent 95 % credible interval. **(a)** near surface oxygen (C_s, red) with pressure compensated oxygen saturation concentration (C_{sat}, blue), **(b)** ECMWF ERA5 hourly wind speed at 10 m for 56.2° N 2° E (centre of the AlterEco transect). mean wind speed shown in red. **(c)** instantaneous air-sea gas exchange, (>0: into the ocean), **(d)** cumulative gas exchange (G, red), oxygen inventory (I, green) and cumulative NCP (J, blue).

If we take a similar approach for 1D NCP as for nitrate and use the same timings as the linear fit from above; a depth integrated oxygen time series and subtract the net gas exchange over the 8 day period results in a net production of (1.6 ± 0.3) mol m^{-2}, equivalent to (200 ± 15) mmol m^{-2} d^{-1}. This suggests a O:N ratio of 7.2. Over the whole AE7 mission we calculate a cumulative NCP of (3.2 ± 0.2) mol m^{-2} (fig. 5.3.12 d).

Splitting the time series into three regions figure 5.3.13 shows that all of the regions show net autotrophy. In contrast to deployments AE1 and AE4, during which the eastern region is productive, is it less productive than both the central and western regions during AE7. We also see indication of termination of the spring bloom, with a drop in productivity in the central region after 2018-04-15, which coincides with our observed nitrate depletion.

5.4 Discussion

5.4.1 NCP rates

Our analysis reveals that the oxygen mass balance in this region has a high degree of horizontal heterogeneity, with the eastern and western regions comprising clearly different water masses, which do not necessarily exist on a continuum between the more inshore and offshore waters. Within the calculated uncertainties, net community production is zero during the winter months, while production signals during the 2019 spring bloom are clear and easy to resolve. Our peak rates are of the order 200 mmol m^{-2} d^{-1} during the spring bloom. For 2019, we estimate cumulative net community production during the spring bloom period of (2.5 ± 0.2) mol m^{-2}. Große et al. (2016) suggested that year-to-year variations in the oxygen conditions are mostly caused by variations in primary production, while spatial differences are mostly due to variation in stratification and water depth.

We apply the same geographic coordinate method to the North Sea biogeochemical climatology of Hinrichs et al. (2017) (fig. 5.4.1). Climatologies such as the NSBC are frequently used for large scale biogeochemical modelling studies (e.g. Wakelin et al. (2020)). Gas exchange is estimated using average monthly wind speed in the period 2014-2019, combined with the climatology surface temperatures to calculate a monthly mean k_w and B. Due to the large uncertainties and inter-annual variability associated with this climatology the oxygen inventory and gas exchange

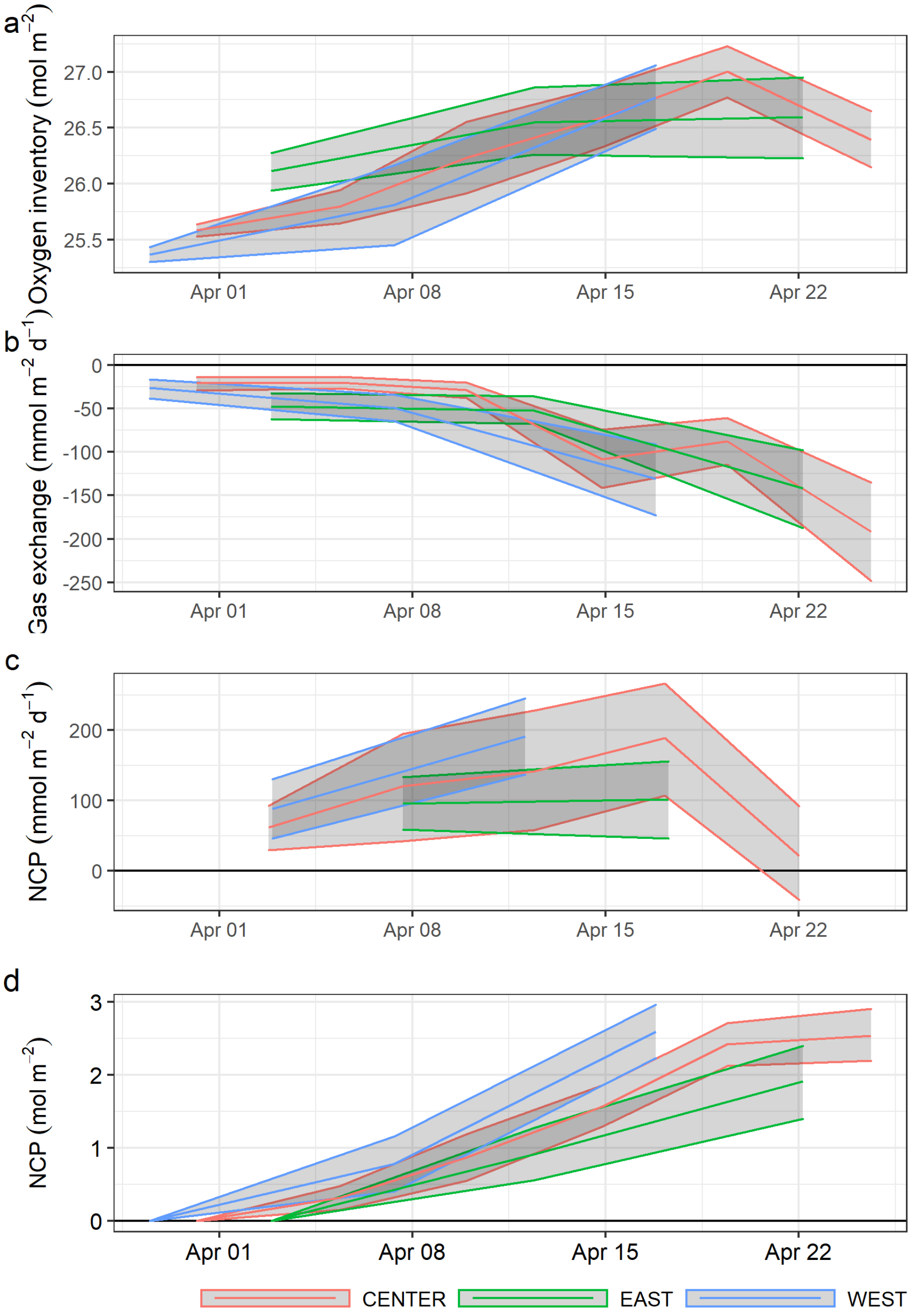

Figure 5.3.13: AE7 sg602 oxygen mass-balance, with transect split into 3 regions, shaded areas represent 95 % credible interval. **(a)** oxygen inventory for each of the three regions, **(b)** instantaneous gas exchange (>0: into the ocean), **(c)** water column integrated NCP, the values are plotted based on t_0, given NCP is calculated between t_0 and t_1, **(d)** cumulative water column integrated NCP, these are plotted with $t_0 = 0$.

is highly uncertain; at the centre of the AlterEco transect the mean error in the oxygen concentration is 14 mmol m^{-3}. As such it is not possible to make any definitive statement of the net community production from the climatological data. Our observations in April 2019 show a clear departure from the climatological 95 % credible interval.

Bozec et al. (2006) in 2001-2002 used ship based nitrate draw-down and DIC inventories to calculate NCP for the ICES boxes within which our study region resides. ICES box 4 comprises the top 30 m and box 14 comprises the remaining water column. This is a large area which spans the majority of the central North Sea, not just the region north of the Dogger Bank. NCP calculated from DIC frequently exceeded that calculated from nitrate draw-down. For further comparison, their monthly (assumed 30 d) DIC based estimates for the relevant boxes are combined and scaled in table 5.2 using a standard O:C ratio of 1.4 (Laws, 1991), While some elements of the seasonal cycle appear similar, with large positive NCP during March and April, we see substantially smaller (near zero) NCP for the winter months compared to the large negative fluxes observed by Bozec et al. (2006). Bozec et al. (2006) do not provide uncertainties, and much of this disparity is likely due to integrating over large temporal and spatial scales, given our analysis indicates significant differences in NCP over a small fraction of the area which comprises the ICES box.

5.4.2 Nitrate inventory

A previous deployment of the Seaglider integrated nitrate sensor by Vincent et al. (2018) saw a surface mixed layer consumption of $-4.3\,\mathrm{mmol\,m^{-3}}$ over 21 days (2015-04-04 to 2015-04-25, $0.2\,\mathrm{mmol\,m^{-3}\,d^{-1}}$) in the Celtic Sea. By contrast we observe surface mixed layer nitrate consumption of $-4.5\,\mathrm{mmol\,m^{-3}}$ over 8 days (2019-04-08 to 2019-04-16, $-0.56\,\mathrm{mmol\,m^{-3}\,d^{-1}}$) at the Eastern end of our transect. Using 40 m as our integration depth (fig. 5.3.11) we see an initial inventory of $(215 \pm 6)\,\mathrm{mmol\,m^{-2}}$ drawn down to 0 between 2019-04-08 and 2019-04-16, a least squares fit results in a nitrate draw-down rate of $(-20 \pm 4)\,\mathrm{mmol\,m^{-2}\,d^{-1}}$. Total NCP for this same section of the water column, during the same period is estimated as $(1.9{\pm}0.1)\,\mathrm{mol\,m^{-2}}$, which equates to a O:N ratio of 8.7, which is close to the traditional Redfield ratio (8.6, Li and Peng (2002)). This is consistent with new production being approximately equivalent to NCP for the 2019 spring bloom, with remineralisation having little influence on the overall budget. By contrast Alkire et al. (2012) report a O:N ratio

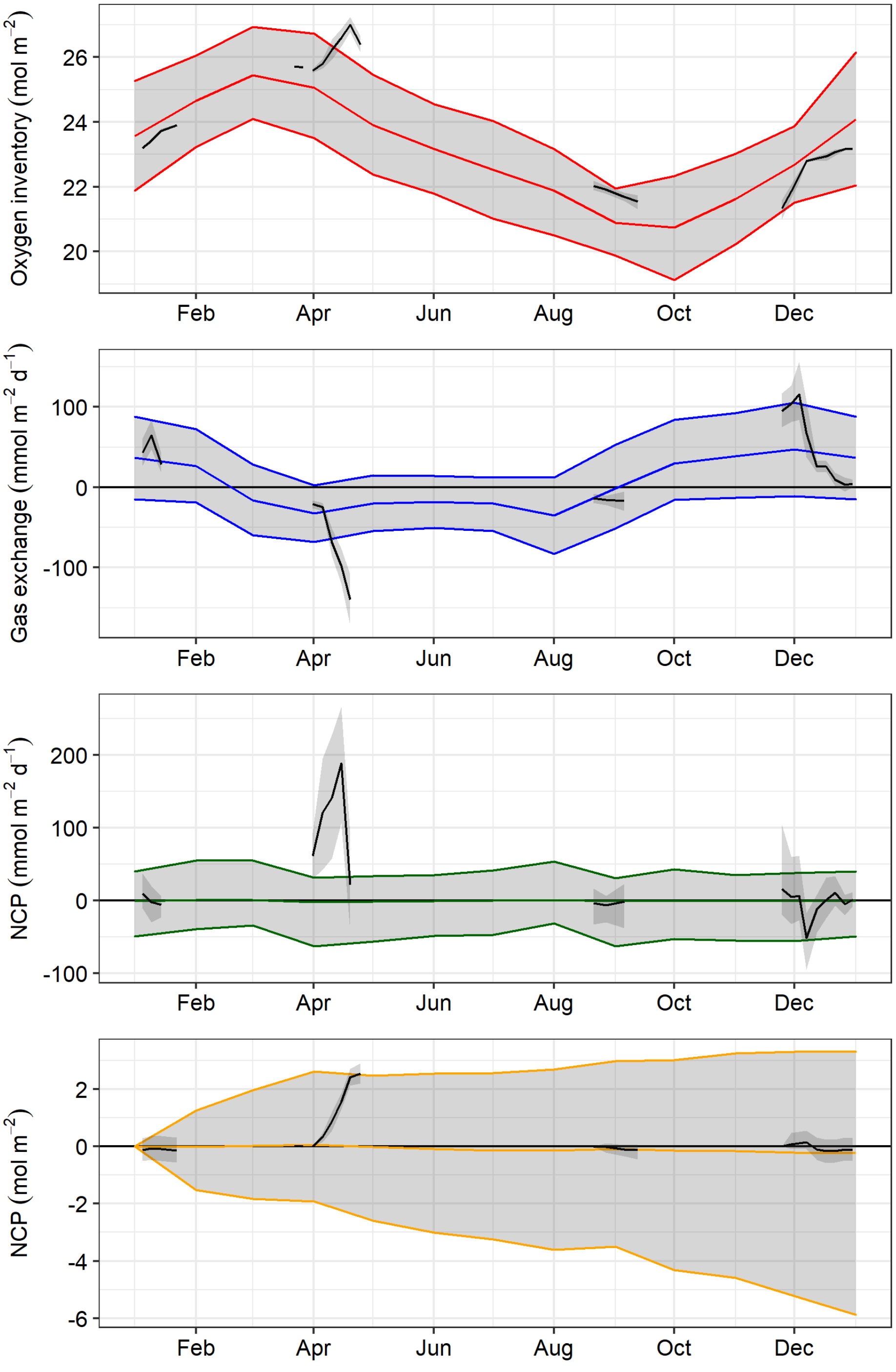

Figure 5.4.1: Air-sea gas exchange, and annual oxygen mass balance at the centre point of the AlterEco transect as predicted based on the North Sea Biogeochemcal climatology. Glider data from AE1, AE2, AE4 and AE7 is overlaid in black

Table 5.2: Central North Sea DIC-based NCP from Bozec et al. (2006) for the ICES regions which contain the AlterEco transect. NCP is expressed in terms of oxygen equivalents, using an O:C ratio of 1.4, in units of $\mathrm{mmol\,m^{-2}\,d^{-1}}$. Box 4 and 14 correspond to the surface and bottom water column of the same region, the sum of which is also shown

Month	Surface (Box 4)	Bottom (Box 14)	Combined
1	-9.8	-6.0	-15.8
2	14.4	-5.6	8.8
3	28.0	-5.2	22.8
4	28.0	-9.8	18.2
5	32.6	-33.6	-1.0
6	32.2	-38.2	-6.0
7	28.4	-38.2	-9.8
8	-14.4	13.0	-1.4
9	-5.2	17.8	12.6
10	-5.2	22.4	17.2
11	0.0	-6.0	-6.0
12	-4.6	-6.6	-11.0

of 14 ± 4.8 in the surface mixed layer during the North Alantic spring bloom in 2008.

Salinity is reduced in 2019 compared to March 2018 by 0.1-0.2. Peak nitrate concentrations are very similar between years; $7.5\,\mathrm{mmol\,m^{-3}}$ for 2018-03-27 and $7.4\,\mathrm{mmol\,m^{-3}}$ for 2019-03-29. The stratified bottom water seen at the start of AE1 had a salinity of < 34.3, while the nitrate concentrations were approximately that of winter Atlantic shelf edge waters ($(7.5 \pm 1.0)\,\mathrm{mmol\,m^{-3}}$, Hydes et al. (1999)).

Heath and Beare (2008) suggest an annual new carbon primary production of $c(\mathrm{C}) = (30.5 \pm 3.4)\,\mathrm{g\,m^{-2}\,a^{-1}}$, determined from water column nitrate draw-down for 2000 to 2003. This is calculated for a large ICES region (IVb), which includes both the Dogger Bank, but also much of the surrounding coastal regions. Nitrate uptake was converted to carbon production via a Redfield ratio of 6.625 and the molecular weight of carbon (12). Reversing this conversion provides a comparative annual nitrate-draw down of $(0.38 \pm 0.04)\,\mathrm{mmol\,m^{-2}\,a^{-1}}$. If we assume that the majority of the annual nitrate consumption takes place during the spring bloom and thus scale our 2019 spring draw-down to an annual estimate provides $(0.59 \pm 0.02)\,\mathrm{mmol\,m^{-2}\,a^{-1}}$. We also note the authors report much higher winter nitrate concentrations ($9\,\mathrm{mmol\,m^{-3}}$) than we observe in 2017 and 2018.

5.4.3 Method discussions

Integration of NCP over an entire transect has some conceptual issues. We can determine instantaneous air-sea gas exchange where we have near surface glider oxygen observations, and remote sensing or model meteorological products. To determine the rate of change in oxygen, and infer the various fluxes, we are required to observe the same water twice. As the glider moves into a new water mass we have no information regarding the air-sea oxygen gradient.

To assess the implication of integrating over a patchy transect we construct three 1D synthetic time series consisting of three vertical layers; the SML, BML and thermocline. These are driven from varying initial conditions with limited surface production, large production in the thermocline and only respiration in the BML (fig. 5.4.2). Production is assumed to be on a diel cycle while respiration is constant. An artificial glider track then samples across these time series moving smoothly from one "region" to another. These data are designed to mimic those seen within the observed data set.

Using these data in our NCP analysis reveals that large anomalous values for the instantaneous NCP can be generated by the glider moving between water regions. It is only in exceptional circumstances that these effects "balance-out", that is to say, the number of transects must be equal and the horizontal structure must be maintained between transects.

AE4 sees the glider move from bottom water with oxygen concentrations in excess of 275 mmol m^{-3} to less than 250 over 34 km. The return transit allows us to confirm that this apparent change in observed oxygen is almost entirely controlled by horizontal variation. This is contrasted with the relatively modest change of 10 mmol m^{-3} over 32 km seen by Queste et al. (2016) in 2011. The large rates seen in the 2011 study could simply be artefacts created by the glider moving into a low oxygen region. We would argue it is thus not possible to assume horizontal spatial homogeneity within this region, which makes assessment of bottom oxygen consumption rates along a transect challenging. Tackling the horizontal variability by splitting the analysis does introduce additional uncertainty in the form of infrequent sampling.

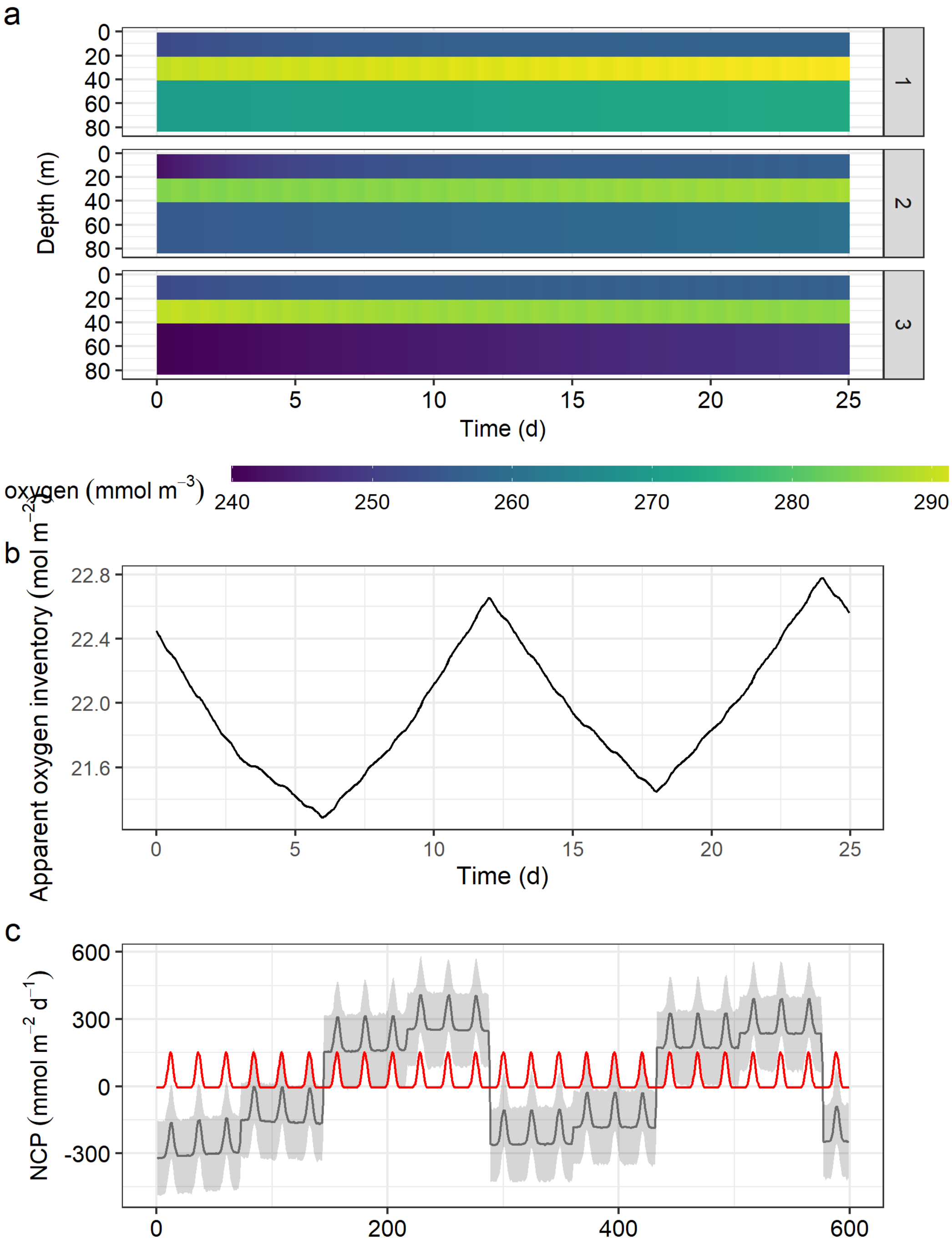

Figure 5.4.2: Simulated “summer” data, **(a)** oxygen concentration within each of the 3 vertical layers at the 3 spatially distinct regions. **(b)** apparent oxygen inventory observed by the simulated glider as it traverses between each of the regions. **(c)** apparent NCP due to the movement of the glider in black, either 95 % errors shown in grey, true value of NCP shown in red

Air-sea gas exchange is at least as variable as the local winds, and production is typically patchy. Our analysis is forced to assume that NCP is constant between observations, but we know this is not the case as production is only possible during the day. These between time step variations likely bias our gas-exchange estimate in either direction as we calculate it against both mean winds and the "wrong" air-sea oxygen gradient.

5.4.4 Are horizontal fluxes important to the mass balance?

While it's clear that horizontal heterogeneity is an important consideration for NCP estimates in this region as the gliders traverse difference water masses, what are the implications for horizontal advection for our 3-region analysis? The AMM15 currents agree well with historic ADCP data collected on the Dogger Bank so we use these modelled currents to describe the horizontal movement of water in this region. However, the semi-Lagrangian nature of the Seagliders makes determining the horizontal oxygen gradients challenging in the absence of a geographically static reference observations, or a network of 3 platforms. It also appears the length scale for the horizontal oxygen gradients is generally much shorter than our transect.

A crude estimate from the Waveglider and Seaglider time series suggests that in summer surface water horizontal gradients are between $0.1\,\mathrm{mmol\,km^{-4}}$ to $0.3\,\mathrm{mmol\,km^{-4}}$. This is calculated by subtracting the mean oxygen concentration from each transect and comparing change in oxygen with distance along the transect (see also figure 5.3.7). We also compared the relative differences in observed surface oxygen concentrations between the AE3 Seaglider, Slocum and Waveglider and calculated the horizontal gradients between these three platforms for the periods they are suitably orthogonal to each other; the gradients are assessed to be $<0.4\,\mathrm{mmol\,km^{-4}}$. Given the residual surface currents are typically $\mathcal{O}(1\text{ km d}^{-1})$, we estimate the horizontal surface fluxes to be $<24\,\mathrm{mmol\,m^{-2}\,d^{-1}}$. This is a fairly large flux compared to our gas exchange and NCP estimates (fig. 5.3.6), and for the winter periods would be the largest flux. Taking AE4 as another example, BML oxygen varies by $30\,\mathrm{mmol\,m^{-3}}$ over 60 km, indicating a BML horizontal gradient of $0.5\,\mathrm{mmol\,km^{-4}}$. However, BML currents are very small and so the horizontal BML fluxes are negligible. During the spring bloom, the rapid temporal changes in oxygen inventory make determining horizontal gradients from a single vehicle impossible.

Bozec et al. (2006) calculated bulk horizontal advection terms, based on 10 year mean water bass transports, and determined that a 50 % change in their horizontal advection term resulted in only a 2 % change on their annual DIC based NCP estimate, which increased to 5 % for the spring bloom periods. Overall the horizontal dissolved inorganic carbon flux was determined to be between $0\,\mathrm{mmol\,m^{-3}\,d^{-1}}$ to $150\,\mathrm{mmol\,m^{-3}\,d^{-1}}$, with the largest advective flux occurring in August. Große et al. (2016) and Rovelli et al. (2016) both suggested that advection has a small effect on bottom oxygen dynamics within most of the North Sea. However, on a larger scale, global modelling studies have shown that horizontal mixing is important in controlling deoxygenation (Bahl et al., 2019). Alkire et al. (2014) argued that for the North Atlantic, advection cannot be ignored when dealing with temporal scales of $<$ 1 month or spatial scales $<$ 20 km.

5.4.5 Recommendations when designing glider-based oxygen monitoring programs

Results from the AtlantOS study (Palmer et al., 2018) drew attention to the issues of calibrating oxygen sensors with glider based campaigns in dynamic regions. In the Celtic Sea, it was shown that only CTDs data within 2 km and 3 hours of the glider position were suitable for calibration of oxygen sensors. Oxygen measurements were compared in density space (as opposed to using depth) with the nearest glider profiles. This is of course only useful if the calibration of the glider CT sensor is not in question. Even within these strict criteria, surface oxygen concentrations were often decorrelated between platforms due to patchiness in phytoplankton distribution and upper ocean meteorological forcing.

Given that calibration is always a problem, as optodes typically drift more in storage and transport than they do in-situ (Bittig et al., 2018b; Bittig and Körtzinger, 2015), efforts must be made to ensure that in-situ calibration is of sufficient quality. Bushinsky and Emerson (2015) demonstrated that in-air calibration is viable with suitable modifications to the gliders, and accuracy of within 0.5 % should be possible.

(Allen et al., 2018) JERICOnext WP5 Task 5.7 outlined guidelines for the delayed mode scientific correction of glider data for operational oceanography. While data treatment principles for the core physical variables were established, biogeochemical parameters are not discussed in detail. In particular issues regarding spatiotemporal alignment of reference CTD casts is not discussed. Oxygen sensors are simply harder to calibrate relative to temperature and salinity.

Comparing profiles in T-S space is also the recommendation from SOCIB. Since temperature and salinity controls the solubility of oxygen, comparing profiles based on the saturation oxygen concentrations allows the raw oxygen profiles and the relevant temperature and salinity information to be included in the figure together with the vertical structure of the profile.

There are thus several recommendations that can be made for future programs to improve the quality of oxygen data from glider in shelf sea environments. The overarching argument is that efforts must be made to ensure that both the validation data and glider data are comparable, and that the length scale of the observations are appropriate to the dynamics of the region.

1. Ensuring that optodes are kept wet prior to deployment. Several gliders showed overly high oxygen readings during the first few casts attributed to dry foils. This was confirmed by observing the decline in oxygen over the first few dives and comparisons with coincident gliders. Given the dynamic environment where these gliders are deployed these values could be misconstrued as spatial or temporal variation, especially during productive periods. This would lead to a mis-calibration against reference casts and an underestimate of oxygen concentrations.
2. Optodes fitted to Seagliders with fast “F” type foils should be mounted with the foil facing away from incident light, that is, towards the housing. Light intrusion effects contributed to noisy data on the majority of the deployments. On later missions the UEA gliders had their optodes remounted which provided an adequate solution (Possenti et al., 2020). We note that Aanderaa instruments newer (since Feb 2018) “F” type optodes have a new formulation of the foil which has improved precision and is less affected by light.
3. When recovering gliders the order of operations is important. Ideally when the recovery vessel is nearby, the glider should be commanded to stop diving and await recovery. The vessel should travel to the position of the last dive and immediately perform a CTD cast. Typically operators are keen to recover their glider and the CTD is performed after the glider is brought aboard, this can result in a CTD which is excessively removed from the last glider dive. This is especially true under unfavourable sea states when visually locating the glider can be challenging and time consuming, while strong winds can push the glider far from its last surfacing position.
4. Similarly during deployment, a glider should be tracked closely for a few dives

while the pilot trims the glider flight. During this time several CTD casts should be performed and care should be taken to ensure these CTD casts are close to the glider position. This requires good coordination between the pilots and the field team.

5. Despite overlapping transects the glider fleet made relatively few crossings where their data were sufficiently spatiotemporally close to allow sensor calibration. Pilots should coordinate to ensure comparability, by instructing a glider to hold station for several hours to enable another vehicle to "catch-up".
6. Deployment length, sampling frequency and intercalibration efforts should be scaled to the dynamics of the system. For the North Sea this means shorter more frequent deployments during spring and summer to mitigate biofouling, and longer deployments with lower sampling frequencies during the stable fully mixed winter periods.
7. The practice needed to become proficient with Winkler sample preparation should not be underestimated.

5.4.6 Survey design

The are also important practical considerations for monitoring shelf-sea NCP using gliders. An initial understanding of the spatial scales of variability is vital for determining the mission plan of the glider. Determining the state is relativity easy, but determining the rate from the state observations requires much more information. Mission design must be mindful of the various length scales; if the process of interest is happening much faster than the glider transit time many of the benefits of frequent sampling will be lost. The data will be of similar structure to a synoptic ship survey but with the additional uncertainty associated with optodes rather than Winkler samples.

One possible approach would be similar to that described by Alkire et al. (2014); to operate one glider as a near-Lagrangian platform, with other vehicles quantifying the horizontal gradients. Not only would this enable high resolution calculation of the oxygen inventory changes, but also the determination of the spatial extent of the mass balance and the horizontal fluxes. Put another way, by observing the horizontal gradients we can determine how representative our single location is of the wider area. This information would greatly improve out understanding of how to scale up these observations (Thompson et al., 2017). Typically glider campaigns are designed to answer several science questions and provide an array of data products. Invariably there are trade-offs, since the optimum sampling strategy to observe one process may not be appropriate for another.

Due to the poor inter-calibration of the glider instruments, determination of horizontal gradients using the multiple platforms was not possible. Better pre-deployment comparison of the glider optodes to some stable standard, such as atmospheric measurements taken at the same time while the vehicles are awaiting for deployment, would allow determination of the gradients, even if the absolute accuracy is not improved.

5.4.7 Future opportunities

Diel cycles in total water column inventory can be clearly seen during the spring and summer which suggest that it would be possible to determine gross primary production from the oxygen time series (Nicholson et al., 2015), if the horizontal advection and glider transit signals can be accounted for. Similarly the nitrate sensor used here has the potential to enable observation of diurnal cycles of nitrate uptake as per Johnson et al. (2006).

5.5 Conclusions

The routine determination of shelf sea NCP from gliders is promising and within reach. We find that for the spring bloom period in 2019 AE7 our nitrate and oxygen based NCP estimates are consistent, with lower uncertainties than previous work. Glider based monitoring programs can provide all of the necessary information for accurate determination of NCP, given appropriate consideration to sampling scales. We note that none of the recommendations we have outlined carry significant cost implications and some could even be argued to be common sense, nevertheless we believe that many of these have been overlooked.

Chapter 6

Synthesis and conclusions

6.1 Platforms for monitoring shelf sea oxygen dynamics

Chapter 3 used an oxygen mass balance to determine that the Warp SmartBuoy site is probably annually net heterotrophic. However, uncertainties introduced by an unconstrained advective flux are significant. Of the constrained uncertainties for short term measurements the temporal integration of the oxygen inventory was the largest source of uncertainty. While over longer periods persistent bubble supersaturation was shown to introduce a large bias into cumulative values. In Chapter 4 bottom mixed layer oxygen consumption was determined through two novel techniques. Additionally the statistical model technique enabled the quantification of the advective fluxes using data from the lander ADCP. Bottom mixed layer oxygen consumption was found to be broadly similar to the incubation studies, although the incubations miss much of the short scale temporal variability. In Chapter 5 Seagliders were used to determine oxygen and nitrate inventories. The two methods provide consistent values for production during the spring bloom. These data revealed a high degree of horizontal heterogeneity which present a challenge for calculating NCP at high temporal resolution. It does however provide useful insight into designing future programs.

This thesis has thus explored shelf sea oxygen mass balances from buoys, seabed landers and submarine gliders. Within this chapter we briefly look at some other platforms which can be used for time series based oxygen mass balances. We then bring this together to provide a conceptual ideal observation framework to enable the best possible determination of shelf-sea oxygen dynamics and the associated NCP signal.

6.1.1 Ferrybox

Ferrybox systems which comprise automated sampling equipment fitted to a volunteer observing ship (VOS), so called ”ships-of-opportunity”, can offer another low cost approach to oxygen monitoring (Hydes et al., 2009). Commercial ferry routes, depending on their length, can offer reasonable temporal and spatial coverage, and can be used to derive NCP estimates (Ostle et al., 2014). As with glider based monitoring, there are trade-offs when using a single observation platform, increases to spatial coverage always come at a cost of temporal resolution. Ferrybox based estimates are heavily reliant on using modelled or climatological mixed layer depth values, as the ventilated volume can not be determined in-situ. While there is little doubt that oxygen optodes can be well calibrated and fully represent the water being observed (Hydes et al., 2009), there is a concern that the water being observed may not be fully representative of the external environment. Juranek et al. (2010) demonstrated that biofouling of underway seawater lines can significantly consume oxygen and thus bias oxygen observations. Research vessels can perform comparative CTD casts to validate the underway data, but for more typical VOS this is not possible. In addition, most VOS do not have a dedicated seawater inlet and thus the optode is typically mounted within the sea chest; a large seawater reservoir used to supply seawater for engine coolant, toilets and fire fighting. This large volume increases the residence time of the water, such that consumption and equilibration processes can bias the observed oxygen concentration. A further issue is the possible changes to the apparent oxygen concentration caused by the physical motion of the vessel. Wave breaking, vertical mixing and bubble injection is known to be a significant control of the oxygen concentrations (Woolf et al., 2007; Liang et al., 2013) and ship motion can induce substantial vertical mixing and bubble injection (Terrill and Taylor, 2015; Nylund et al., 2020).

6.1.2 Liverpool Bay SmartBuoy

The Warp SmartBuoy site from Chapter 3 represents a fairly simplistic system relative to other coastal sites. Within the same UK SmartBuoy program the Liverpool Bay buoy site represents a significantly more challenging environment for monitoring (Panton et al., 2012). As a macrotidal estuary with a spring tidal range in excess of 10 m, the region experiences one of the largest tidal ranges on Earth (Polton et al., 2011). The bay experiences a complex circulation which varies between well-mixed and vertically stratified conditions dependent on the neap–spring cycle and prevailing weather conditions (Palmer, 2010). For the majority of tidal cycles the bay alternates between vertically mixed and stratified. During these periods strong tidal current flow interacts with a persistent freshwater-induced horizontal density gradient which produces strain-induced periodic stratification (SIPS) (Palmer and Polton, 2011). On a falling tide freshwater is advected over the ambient denser water establishing a density gradient. The flow is reversed on the rising tide and the stratification breaks down. SIPS is the dominant steady state whilst enduring stratification exists for only 21 % of the year and full mixed periods less than 1 % (Palmer and Polton, 2011).

The site has been the subject of extensive high resolution numerical modelling (Polton et al., 2013). While these studies have provided important insights into how the bay behaves, and demonstrate the frequency and magnitude of mixed layer and density changes, they do not provide the accuracy needed for determining an oxygen mass balance. The models under or overestimate the degree of stratification, and frequently predict a stratified water column when observations show mixed, and vice versa. Capturing these dynamics is important, as these physical forcings have a profound effect on the biogeochemical cycling within the bay (Howarth and Palmer, 2011) The bay is highly turbid, significantly reducing light penetration, limiting light, and thus production to less than one third of the water column on average (Greenwood et al., 2011). The spring-neap cycle is seen to be the primary control on the formation of the spring phytoplankton bloom, which is in stark contrast with less dynamic regions (Greenwood et al., 2011).

The SmartBuoy was supplemented with an optode-equipped seabed lander, and two mid-water CT sensors. These additional water column measurements demonstrate these dynamics and are highlighted in figure 6.1.1. Upper and lower bounds for a mixed layer depth can be determined from comparisons between the sensors, but the vertical resolution is coarse. Regardless of potential density threshold choice, at best we can determine that the pycnocline lies somewhere between our two observation heights. Given that we are calculating areal integrated fluxes, using volumetric measurements of oxygen, uncertainty in the size of the observed mixed part of the water column has a massive impact on the overall uncertainty; an uncertainty of 5 - 10 m represents an overall mass balance uncertainty of 20 - 45 % for a water column only 22 m deep.

From the buoy's perspective the water column is apparently stratifying and remixing on each tide during SIPS, while in actuality it is observing two water masses which are passing each other. As such it is incorrect for this cycling to be parametrised as an entrainment or a mixing process as the two layers remain distinct throughout the tidal cycle, although one layer is removed from contact with the atmosphere and will undoubtedly undergo some mixing with the other water mass. As these water masses move past the buoy we are presented with a similar situation to our glider observations in Chapter 5; our water mass of interest is no longer being observed, and we do not know the conditions of our water mass when it is not in our observation window. Our high resolution time series is no longer high resolution. Further complexity is added as the combined riverine plume meanders relative to the Liverpool Bay buoy such that sometimes the buoy is not within the plume. Thus the plume, which is formed from the confluence of several rivers, varies in position dependent on freshwater inputs and prevailing weather (Palmer, 2010). This contrasts with the Warp buoy, where the flow past the buoy can be reduced to a one dimensional in-out flow regime as in Chapter 3 (Hull et al., 2016). On short timescales freshwater forcing is characterised by high intensity but short duration rainfall events (Palmer, 2010), as such salinity is not viable as a tracer for a water mass.

A prior study estimated NCP by treating the Liverpool Bay buoy observations as a continuous half-hourly time series, ignoring tidal advection, assuming a fully mixed water column and neglecting the influence of SIPS on air-sea gas exchange (Panton et al., 2012). The oxygen mass balance and incubations both supported the conclusion that Liverpool Bay is a net sink for CO_2. However, the assumption of a fully mixed water column was thought to introduce a 20 to 25 % uncertainty in the NCP estimates, based on the frequency of stratification over a typical year. As with the Warp SmartBuoy the observed oxygen concentration is strongly controlled by tidal advection (fig 6.1.1) and as such treating the observations as representative of a single water mass would mean these tidal forcings would incorrectly be interpreted as NCP.

We see that even with an abundance of good quality data it is still sometimes extremely difficult to accurately determine the size of the ventilated volume, and to ensure that repeat observations are made of a single representative water mass. A Fourier based approach of Cox et al. (2015) similarly struggles to provide useful estimates as this assumes the volume of the observed water mass is both known

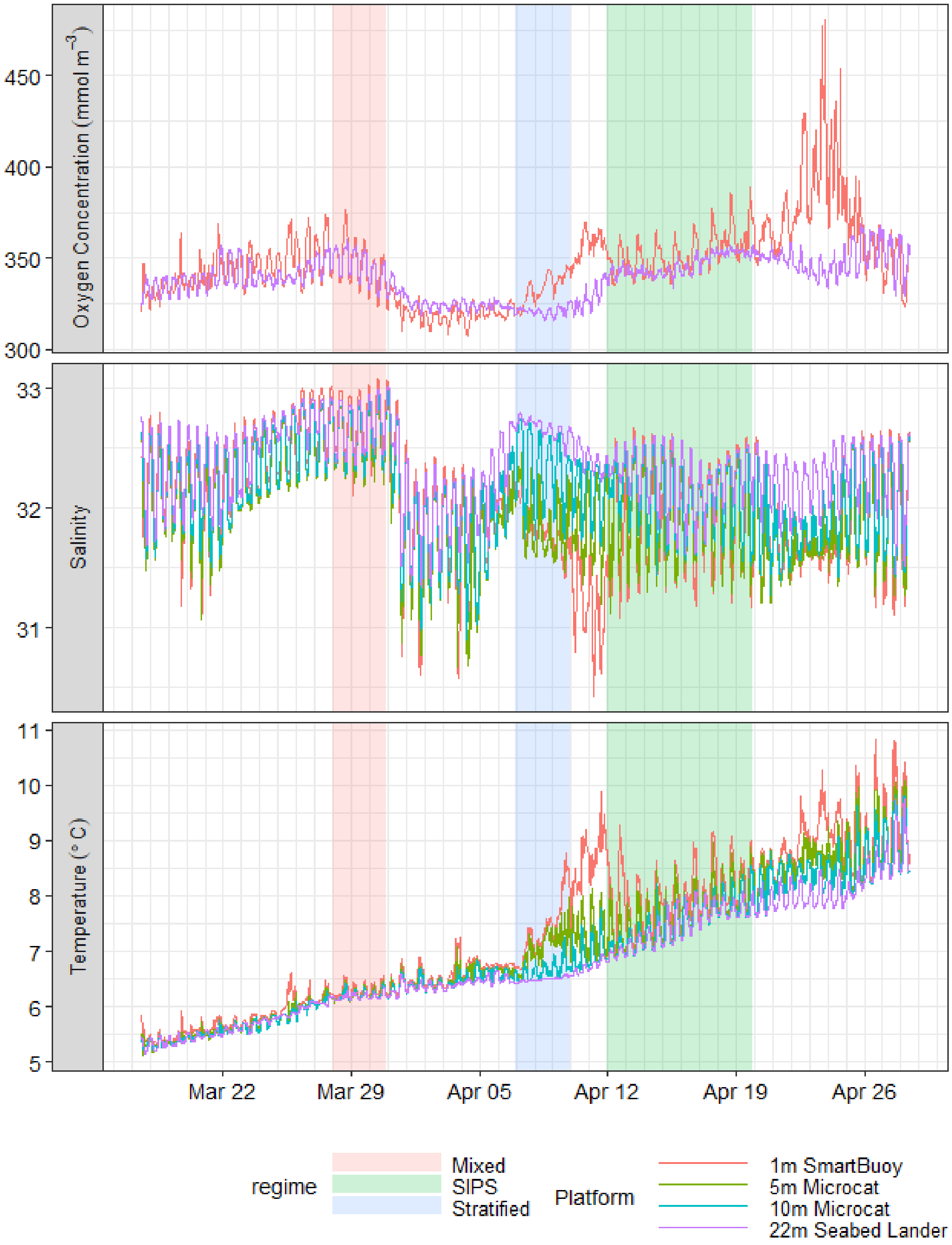

Figure 6.1.1: Observations from Spring 2008 at the Liverpool Bay SmartBuoy monitoring site, with the three stratification regimes highlighted.

and constant.

6.2 Future improvements to NCP monitoring

The studies presented within this thesis are all attempts at exploring the local oxygen dynamics at finer spatial or temporal scales than have previously been studied for those regions. We quantify key physical and biological oxygen fluxes and highlight the limitations and areas for improvement when using a particular platform for monitoring NCP. We find that historic datasets which were not designed for oxygen mass-balance NCP estimation can still be used to gain new insights into shelf sea oxygen dynamics (Chapter 3). However, we demonstrate that careful design of an observational-analysis model, tested against simulated data, itself built using our best knowledge of the physical processes is preferred for robust NCP estimates (Chapter 5).

As described by Bean et al. (2017) the "total ecosystem approach" is anticipated to establish a dynamic ecosystem model which presents a coherent view of the current state of the system, and can then be used for predicting ecosystem change into the future. Studies such as those presented in this thesis are required to verify the state and parametrise the relationships within such a model. Monitoring initiatives do not have the resources to directly observe an entire sea, and as such the extrapolation of small scale studies is required to quantify shelf or regional scale nutrient or carbon fluxes (Thompson et al., 2017). These small scale studies can also discover new dynamics which would be missed with a more coarse study (Wihsgott et al., 2019).

Assimilating high resolution observational data, with associated uncertainties, onto a coarse model grid is not a trivial task. Physical processes are generally well described by regional coupled biogeochemical models, and the assimilation of temperature and salinity observations is becoming routine (Aldridge et al., 2017; Graham et al., 2018; Meier et al., 2019). Bringing oxygen concentration, and other biogeochemical parameters into the assimilation is typically more challenging and is a current area of research (Meier et al. (2019), Skákala et al. (2021)).

We have explored the uncertainties associated with the various approaches to constraining the mass-balance, as reducing these uncertainties is an important objective for improving our understanding of shelf sea oxygen (and carbon) dynamics (Legge et al., 2020). As many other studies have noted (Emerson and

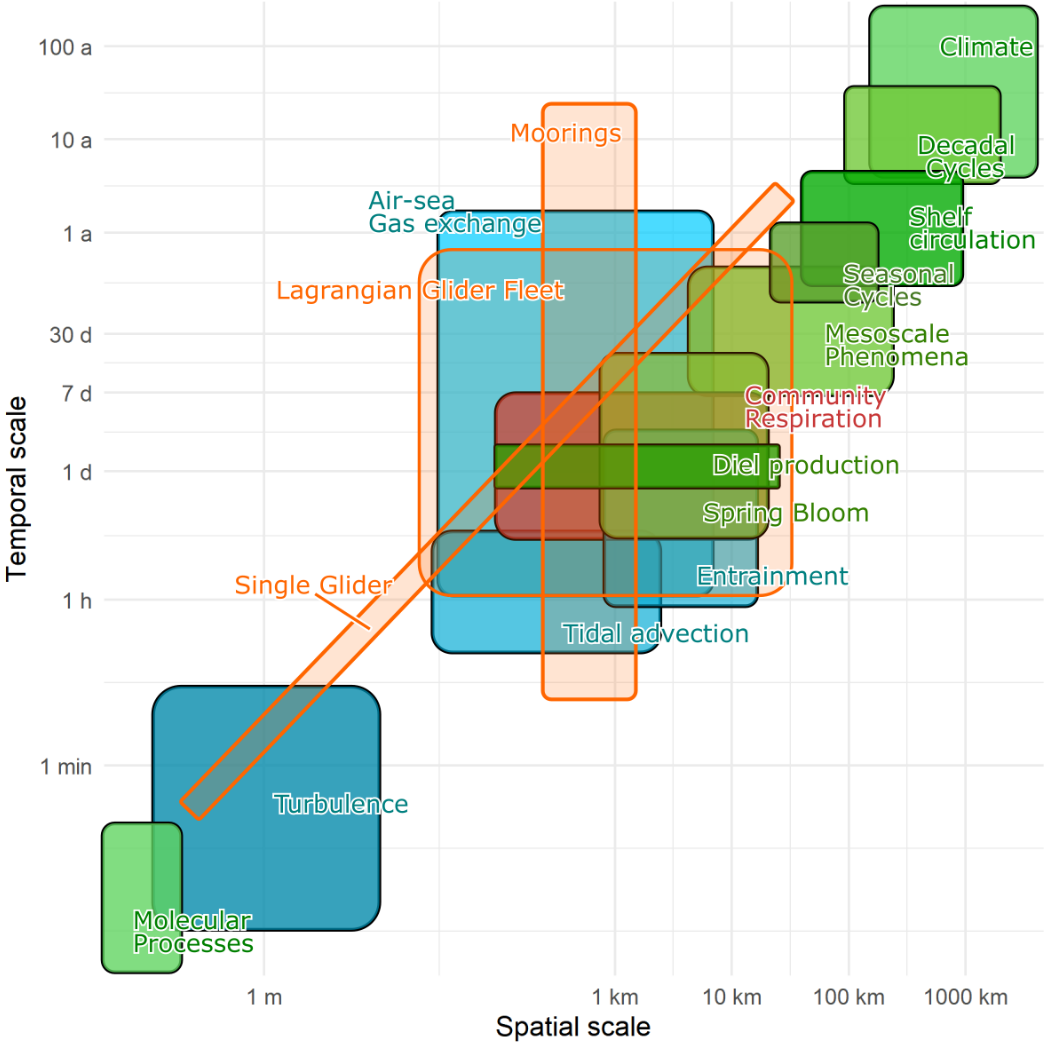

Figure 6.2.1: A Stommel diagram indicating the various temporal and spatial scales the processes important to the oxygen mass-balance act over. The temporal and spatial scales of three observational frameworks are also indicated. We see that depending on the mission design a single glider can observe several of the shorter term processes, but will struggle to observe all of them at the same time. Mooring based approaches are limited in their spatial extent. A Lagrangian glider fleet concept could encompass more of the critical temporal and spatial scales needed to determine the most important drivers of the oxygen dynamics.

Bushinsky, 2016; Woolf et al., 2019) air-sea gas exchange is still a large source of uncertainty, a potentially larger and often unquantified source is from the integration of our observations. Figure 6.2.1 brings together the processes which affect the shelf-sea oxygen dynamics over the various spatial-temporal scales. We have shown that as we increase the temporal (using the SmartBuoy and lander) or spatial (using gliders) resolution of our observations, we gain a more complete understanding of the relevant scales of variability. We can then re-target, or re-scale our monitoring efforts to focus on the areas of greatest uncertainty, or most interest. We note that with many of these studies, especially Chapter 5, the extent of the local heterogeneity in oxygen concentrations was not known a priori. Until we start monitoring, and/or until we monitor at sufficiently high resolution, we often do not know if our chosen study area is representative of a larger region, or is a small microcosm within.

6.2.1 Improved state-space methods

As discussed in section 1.6.1, the state-space approach used for the studies in chapters 4 and 5 can become computationally expensive. A fundamental problem of time series analysis is as the time series becomes longer or higher resolution, the number of parameters that must be estimated increases. Furthermore, by design, these parameters are very highly correlated, which makes exploring the posterior density increasingly harder for a MCMC sampler, meaning the computation time does not scale predictably with the time series length. While the models and data within this thesis could be fit within less than 30 minutes on a powerful modern desktop PC (i5-4690K), the time series here are generally short sections of larger time series. Various techniques could be applied to aid the MCMC to take more efficient samples, such as converting the state-space model to use a linear form and using a Kalman filter to derive the log-likelihood. The MCMC sampler can then be used just to estimate the relevant correlation and error matrices in what is known as sequential Monte-Carlo (SMC) (Durbin and Koopman, 2012). Unfortunately, for a gas-exchange based model the k_w term, which can be highly variable, introduces non-linearities which break the assumptions of the filter. Non-linear forms of filter or a particle filter could be used (Durbin and Koopman, 2012). SMC could also perform better where partial information is missing, such as when wind speed information is available but near surface oxygen concentration must be inferred. A further refinement for the AlterEco study would be to incorporate the multiple glider platforms as a hierarchical model (Wikle et al., 2013). Specifically we could treat each glider and sampling region of the time series as extra parameters, and estimate these at the same time. This would explicitly model the variation due to differing instrument calibrations and likely result in better constrained estimates.

6.2.2 A new concept

Taking what we have learned from the studies within the previous chapters we can identify two key requirements for a shelf sea oxygen dynamics (and NCP) focused observational framework.

Firstly, uncertainty in the air-sea gas exchange and inventory changes are typically the largest source of uncertainty. It is beyond the scope of a monitoring program to reduce the uncertainty associated with the k_w term; however the air-sea flux can be better constrained by better determination of the concentration gradient. As we have seen in chapters 3 and 4, the absolute accuracy, as apposed to relative accuracy, of the oxygen measurements is only important for determining the air-sea concentration gradient. Determining the absolute accuracy can also be useful for comparing inventory changes across different platforms, but it is not always essential. Given that optodes measure equally well in-air as they do when submerged (see section 1.5.1), gliders modified to take in-air measurements can both directly measure the air-sea concentration gradient while also being able to monitor and correct drift (Bittig and Körtzinger, 2015; Nicholson and Feen, 2017). The disadvantage to this design is that the optode must now be mounted far away from the rest of the sensor suite and be exposed to increased UV radiation, necessitating the use of a ”slow” foil (see section 1.5.1). We therefore propose for a Seaglider-like glider to have a ”slow” optode mounted at the rear to take in-air measurements, together with a second fast response sensor mounted close to the CT sensor. The less-stable fast sensor can be referenced to the in-air measuring sensor when the glider is in homogeneous parts of the water column. This would grant the benefits of in-air measurements, while also resolving the sharp oxygen gradients often seen.

Chapters 3, 4 and 5 all demonstrated the potential for horizontal heterogeneity to interfere with mass-balance estimates. The movement of shelf sea waters is complex (Polton et al., 2011) and horizontal gradients are often variable (Lehahn et al. (2018), chapter 4 and 5). It is difficult to correct inventory changes for observations made at a geographically fixed point, such as a mooring, without mapping these gradients. Monitoring floats are an ideal solution for moving with a patch of water and making the repeat observations needed for good mass-balance determination

(Alkire et al., 2012). These are not well suited to shelf seas however, as these platforms will necessarily have a short endurance before they drift outside of the region of interest, either to shore or into other territorial waters. We propose a solution in the form of a Lagrangian glider (fig 6.2.2). A Lagrangian glider would be an autonomous vehicle capable of behaving as a buoyancy glider and as a drifting float. It can move with a patch of water and make the repeat observations needed for good mass-balance estimates, while also place itself back on station when it has drifted outside of the region of interest. This glider could serve as a centre point for supplementary gliders which would then map the extent of the region over which the mass-balance observations are representative. This observational scheme could provide both well constrained local estimates of NCP and GPP, but also provide the spatial context to aid assimilation of these observations into modern ecosystem models.

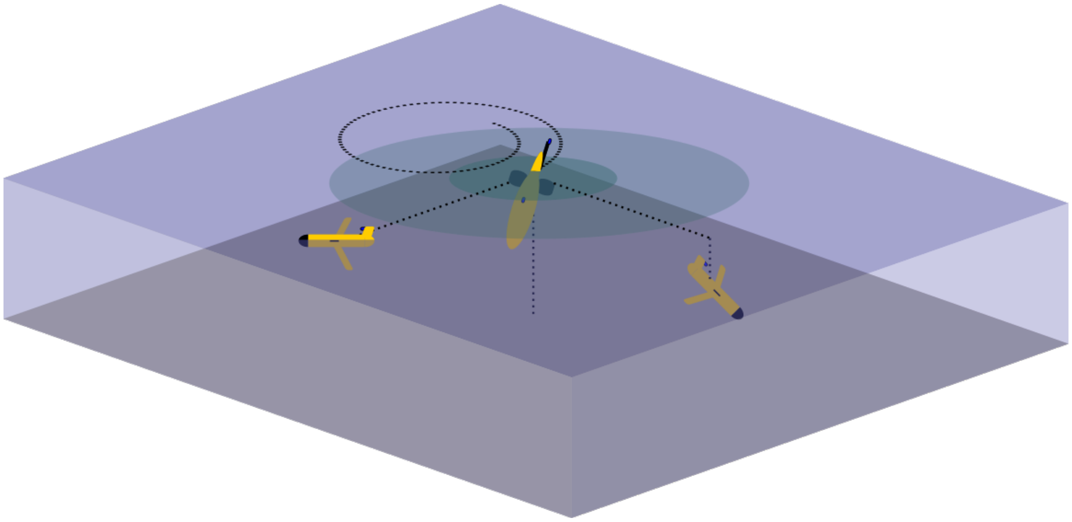

Figure 6.2.2: A schematic demonstrating an idealised shelf sea glider based monitoring concept optimised for determining an oxygen mass balance. A "Lagrangian" glider, which is designed to drift with the surface currents, forms the centre of an observation patch. This glider determines the air-sea flux and inventory changes using in-air referenced measurements. Other gliders travel to and from this centre to map the extent of the patch and determine horizontal gradients.

Appendix A

Chapter 2 supplementary material

$$k_b = \frac{5.5\ U_*^{2.76}}{(S_c/660)^{(2/3)}} \tag{A.0.1}$$

$$\Delta_\mathrm{b} = 1.5244\ U_*^{1.06} \tag{A.0.2}$$

$$F_i = 5.56\ U_*^{3.86} \tag{A.0.3}$$

$$\tag{A.0.4}$$

Where U_* is the frictional velocity defined as in equation A.0.5

$$U_* = \frac{\sqrt{C_\mathrm{D}}U}{\sqrt{1000}} \tag{A.0.5}$$

where C_D is the drag coefficient formulation of Large and Pond (1981) with the high wind speed saturation modification of Sullivan et al. (2012) shown in Eq. (B.1.2).

Appendix B

Chapter 3 supplementary material

B.1 Wind speed validation

Shipborne anemometers data was adjusted to 10 m height using the scheme of Liu et al. (2010). We make the assumption that the surface current is small compared to wind speed and that the atmosphere has near neutral stability. Thus the U_s and ψ terms are not used giving the form shown in Eq. (B.1.1). where C_D is the drag coefficient shown in Eq. (B.1.2).

$$\frac{U_z}{U} = 1 + 2.5\sqrt{C_\mathrm{D}\ln(\frac{z}{10\,m})} \tag{B.1.1}$$

$$C_\mathrm{D} = \begin{cases} 0.0012 & \iff & U \leq 11\,m\,s^{-1} \\ (0.49 + 0.0065U) \times 10^{-3} & \iff & 11\,m\,s^{-1} < U < 20\,m\,s^{-1} \\ 0.0018 & \iff & U \geq 20\,m\,s^{-1} \end{cases} \tag{B.1.2}$$

B.2 Current meter data

Acoustic Doppler current profilers were deployed at the Warp SmartBuoy site between November 2001 and April 2002. Three deployments were made using 1 MHz Nortek AWACs fitted to a Cefas designed seabed lander. A small subset of

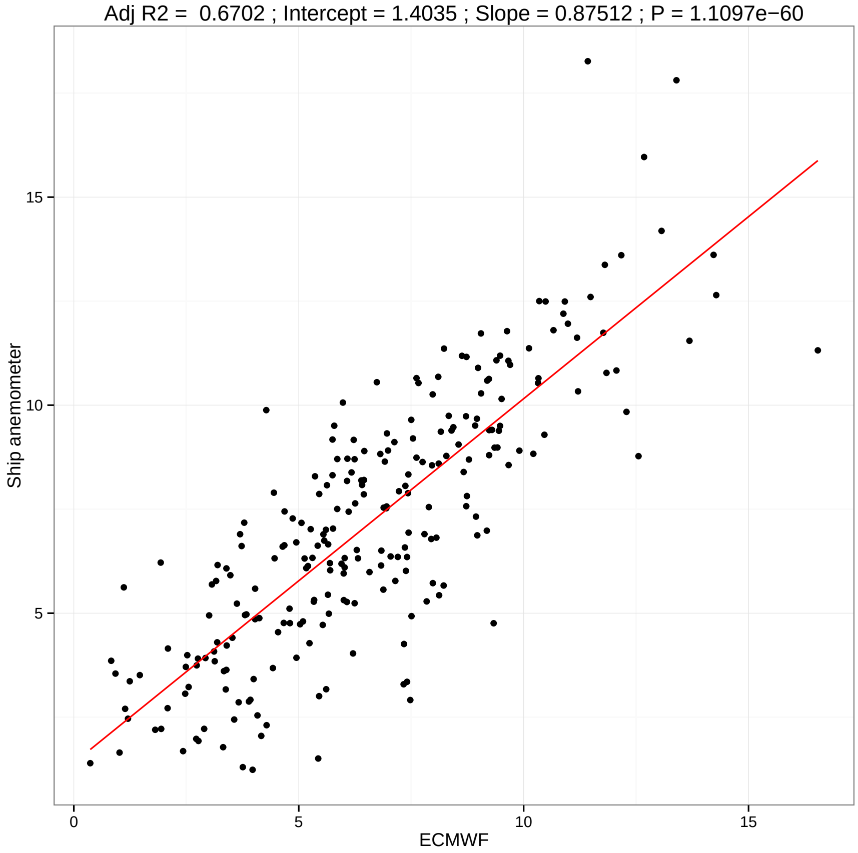

Figure B.1.1: Validation of ECMWF MACC reanalysis 10 m wind speed vs height corrected shipborne anemometer wind speed.

the processed data is presented in Fig. B.2.1.

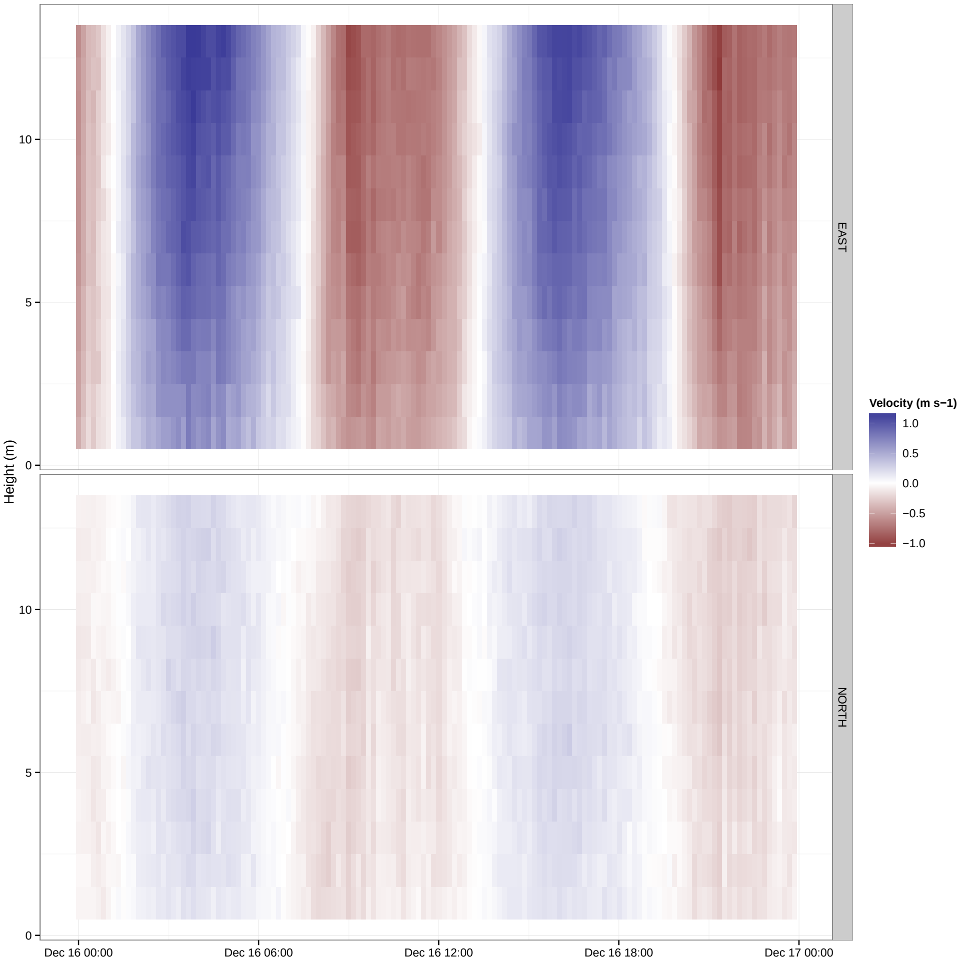

Figure B.2.1: Acoustic Doppler current profiler data from the Warp SmartBuoy site showing the tidally dominated current regime. Top panel vectors for east, bottom panel north.

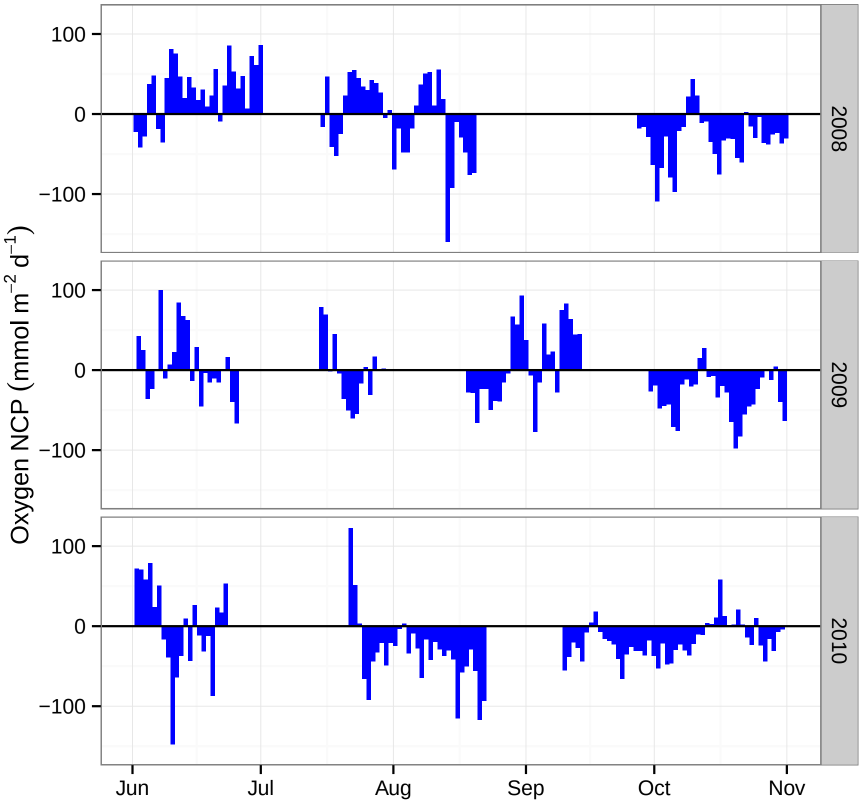

Figure B.2.2: Warp June to October NCP estimates from other years demonstrating no significant periods of net production.

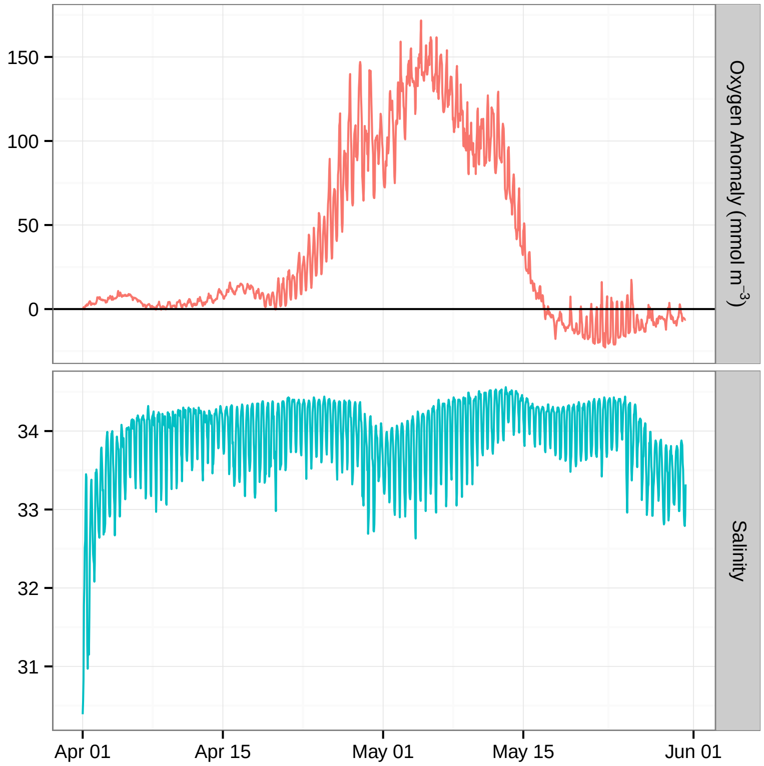

Figure B.2.3: Raw (30 min) Warp SmartBuoy time series showing significant variability in oxygen anomaly (red) and salinity (blue) within each tidal cycle. Here the oxygen anomaly neglects the supersaturating effects of bubbles.

Appendix C

Chapter 4 supplementary material

C.1 Probability model

We define the probabilistic relationship between the observed and predicted oxygen concentration (mmol m^{-3}) in equation C.1.1.

$$\hat{C} \sim \mathcal{N}(C, \sigma) \tag{C.1.1}$$

That is to say, the observed oxygen value $\hat{C}$ is from a normal distribution with the mean C (our prediction of the true concentration) and standard deviation σ.

The time evolution of C is discretized as follows:

$$C_t = C_{t-\Delta t} + u\ \Delta t\ \beta_u + v\ \Delta t\ \beta_v + \Delta t\ \frac{M_{\mathrm{z}} - R}{h_{\mathrm{b}}} \tag{C.1.2}$$

Where Δt is our our time-step in seconds derived from our 30 minute observations. β_u and β_v are the horizontal oxygen gradients (mmol m^{-4}) in the east and north directions.

These parameters are modelled in a multi-level approach (equation C.1.3) as such the estimates for each β are partially pooled ($\bar{\beta}$), so that each estimate contains information which is optimally used to improve all other estimates (Gelman et al. (2017)). Specifically this approach primarily improves estimates during neap tides when currents are weak.

$$\beta_u \sim \mathcal{N}(\bar{\beta_u}, \tau_u) \tag{C.1.3}$$

$$\beta_v \sim \mathcal{N}(\bar{\beta_v}, \tau_v) \tag{C.1.4}$$

The model is run with the following priors:

$$\sigma \sim \text{Cauchy}(0, 1) \tag{C.1.5}$$

$$R \sim \mathcal{N}(0, 1) \tag{C.1.6}$$

$$\bar{\beta_u} \sim \mathcal{N}(0, 5) \tag{C.1.7}$$

$$\bar{\beta_v} \sim \mathcal{N}(0, 5) \tag{C.1.8}$$

$$\tau_u \sim \text{Cauchy}(0, 1) \tag{C.1.9}$$

$$\tau_v \sim \text{Cauchy}(0, 1) \tag{C.1.10}$$

Varying these priors over two orders of magnitude has a minimal effect on parameter estimation. They are weakly regularising and are chosen primarily for improved model convergence. A half-Cauchy distribution is used for the standard deviation (σ) as a weakly regularising prior as per Polson and Scott (2012).

The initial conditions are initialised as the first observation plus normally distributed zero mean noise (ε)(equation C.1.11).

$$C_0 = \hat{C}_0 + \varepsilon \tag{C.1.11}$$

and the following prior:

$$\varepsilon \sim \mathcal{N}(0, 1) \tag{C.1.12}$$

To capture our uncertainty regarding the AMM7 model outputs we apply the following further parametrisations (equation C.1.13, C.1.14). Where $\hat{h_{\text{b}}}$ and $\hat{h_{\text{TC}}}$ are the bottom mixed layer thickness and thermocline thickness observations respectively. Uncertainty in the value of K_z is additionally incorporated into the estimates for the thermocline mixing and bottom mixed layer depth parameters (equation C.1.15). For computational reasons we do not model the vertical diffusion coefficient (K_z) as a time varying parameter, we estimate an average value for each deployment.

$$\hat{h_{\text{b}}} = \mathcal{N}(h_{\text{b}}, \sigma_{\text{b}}) \tag{C.1.13}$$

$$\hat{h_{\text{TC}}} = \mathcal{N}(h_{\text{TC}}, \sigma_{\text{TC}}) \tag{C.1.14}$$

$$k_z = \mathcal{N}(4.5\text{x}10^{-5}, \sigma_{k_z}) \tag{C.1.15}$$

$$C_s \sim \mathcal{N}(\hat{C}_s, \sigma_{C_s}) \tag{C.1.16}$$

Where σ_{b}, σ_{TC}, σ_{K_z} and σ_{C_s} are standard deviations adjustable to our best estimate for each parameter. For this study σ_{k_z} = 0.5 x 10^{-5} mmol m^{-2} s^{-1}.

The above probability model was implemented using the probabilistic programming language Stan (Carpenter et al. (2017)). Stan and its use of dynamic Hamiltonian Markov-Chain Monte Carlo (MCMC) is an extremely powerful tool for specifying and then fitting complex Bayesian models.

MCMC facilitates the simultaneous estimation of both β parameters, thus the horizontal adjective flux, and also R. This is based on the assumption that changes in β and R are on relatively long timescales compared to the tidal signal, and that R can not be negative. This is done while indicating the quality of the model fit in the form of σ, which also accounts for unknown processes not modelled directly, such as instrument noise. σ is thus analogous to the standard deviation of the residuals of a standard linear regression. The model is run several times with varying window sizes, (starting with a single value R and daily β) to determine window sizes which can resolve change in R and β. We have opted for 3 d R varying window and a 12.5 h varying β. These window sizes provide good fits with the observed data and reproduce well smoothly varying changes in β and R with our synthetic data. With shorter windows the model struggles to distinguish sampling error from varying β and fails to converge. With longer windows the model tends to underestimates the dynamics and excessively smooth the signal.

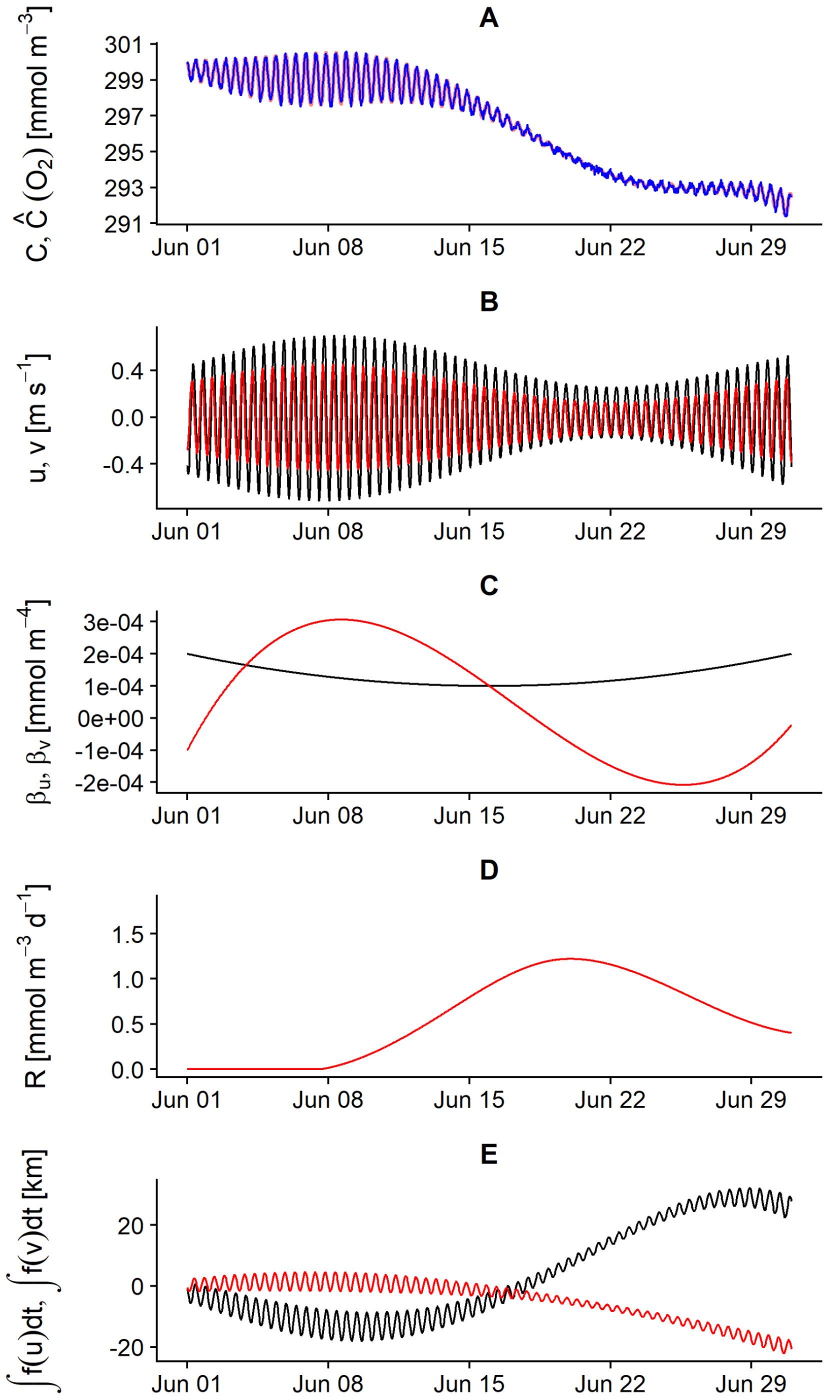

Figure C.1.1: An example of the synthetic data used for validating the probabilistic model

Within the range of window sizes where the model can converge varying window size does not influence the average (integrated) estimates for these parameters i.e. The mean R estimate is within the same uncertainty bounds regardless of window size.

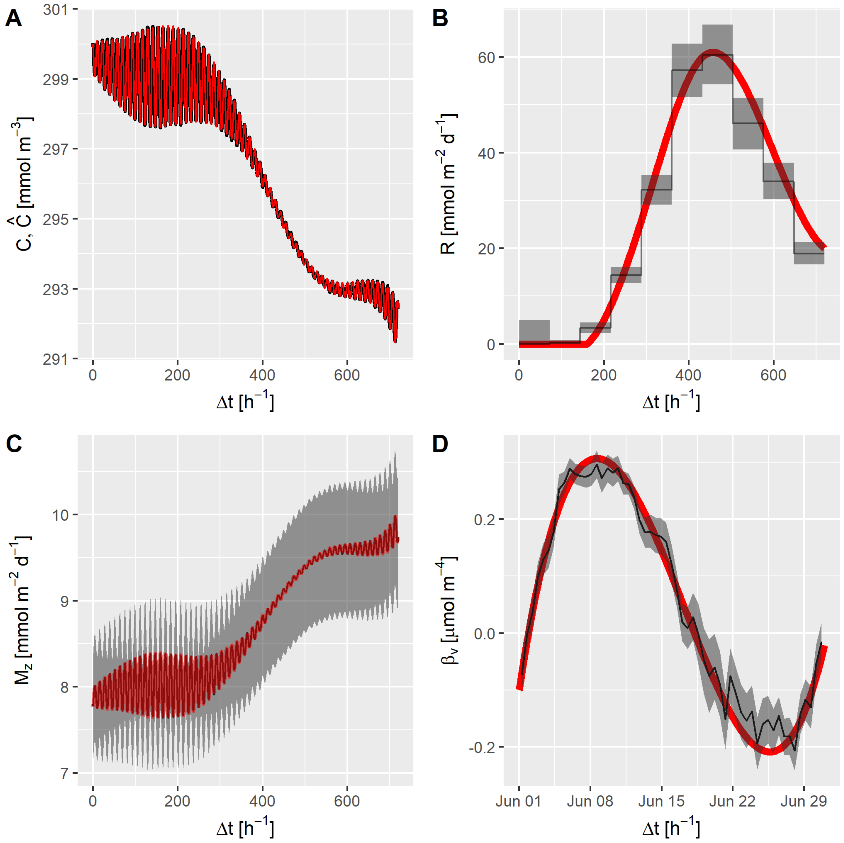

Figure C.1.2: Validation of statistical model against synthetic data. True values shown in red, true + random noise in blue, mean model estimate in black and 95 % credible intervals shown in grey.

Unlike other MCMC algorithms, when Hamiltonian MCMC fails, it fails spectacularly and problems are easy to identify (Carpenter et al. (2017)). The presence of a large number of divergent transitions (> 1% of total samples) is an indication that the model fit has failed. The potential scale reduction factor is another MCMC specific metric which when < 1.1 indicates that all sampling chains have reached a stable posterior distribution, that is to say, the model fit is complete (Carpenter et al. (2017)). No divergent transitions are observed and the potential scale factors for each run are all <1.1. The model fit is further assessed based on σ being a suitably low value close to the expected precision of the oxygen observations (<1 mmol m^{-3}). A graphical posterior predictive check (Carpenter et al. (2017)) is used to further assess the model fit where the modeled state for C is compared to the observations (fig. C.1.2, D.).

Our implementation was tested against synthetic data using the same data generating processes as the model. That is to say we run the model with known parameters (fig. C.1.1), we then check the model can correctly re-estimate these parameters (fig. C.1.2). The diagnostic variables for each of the model runs are summarised in figure C.1.3.

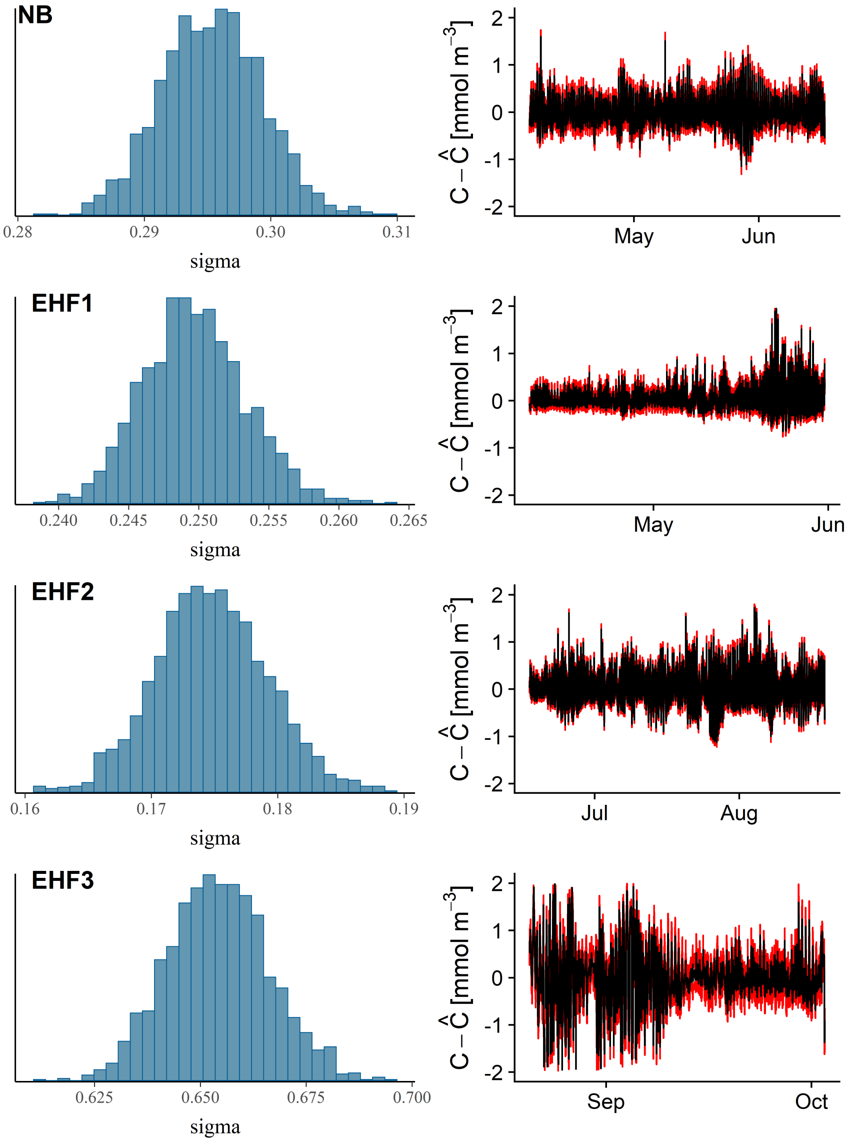

Figure C.1.3: Validation of statistical model for each run. Left panels show histogram for the σ model fit parameter, units are mmol m^{-3}. Right panels show differerence between BML oxygen concentration observations ($\hat{C}$) and the modeled state (C)

C.2 AMM7

AMM7 reanalysis water column temperatures were extracted from the UK Met Office JASMIN archive. These temperatures are provided for 50 depth bins scaled over the local bathymetry (O'Dea et al. (2017)). These bins are closer together near the surface, equating to depth intervals not exceeding 5 m and typically 1 m for the top 60 m. From these data the top of thermocline was defined by a 0.2 °C temperature threshold with a 10 m reference depth (Kara et al. (2000)). The base of the thermocline was defined by the same threshold, with the reference depth being the depth of the lander.

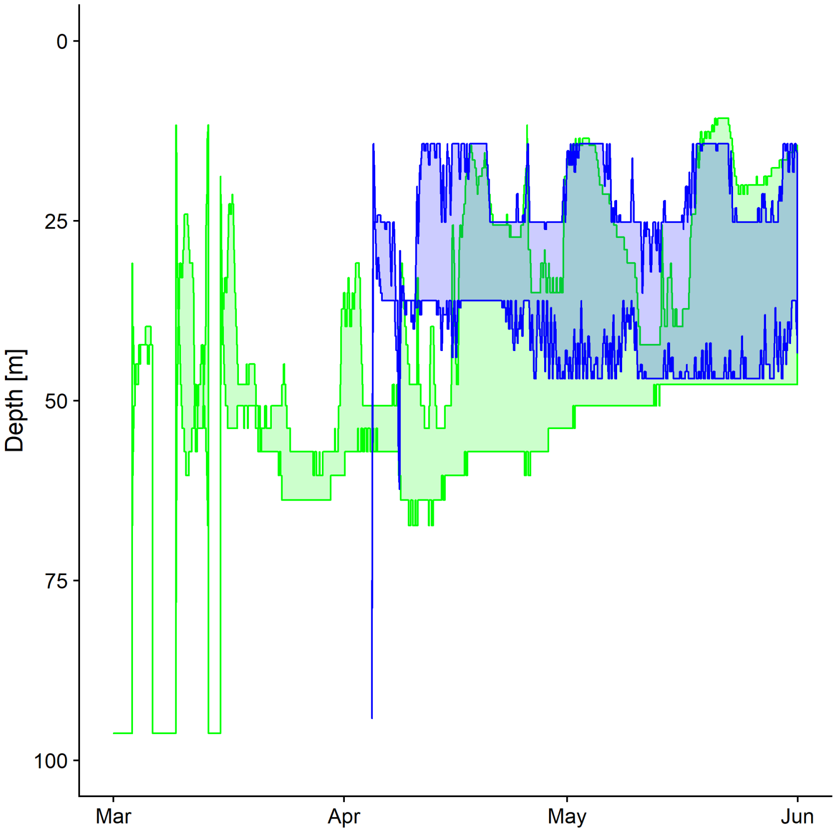

Figure C.2.1: Bottom mixed layer depth calculated with 0.2°C threshold for AMM7 (green) and from the Celtic Deep thermistor chain (blue)

These data were compared to the buoy and thermistor string observations at Celtic Deep (Wihsgott et al. (2016)), The model does not correctly resolve the stratifying period in March, during which there are short lived transient periods of stratification (See fig. C.2.1). However after the 1^{st} of April the seasonal thermocline has fully formed and persists though until late December (Thompson et al. (2017)). We thus restrict our analysis to where the modelled mixed layer depth more closely agrees with the Celtic Deep observations.

Appendix D

Chapter 5 supplementary material

D.1 Glider calibration

The deployment location for the gliders during AlterEco was restricted by the choice of vessel, such that the closest location that could be reached was 110 km from the closest section of the transect (fig. D.1.1). This is by design as deploying these vehicles in a low cost manner, without the expense of research vessels was a primary aim for the project. However, the deployment area was realised to be a frontal region, with strong horizontal gradients. This is exemplified with figure D.1.2 which demonstrates the calibration reference SBE16 CTD, taken at 2017-11-06 12:17 UTC (55.6300 °N, 0.0328 °W) compared to the first few dives from the gliders. The Slocum "Stella" appears to have issues with the conductivity cell, which is resolved after some fast dives to flush the cell (fig. D.1.2 panel b). Figure D.1.2 c shows the severe lag observed with the 4330 optode on the Slocum gliders, this is a combination of the diffusive foil lag as described by Bittig et al. (2018b) and also a "geometric" lag caused by inadequate flow to the sensor. The Seaglider (sg537 "Fin") had a faulty "sticky" pressure sensor for which the first few dives results in the thermocline being clearly misaligned relative to the reference CTD cast (fig. D.1.2 a.). The pressure response during these dives shows significant hysteresis, and appears to "flick" between a typical response and a lagged state, and as such can not be correct with a simple change to offset or gain. After 410 subsequent dives the sensor operates normally normal operation, such that data collected on the transect is of acceptable quality.

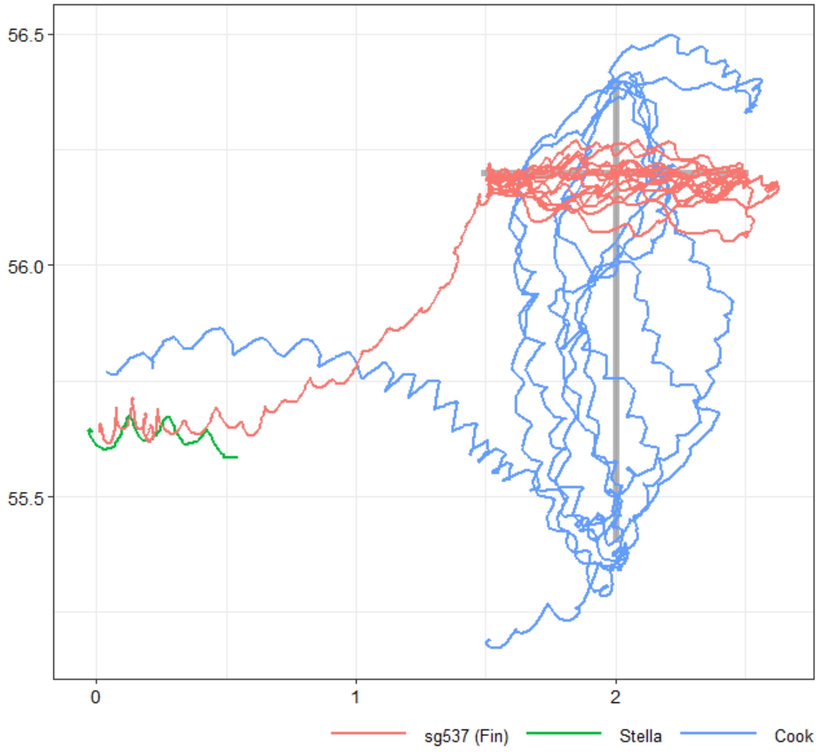

Figure D.1.1: Glider tracks for the AE1 mission, showing the coastal deployment location, the path taken to the transect and each glider's transect occupation. Grey lines indicate the two idealised transects.

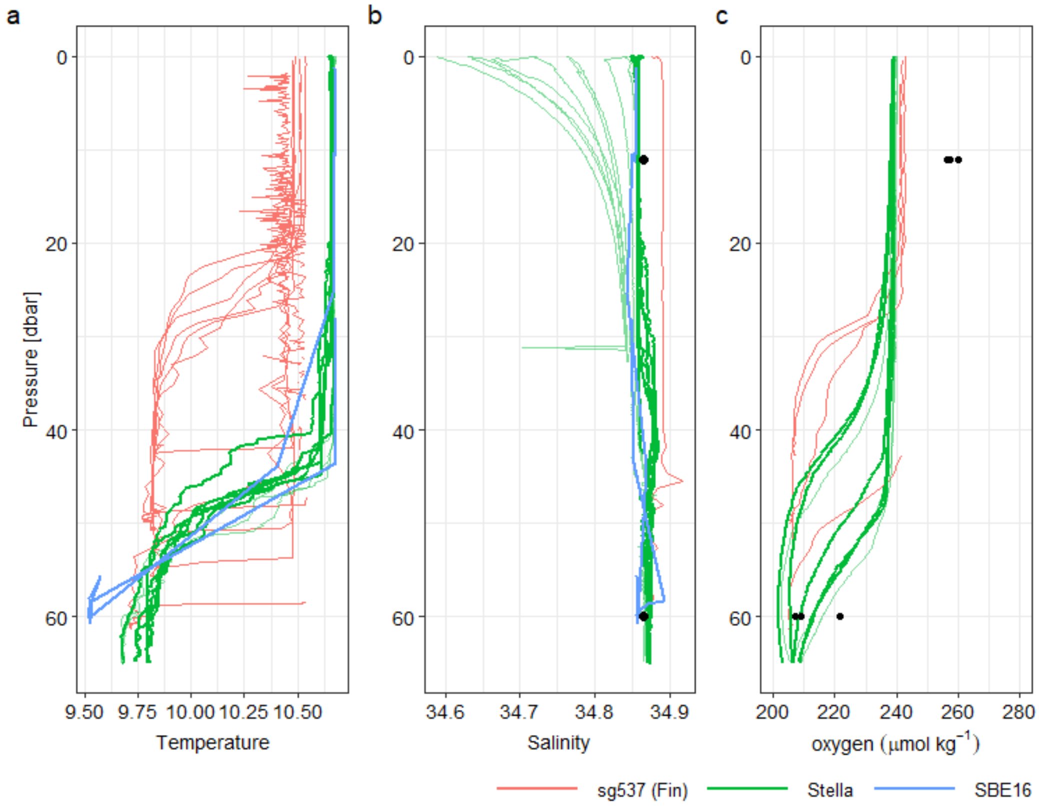

Figure D.1.2: Post-deployment AE1 Seaglider and Slocum casts compared to the calibration CTD, discrete samples (salinity and Winkler titrations) shown in as black circles.

These casts, shown in figure D.1.2, highlight the horizontal variability in both the surface and bottom mixed layers. Upon deployment, the first 8 slocum dives are between 1.3 and 1.8 km from the nominal CTD location, and within 1 hour. This is considered by many researchers to be ”close” (e.g. (Barone et al., 2019)), it is however clearly seen that there are substantial differences in BML temperature between the reference cast and glider. We see from figure 5.3.1 that BML oxygen concentrations are strongly associated with BML, such that it’s not appropriate to use the BML Winkler as a reference for this glider. The glider optode is thus only corrected using a single factor, rather than a slope + offset, on the temperature and salinity compensated oxygen concentration as per Bittig et al. (2018b). The Seaglider closest profiles, seen in the figure, were collected between 3.9 and 4.3 km and within 30 minutes of the CTD cast. Neglecting the known issue with the pressure it is still obvious that the disparity in SML and BML temperatures indicate the Seaglider is in a different water mass, and reference to the Winklers is inappropriate.

Following the emergency recovery of ”Stella” early in the mission, a replacement glider ”Cook” was deployed. The group deploying the replacement glider were not experienced in collecting Winkler samples, and no discrete samples are available for calibration of the glider optode. Following this sg537 was also recovered by a vessel of opportunity, which similarly did not collect any reference samples. It would be unlikely for these to be of value as typically a glider awaiting recovery is not collecting data. Samples were taken on the recovery of Cook.

Adopting a minimum distance-time threshold of 1 km and 1 hour during the mission each of these gliders was spatial-temporally close to one or more of the others, which can be confirmed by visual inspection of the matching profiles. From these comparisons we are present with a set of unknowns: We know the correction factor for Stella at the start of the mission, for Cook at the end, and no information for the Seaglider or for the drift over time for any of the instruments. The comparison ”crossover” between Stella and Fin is on the first day of deployment, so we assume the drift is minimal and can thus determine the correction factor for the Fin a_b at $t = 0$. Translating to a system of equations provides equation D.1.1.

$$\begin{aligned}
a_\mathrm{f} + b_\mathrm{f} t_0 &= 1.044 \\
a_\mathrm{f} + b_\mathrm{f} t_1 &= \frac{n_1}{m_1}(a_\mathrm{c} + b_\mathrm{c} t_1) \\
a_\mathrm{f} + b_\mathrm{f} t_2 &= \frac{n_2}{m_2}(a_\mathrm{c} + b_\mathrm{c} t_2) \\
(a_\mathrm{c} + b_\mathrm{c} t_3) &= 1.0352
\end{aligned} \tag{D.1.1}$$

Where t represents the days since deployment of Fin. $t_0 = 0$ (deployment of Fin and Stella). $t_1 = 17$ (first crossover between Fin and Cook), $t_2 = 50$ (second crossover), $t_3 = 93$ (Cook recovery Winkler samples).

a_{f} and b_{f} are the intercept and slope for Fin oxygen. a_{c} and b_{c} are the intercept and slope for Cook oxygen. m and n are the raw (uncorrected) oxygen concentrations from Fin and cook respectively.

Solving equation D.1.1 provides us with an intercept, equivalent to the correction factor as the start of the mission and a slope which is a time dependent drift correction for both vehicles.

D.2 Optode lag correction

As discussed in section 1.5.1 and 5 standard optodes have slow response time of 25 s. Approaches to overcome these issues revolve around inverse filtering either the oxygen concentration values or the phase values (Bittig et al., 2018b). Bittig et al. (2018b) advocates for τ which is dependent on the boundary layer thickness in-front of the foil. Bittig et al. (2014) provides a model for estimating this boundary layer thickness, based on the Slocum glider platform. Using a minimization algorithm, and some trial and error we find this Slocum based framework can be adapted for Seagliders with a 0.48 scaling factor. Suggesting that the boundary layer is thinner with a Seaglider and the optode thus responds faster. In general we find the Bittig et al. (2018b) approach performs poorly relative the method of Hahn (2013) as shown in figure D.2.1. The Hahn (2013) method is the default used by the UEA Seaglider toolbox (Queste, 2013) and is the method used for Chapter 5. We find the standard τ parametrisation, reproduced in equation D.2.1, performs better than any modification. Figure D.2.1b the Hahn method does still result in some artefacts near the base of the mixed layer where the thermal gradient is strongest. The improvement is still marked compared to either the raw or Bittig et al. corrected profiles.

$$\tau = 14.8 + -0.4(T - 20) \tag{D.2.1}$$

Where T is the optode temperature (°C) and τ is the time constant (s).

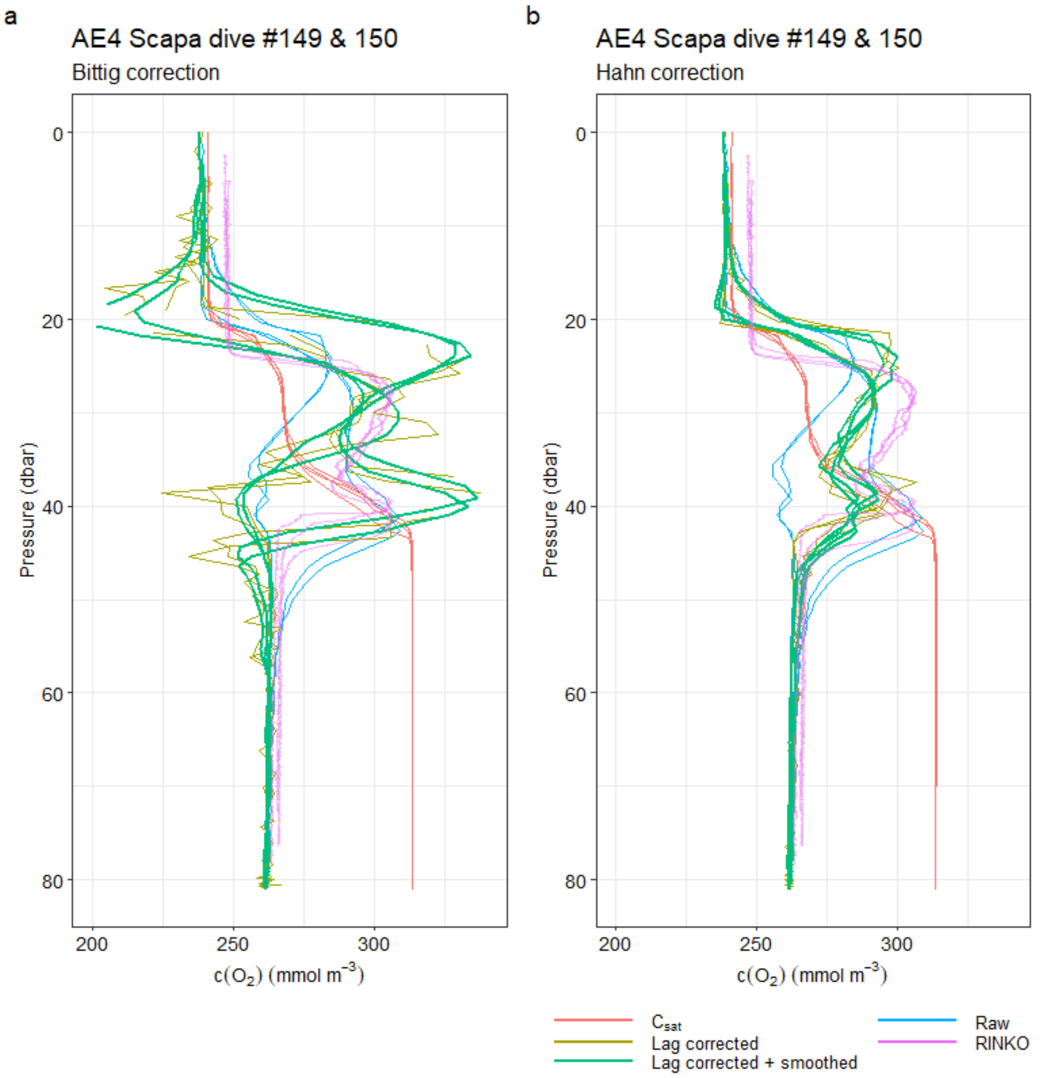

Figure D.2.1: Comparison of two optode lag correction methods using two example profiles from AlterEco Seaglider "Scapa" during August 2018. Smoothing is from a 30 s bandwith kernel smoother, RINKO refers to the RINKO III used on the Cefas Endeavour CTD, a fast responding optical oxygen sensor ($\tau < 1$ s). **(a)** Bittig et al. (2014) method using a boundary layer thickness adapted for the Seaglider. **(b)** Hahn (2013) method

.

Appendix E

List of symbols

- C, oxygen concentration (mmol m^{-3}).
- C_{sat}, equilibrium saturation concentration, the concentration of oxygen expected at a given temperature and salinity and 1013.25 hPa if the water is in equilibrium with the atmosphere (mmol m^{-3}).
- C_{b}, bottom mixed layer oxygen concentration (mmol m^{-3}).
- C_{s}, surface mixed layer oxygen concentration (mmol m^{-3}).
- I, oxygen inventory integrated over some depth (z) or height (h) (mmol m^{-2}).
- z, depth (m).
- h, water column height (m).
- S_c, Schmidt number (dimensionless).
- k_w, water-side air-sea gas transfer coefficient ($\mathrm{m\,s^{-1}}$)
- B, bubble equilibrium fraction supersaturation coefficient (dimensionless)
- P, local atmospheric pressure (hPa)
- P_0, standard sea level atmospheric pressure (1013.25 hPa)
- U, wind speed at 10 m ($\mathrm{m\,s^{-1}}$)
- K_z, vertical (diapycnal) eddy diffusion coefficient (m^2 s^{-1}).
- h_{TC}, thickness of the thermocline (m).

- M_z, diapycnal (cross-thermocline) flux (mmol m^{-2} s^{-1}).
- u, east-west (zonal) velocity ($\mathrm{m\,s^{-1}}$).
- v, north-south (meridional) velocity ($\mathrm{m\,s^{-1}}$).
- A_u, horizontal advection in the east-west (u) direction (mmol m^{-2} s^{-1}).
- A_v, horizontal advection in north-south (v) direction (mmol m^{-2} s^{-1}).
- β_u, horizontal oxygen gradient in the east-west (u) direction (mmol m^{-4}).
- β_v, horizontal oxygen gradient in the north-south (v) direction (mmol m^{-4}).
- R, oxygen consumption, through mixed layer processes, primarily respiration ($\mathrm{mmol\,m^{-2}\,s^{-1}}$ if vertically integrated, or $\mathrm{mmol\,m^{-3}\,s^{-1}}$ if volumetric).
- J, net community production ($\mathrm{mmol\,m^{-2}\,s^{-1}}$ if vertically integrated, or $\mathrm{mmol\,m^{-3}\,s^{-1}}$ if volumetric).
- h_b, is the bottom mixed layer thickness (m).

Bibliography

Aldridge, J. N., Lessin, G., Amoudry, L. O., Hicks, N., Hull, T., Klar, J. K., Kitidis, V., McNeill, C. L., Ingels, J., Parker, E. R., Silburn, B., Silva, T., Sivyer, D. B., Smith, H. E., Widdicombe, S., Woodward, E. M., van der Molen, J., Garcia, L., and Kröger, S. (2017). Comparing benthic biogeochemistry at a sandy and a muddy site in the Celtic Sea using a model and observations. *Biogeochemistry*, 135(1-2):155–182.

Alkire, M. B., D'Asaro, E., Lee, C., Jane Perry, M., Gray, A., Cetinić, I., Briggs, N., Rehm, E., Kallin, E., Kaiser, J., and González-Posada, A. (2012). Estimates of net community production and export using high-resolution, Lagrangian measurements of O2, NO3-, and POC through the evolution of a spring diatom bloom in the North Atlantic. *Deep Sea Research Part I: Oceanographic Research Papers*, 64:157–174.

Alkire, M. B., Lee, C. M., a. D'Asaro, E., Perry, M. J., Briggs, N. T., Cetinić, I., and Gray, A. M. (2014). Net community production and export from Seaglider measurements in the North Atlantic after the spring bloom. *Journal of Geophysical Research: Oceans*, 119(9):6121–6139.

Allen, J. T., Fuda, J.-L., Perivoliotis, L., Munoz-Mas, C., Alou, E., and Reeve, K. (2018). Guidelines for the delayed mode scientific correction of glider data. WP 5 , Task 5.7, D5.15. Version 4.1. Report, SOCIB - Balearic Islands Coastal Observing and Forecasting System for JERICO-NEXT.

Anderson, L. A. (1995). On the hydrogen and oxygen content of marine phytoplankton. *Deep Sea Research Part I: Oceanographic Research Papers*, 42(9):1675–1680.

Anderson, L. A. and Sarmiento, J. L. (1994). Redfield ratios of remineralization determined by nutrient data analysis. *Global Biogeochemical Cycles*, 8(1):65–80.

Andrieu, C., Doucet, A., and Holenstein, R. (2010). Particle Markov chain Monte Carlo methods. *Journal of the Royal Statistical Society: Series B (Statistical Methodology)*, 72(3):269–342.

Ashton, I. G., Shutler, J. D., Land, P. E., Woolf, D. K., and Quartly, G. D. (2016). A Sensitivity Analysis of the Impact of Rain on Regional and Global Sea-Air Fluxes of CO2. *PLOS ONE*, 11(9):e0161105.

Bahl, A., Gnanadesikan, A., and Pradal, M.-A. (2019). Variations in Ocean Deoxygenation Across Earth System Models: Isolating the Role of Parameterized Lateral Mixing. *Global Biogeochemical Cycles*, 33(6):2018GB006121.

Barone, B., Nicholson, D., Ferrón, S., Firing, E., and Karl, D. (2019). The estimation of gross oxygen production and community respiration from autonomous time-series measurements in the oligotrophic ocean. *Limnology and Oceanography: Methods*, page lom3.10340.

Bauer, J. E., Cai, W.-J., Raymond, P. A., Bianchi, T. S., Hopkinson, C. S., and Regnier, P. A. G. (2013). The changing carbon cycle of the coastal ocean. *Nature*, 504(7478):61–70.

Beale, R., Johnson, M., Liss, P., and Nightingale, P. (2014). Air–Sea Exchange of Marine Trace Gases. In *Treatise on Geochemistry*, pages 53–92. Elsevier.

Bean, T. P., Greenwood, N., Beckett, R., Biermann, L., Bignell, J. P., Brant, J. L., Copp, G. H., Devlin, M. J., Dye, S., Feist, S. W., Fernand, L., Foden, D., Hyder, K., Jenkins, C. M., van der Kooij, J., Kröger, S., Kupschus, S., Leech, C., Leonard, K. S., Lynam, C. P., Lyons, B. P., Maes, T., Nicolaus, E. E. M., Malcolm, S. J., McIlwaine, P., Merchant, N. D., Paltriguera, L., Pearce, D. J., Pitois, S. G., Stebbing, P. D., Townhill, B., Ware, S., Williams, O., and Righton, D. (2017). A Review of the Tools Used for Marine Monitoring in the UK: Combining Historic and Contemporary Methods with Modeling and Socioeconomics to Fulfill Legislative Needs and Scientific Ambitions. *Frontiers in Marine Science*, 4.

Behrenfeld, M. J. and Boss, E. S. (2014). Resurrecting the Ecological Underpinnings of Ocean Plankton Blooms. *Annual Review of Marine Science*, 6(1):167–194.

Bell, T. G., Landwehr, S., Miller, S. D., de Bruyn, W. J., Callaghan, A. H., Scanlon, B., Ward, B., Yang, M., and Saltzman, E. S. (2017). Estimation of bubble-mediated air–sea gas exchange from concurrent DMS and CO_2 transfer velocities at intermediate–high wind speeds. *Atmospheric Chemistry and Physics*, 17(14):9019–9033.

Bendtsen, J., Gustafsson, K. E., Söderkvist, J., and Hansen, J. L. (2009). Ventilation of bottom water in the North Sea–Baltic Sea transition zone. *Journal of Marine Systems*, 75(1-2):138–149.

Benson, B. B. and Krause, D. (1984). The concentration and isotopic fractionation of oxygen dissolved in freshwater and seawater in equilibrium with the atmosphere1. *Limnology and Oceanography*, 29(3):620–632.

Binetti, U., Kaiser, J., Damerell, G. M., Rumyantseva, A., Martin, A. P., Henson, S., and Heywood, K. J. (2020). Net community oxygen production derived from Seaglider deployments at the Porcupine Abyssal Plain site (PAP; northeast Atlantic) in 2012–13. *Progress in Oceanography*, 183:102293.

Bittig, H., Kortzinger, A., Johnson, K., Claustre, H., Emerson, S., Fennel, K., Garcia, H., Gilbert, D., Gruber, N., Kang, D.-J., Naqvi, W., Prakash, S., Riser, S., Thierry, V., Tilbrook, B., Uchida, H., Ulloa, O., and Xing, X. (2015). SCOR WG 142: Quality Control Procedures for Oxygen and Other Biogeochemical Sensors on Floats and Gliders. Recommendation for oxygen measurements from Argo floats, implementation of in-air-measurement routine to assure highest long-term accuracy. Technical report, SCOR WG 142.

Bittig, H., Körtzinger, A., Johnson, K., Claustre, H., Emerson, S., Fennel, K., Garcia, H., Gilbert, D., Gruber, N., Kang, D.-J., Naqvi, W., Prakash, S., Riser, S., Thierry, V., Tilbrook, B., Uchida, H., Ulloa, O., and Xing, X. (2018a). Quality Control Procedures for Oxygen and Other Biogeochemical Sensors on Floats and Gliders. Recommendations on the conversion between oxygen quantities for Bio-Argo floats and other autonomous sensor platforms. Technical report, SCOR WG 142.

Bittig, H. C., Fiedler, B., Scholz, R., Krahmann, G., and Körtzinger, A. (2014). Time response of oxygen optodes on profiling platforms and its dependence on flow speed and temperature. *Limnology and Oceanography: Methods*, 12(8):617–636.

Bittig, H. C. and Körtzinger, A. (2015). Tackling Oxygen Optode Drift: Near-Surface and In-Air Oxygen Optode Measurements on a Float Provide an Accurate in Situ Reference. *Journal of Atmospheric and Oceanic Technology*, 32(8):1536–1543.

Bittig, H. C., Körtzinger, A., Neill, C., van Ooijen, E., Plant, J. N., Hahn, J., Johnson, K. S., Yang, B., and Emerson, S. R. (2018b). Oxygen Optode Sensors: Principle, Characterization, Calibration, and Application in the Ocean. *Frontiers in Marine Science*, 4(January):1–25.

Blauw, A. N., Benincà, E., Laane, R. W. P. M., Greenwood, N., and Huisman, J. (2012). Dancing with the Tides: Fluctuations of Coastal Phytoplankton Orchestrated by Different Oscillatory Modes of the Tidal Cycle. *PLoS ONE*, 7(11):e49319.

Bozec, Y., Thomas, H., Elkalay, K., and De Baar, H. J. (2005). The continental shelf pump for CO 2 in the North Sea - Evidence from summer observation. *Marine Chemistry*, 93(2-4):131–147.

Bozec, Y., Thomas, H., Schiettecatte, L.-S., Borges, A. V., Elkalay, K., and de Baar, H. J. W. (2006). Assessment of the processes controlling the seasonal variations of dissolved inorganic carbon in the North Sea. *Limnology and Oceanography*, 51(6):2746–2762.

Braeckman, U., Van Colen, C., Guilini, K., Van Gansbeke, D., Soetaert, K., Vincx, M., and Vanaverbeke, J. (2014). Empirical Evidence Reveals Seasonally Dependent Reduction in Nitrification in Coastal Sediments Subjected to Near Future Ocean Acidification. *PLoS ONE*, 9(10):e108153.

Brainerd, K. E. and Gregg, M. C. (1995). Surface mixed and mixing layer depths. *Deep Sea Research Part I: Oceanographic Research Papers*, 42(9):1521–1543.

Breitburg, D., Levin, L. A., Oschlies, A., Grégoire, M., Chavez, F. P., Conley, D. J., Garçon, V., Gilbert, D., Gutiérrez, D., Isensee, K., Jacinto, G. S., Limburg, K. E., Montes, I., Naqvi, S. W. A., Pitcher, G. C., Rabalais, N. N., Roman, M. R., Rose, K. A., Seibel, B. A., Telszewski, M., Yasuhara, M., and Zhang, J. (2018). Declining oxygen in the global ocean and coastal waters. *Science*, 359(6371):eaam7240.

Brown, J., Carrillo, L., Fernand, L., Horsburgh, K., Hill, A., Young, E., and Medler, K. (2003). Observations of the physical structure and seasonal jet-like circulation of the Celtic Sea and St. George's Channel of the Irish Sea. *Continental Shelf Research*, 23(6):533–561.

Burson, A., Stomp, M., Akil, L., Brussaard, C. P. D., and Huisman, J. (2016). Unbalanced reduction of nutrient loads has created an offshore gradient from phosphorus to nitrogen limitation in the North Sea. *Limnology and Oceanography*, 61(3):869–888.

Bushinsky, S. M. and Emerson, S. (2013). A method for in-situ calibration of Aanderaa oxygen sensors on surface moorings. *Marine Chemistry*, 155:22–28.

Bushinsky, S. M. and Emerson, S. (2015). Marine biological production from in situ oxygen measurements on a profiling float in the subarctic Pacific Ocean. *Global Biogeochemical Cycles*, 29(12):2050–2060.

Bushinsky, S. M., Emerson, S. R., Riser, S. C., and Swift, D. D. (2016). Accurate oxygen measurements on modified argo floats using in situ air calibrations. *Limnology and Oceanography: Methods*, 14(8):491–505.

Campbell, J., Antoine, D., Armstrong, R., Arrigo, K., Balch, W., Barber, R., Behrenfeld, M., Bidigare, R., Bishop, J., Carr, M.-E., Esaias, W., Falkowski, P., Hoepffner, N., Iverson, R., Kiefer, D., Lohrenz, S., Marra, J., Morel, A., Ryan, J., Vedernikov, V., Waters, K., Yentsch, C., and Yoder, J. (2002). Comparison of algorithms for estimating ocean primary production from surface chlorophyll, temperature, and irradiance: COMPARISON OF PRIMARY PRODUCTIVITY ALGORITHMS. *Global Biogeochemical Cycles*, 16(3):9–1–9–15.

Canfield, D. E. (2014). *Oxygen: A Four Billion Year History*. Science Essentials. Princeton University Press, [2014], Princeton.

Capuzzo, E., Lynam, C. P., Barry, J., Stephens, D., Forster, R. M., Greenwood, N., McQuatters-Gollop, A., Silva, T., van Leeuwen, S. M., and Engelhard, G. H. (2018). A decline in primary production in the North Sea over 25 years, associated with reductions in zooplankton abundance and fish stock recruitment. *Global Change Biology*, 24(1):e352–e364.

Carnell, R. (2012). Lhs: Latin Hypercube Samples.

Carpenter, B., Gelman, A., Hoffman, M. D., Lee, D., Goodrich, B., Betancourt, M., Brubaker, M., Guo, J., Li, P., and Riddell, A. (2017). Stan : A Probabilistic Programming Language. *Journal of Statistical Software*, 76(1).

Carpenter, J. (1965). The Chesapeake Bay Institute technique for the winkler dissolved oxygen method. *Limnology and Oceanography*, 10(1):141–143.

Carrillo, L., Souza, A. J., Hill, A. E., Brown, J., Fernand, L., and Candela, J. (2005). Detiding ADCP data in a highly variable shelf area: The Celtic Sea. *Journal of Atmospheric and Oceanic Technology*, 22(1):84–97.

Castro-Morales, K. and Kaiser, J. (2012). Using dissolved oxygen concentrations to determine mixed layer depths in the Bellingshausen Sea. *Ocean Science*, 8(1):1–10.

Chaichana, S., Jickells, T., and Johnson, M. (2019). Interannual variability in the summer dissolved organic matter inventory of the North Sea: Implications for the continental shelf pump. *Biogeosciences*, 16(5):1073–1096.

Clarke, J. S., Humphreys, M. P., Tynan, E., Kitidis, V., Brown, I., Mowlem, M., and Achterberg, E. P. (2017). Characterization of a Time-Domain Dual Lifetime Referencing pCO2 Optode and Deployment as a High-Resolution Underway Sensor across the High Latitude North Atlantic Ocean. *Frontiers in Marine Science*, 4.

Copernicus, C. C. S. (2018). ERA5: Fifth generation of ECMWF atmospheric reanalyses of the global climate.

Cox, T. J. S., Maris, T., Soetaert, K., Kromkamp, J. C., Meire, P., and Meysman, F. (2015). Estimating primary production from oxygen time series: A novel approach in the frequency domain. *Limnology and Oceanography: Methods*, 13(10):529–552.

D'Asaro, E. A. and McNeil, C. (2013). Calibration and Stability of Oxygen Sensors on Autonomous Floats. *Journal of Atmospheric and Oceanic Technology*, 30(8):1896–1906.

de Boyer Montégut, C. (2004). Mixed layer depth over the global ocean: An examination of profile data and a profile-based climatology. *Journal of Geophysical Research*, 109(C12):C12003.

Diaz, R. J. and Rosenberg, R. (2008). Spreading Dead Zones and Consequences for Marine Ecosystems. *Science*, 321(5891):926–929.

Diesing, M., Kröger, S., Parker, R., Jenkins, C., Mason, C., and Weston, K. (2017). Predicting the standing stock of organic carbon in surface sediments of the North–West European continental shelf. *Biogeochemistry*, 135(1-2):183–200.

Doney, S. C. and Steinberg, D. K. (2013). Marine biogeochemistry: The ups and downs of ocean oxygen. *Nature Geoscience*, 6(7):515–516.

Duarte, C. M., Regaudie-de-Gioux, A., Arrieta, J. M., Delgado-Huertas, A., and Agustí, S. (2013). The Oligotrophic Ocean Is Heterotrophic. *Annual Review of Marine Science*, 5(1):551–569.

Ducklow, H. W. and Doney, S. C. (2013). What Is the Metabolic State of the Oligotrophic Ocean? A Debate. *Annual Review of Marine Science*, 5(1):525–533.

Dulière, V., Gypens, N., Lancelot, C., Luyten, P., and Lacroix, G. (2019). Origin of nitrogen in the English Channel and Southern Bight of the North Sea ecosystems. *Hydrobiologia*, 845(1):13–33.

Durbin, J. and Koopman, S. J. (2012). *Time Series Analysis by State Space Methods*. Number 38 in Oxford Statistical Science Series. Oxford University Press, Oxford, 2nd ed edition.

Duteil, O., Koeve, W., Oschlies, A., Bianchi, D., Galbraith, E., Kriest, I., and Matear, R. (2013). A novel estimate of ocean oxygen utilisation points to a reduced rate of respiration in the ocean interior. *Biogeosciences*, 10(11):7723–7738.

Emeis, K.-C., van Beusekom, J., Callies, U., Ebinghaus, R., Kannen, A., Kraus, G., Kröncke, I., Lenhart, H., Lorkowski, I., Matthias, V., Möllmann, C., Pätsch, J., Scharfe, M., Thomas, H., Weisse, R., and Zorita, E. (2015). The North Sea - A shelf sea in the Anthropocene. *Journal of Marine Systems*, 141:18–33.

Emerson, S. (1987). Seasonal oxygen cycles and biological new production in surface waters of the subarctic Pacific Ocean. *Journal of Geophysical Research*, 92(C6):6535.

Emerson, S. (2014). Annual net community production and the biological carbon flux in the ocean. *Global Biogeochemical Cycles*, 28(1):14–28.

Emerson, S. and Bushinsky, S. (2016). The role of bubbles during air-sea gas exchange. *Journal of Geophysical Research: Oceans*, 121(6):4360–4376.

Emerson, S. and Stump, C. (2010). Net biological oxygen production in the ocean—II: Remote in situ measurements of O2 and N2 in subarctic pacific surface waters. *Deep Sea Research Part I: Oceanographic Research Papers*, 57(10):1255–1265.

Emerson, S., Stump, C., and Nicholson, D. (2008). Net biological oxygen production in the ocean: Remote in situ measurements of O 2 and N 2 in surface waters. *Global Biogeochemical Cycles*, 22(3):n/a–n/a.

Fairall, C. W., Yang, M., Bariteau, L., Edson, J. B., Helmig, D., McGillis, W., Pezoa, S., Hare, J. E., Huebert, B., and Blomquist, B. (2011). Implementation of the Coupled Ocean-Atmosphere Response Experiment flux algorithm with CO 2 , dimethyl sulfide, and O 3. *Journal of Geophysical Research*, 116(10):C00F09.

Fernand, L., Weston, K., Morris, T., Greenwood, N., Brown, J., and Jickells, T. (2013). The contribution of the deep chlorophyll maximum to primary production in a seasonally stratified shelf sea, the North Sea. *Biogeochemistry*, 113(1-3):153–166.

Foden, J., Devlin, M. J., Mills, D. K., and Malcolm, S. J. (2011). Searching for undesirable disturbance: An application of the OSPAR eutrophication assessment method to marine waters of England and Wales. *Biogeochemistry*, 106(2):157–175.

Foden, J., Sivyer, D., Mills, D., and Devlin, M. (2008). Spatial and temporal distribution of chromophoric dissolved organic matter (CDOM) fluorescence and its contribution to light attenuation in UK waterbodies. *Estuarine, Coastal and Shelf Science*, 79(4):707–717.

Frew, N. M., Bock, E. J., Schimpf, U., Hara, T., Haußecker, H., Edson, J. B., McGillis, W. R., Nelson, R. K., McKenna, S. P., Uz, B. M., and Jähne, B. (2004). Air-sea gas transfer: Its dependence on wind stress, small-scale roughness, and surface films: GAS TRANSFER AND SURFACE ROUGHNESS. *Journal of Geophysical Research: Oceans*, 109(C8):n/a–n/a.

Garau, B., Ruiz, S., Zhang, W. G., Pascual, A., Heslop, E., Kerfoot, J., and Tintoré, J. (2011). Thermal lag correction on slocum CTD glider data. *Journal of Atmospheric and Oceanic Technology*, 28(9):1065–1071.

Garbe, C. S., Rutgersson, A., Boutin, J., de Leeuw, G., Delille, B., Fairall, C. W., Gruber, N., Hare, J., Ho, D. T., Johnson, M. T., Nightingale, P. D., Pettersson, H., Piskozub, J., Sahlée, E., Tsai, W.-t., Ward, B., Woolf, D. K., and Zappa, C. J. (2014). Transfer Across the Air-Sea Interface. In Liss, P. S. and Johnson, M. T., editors, *Ocean-Atmosphere Interactions of Gases and Particles*, Springer Earth System Sciences, pages 55–112. Springer, Berlin, Heidelberg.

Garcia, H. E. and Gordon, L. I. (1992). Oxygen solubility in seawater: Better fitting equations. *Limnology and Oceanography*, 37(6):1307–1312.

García-Martín, E. E., Daniels, C. J., Davidson, K., Davis, C. E., Mahaffey, C., Mayers, K. M., McNeill, S., Poulton, A. J., Purdie, D. A., Tarran, G. A., and Robinson, C. (2017a). Seasonal changes in plankton respiration and bacterial metabolism in a temperate shelf sea. *Progress in Oceanography*, page 101884.

García-Martín, E. E., Daniels, C. J., Davidson, K., Lozano, J., Mayers, K. M., McNeill, S., Mitchell, E., Poulton, A. J., Purdie, D. A., Tarran, G. A., Whyte, C., and Robinson, C. (2017b). Plankton community respiration and bacterial metabolism in a North Atlantic Shelf Sea during spring bloom development (April 2015). *Progress in Oceanography*, 177(xxxx):101873.

GEBCO, B. C. G. (2019). The GEBCO_2019 Grid - a continuous terrain model of the global oceans and land.

Gelman, A., Simpson, D., and Betancourt, M. (2017). The Prior Can Often Only Be Understood in the Context of the Likelihood. *Entropy*, 19(10):555.

Glud, R. N., Berg, P., Stahl, H., Hume, A., Larsen, M., Eyre, B. D., and Cook, P. L. M. (2016). Benthic Carbon Mineralization and Nutrient Turnover in a Scottish Sea Loch: An Integrative In Situ Study. *Aquatic Geochemistry*, 22(5-6):443–467.

Grace, M. R., Giling, D. P., Hladyz, S., Caron, V., Thompson, R. M., and Mac Nally, R. (2015). Fast processing of diel oxygen curves: Estimating stream metabolism with base (BAyesian single-station estimation). *Limnology and Oceanography: Methods*, 13(3):103–114.

Graham, J. A., O'Dea, E., Holt, J., Polton, J., Hewitt, H. T., Furner, R., Guihou, K., Brereton, A., Arnold, A., Wakelin, S., Castillo Sanchez, J. M., and Mayorga Adame, C. G. (2018). AMM15: A new high-resolution NEMO configuration for operational simulation of the European north-west shelf. *Geoscientific Model Development*, 11(2):681–696.

Greenwood, N. (2016). SmartBuoy observational network - North Dogger.

Greenwood, N., Forster, R. M., Créach, V., Painting, S. J., Dennis, A., Cutchey, S. J., Silva, T., Sivyer, D. B., and Jickells, T. (2012). Seasonal and interannual variation of the phytoplankton and copepod dynamics in Liverpool Bay. *Ocean Dynamics*, 62(2):307–320.

Greenwood, N., Hydes, D. J., Mahaffey, C., Wither, A., Barry, J., Sivyer, D. B., Pearce, D. J., Hartman, S. E., Andres, O., and Lees, H. E. (2011). Spatial and temporal variability in nutrient concentrations in Liverpool Bay, a temperate latitude region of freshwater influence. *Ocean Dynamics*, 61(12):2181–2199.

Greenwood, N., Parker, E. R., Fernand, L., Sivyer, D. B., Weston, K., Painting, S. J., Kröger, S., Forster, R. M., Lees, H. E., Mills, D. K., and Laane, R. W. P. M. (2010). Detection of low bottom water oxygen concentrations in the North Sea; implications for monitoring and assessment of ecosystem health. *Biogeosciences*, 7(4):1357–1373.

Große, F., Greenwood, N., Kreus, M., Lenhart, H.-J., Machoczek, D., Pätsch, J., Salt, L., and Thomas, H. (2016). Looking beyond stratification: A model-based analysis of the biological drivers of oxygen deficiency in the North Sea. *Biogeosciences*, 13(8):2511–2535.

Große, F., Kreus, M., Lenhart, H.-J., Pätsch, J., and Pohlmann, T. (2017). A Novel Modeling Approach to Quantify the Influence of Nitrogen Inputs on the Oxygen Dynamics of the North Sea. *Frontiers in Marine Science*, 4(November):1–21.

Gruber, N., Doney, S. C., Emerson, S. R., Gilbert, D., Kobayashi, T., Kortzinger, A., Johnson, G. C., Johnson, K. S., Riser, S. C., and Ulloa, O. (2010). Adding Oxygen to Argo: Developing a Global In Situ Observatory for Ocean Deoxygenation and Biogeochemistry. In *Proceedings of OceanObs'09: Sustained Ocean Observations and Information for Society*, pages 432–441. European Space Agency.

Guo, X., Cai, W.-J., Huang, W.-J., Wang, Y., Chen, F., Murrell, M. C., Lohrenz, S. E., Jiang, L.-Q., Dai, M., Hartmann, J., Lin, Q., and Culp, R. (2012). Carbon dynamics and community production in the Mississippi River plume. *Limnology and Oceanography*, 57(1):1–17.

Hahn, J. (2013). *Oxygen Variability and Eddy-Driven Meridional Oxygen Supply in the Tropical North East Atlantic Oxygen Minimum Zone.* Thesis, Christian-Albrechts-Universität Kiel.

Halpern, B. S., Longo, C., Lowndes, J. S. S., Best, B. D., Frazier, M., Katona, S. K., Kleisner, K. M., Rosenberg, A. A., Scarborough, C., and Selig, E. R. (2015). Patterns and Emerging Trends in Global Ocean Health. *PLOS ONE*, 10(3):e0117863.

Halpern, B. S., Walbridge, S., Selkoe, K. A., Kappel, C. V., Micheli, F., D'Agrosa, C., Bruno, J. F., Casey, K. S., Ebert, C., Fox, H. E., Fujita, R., Heinemann, D., Lenihan, H. S., Madin, E. M. P., Perry, M. T., Selig, E. R., Spalding, M., Steneck, R., and Watson, R. (2008). A Global Map of Human Impact on Marine Ecosystems. *Science*, 319(5865):948–952.

Harris, P. T., Macmillan-Lawler, M., Rupp, J., and Baker, E. K. (2014). Geomorphology of the oceans. *Marine Geology*, 352:4–24.

Haskell, W., Hammond, D., Prokopenko, M., Teel, E., Seegers, B., Ragan, M., Rollins, N., and Jones, B. (2019). Net community production in a productive coastal ocean from an autonomous buoyancy-driven glider. *Journal of Geophysical Research: Oceans*, page 2019JC015048.

Haskell, W. Z. and Fleming, J. C. (2018). Concurrent estimates of carbon export reveal physical biases in ΔO2/Ar-based net community production estimates in the Southern California Bight. *Journal of Marine Systems*, 183:23–31.

Hayduk, W. and Laudie, H. (1974). Prediction of diffusion coefficients for nonelectrolytes in dilute aqueous solutions. *AIChE Journal*, 20(3):611–615.

Hayduk, W. and Minhas, B. S. (1982). Correlations for prediction of molecular diffusivities in liquids. *The Canadian Journal of Chemical Engineering*, 60(2):295–299.

Heath, M. and Beare, D. (2008). New primary production in northwest European shelf seas, 1960–2003. *Marine Ecology Progress Series*, 363:183–203.

Hedges, J., Baldock, J., Gélinas, Y., Lee, C., Peterson, M., and Wakeham, S. (2002). The biochemical and elemental compositions of marine plankton: A NMR perspective. *Marine Chemistry*, 78(1):47–63.

Helm, I., Jalukse, L., and Leito, I. (2012). A highly accurate method for determination of dissolved oxygen: Gravimetric Winkler method. *Analytica Chimica Acta*, 741:21–31.

Helm, K. P., Bindoff, N. L., and Church, J. A. (2011). Observed decreases in oxygen content of the global ocean. *Geophysical Research Letters*, 38(23).

Hemsley, V. S., Smyth, T. J., Martin, A. P., Frajka-Williams, E., Thompson, A. F., Damerell, G., and Painter, S. C. (2015). Estimating Oceanic Primary Production Using Vertical Irradiance and Chlorophyll Profiles from Ocean Gliders in the North Atlantic. *Environmental Science & Technology*, 49(19):11612–11621.

Hickman, A. E., Holligan, P. M., Moore, C. M., Sharples, J., Krivtsov, V., and Palmer, M. R. (2009). Distribution and chromatic adaptation of phytoplankton within a shelf sea thermocline. *Limnology and Oceanography*, 54(2):525–536.

Hicks, N., Ubbara, G. R., Silburn, B., Smith, H. E., Kröger, S., Parker, E. R., Sivyer, D., Kitidis, V., Hatton, A., Mayor, D. J., and Stahl, H. (2017). Oxygen dynamics in shelf seas sediments incorporating seasonal variability. *Biogeochemistry*, 135(1-2):35–47.

Hill, A. E., Brown, J., Fernand, L., Holt, J., Horsburgh, K. J., Proctor, R., Raine, R., and Turrell, W. R. (2008). Thermohaline circulation of shallow tidal seas. *Geophysical Research Letters*, 35(11):L11605.

Hinrichs, I., Gouretski, V., Pätsch, J., Emeis, K.-C., and Stammer, D. (2017). North Sea Biogeochemical Climatology (Version 1.1).

Hoellein, T. J., Bruesewitz, D. A., and Richardson, D. C. (2013). Revisiting Odum (1956): A synthesis of aquatic ecosystem metabolism. *Limnology and Oceanography*, 58(6):2089–2100.

Holt, J., Butenschön, M., Wakelin, S. L., Artioli, Y., and Allen, J. I. (2012). Oceanic controls on the primary production of the northwest European continental shelf: Model experiments under recent past conditions and a potential future scenario. *Biogeosciences*, 9(1):97–117.

Holt, J., Wakelin, S., and Huthnance, J. (2009). Down-welling circulation of the northwest European continental shelf: A driving mechanism for the continental shelf carbon pump. *Geophysical Research Letters*, 36(14).

Holtermann, P., Prien, R., Naumann, M., and Umlauf, L. (2019). Interleaving of oxygenized intrusions into the Baltic Sea redoxcline. *Limnology and Oceanography*, n/a(00):1–22.

Holtgrieve, G. W., Schindler, D. E., Branch, T. A., and A'mar, Z. T. (2010). Simultaneous quantification of aquatic ecosystem metabolism and reaeration using a Bayesian statistical model of oxygen dynamics. *Limnology and Oceanography*, 55(3):1047–1063.

Holtgrieve, G. W., Schindler, D. E., and Jankowski, K. (2016). Comment on Demars et al. 2015, "Stream metabolism and the open diel oxygen method: Principles, practice, and perspectives". *Limnology and Oceanography: Methods*, 14(2):110–113.

Howarth, J. and Palmer, M. (2011). The Liverpool Bay Coastal Observatory. *Ocean Dynamics*, 61(11):1917–1926.

Hull, T., Greenwood, N., Kaiser, J., and Johnson, M. (2016). Uncertainty and sensitivity in optode-based shelf-sea net community production estimates. *Biogeosciences*, 13(4):943–959.

Hull, T. and Johnson, M. (2015). Airsea: R tools for air-sea gas exchange studies (0.2). Cefas.

Hull, T., Johnson, M., Greenwood, N., and Kaiser, J. (2020). Bottom mixed layer oxygen dynamics in the Celtic Sea. *Biogeochemistry*, 149(3):263–289.

Hull, T., Sivyer, D. B., Pearce, D., Greenwood, N., Needham, N., Read, C., and Fitton, E. (2017a). Shelf Sea Biogeochemistry - Celtic Deep 2 SmartBuoy.

Hull, T., Sivyer, D. B., Pearce, D., Greenwood, N., Needham, N., Read, C., and Fitton, E. (2017b). Shelf Sea Biogeochemistry - East Of Haig Fras Seabed Lander.

Hull, T., Sivyer, D. B., Pearce, D., Greenwood, N., Needham, N., Read, C., and Fitton, E. (2017c). Shelf Sea Biogeochemistry - Nymph Bank Lander.

Humphreys, M. P., Achterberg, E. P., Hopkins, J. E., Chowdhury, M. Z., Griffiths, A. M., Hartman, S. E., Hull, T., Smilenova, A., Wihsgott, J. U., S. Woodward, E. M., and Mark Moore, C. (2018). Mechanisms for a nutrient-conserving carbon pump in a seasonally stratified, temperate continental shelf sea. *Progress in Oceanography*.

Hydes, D., Hartman, M., Kaiser, J., and Campbell, J. (2009). Measurement of dissolved oxygen using optodes in a FerryBox system. *Estuarine, Coastal and Shelf Science*, 83(4):485–490.

Hydes, D. J., Kelly-Gerreyn, B. A., Le Gall, A. C., and Proctor, R. (1999). The balance of supply of nutrients and demands of biological production and denitrification in a temperate latitude shelf sea - A treatment of the southern North Sea as an extended estuary. *Marine Chemistry*, 68(1-2):117–131.

Jackson, J. B. C., Kirby, M. X., Berger, W. H., Bjorndal, K. A., Botsford, L. W., Bourque, B. J., Bradbury, R. H., Cooke, R., Erlandson, J., Estes, J. A., Hughes, T. P., Kidwell, S., Lange, C. B., Lenihan, H. S., Pandolfi, J. M., Peterson, C. H., Steneck, R. S., Tegner, M. J., and Warner, R. R. (2001). Historical Overfishing and the Recent Collapse of Coastal Ecosystems. *Science*, 293(5530):629–637.

Jafar-Sidik, M., Gohin, F., Bowers, D., Howarth, J., and Hull, T. (2017). The relationship between Suspended Particulate Matter and Turbidity at a mooring station in a coastal environment: Consequences for satellite-derived products. *Oceanologia*, 59(3):365–378.

Jickells, T. D. (1998). Nutrient Biogeochemistry of the Coastal Zone. *Science*, 281(5374):217–222.

Johnson, K. S., Coletti, L. J., and Chavez, F. P. (2006). Diel nitrate cycles observed with in situ sensors predict monthly and annual new production. *Deep Sea Research Part I: Oceanographic Research Papers*, 53(3):561–573.

Johnson, M. T. (2010). A numerical scheme to calculate temperature and salinity dependent air-water transfer velocities for any gas. *Ocean Science*, 6(4):913–932.

Johnson, M. T., Greenwood, N., Sivyer, D. B., Thomson, M., Reeve, A., Weston, K., and Jickells, T. D. (2013). Characterising the seasonal cycle of dissolved organic nitrogen using Cefas SmartBuoy high-resolution time-series samples from the southern North Sea. *Biogeochemistry*, 113(1-3):23–36.

Johnson, M. T., Hughes, C., Bell, T. G., and Liss, P. S. (2011). A Rumsfeldian analysis of uncertainty in air-sea gas exchange. In Komori, S., McGillis, W., and Kurose, R., editors, *Gas Transfer at Water Surfaces*, pages 464–485. Kyoto University Press.

Joint, I., Owens, N., and Pomeroy, A. (1986). Seasonal production of photosynthetic picoplankton and nanoplankton in the Celtic Sea. *Marine Ecology Progress Series*, 28:251–258.

Juranek, L. W., Hamme, R. C., Kaiser, J., Wanninkhof, R., and Quay, P. D. (2010). Evidence of O $_2$ consumption in underway seawater lines: Implications for air-sea O $_2$ and CO $_2$ fluxes: RESPIRATION IN UNDERWAY LINES. *Geophysical Research Letters*, 37(1):n/a–n/a.

Kaiser, J., Reuer, M. K., Barnett, B., and Bender, M. L. (2005). Marine productivity estimates from continuous O 2 /Ar ratio measurements by membrane inlet mass spectrometry. *Geophysical Research Letters*, 32(19):n/a–n/a.

Kara, A. B., Rochford, P. A., and Hurlburt, H. E. (2000). An optimal definition for ocean mixed layer depth. *Journal of Geophysical Research: Oceans*, 105(C7):16803–16821.

Karl, D. M., Laws, E. A., Morris, P., leB. Williams, P. J., and Emerson, S. (2003). Metabolic balance of the open sea: Global carbon cycle (communication arising). *Nature*, 426(6962):32–32.

Keeling, R. F. (1993). On the role of large bubbles in air-sea gas exchange and supersaturation in the ocean. *Journal of Marine Research*, 51(2):237–271.

Keeling, R. F. and Shertz, S. R. (1992). Seasonal and interannual variations in atmospheric oxygen and implications for the global carbon cycle. *Nature*, 358(6389):723–727.

Keeling, R. F., Stephens, B. B., Najjar, R. G., Doney, S. C., Archer, D., and Heimann, M. (1998). Seasonal variations in the atmospheric O2/N2 ratio in relation to the kinetics of air-sea gas exchange. *Global Biogeochemical Cycles*, 12(1):141–163.

Kemp, W. M., Testa, J. M., Conley, D. J., Gilbert, D., and Hagy, J. D. (2009). Temporal responses of coastal hypoxia to nutrient loading and physical controls. *Biogeosciences*, 6(12):2985–3008.

Kitidis, V., Hardman-Mountford, N. J., Litt, E., Brown, I., Cummings, D., Hartman, S., Hydes, D., Fishwick, J. R., Harris, C., Martinez-Vicente, V., Woodward, E. M. S., and Smyth, T. J. (2012). Seasonal dynamics of the carbonate system in the Western English Channel. *Continental Shelf Research*, 42:30–40.

Kitidis, V., Shutler, J. D., Ashton, I., Warren, M., Brown, I., Findlay, H., Hartman, S. E., Sanders, R., Humphreys, M., Kivimäe, C., Greenwood, N., Hull, T., Pearce, D., McGrath, T., Stewart, B. M., Walsham, P., McGovern, E., Bozec, Y., Gac, J.-P., van Heuven, S. M. A. C., Hoppema, M., Schuster, U., Johannessen, T., Omar, A., Lauvset, S. K., Skjelvan, I., Olsen, A., Steinhoff, T., Körtzinger, A., Becker, M., Lefevre, N., Diverrès, D., Gkritzalis, T., Cattrijsse, A., Petersen, W., Voynova, Y. G., Chapron, B., Grouazel, A., Land, P. E., Sharples, J., and Nightingale, P. D. (2019). Winter weather controls net influx of atmospheric CO 2 on the north-west European shelf. *Scientific Reports*, 9(1):20153.

Kitidis, V., Tait, K., Nunes, J., Brown, I., Woodward, E. M., Harris, C., Sabadel, A. J., Sivyer, D. B., Silburn, B., and Kröger, S. (2017). Seasonal benthic nitrogen cycling in a temperate shelf sea: The Celtic Sea. *Biogeochemistry*, 135(1-2):103–119.

Kitidis, V., Tilstone, G. H., Serret, P., Smyth, T. J., Torres, R., and Robinson, C. (2014). Oxygen photolysis in the Mauritanian upwelling: Implications for net community production. *Limnology and Oceanography*, 59(2):299–310.

Klar, J. K., Homoky, W. B., Statham, P. J., Birchill, A. J., Harris, E. L., Woodward, E. M. S., Silburn, B., Cooper, M. J., James, R. H., Connelly, D. P., Chever, F., Lichtschlag, A., and Graves, C. (2017). Stability of dissolved and soluble Fe(II) in shelf sediment pore waters and release to an oxic water column. *Biogeochemistry*, 135(1-2):49–67.

Kummu, M., de Moel, H., Salvucci, G., Viviroli, D., Ward, P. J., and Varis, O. (2016). Over the hills and further away from coast: Global geospatial patterns of human and environment over the 20th–21st centuries. *Environmental Research Letters*, 11(3):034010.

Laliberté, M. (2007). Model for Calculating the Viscosity of Aqueous Solutions. *Journal of Chemical & Engineering Data*, 52(2):321–335.

Langdon, C. (2010). Determination of Dissolved Oxygen in Seawater by Winkler Titration Using the Amperometric Technique. In *GO-SHIP Repeat Hydrography Manual: A Collection of Expert Reports and Guidelines*, volume ICPO Publication Series 134 of *IOCCP Report 14*. ICPO.

Large, W. G. and Pond, S. (1981). Open Ocean Momentum Flux Measurements in Moderate to Strong Winds. *Journal of Physical Oceanography*, 11(3):324–336.

Larsen, M., Thamdrup, B., Shimmield, T., and Glud, R. N. (2013). Benthic mineralization and solute exchange on a Celtic Sea sand-bank (Jones Bank). *Progress in Oceanography*, 117:64–75.

Laruelle, G. G., Cai, W.-J., Hu, X., Gruber, N., Mackenzie, F. T., and Regnier, P. (2018). Continental shelves as a variable but increasing global sink for atmospheric carbon dioxide. *Nature Communications*, 9(1):454.

Lawrenz, E., Silsbe, G., Capuzzo, E., Ylöstalo, P., Forster, R. M., Simis, S. G. H., Prášil, O., Kromkamp, J. C., Hickman, A. E., Moore, C. M., Forget, M.-H., Geider, R. J., and Suggett, D. J. (2013). Predicting the Electron Requirement for Carbon Fixation in Seas and Oceans. *PLoS ONE*, 8(3):e58137.

Laws, E. A. (1991). Photosynthetic quotients, new production and net community production in the open ocean. *Deep Sea Research Part A. Oceanographic Research Papers*, 38(1):143–167.

Legge, O., Johnson, M., Hicks, N., Jickells, T., Diesing, M., Aldridge, J., Andrews, J., Artioli, Y., Bakker, D. C. E., Burrows, M. T., Carr, N., Cripps, G., Felgate, S. L., Fernand, L., Greenwood, N., Hartman, S., Kröger, S., Lessin, G., Mahaffey, C., Mayor, D. J., Parker, R., Queirós, A. M., Shutler, J. D., Silva, T., Stahl, H., Tinker, J., Underwood, G. J. C., Van Der Molen, J., Wakelin, S., Weston, K., and Williamson, P. (2020). Carbon on the Northwest European Shelf: Contemporary Budget and Future Influences. *Frontiers in Marine Science*, 7.

Lehahn, Y., D'Ovidio, F., and Koren, I. (2018). A Satellite-Based Lagrangian View on Phytoplankton Dynamics. *Annual Review of Marine Science*, 10(1):99–119.

Li, Y.-H. and Peng, T.-H. (2002). Latitudinal change of remineralization ratios in the oceans and its implication for nutrient cycles. *Global Biogeochemical Cycles*, 16(4):77–1–77–16.

Liang, J.-H., Deutsch, C., McWilliams, J. C., Baschek, B., Sullivan, P. P., and Chiba, D. (2013). Parameterizing bubble-mediated air-sea gas exchange and its effect on ocean ventilation. *Global Biogeochemical Cycles*, 27(3):894–905.

Liang, J.-H., Emerson, S. R., D'Asaro, E. A., McNeil, C. L., Harcourt, R. R., Sullivan, P. P., Yang, B., and Cronin, M. F. (2017). On the role of sea-state in bubble-mediated air-sea gas flux during a winter storm. *Journal of Geophysical Research: Oceans*, 122(4):2671–2685.

Liss, P. S. and Duce, R. A. (1997). *The Sea Surface and Global Change*. Cambridge University Press.

Liu, K.-K., Atkinson, L., Quiñones, R., Talaue-McManus, L., and International Geosphere-Biosphere Programme, editors (2010). *Carbon and Nutrient Fluxes in Continental Margins*. Global Change – The IGBP Series. Springer Berlin Heidelberg, Berlin, Heidelberg.

Luisetti, T., Turner, R. K., Andrews, J. E., Jickells, T. D., Kröger, S., Diesing, M., Paltriguera, L., Johnson, M. T., Parker, E. R., Bakker, D. C. E., and Weston, K. (2019). Quantifying and valuing carbon flows and stores in coastal and shelf ecosystems in the UK. *Ecosystem Services*, 35:67–76.

Mahaffey, C., Palmer, M., Greenwood, N., and Sharples, J. (2020). Impacts of climate change on dissolved oxygen concentration relevant to the coastal and marine environment around the UK. *MCCIP Science Review 2020*, page 23 pages.

Marino, S., Hogue, I. B., Ray, C. J., and Kirschner, D. E. (2008). A methodology for performing global uncertainty and sensitivity analysis in systems biology. *Journal of Theoretical Biology*, 254(1):178–196.

Marrec, P., Cariou, T., Macé, E., Morin, P., Salt, L. A., Vernet, M., Taylor, B., Paxman, K., and Bozec, Y. (2015). Dynamics of air-sea CO2 fluxes in the northwestern European shelf based on voluntary observing ship and satellite observations. *Biogeosciences*, 12(18):5371–5391.

Mathis, M., Elizalde, A., Mikolajewicz, U., and Pohlmann, T. (2015). Variability patterns of the general circulation and sea water temperature in the North Sea. *Progress in Oceanography*, 135:91–112.

McKinley, G. A., Fay, A. R., Lovenduski, N. S., and Pilcher, D. J. (2017). Natural Variability and Anthropogenic Trends in the Ocean Carbon Sink. *Annual Review of Marine Science*, 9(1):125–150.

McNeil, C. and D'Asaro, E. (2007). Parameterization of air–sea gas fluxes at extreme wind speeds. *Journal of Marine Systems*, 66(1-4):110–121.

McNeil, C. L. and D'Asaro, E. A. (2014). A calibration equation for oxygen optodes based on physical properties of the sensing foil. *Limnology and Oceanography: Methods*, 12(3):139–154.

Meier, H. E. M., Edman, M., Eilola, K., Placke, M., Neumann, T., Andersson, H. C., Brunnabend, S.-E., Dieterich, C., Frauen, C., Friedland, R., Gröger, M., Gustafsson, B. G., Gustafsson, E., Isaev, A., Kniebusch, M., Kuznetsov, I., Müller-Karulis, B., Naumann, M., Omstedt, A., Ryabchenko, V., Saraiva, S., and Savchuk, O. P. (2019). Assessment of Uncertainties in Scenario Simulations of Biogeochemical Cycles in the Baltic Sea. *Frontiers in Marine Science*, 6.

Millero, F. J. and Poisson, A. (1981). International one-atmosphere equation of state of seawater. *Deep Sea Research Part A. Oceanographic Research Papers*, 28(6):625–629.

Moreno, A. R., Garcia, C. A., Larkin, A. A., Lee, J. A., Wang, W.-L., Moore, J. K., Primeau, F. W., and Martiny, A. C. (2020). Latitudinal gradient in the respiration quotient and the implications for ocean oxygen availability. *Proceedings of the National Academy of Sciences*, 117(37):22866–22872.

Moum, J. N. and Smyth, W. D. (2001). Upper Ocean Mixing Processes*. In Steele, J. H., editor, *Encyclopedia of Ocean Sciences (Second Edition)*, pages 185–191. Academic Press, Oxford.

Mouriño-Carballido, B. and Anderson, L. A. (2009). Net community production of oxygen derived from in vitro and in situ 1-D modeling techniques in a cyclonic mesoscale eddy in the Sargasso Sea. *Biogeosciences*, 6(8):1799–1810.

Muller-Karger, F. E., Varela, R., Thunell, R., Luerssen, R., Hu, C., and Walsh, J. J. (2005). The importance of continental margins in the global carbon cycle. *Geophysical Research Letters*, 32(1).

Najjar, R. G. and Keeling, R. F. (2000). Mean annual cycle of the air-sea oxygen flux: A global view. *Global Biogeochemical Cycles*, 14(2):573–584.

Neubacher, E. C., Parker, R. E., and Trimmer, M. (2013). The potential effect of sustained hypoxia on nitrogen cycling in sediment from the southern North Sea: A mesocosm experiment. *Biogeochemistry*, 113(1-3):69–84.

Nicholson, D., Emerson, S., and Eriksen, C. C. (2008). Net community production in the deep euphotic zone of the subtropical North Pacific gyre from glider surveys. *Limnology and Oceanography*, 53(5part2):2226–2236.

Nicholson, D. P. and Feen, M. L. (2017). Air calibration of an oxygen optode on an underwater glider. *Limnology and Oceanography: Methods*, 15(5):495–502.

Nicholson, D. P., Wilson, S. T., Doney, S. C., and Karl, D. M. (2015). Quantifying subtropical North Pacific gyre mixed layer primary productivity from Seaglider observations of diel oxygen cycles. *Geophysical Research Letters*, 42(10):4032–4039.

Nielsen, T., Løkkegaard, B., Richardson, K., Bo Pedersen, R., and Hansen, L. (1993). Structure of plankton communities in the Dogger Bank area (North Sea) during a stratified situation. *Marine Ecology Progress Series*, 95:115–131.

Nightingale, P. D., Malin, G., Law, C. S., Watson, A. J., Liss, P. S., Liddicoat, M. I., Boutin, J., and Upstill-Goddard, R. C. (2000). In situ evaluation of air-sea gas exchange parameterizations using novel conservative and volatile tracers. *Global Biogeochemical Cycles*, 14(1):373–387.

Nunes, M. S. w. c. f. T., Heuer, C., Marshall, J., Sanchez, J., Thornton, R., Reiczigel, J., Robison-Cox, J., Sebastiani, P., Solymos, P., Yoshida, K., Jones, G., Pirikahu, S., Firestone, S., Kyle, R., Popp, J., and Reynard, M. J. a. C. (2014). epiR: Tools for the Analysis of Epidemiological Data.

Nylund, A. T., Arneborg, L., Tengberg, A., Mallast, U., and Hassellöv, I.-M. (2020). *In Situ* observations of turbulent ship wakes and their potential implications for vertical mixing. *Ocean Science Discussions*, pages 1–29.

O'Dea, E., Furner, R., Wakelin, S., Siddorn, J., While, J., Sykes, P., King, R., Holt, J., and Hewitt, H. (2017). The CO5 configuration of the 7 km Atlantic Margin Model: Large-scale biases and sensitivity to forcing, physics options and vertical resolution. *Geoscientific Model Development*, 10(8):2947–2969.

Odum, H. T. (1956). Primary Production in Flowing Waters. *Limnology and Oceanography*, 1(2):102–117.

Ostle, C., Johnson, M., Landschützer, P., Schuster, U., Hartman, S., Hull, T., and Robinson, C. (2014). Net community production in the North Atlantic Ocean derived from Volunteer Observing Ship data. *Global Biogeochemical Cycles*, 29(1):80–95.

Painting, S. J. and Forster, R. M. (2013). Marine Ecosystem Connections: Essential indicators of healthy, productive and biologically diverse seas. *Biogeochemistry*, 113(1-3):1–7.

Painting, S. J., van der Molen, J., Parker, E. R., Coughlan, C., Birchenough, S., Bolam, S., Aldridge, J. N., Forster, R. M., and Greenwood, N. (2013). Development of indicators of ecosystem functioning in a temperate shelf sea: A combined fieldwork and modelling approach. *Biogeochemistry*, 113(1):237–257.

Palevsky, H. I., Quay, P. D., and Nicholson, D. P. (2016). Discrepant estimates of primary and export production from satellite algorithms, a biogeochemical model, and geochemical tracer measurements in the North Pacific Ocean. *Geophysical Research Letters*, 43(16):8645–8653.

Palevsky, H. I., Ribalet, F., Swalwell, J. E., Cosca, C. E., Cokelet, E. D., Feely, R. A., Armbrust, E. V., and Quay, P. D. (2013). The influence of net community production and phytoplankton community structure on CO $_2$ uptake in the Gulf of Alaska: GULF OF ALASKA NCP, PHYTOPLANKTON, AND CO $_2$. *Global Biogeochemical Cycles*, 27(3):664–676.

Palmer, M. R. (2010). The modification of current ellipses by stratification in the Liverpool Bay ROFI. *Ocean Dynamics*, 60(2):219–226.

Palmer, M. R. and Polton, J. A. (2011). A strain-induced freshwater pump in the Liverpool Bay ROFI. *Ocean Dynamics*, 61(11):1905–1915.

Palmer, M. R., Rippeth, T. P., and Simpson, J. H. (2008). An investigation of internal mixing in a seasonally stratified shelf sea. *Journal of Geophysical Research: Oceans*, 113(C12):1–14.

Palmer, M. R., Williams, C., and Horseburgh, K. (2018). Synoptic multi-variable multi-glider study. Technical Report D4.3, NERC.

Panton, A., Mahaffey, C., Greenwood, N., Hopkins, J., Montagnes, D., and Sharples, J. (2012). Short-term and seasonal variation in metabolic balance in Liverpool Bay. *Ocean Dynamics*, 62(2):295–306.

Pauly, D., Christensen, V., Guénette, S., Pitcher, T. J., Sumaila, U. R., Walters, C. J., Watson, R., and Zeller, D. (2002). Towards sustainability in world fisheries. *Nature*, 418(6898):689–695.

Pelland, N. A., Eriksen, C. C., Emerson, S. R., and Cronin, M. F. (2018). Seaglider surveys at Ocean Station Papa: Oxygen kinematics and upper-ocean metabolism. *Journal of Geophysical Research: Oceans.*

Pereira, R., Ashton, I., Sabbaghzadeh, B., Shutler, J. D., and Upstill-Goddard, R. C. (2018). Reduced air–sea CO2 exchange in the Atlantic Ocean due to biological surfactants. *Nature Geoscience*, 11(7):492–496.

Pingree, R. D., Holligan, P. M., Mardell, G. T., and Head, R. N. (1976). The influence of physical stability on spring, summer and autumn phytoplankton blooms in the Celtic Sea. *Journal of the Marine Biological Association of the United Kingdom*, 56(04):845.

Platt, T. and Sathyendranath, S. (2008). Ecological indicators for the pelagic zone of the ocean from remote sensing. *Remote Sensing of Environment*, 112(8):3426–3436.

Platt, T., Sathyendranath, S., Joint, I., and Fasham, M. J. R. (1993). Photosynthesis characteristics of the phytoplankton in the Celtic Sea during late spring. *Fisheries Oceanography*, 2(3-4):191–201.

Plumeridge, A. A. and Roberts, C. M. (2017). Conservation targets in marine protected area management suffer from shifting baseline syndrome: A case study on the Dogger Bank. *Marine Pollution Bulletin*, 116(1):395–404.

Polson, N. G. and Scott, J. G. (2012). On the Half-Cauchy Prior for a Global Scale Parameter. *Bayesian Analysis*, 7(4):887–902.

Polton, J. A., Palmer, M. R., and Howarth, M. J. (2011). Physical and dynamical oceanography of Liverpool Bay. *Ocean Dynamics*, 61(9):1421–1439.

Polton, J. A., Palmer, M. R., and Howarth, M. J. (2013). The vertical structure of time-mean estuarine circulation in a shallow, rotating, semi-enclosed coastal bay: A Liverpool Bay case study with application for monitoring. *Continental Shelf Research*, 59:115–126.

Possenti, L., Skjelvan, I., Atamanchuk, D., Tengberg, A., Humphreys, M. P., Loucaides, S., Fernand, L., and Kaiser, J. (2020). Norwegian Sea net community production estimated from O_2 and prototype CO_2 optode measurements on a Seaglider. *Ocean Science Discussions*, pages 1–35.

Powley, H. R., Bruggeman, J., Hopkins, J., Smyth, T., and Blackford, J. (2020). Sensitivity of Shelf Sea Marine Ecosystems to Temporal Resolution of Meteorological Forcing. *Journal of Geophysical Research: Oceans*, 125(7):e2019JC015922.

Pujol, A. J. a. G., Iooss, B., Veiga, S. D., Broto, w. c. f. B., Boumhaout, K., Delage, T., Amri, R. E., Fruth, J., Gilquin, L., Guillaume, J., Gratiet, L. L., Lemaitre, P., Marrel, A., Meynaoui, A., Nelson, B. L., Monari, F., Oomen, R., Rakovec, O., Ramos, B., Roustant, O., Song, E., Staum, J., Sueur, R., Touati, T., and Weber, F. (2014). Sensitivity: Global Sensitivity Analysis of Model Outputs.

Queste, B. (2013). *Hydrographic Observations of Oxygen and Related Physical Variables in the North Sea and Western Ross Sea Polynya.* PhD thesis, University of East Anglia.

Queste, B. Y., Fernand, L., Jickells, T. D., and Heywood, K. J. (2013). Spatial extent and historical context of North Sea oxygen depletion in August 2010. *Biogeochemistry*, 113(1):53–68.

Queste, B. Y., Fernand, L., Jickells, T. D., Heywood, K. J., and Hind, A. J. (2016). Drivers of summer oxygen depletion in the central North Sea. *Biogeosciences*, 13(4):1209–1222.

Reuer, M. K., Barnett, B. A., Bender, M. L., Falkowski, P. G., and Hendricks, M. B. (2007). New estimates of Southern Ocean biological production rates from O2/Ar ratios and the triple isotope composition of O2. *Deep Sea Research Part I: Oceanographic Research Papers*, 54(6):951–974.

Riegman, R., Malschaert, H., and Colijn, F. (1990). Primary production of phytoplankton at a frontal zone located at the northern slope of the Dogger Bank (North Sea). *Marine Biology*, 105(2):329–336.

Robinson, C., Tilstone, G., Rees, A., Smyth, T., Fishwick, J., Tarran, G., Luz, B., Barkan, E., and David, E. (2009). Comparison of in vitro and in situ plankton production determinations. *Aquatic Microbial Ecology*, 54(1):13–34.

Rovelli, L., Dengler, M., Schmidt, M., Sommer, S., Linke, P., and McGinnis, D. F. (2016). Thermocline mixing and vertical oxygen fluxes in the stratified central North Sea. *Biogeosciences*, 13(5):1609–1620.

Salt, L. A., Thomas, H., Prowe, A. E. F., Borges, A. V., Bozec, Y., and de Baar, H. J. W. (2013). Variability of North Sea pH and CO2 in response to North Atlantic Oscillation forcing. *Journal of Geophysical Research: Biogeosciences*, 118(4):1584–1592.

Saltelli, A., editor (2008). *Sensitivity Analysis.* Wiley Paperback Series. Wiley, Chichester, paperback ed edition.

Schmidtko, S., Stramma, L., and Visbeck, M. (2017). Decline in global oceanic oxygen content during the past five decades. *Nature*, 542(7641):335–339.

Seguro, I., Marca, A. D., Painting, S. J., Shutler, J. D., Suggett, D. J., and Kaiser, J. (2019). High-resolution net and gross biological production during a Celtic Sea spring bloom. *Progress in Oceanography*, 177:101885.

Sharples, J., Ellis, J. R., Nolan, G., and Scott, B. E. (2013). Fishing and the oceanography of a stratified shelf sea. *Progress in Oceanography*, 117:130–139.

Sharples, J., Mayor, D. J., Poulton, A. J., Rees, A. P., and Robinson, C. (2019). Shelf Sea Biogeochemistry: Nutrient and carbon cycling in a temperate shelf sea water column. *Progress in Oceanography*, 177:102182.

Sharples, J., Middelburg, J. J., Fennel, K., and Jickells, T. D. (2017). What proportion of riverine nutrients reaches the open ocean?: Riverine Nutrients Reaching the Ocean. *Global Biogeochemical Cycles*, 31(1):39–58.

Sharples, J., Moore, C. M., Hickman, A. E., Holligan, P. M., Tweddle, J. F., Palmer, M. R., and Simpson, J. H. (2009). Internal tidal mixing as a control on continental margin ecosystems. *Geophysical Research Letters*, 36(23).

Sharples, J., Tweddle, J. F., Green, J. A. M., Palmer, M. R., Kim, Y.-N., Hickman, A. E., Holligan, P. M., Moore, C. M., Rippeth, T. P., Simpson, J. H., and Krivtsov, V. (2007). Spring-neap modulation of internal tide mixing and vertical nitrate fluxes at a shelf edge in summer. *Limnology and Oceanography*, 52(5):1735–1747.

Silburn, B., Kröger, S., Parker, E. R., Sivyer, D. B., Hicks, N., Powell, C. F., Johnson, M., and Greenwood, N. (2017). Benthic pH gradients across a range of shelf sea sediment types linked to sediment characteristics and seasonal variability. *Biogeochemistry*, 135(1-2):69–88.

Silverman, J., Lazar, B., and Erez, J. (2004). Monitoring the Health of Coral Reef Ecosystems Using Community Metabolism. In Rosenberg, E. and Loya, Y., editors, *Coral Health and Disease*, pages 367–376. Springer, Berlin, Heidelberg.

Skákala, J., Ford, D., Bruggeman, J., Hull, T., Kaiser, J., King, R. R., Loveday, B., Palmer, M. R., Smyth, T., Williams, C. A. J., and Ciavatta, S. (2021). Towards a Multi-Platform Assimilative System for North Sea Biogeochemistry. *Journal of Geophysical Research: Oceans*, 126(4):e2020JC016649.

Smyth, T. J., Allen, I., Atkinson, A., Bruun, J. T., Harmer, R. A., Pingree, R. D., Widdicombe, C. E., and Somerfield, P. J. (2014). Ocean Net Heat Flux

Influences Seasonal to Interannual Patterns of Plankton Abundance. *PLOS ONE*, 9(6):e98709.

Solan, M., Bennett, E. M., Mumby, P. J., Leyland, J., and Godbold, J. A. (2020). Benthic-based contributions to climate change mitigation and adaptation. *Philosophical Transactions of the Royal Society B: Biological Sciences*, 375(1794):20190107.

Stanev, E., Badewien, T., Freund, H., Grayek, S., Hahner, F., Meyerjürgens, J., Ricker, M., Schöneich-Argent, R., Wolff, J., and Zielinski, O. (2019). Extreme westward surface drift in the North Sea: Public reports of stranded drifters and Lagrangian tracking. *Continental Shelf Research*, 177(March):24–32.

Stanley, R. H. R., Jenkins, W. J., Lott, D. E., and Doney, S. C. (2009). Noble gas constraints on air-sea gas exchange and bubble fluxes. *Journal of Geophysical Research*, 114(C11):C11020.

Stanley, R. H. R., Kirkpatrick, J. B., Cassar, N., Barnett, B. A., and Bender, M. L. (2010). Net community production and gross primary production rates in the western equatorial Pacific: WESTERN EQUATORIAL PACIFIC PRODUCTION. *Global Biogeochemical Cycles*, 24(4):n/a–n/a.

Stevens, E. D. (1992). Use of plastic materials in oxygen-measuring systems. *Journal of Applied Physiology*, 72(2):801–804.

Stramma, L., Schmidtko, S., Levin, L. A., and Johnson, G. C. (2010). Ocean oxygen minima expansions and their biological impacts. *Deep Sea Research Part I: Oceanographic Research Papers*, 57(4):587–595.

Sullivan, P. P., Romero, L., McWilliams, J. C., and Melville, W. K. (2012). Transient Evolution of Langmuir Turbulence in Ocean Boundary Layers Driven by Hurricane Winds and Waves. *Journal of Physical Oceanography*, 42(11):1959–1980.

Takagaki, N. and Komori, S. (2007). Effects of rainfall on mass transfer across the air-water interface. *Journal of Geophysical Research*, 112(C6):C06006.

Takeshita, Y., McGillis, W., Briggs, E. M., Carter, A. L., Donham, E. M., Martz, T. R., Price, N. N., and Smith, J. E. (2016). Assessment of net community production and calcification of a coral reef using a boundary layer approach. *Journal of Geophysical Research: Oceans*, 121(8):5655–5671.

Tengberg, A. and Hovdenes, J. (2014). Information on long-term stability and accuracy of Aanderaa oxygen optodes. Information about multipoint calibration system and sensor option overview. Technical report, Aanderaa Data Instruments.

Tengberg, A., Hovdenes, J., Andersson, H. J., Brocandel, O., Diaz, R., Hebert, D., Arnerich, T., Huber, C., Körtzinger, A., Khripounoff, A., Rey, F., Rönning, C., Schimanski, J., Sommer, S., and Stangelmayer, A. (2006). Evaluation of a lifetime-based optode to measure oxygen in aquatic systems. *Limnology and Oceanography: Methods*, 4(2):7–17.

Terrill, E. J. and Taylor, G. R. L. (2015). Entrainment of Air at the Transoms of Full-Scale Surface Ships. *Journal of Ship Research*, 59(1):49–65.

Tett, P., Gowen, R., Mills, D., Fernandes, T., Gilpin, L., Huxham, M., Kennington, K., Read, P., Service, M., Wilkinson, M., and Malcolm, S. (2007). Defining and detecting undesirable disturbance in the context of marine eutrophication. *Marine Pollution Bulletin*, 55(1):282–297.

Tett, P., Gowen, R., Painting, S., Elliott, M., Forster, R., Mills, D., Bresnan, E., Capuzzo, E., Fernandes, T., Foden, J., Geider, R., Gilpin, L., Huxham, M., McQuatters-Gollop, A., Malcolm, S., Saux-Picart, S., Platt, T., Racault, M., Sathyendranath, S., van der Molen, J., and Wilkinson, M. (2013). Framework for understanding marine ecosystem health. *Marine Ecology Progress Series*, 494:1–27.

Thomas, H. (2004). Enhanced Open Ocean Storage of CO2 from Shelf Sea Pumping. *Science*, 304(5673):1005–1008.

Thomas, H., Bozec, Y., de Baar, H. J. W., Elkalay, K., Frankignoulle, M., Schiettecatte, L.-S., Kattner, G., and Borges, A. V. (2005a). The carbon budget of the North Sea. *Biogeosciences*, 2(1):87–96.

Thomas, H., Bozec, Y., Elkalay, K., de Baar, H. J. W., Borges, A. V., and Schiettecatte, L.-S. (2005b). Controls of the surface water partial pressure of CO_2 in the North Sea. *Biogeosciences*, 2(4):323–334.

Thompson, C. E. L., Silburn, B., Williams, M. E., Hull, T., Sivyer, D., Amoudry, L. O., Widdicombe, S., Ingels, J., Carnovale, G., McNeill, C. L., Hale, R., Marchais, C. L., Hicks, N., Smith, H. E. K., Klar, J. K., Hiddink, J. G., Kowalik, J., Kitidis, V., Reynolds, S., Woodward, E. M. S., Tait, K., Homoky, W. B., Kröger, S., Bolam, S., Godbold, J. A., Aldridge, J., Mayor, D. J., Benoist, N. M. A., Bett, B. J., Morris, K. J., Parker, E. R., Ruhl, H. A., Statham, P. J., and Solan, M. (2017). An approach for the identification of exemplar sites for scaling up targeted field observations of benthic biogeochemistry in heterogeneous environments. *Biogeochemistry*, 135(1-2):1–34.

Thomson, R. E. (2003). Estimating Mixed Layer Depth from Oceanic Profile Data. *JOURNAL OF ATMOSPHERIC AND OCEANIC TECHNOLOGY*, 20:11.

Tijssen, S. and Eijgenraam, A. (1982). Primary and community production in the southern bight of the north sea deduced from oxygen concentration variations in the spring of 1980. *Netherlands Journal of Sea Research*, 16:247–259.

Tilstone, G. H., Xie, Y.-y., Robinson, C., Serret, P., Raitsos, D. E., Powell, T., Aranguren-Gassis, M., Garcia-Martin, E. E., and Kitidis, V. (2015). Satellite estimates of net community production indicate predominance of net autotrophy in the Atlantic Ocean. *Remote Sensing of Environment*, 164:254–269.

Trimmer, M., Nedwell, D., Sivyer, D., and Malcolm, S. (2000). Seasonal benthic organic matter mineralisation measured by oxygen uptake and denitrification along a transect of the inner and outer River Thames estuary, UK. *Marine Ecology Progress Series*, 197:103–119.

Uchida, H. (2010). CTD oxygen sensor calibration procedures. In *GO-SHIP Repeat Hydrography Manual : A Collection of Expert Reports and Guidelines*, volume ICPO Publication Series 134 of *IOCCP Report 14*. ICPO.

Uchida, H., Kawano, T., Kaneko, I., and Fukasawa, M. (2008). In Situ Calibration of Optode-Based Oxygen Sensors. *Journal of Atmospheric and Oceanic Technology*, 25(12):2271–2281.

Vincent, A. G., Pascal, R. W., Beaton, A. D., Walk, J., Hopkins, J. E., Woodward, E. M. S., Mowlem, M., and Lohan, M. C. (2018). Nitrate drawdown during a shelf sea spring bloom revealed using a novel microfluidic in situ chemical sensor deployed within an autonomous underwater glider. *Marine Chemistry*, 205(July):29–36.

Volk, T. and Hoffert, M. I. (1985). Ocean Carbon Pumps: Analysis of Relative Strengths and Efficiencies in Ocean-Driven Atmospheric CO2 Changes. In *The Carbon Cycle and Atmospheric CO2: Natural Variations Archean to Present*, Geophysical Monograph Series, pages 99–110. American Geophysical Union (AGU).

Wakelin, S. L., Artioli, Y., Holt, J. T., Butenschön, M., and Blackford, J. (2020). Controls on near-bed oxygen concentration on the Northwest European Continental Shelf under a potential future climate scenario. *Progress in Oceanography*, 187:102400.

Wanninkhof, R. (1992). Relationship between wind speed and gas exchange over the ocean. *Journal of Geophysical Research*, 97(C5):7373.

Wanninkhof, R. (2014). Relationship between wind speed and gas exchange over the ocean revisited. *Limnology and Oceanography: Methods*, 12(6):351–362.

Wanninkhof, R., Asher, W. E., Ho, D. T., Sweeney, C., and McGillis, W. R. (2009). Advances in Quantifying Air-Sea Gas Exchange and Environmental Forcing. *Annual Review of Marine Science*, 1(1):213–244.

Weiss, R. and Price, B. (1980). Nitrous oxide solubility in water and seawater. *Marine Chemistry*, 8(4):347–359.

Weiss, R. F. (1970). The solubility of nitrogen, oxygen and argon in water and seawater. *Deep Sea Research and Oceanographic Abstracts*, 17(4):721–735.

Weston, K., Fernand, L., Mills, D. K., Delahunty, R., and Brown, J. (2005). Primary production in the deep chlorophyll maximum of the central North Sea. *Journal of Plankton Research*, 27(9):909–922.

Weston, K., Greenwood, N., Fernand, L., Pearce, D. J., and Sivyer, D. B. (2008). Environmental controls on phytoplankton community composition in the Thames plume, U.K. *Journal of Sea Research*, 60(4):246–254.

Wihsgott, J., Hopkins, J. E., Sharples, J., Jones, E., and Balfour, C. A. (2016). Long-term mooring observations of full depth water column structure spanning 17 months, collected in a temperate shelf sea (Celtic Sea).

Wihsgott, J. U., Sharples, J., Hopkins, J. E., Woodward, E. M. S., Hull, T., Greenwood, N., and Sivyer, D. B. (2019). Observations of vertical mixing in autumn and its effect on the autumn phytoplankton bloom. *Progress in Oceanography*, 177(August 2018):102059.

Wikle, C. K., Milliff, R. F., Herbei, R., and Leeds, W. B. (2013). Modern Statistical Methods in Oceanography: A Hierarchical Perspective. *Statistical Science*, 28(4):466–486.

Wikner, J., Panigrahi, S., Nydahl, A., Lundberg, E., Båmstedt, U., and Tengberg, A. (2013). Precise continuous measurements of pelagic respiration in coastal waters with Oxygen Optodes: Precise continuous respiration method. *Limnology and Oceanography: Methods*, 11(1):1–15.

Wilke, C. R. and Chang, P. (1955). Correlation of diffusion coefficients in dilute solutions. *AIChE Journal*, 1(2):264–270.

Williams, C., Sharples, J., Mahaffey, C., and Rippeth, T. (2013a). Wind-driven nutrient pulses to the subsurface chlorophyll maximum in seasonally stratified shelf seas. *Geophysical Research Letters*, 40(20):5467–5472.

Williams, P. J. L. B. (1998). The balance of plankton respiration and photosynthesis in the open oceans. *Nature*, 394(6688):55–57.

Williams, P. J. l. B., Quay, P. D., Westberry, T. K., and Behrenfeld, M. J. (2013b). The Oligotrophic Ocean Is Autotrophic. *Annual Review of Marine Science*, 5(1):535–549.

Woolf, D., Shutler, J., Goddijn-Murphy, L., Watson, A., Chapron, B., Nightingale, P., Donlon, C., Piskozub, J., Yelland, M., Ashton, I., Holding, T., Schuster, U., Girard-Ardhuin, F., Grouazel, A., Piolle, J.-F., Warren, M., Wrobel-Niedzwiecka, I., Land, P., Torres, R., Prytherch, J., Moat, B., Hanafin, J., Ardhuin, F., and Paul, F. (2019). Key Uncertainties in the Recent Air-Sea Flux of CO 2. *Global Biogeochemical Cycles*, page 2018GB006041.

Woolf, D. K. (2005). Parametrization of gas transfer velocities and sea-state-dependent wave breaking. *Tellus B*, 57(2):87–94.

Woolf, D. K., Land, P. E., Shutler, J. D., Goddijn-Murphy, L. M., and Donlon, C. J. (2016). On the calculation of air-sea fluxes of CO 2 in the presence of temperature and salinity gradients. *Journal of Geophysical Research: Oceans*, 121(2):1229–1248.

Woolf, D. K., Leifer, I. S., Nightingale, P. D., Rhee, T. S., Bowyer, P., Caulliez, G., de Leeuw, G., Larsen, S. E., Liddicoat, M., Baker, J., and Andreae, M. O. (2007). Modelling of bubble-mediated gas transfer: Fundamental principles and a laboratory test. *Journal of Marine Systems*, 66(1-4):71–91.

Woolf, D. K. and Thorpe, S. A. (1991). Bubbles and the air-sea exchange of gases in near-saturation conditions. *Journal of Marine Research*, 49(3):435–466.

Zhang, J.-Z., Berberian, G., and Wanninkhof, R. (2002). Long-term storage of natural water samples for dissolved oxygen determination. *Water Research*, 36(16):4165–4168.